



# **FORMATION OF SILICON NITRIDE STRUCTURES BY DIRECT ELECTRON-BEAM WRITING**

BRYMER HAN-YU CHIN

APPROVED FOR PUBLIC RELEASE. DISTRIBUTION UNLIMITED.

REPORT DOCUMENTATION PAGE		READ INSTRUCTIONS BEFORE COMPLETING FORM
1. REPORT NUMBER	2. GOVT ACCESSION NO.	3. RECIPIENT'S CATALOG NUMBER
4. TITLE (and Subtitle) FORMATION OF SILICON NITRIDE STRUCTURES BY DIRECT ELECTRON-BEAM WRITING		5. TYPE OF REPORT & PERIOD COVERED Technical Report
7. AUTHOR(s) Brymer Han-Yu Chin		6. PERFORMING ORG. REPORT NUMBER R-940; UILU-ENG 82-2206
9. PERFORMING ORGANIZATION NAME AND ADDRESS Coordinated Science Laboratory University of Illinois at Urbana-Champaign Urbana, IL 61801		8. CONTRACT OR GRANT NUMBER(s) N00014-79-C-0424
11. CONTROLLING OFFICE NAME AND ADDRESS Joint Services Electronics Program		10. PROGRAM ELEMENT, PROJECT, TASK AREA & WORK UNIT NUMBERS
14. MONITORING AGENCY NAME & ADDRESS (if different from Controlling Office)		12. REPORT DATE February 1982
		13. NUMBER OF PAGES 255
		15. SECURITY CLASS. (of this report) UNCLASSIFIED
		15a. DECLASSIFICATION/DOWNGRADING SCHEDULE
16. DISTRIBUTION STATEMENT (of this Report)  Approved for public release; distribution unlimited		
17. DISTRIBUTION STATEMENT (of the abstract entered in Block 20, if different from Report)		
18. SUPPLEMENTARY NOTES		
19. KEY WORDS (Continue on reverse side if necessary and identify by block number)		
20. ABSTRACT (Continue on reverse side if necessary and identify by block number) Localized deposits of silicon nitride, which are stable to at least 500° C, have been formed by a new technique: electron bombardment of nitrogen molecules weakly bound on a clean Si(100)-(2 × 1) surface chilled to T ~ 30° K. This process is fairly efficient; for an initial coverage of one monolayer of molecular nitrogen, we estimate the effective dissociation cross section (primary electron energy = 2000 eV) to be (0.54 - 1.2) × 10 <sup>-15</sup> cm <sup>2</sup> . Using Auger electron spectroscopy and LEED, we have studied the growth of a silicon		



nitride/silicon interface rigorously free from contamination and from damage due to sputtering or ion implantation. In the Si(LVV) Auger spectrum of silicon nitride, a strong peak at 83 eV predominates; the 91-eV peak characteristic of clean Si vanishes entirely for sufficiently thick nitride films ( $\sim 25 - 30 \text{ \AA}$ ). LEED measurements, with the substrate at  $T \sim 30^\circ \text{ K}$ , reveal no ordered overlayers--the pattern stays  $(2 \times 1)$ , but the background increases with nitridation until a fully disordered structure results. Our Auger and LEED data further indicates that the initial stage of electron-induced nitridation is the formation of a monolayer of chemisorbed nitrogen via the nucleation and lateral growth of islands.

Preliminary experiments have demonstrated that local deposits of silicon dioxide may be formed by the same technique used for nitridation: electron-stimulated oxidation is more rapid with the substrate at  $T \sim 30^\circ \text{ K}$  than at room temperature. With proper outgassing of all vacuum components, particularly hot filaments, oxidation proceeds without the simultaneous growth of a surface carbon layer.

FORMATION OF SILICON NITRIDE STRUCTURES  
BY DIRECT ELECTRON-BEAM WRITING

BY

BRYMER HAN-YU CHIN

B.S., Massachusetts Institute of Technology, 1974  
M.S., University of Illinois, 1975

THESIS

Submitted in partial fulfillment of the requirements  
for the degree of Doctor of Philosophy in Physics  
in the Graduate College of the  
University of Illinois at Urbana-Champaign, 1982

Urbana, Illinois



To My Very Own Sivvy

...We have come so far, it is over...

from "Edge" by Sylvia Plath

## ACKNOWLEDGEMENTS

I welcome this opportunity to thank the key people responsible for the success of this program. First plaudits go to the technical staff of the Coordinated Science Laboratory: in particular, I wish to express my deepest respect and gratitude to two first-rate craftsmen (and great guys, to boot!) Bill Lawrence and George Bouck. Next, I would like to commend the storekeepers in the Coordinated Science Laboratory, Materials Research Laboratory, and Electrical Engineering Department who procured the (literally) thousands of parts necessary for this project--special thanks to Clay Lofton of CSL and Carroll Sarver and Jack Rindt of MRL. With particular pleasure, I present my personal kudos to John Woodhouse of MRL for the SEM analyses and Cliff Herman of M.I.T. for continuing aid through all these long years. Lastly, a blanket encomium for the sundry members of the CSL secretarial, drafting, photographic, and printing services who assisted with the production of this thesis--however, Jack Gladin, photographer extraordinaire, deserves individual note for his paradigmatic professionalism; and Phyllis Young gets my personal 'Thanks, Kiddo' for typing the final copy on short notice.

This work was supported by the Joint Services Electronics Program (U.S. Army, U.S. Navy, and U.S. Air Force) under Contract No. N00014-79-C-0424.



CHAPTER	Page
I. INTRODUCTION.....	1
I.A. General Orientation.....	1
I.B. Review of Surface-Analysis Techniques.....	3
I.B.1. LEED.....	4
I.B.2. Auger Electron Spectroscopy.....	9
REFERENCES FOR CHAPTER I.....	17
II. REVIEW OF PREVIOUS WORK.....	19
II.A. Adsorption of Nitrogen on Silicon and Germanium.....	19
II.B. Auger Spectra of CVD-Si <sub>3</sub> N <sub>4</sub> .....	22
II.C. Electron-Beam Induced Adsorption.....	24
REFERENCES FOR CHAPTER II.....	26
III. EXPERIMENTAL APPARATUS.....	29
III.A. Vacuum System.....	29
III.B. Sample Holder and Chill.....	34
III.C. Temperature Control.....	46
III.C.1. High Temperatures.....	46
III.C.2. Low Temperatures.....	59
III.D. Limitations of the Present Designs.....	66
III.E. Surface-Analysis Instrumentation.....	67
III.E.1. LEED.....	67
III.E.2. Auger.....	70
REFERENCES FOR CHAPTER III.....	76

CHAPTER	Page
IV. SAMPLE PREPARATION.....	77
IV.A. Wafer Preparation.....	77
IV.A.1. Cutting and Grinding.....	77
IV.A.2. Polishing.....	78
IV.A.3. Chemical Cleaning.....	91
IV.A.4. Characterization.....	92
IV.B. Vacuum Processing.....	92
IV.B.1. Review of Techniques.....	92
IV.B.2. Ion Bombardment and Annealing.....	96
REFERENCES FOR CHAPTER IV.....	110
V. RESULTS.....	113
V.A. Auger Spectrum of Clean Si.....	113
V.B. Adsorption of Nitrogen at Room Temperature.....	113
V.C. Adsorption of Nitrogen at Low Temperatures.....	116
V.C.1. Experimental Procedures.....	116
V.C.2. Uniformity and Stability of Molecular Nitrogen Layers.....	118
V.D. Electron-Beam Induced Nitridation.....	119
V.E. Key Features of the Auger Spectra.....	142
V.F. Auger Intensities as a Function of Nitridation.....	146
V.F.1. Convention for Auger Intensities.....	146
V.F.2. Specific Features of the Auger Spectra.....	147
V.F.3. Normalization of Auger Intensities.....	151
V.F.4. Plots of Auger Intensities.....	151



CHAPTER	Page
V.G. Speculations on Growth Mechanisms.....	160
V.G.1. Maximum Thickness.....	176
V.G.2. Initial Stage of Nitridation.....	178
V.G.3. Intermediate Stage of Nitridation.....	184
V.G.4. Final Stage of Nitridation.....	190
V.H. Beam-Enhanced Adsorption.....	191
V.I. Further Characterization.....	192
V.I.1. LEED Examination.....	192
V.I.2. Saturation Electron Dose.....	194
V.J. Silicon Nitride Structures Formed by Direct Electron-Beam Writing: Thermal Stability and Spatial Profile.....	217
V.K. Summary: Nitrogen on Si(100).....	217
V.L. Formation of Silicon Dioxide Structures by Direct Electron-Beam Writing: Preliminary Results.....	227
V.L.1. Chemisorption of Oxygen on Si(100) at Room Temperature.....	228
V.L.2. Electron-Stimulated Oxidation at Room Temperature.....	234
V.L.3. Electron-Stimulated Oxidation at Low Temperatures.....	239
V.L.4. Summary: Oxygen on Si(100).....	248
REFERENCES FOR CHAPTER V.....	250
VITA.....	255

## FORMATION OF SILICON NITRIDE STRUCTURES

BY DIRECT ELECTRON-BEAM WRITING

Brymer Han-Yu Chin, Ph.D.

Coordinated Science Laboratory  
and Department of Physics  
University of Illinois at Urbana-Champaign, 1982

## ABSTRACT

Localized deposits of silicon nitride, which are stable to at least 500° C, have been formed by a new technique: electron bombardment of nitrogen molecules weakly bound on a clean Si(100)-(2 × 1) surface chilled to  $T \sim 30^\circ$  K. This process is fairly efficient; for an initial coverage of one monolayer of molecular nitrogen, we estimate the effective dissociation cross section (primary electron energy = 2000 eV) to be  $(0.54 - 1.2) \times 10^{-15} \text{ cm}^2$ . Using Auger electron spectroscopy and LEED, we have studied the growth of a silicon nitride/silicon interface rigorously free from contamination and from damage due to sputtering or ion implantation. In the Si(LVV) Auger spectrum of silicon nitride, a strong peak at 83 eV predominates; the 91-eV peak characteristic of clean Si vanishes entirely for sufficiently thick nitride films ( $\sim 25 - 30 \text{ \AA}$ ). LEED measurements, with the substrate at  $T \sim 30^\circ$  K, reveal no ordered overlayers--the pattern stays (2 × 1), but the background increases with nitridation until a fully disordered structure results. Our Auger and LEED data further indicates that the initial stage of electron-induced nitridation is the formation of a monolayer of chemisorbed nitrogen via the nucleation and lateral growth of islands.



Preliminary experiments have demonstrated that local deposits of silicon dioxide may be formed by the same technique used for nitridation: electron-stimulated oxidation is more rapid with the substrate at  $T \sim 30^\circ \text{K}$  than at room temperature. With proper outgassing of all vacuum components, particularly hot filaments, oxidation proceeds without the simultaneous growth of a surface carbon layer.

## CHAPTER I

### INTRODUCTION

#### I.A. General Orientation

Since the early days of transistor development, the interaction of adsorbates with semiconductors has been extensively studied. In very general terms, most of the research has fallen into either of two categories: (1) the characterization of thin films grown on 'real' surfaces under process conditions<sup>1</sup> or (2) fundamental studies of adsorbate behavior on 'atomically clean' surfaces under ultrahigh vacuum conditions.<sup>2</sup> But, now, with the big push into very large scale integration (VLSI)<sup>3</sup> and with molecular beam epitaxy (MBE)<sup>4</sup> coming on line, process control on the atomic level has become essential; and the distinction between the two categories is rapidly blurring. There is increasing interest, then, in understanding adsorbates from the initial interactions of atoms or molecules with a clean surface to the subsequent growth of thin films. As one very important example, we may cite the numerous experiments involving the chemisorption of oxygen on silicon and the growth of silicon dioxide layers.<sup>5</sup> The oxygen/silicon system has received considerable attention not only because  $\text{SiO}_2$  is a crucial insulator in semiconductor device fabrication but also because oxygen readily reacts with silicon--that is, the oxygen/silicon system is amenable to analysis under controlled conditions. As a note of caution, however, we should point out that, in spite of the extensive studies, this system is by no means well understood.

Another insulator which is widely utilized in microelectronics is silicon nitride ( $\text{Si}_3\text{N}_4$ ).<sup>6</sup> In contrast to the oxygen/silicon system, there have been no studies of the chemisorption of nitrogen on silicon and few surface analyses of  $\text{Si}_3\text{N}_4$  films.<sup>7</sup> This situation has arisen, partly because silicon

nitride was introduced into device manufacture much later than silicon dioxide, but principally because nitrogen does not readily react with silicon. At room temperature, nitrogen does not adsorb on a silicon surface<sup>8</sup>; and, even with pressures of  $\sim 1$  atm and substrate temperatures of  $\sim 1200^\circ\text{C}$ , the thermal reaction is very slow.<sup>9</sup> For device applications, silicon nitride films  $\sim 500$ - $1500\text{ \AA}$  thick have been routinely produced by chemical vapor deposition<sup>6</sup> on a heated silicon substrate; but this technique cannot be used in situ in an ultrahigh vacuum surface-analysis chamber. Additionally, if a film is produced in a separate vessel and then transferred into the analysis chamber, the outer, contaminated layer of the film needs to be sputtered away prior to surface analysis. Sputtering, however, alters the chemical composition of the film and leads to confusing results.<sup>7</sup>

Obviously, a new approach to the nitrogen/silicon system is needed. As in the oxygen/silicon system, we would ideally like to study the chemisorption of nitrogen on silicon and the growth of  $\text{Si}_3\text{N}_4$  films under atomically clean conditions. Indeed, direct nitridation of silicon would be important not only for analytical studies but also for practical film growth: new VLSI designs require silicon nitride films less than  $100\text{ \AA}$  thick for improved device characteristics, and CVD films in this thickness range are inadequate.<sup>9</sup> Direct nitridation should yield superior results; but, so far, thermal nitridation has proven difficult to achieve and control.<sup>9,10</sup> Furthermore, a nitridation process inherently capable of producing localized deposits with fine spatial resolution would be highly desirable for both basic studies and VLSI fabrication. Experiments on surface diffusion<sup>11</sup> have yielded much valuable information on the binding and mobility of adsorbates;

such experiments require the formation of an initial concentration gradient--in other words, a localized deposit. For VLSI processing, conventional photolithography is not suitable<sup>12</sup>; a possible alternative approach is the fabrication of device structures by direct writing,<sup>13,14</sup> that is, without masking and etching.

The major thrust of this work is the presentation of a new technique for the nitridation of silicon under atomically clean conditions. Following Polak's<sup>15</sup> work on the electron-induced chemisorption of nitrogen on W(110), we have succeeded in creating localized deposits of silicon nitride by using an electron beam to dissociate nitrogen molecules adsorbed on a clean silicon surface at cryogenic temperatures. The experimental results are presented in the first (and major) portion of Chapter V. To check the generality of this technique, we have also briefly explored its application to  $\text{SiO}_2$  structures; preliminary results are reported at the end of Chapter V. The rest of the thesis is organized as follows. After a review of the apropos literature (Chapter II), a detailed description of the ultrahigh vacuum equipment especially constructed for this project is given in Chapter III. Chapter IV is a step-by-step prescription for preparing atomically clean and ordered silicon surfaces.

#### I.B. Review of Surface-Analysis Techniques

Before we launch into the details of our program a brief review of surface-analysis techniques is in order. The two fundamental properties of any solid-state system are, of course, atomic structure and chemical composition. In surface work, the chief tools for examining these properties are, respectively, low energy electron diffraction (LEED) and Auger electron spectroscopy.



## I.B.1. LEED

First, let's consider LEED.<sup>16</sup> For tutorial purposes, we can consider LEED as the surface analog of Laue back reflection. Instead of using X-rays, which penetrate into the bulk, we use low-energy electrons (typically  $\sim 20$ -500 eV) to sample the top several atomic layers. In the idealized situation, a monochromatic plane wave with wavevector  $\vec{k}_i$  and energy  $E_i = \hbar^2 k_i^2 / (2M)$ , where  $M$  = electron mass, is incident on an infinite two-dimensional lattice defined by the basis vectors  $\vec{a}_1$  and  $\vec{a}_2$ . The diffracted beams are determined by the Laue conditions

$$k_s = k_i \quad (1.1)$$

$$\vec{k}_{s,mn} = \vec{k}_i + \vec{G}_{mn}, \quad (1.2)$$

where  $\vec{k}$  is the surface component of  $\vec{k}$ , and the subscripts  $s$  and  $i$  refer to the scattered and incident waves, respectively.  $\vec{G}_{mn}$  are the surface reciprocal lattice vectors

$$\vec{G}_{mn} = m\vec{A}_1 + n\vec{A}_2. \quad (1.3)$$

Here,  $m$  and  $n$  are integers, and  $\vec{A}_1$  and  $\vec{A}_2$  are basis vectors of the reciprocal lattice ( $\vec{a}_1 \cdot \vec{A}_1 = \vec{a}_2 \cdot \vec{A}_2 = 2\pi, \vec{a}_1 \cdot \vec{A}_2 = \vec{a}_2 \cdot \vec{A}_1 = 0$ ). The Laue conditions are neatly displayed in the Ewald-sphere construction (see Fig. 1.1).

Many surfaces exhibit reconstruction; that is, the surface unit cell is not the same as that of an ideally truncated bulk lattice. For the surface of interest, Si(100), there are two possible reconstructions, which depend on the method of surface preparation.<sup>17</sup> The so-called  $(2 \times 1)$  reconstruction, which is produced by ion bombardment and annealing, is shown in Fig. 1.2.

Figure 1.1. Ewald sphere construction for primary wave  $\vec{k}_i$  normally incident on a square surface lattice (lying in X-Y plane). (a) Projection onto X-Y plane. (b) Projection onto X-Z plane. Diffraction occurs when the constant energy sphere of radius  $k_i$  intersects the surface reciprocal lattice rods. Projection (a) shows diffraction spots as they would actually appear on LEED screen.

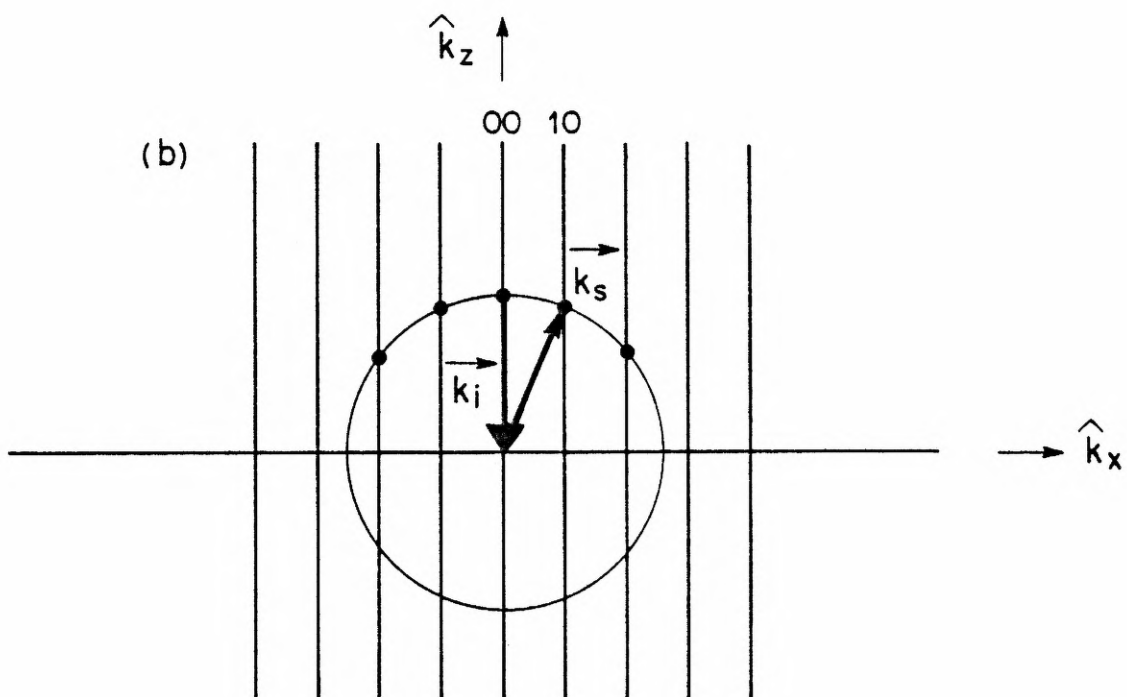
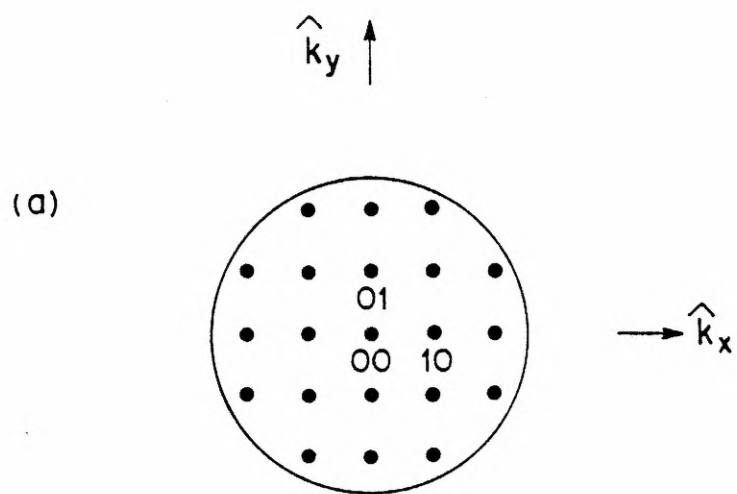


Figure 1.2. LEED pattern for Si(100)-(2×1) reconstruction. (a) Reciprocal space.

Solid dots show ideal square unit cell. Open circles are diffraction spots actually observed. Extra circles are referred to as 'half-order' spots.

(b) Reciprocal space. Decomposition of pattern (a) into

mixture of two domains oriented at  $90^\circ$  to each other. Each domain

has a rectangular unit cell with one side the same as that of the

ideal square cell and the other side half as long. (c) Real space

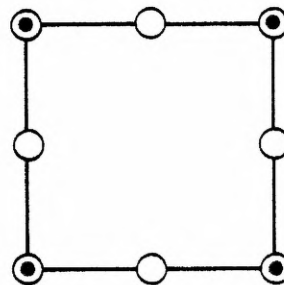
unit cells corresponding to (b). Closed dots form ideal square lattice.

Open circles indicate rectangular unit cell with one side the same as

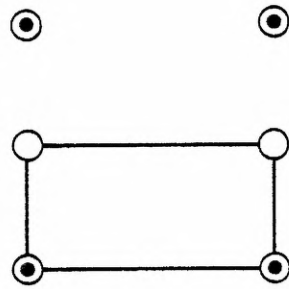
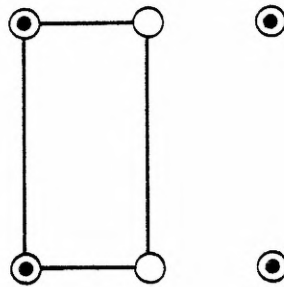
that of the ideal square cell and the other side twice as long--

hence, the designation (2×1).

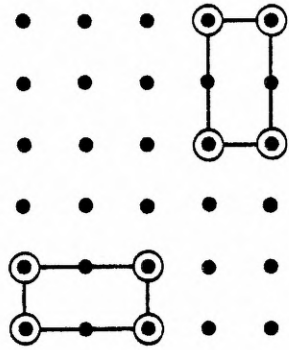
(a)



(b)



(c)





Although LEED specialists do extensive measurements in an attempt to sort out precise atomic positions, we can also use LEED simply as a diagnostic technique (much as most people use Laue) (1) to check basic symmetry and alignment,<sup>18</sup> (2) to get a qualitative indication of the degree of surface ordering (from spot/background sharpness),<sup>18</sup> and (3) to determine the presence of topographical features such as step arrays (from splitting of spots).<sup>19</sup>

#### I.B.2. Auger Electron Spectroscopy

Auger electron spectroscopy<sup>20</sup> is quite similar to X-ray fluorescence: instead of detecting characteristic X-rays, we detect characteristic secondary electrons, which have a short escape depth and, so, are surface sensitive. The basic process is as follows. Consider a simplistic shell diagram of electrons in an atom (Fig. 1.3). An incident electron (1), with typical primary energy  $\sim 1\text{-}10$  keV, crashes into the atom and knocks out an electron (2) from the Z shell. An electron (3) then drops from the Y shell into the hole left behind in the Z shell. The atom is still energetically unstable so an Auger electron (4) can be ejected. The important thing to note is that the exit Auger energy is characteristic of the particular atom

$$E_{\text{Auger}} = E_Z - E_Y - E_X \quad . \quad (1.4)$$

Additionally, Auger electrons from a solid can yield information about chemical binding. In a solid, of course, the outer electrons form a valence band with a density of states characteristic of the chemical environment. Transitions of the LVV sort (see Fig. 1.4), for instance, can probe the

Figure 1.3. Schematic of an atomic Auger transition.

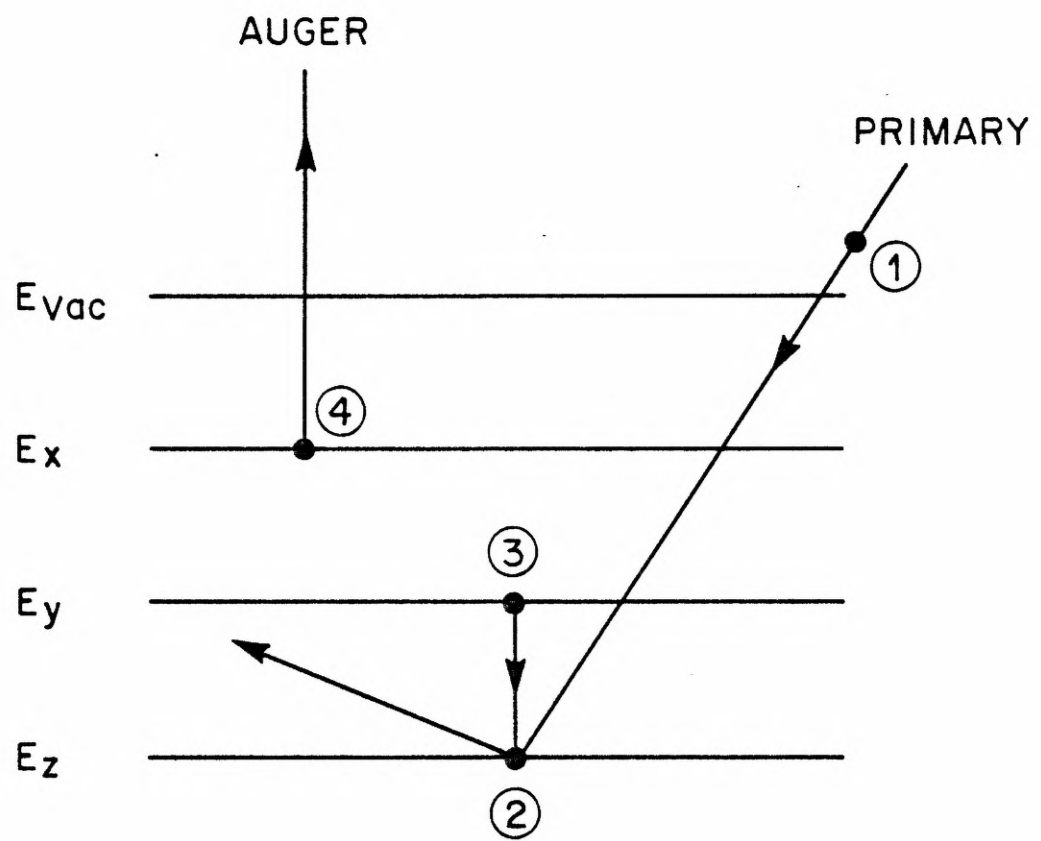
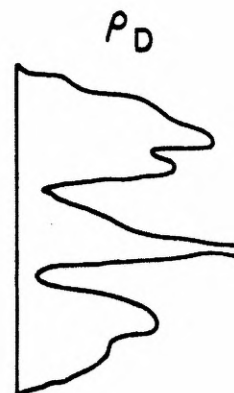
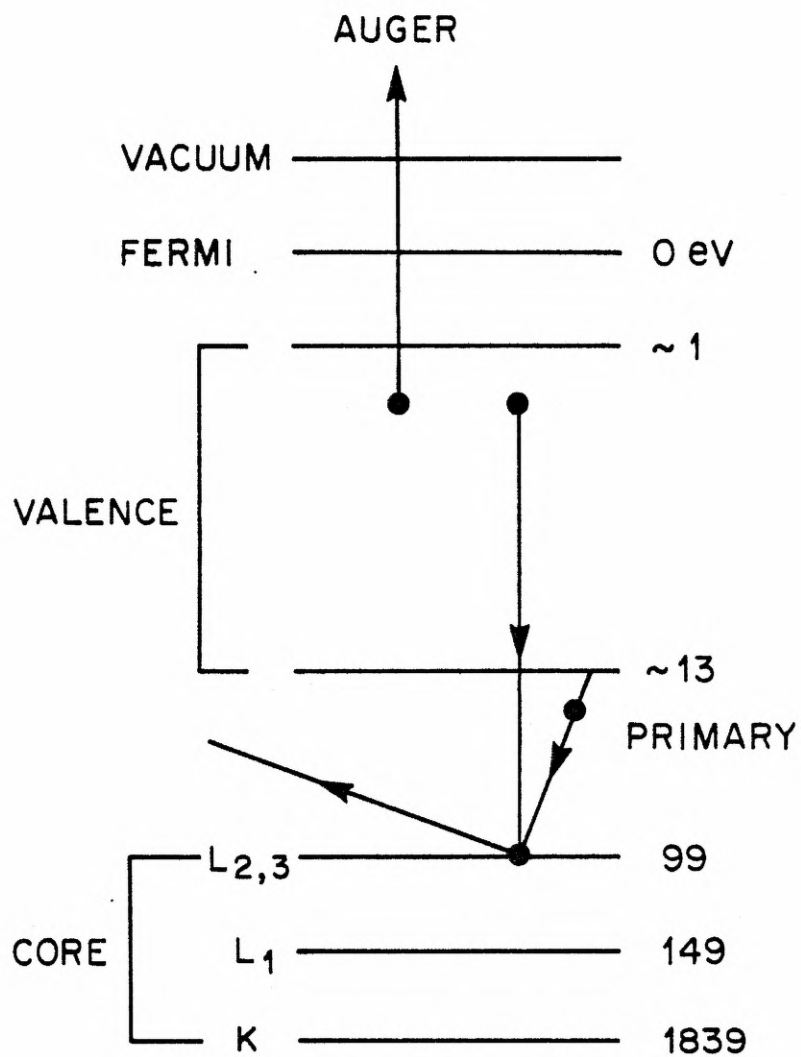


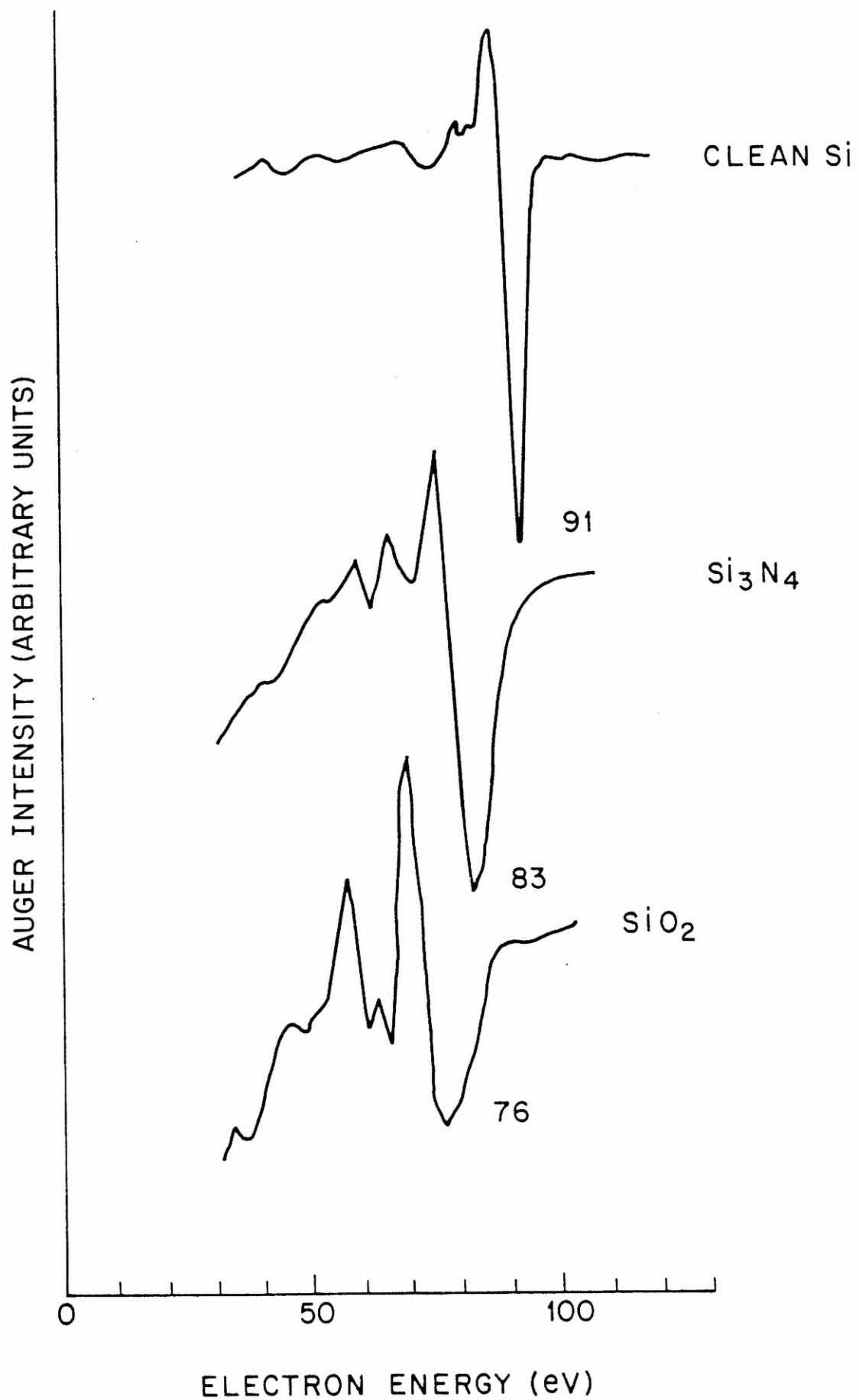
Figure 1.4. Schematic of a Si(LVV) Auger transition.  $\rho_D$  is the density of states.



valence structure. (Chemical shifts in core levels can also be seen in some cases.) As a specific example, we compare the Si(LVV) spectra in three different states (Fig. 1.5). The strongest line shifts from 91 eV in clean Si to 83 eV in  $\text{Si}_3\text{N}_4$  to 76 eV in  $\text{SiO}_2$ .<sup>21</sup>



Figure 1.5. Si(LVV) Auger spectra in three different chemical states.



## REFERENCES FOR CHAPTER I.

1. For a review of older studies, see A. Many, Y. Goldstein, and N. B. Grover, Semiconductor Surfaces (North-Holland Publishing Co., Amsterdam, 1965).
2. For more recent work, see C. G. Scott and C. E. Reed, editors, Surface Physics of Phosphors and Semiconductors (Academic Press, London, 1975).
3. J. Lyman, Electronics 53 (14), 115 (1980).
4. P. E. Luscher, W. S. Knodle, and Y. Chai, Electronics 53 (19), 160 (1980).
5. For a recent summary, see C. M. Garner, I. Lindau, C. Y. Su, P. Pianetta, and W. E. Spicer, Phys. Rev. B 19, 3944 (1979).
6. For a recent review on silicon nitride thin films, see C.-E. Morosanu, Thin Solid Films 65, 171 (1980).
7. See Chapter II.
8. J. T. Law and E. E. Francois, J. Phys. Chem. 59, 543 (1955).
9. T. Ito, S. Hijiya, T. Nozaki, H. Arakawa, M. Shinoda, and Y. Fukukawa, J. Electrochem. Soc. 125, 448 (1978).
10. T. Ito, T. Nozaki, H. Arakawa, and M. Shinoda, Appl. Phys. Lett. 32, 330 (1978).
11. For a review, see H. P. Bonzel, in Surface Physics of Materials, V. II., edited by J. M. Blakely (Academic Press, New York, 1975), Chapter 6, pp. 279-338.

12. R. K. Watts and J. H. Bruning, Solid State Technol. 24 (5), 99 (1981).
13. D. H. Phillips, Solid State Technol. 24 (7), 77 (1981).
14. D. J. Ehrlich, R. M. Osgood, Jr., and T. F. Deutsch, Appl. Phys. Lett. 38, 1018 (1981).
15. A. J. Polak, Ph.D. Thesis, University of Illinois at Urbana-Champaign (1977).
16. A detailed account of LEED is given by J. B. Pendry, Low Energy Electron Diffraction (Academic Press, London, 1974).
17. See, for example, M. J. Cardillo and G. E. Becker, Phys. Rev. B 21, 1497 (1980).
18. P. J. Estrup and E. G. McRae, Surf. Sci. 25, 1 (1975).
19. M. Henzler, Appl. Phys. 9, 11 (1976).
20. Although many reviews of Auger electron spectroscopy have appeared in recent years, the two most useful ones are still C. C. Chang, Surf. Sci. 25, 53 (1971) and C. C. Chang, in Characterization of Solid Surfaces, edited by P. F. Kane and G. B. Larrabee (Plenum Press, New York, 1974), Chapter 20, pp. 509-575.
21. The clean Si spectrum was taken by the author. The other two spectra were copied from R. Hezel and N. Lieske, J. Appl. Phys. 51, 2566 (1980).

## CHAPTER II

## REVIEW OF PREVIOUS WORK

In this chapter, we will briefly review the existing literature in the following major areas: (1) adsorption of nitrogen on silicon (also on germanium, which, of course, is very similar to silicon), (2) Auger spectra of CVD-Si<sub>3</sub>N<sub>4</sub>, and (3) electron-beam induced adsorption.

## II.A. Adsorption of Nitrogen on Silicon and Germanium

Relatively few studies of nitrogen on silicon and germanium have been performed because nitrogen does not adsorb on these materials at room temperature. Additionally, with two recent exceptions, all of the existing work was done prior to 1970, and the surface conditions were not well characterized.

In 1955, Law<sup>1</sup> studied the adsorption of nitrogen on germanium with the flash-filament technique. The Ge sample was cleaned by heating to 900° C in a base vacuum of  $10^{-10}$ - $10^{-9}$  Torr. At room temperature, no nitrogen adsorption was found over the pressure range  $10^{-8}$ - $10^{-4}$  Torr. At lower temperatures, 195° and 77° K, physisorbed nitrogen was detected; from the isotherms, Law estimated that a monolayer coverage was completed at 77° K for a pressure of  $4-5 \times 10^{-5}$  Torr. In the following year, Law and Francois<sup>2</sup> repeated the measurements for a silicon filament cleaned by heating to 1200° C. This time, however, adsorption only at room temperature was studied; no adsorbed nitrogen was detected over the range  $10^{-7}$ - $10^{-4}$  Torr. Law's room-temperature results were corroborated by two other groups. Boonstra<sup>3</sup> measured the adsorption of many gases on powdered Ge and Si (cleaned by heating in a base vacuum of  $10^{-8}$  Torr) and found no adsorption of nitrogen on Ge; the pressure range of the nitrogen was not stated. Using the volumetric

technique, Bennett and Tompkins<sup>4</sup> measured adsorption isotherms for nitrogen on Ge films prepared by evaporation (base pressure less than  $5 \times 10^{-8}$  Torr). Both 'clean' and oxidized films were studied; the adsorption behavior on the two films was essentially identical. In the pressure range  $10^{-6}$ -1 Torr, no adsorption was found at 273° K. Contrary to Law, however, there was also no adsorption at 195° K. Physisorption did occur at 90° and 78° K, but coverages were considerably less than those reported by Law: at 78° K, only 50-60% of a monolayer formed at 1 Torr.

In 1969, two groups reported LEED results. Fujinaga, et. al.,<sup>5</sup> exposed a 'clean' Si(111)-(7×7) surface at room temperature to  $10^{-7}$  Torr N<sub>2</sub> and then annealed the surface up to 800° C for 10 min; they found no change in the LEED pattern. In a more detailed study, Heckingbottom<sup>6</sup> also examined the effect of nitrogen on the Si(111)-(7×7) surface (produced by thermal cleaning in a base vacuum of  $< 1 \times 10^{-9}$  Torr); in these experiments, the sample was heated up to 1200° C during exposure. At  $10^{-6}$  Torr N<sub>2</sub>, over the whole temperature range, he noted only slight weakening of the (7×7) pattern, which deteriorated within a few minutes at  $10^{-3}$  Torr N<sub>2</sub>, 900° C. No new LEED patterns were observed until extremely high exposures: an 1/8th order pattern after 30 min at 40 Torr N<sub>2</sub>, 1130° C, and a 'doublet' pattern after 15 min at several Torr, 1150° C. Under such extreme conditions, however, the level of impurities was not ascertained. At high temperatures, tight control of impurities is essential because oxidation of silicon occurs much more readily than nitridation. Ito et. al.,<sup>7</sup> for example, investigated the direct thermal nitridation of silicon by reacting (100) and (111) wafers at 1200°-1300° C with a stream of nitrogen gas (in excess of atmospheric pressure); the main oxidizing contaminants, O<sub>2</sub> and H<sub>2</sub>O, were carefully



monitored in the exhaust. Subsequent Auger analyses revealed carbon and oxygen, but no nitrogen, on those wafers which had been 'nitrided' in an atmosphere with  $\text{H}_2\text{O} > 1$  ppm and  $\text{O}_2 > 0.1$  ppm. On wafers reacted in higher purity nitrogen, a silicon nitride layer up to 100 Å thick, was formed (carbon and oxygen contamination were still detected).

Since molecular nitrogen does not readily react with silicon, more recent work, performed under ultrahigh vacuum with Auger monitoring of surface impurities, has utilized atomic and ionized nitrogen. In 1978, Taylor, et. al.,<sup>8</sup> bombarded (100) and (111) wafers, which had been cleaned by argon bombardment but not annealed, at room temperature with nitrogen ions in the energy range 30-3000 eV. Using X-ray and ultraviolet photoelectron spectroscopy, they detected the formation of  $\text{Si}_3\text{N}_4$ ; for 500 eV ions, the resulting layer was 19 Å thick. Although the incident beam consisted of 96%  $\text{N}_2^+$  and 4%  $\text{N}^+$ , the authors concluded that the ions were neutralized as they approached the surface and that the molecular nitrogen so formed was then dissociated at the surface. Hence, the nitride layer was due to the reaction of energetic atomic nitrogen with silicon. Similarly, Delord, et. al.,<sup>9</sup> used an ion gun, operated at 140-250 eV, to spray nitrogen ions and neutrals onto a clean  $\text{Si}(111)-(7 \times 7)$  surface, which was produced by argon bombardment and annealing. During exposure, the substrate temperature was varied from room to 1100° C; LEED and Auger measurements were taken at room temperature. Their LEED results showed three different patterns, which depended on the substrate temperature during exposure, on the duration of exposure, and on subsequent annealing after exposure. The three patterns were (1) diffuse, (2)  $(8 \times 8)$ , and (3) 'doublet'; when nitrided surfaces were

heated above  $1000^{\circ}\text{C}$ , the nitrogen desorbed and the clean (7×7) pattern reappeared. The authors also studied the evolution of the Auger spectra from clean Si to  $\text{Si}_3\text{N}_4$  and determined the effects of oxygen contamination and argon bombardment on the Auger spectra (these results will be mentioned below).

## II.B. Auger Spectra of CVD- $\text{Si}_3\text{N}_4$

Amorphous thin films ( $\sim 500\text{--}1500\text{ \AA}$  thick) of silicon nitride deposited on silicon substrates are widely utilized in microelectronics.<sup>10</sup> The stoichiometry and, hence, the properties of such films vary widely with the deposition technique and the particular process conditions. Of the various techniques available, the most common is chemical vapor deposition (CVD), with ammonia and silane reactants, on a wafer at  $\sim 850^{\circ}\text{C}$ . From helium backscattering measurements, Gyulai, et. al.,<sup>11,12</sup> determined that stoichiometric  $\text{Si}_3\text{N}_4$  films were attained for high ammonia/silane volume ratios (greater than 20). The depth resolution of such measurements, however, is limited to  $\sim 100\text{--}200\text{ \AA}$ ; and better resolution ( $\sim 10\text{ \AA}$  or less) is needed for device characterization.<sup>13</sup> In particular, there is great interest in possible compositional variations at the air/nitride<sup>14</sup> and nitride/substrate<sup>13</sup> interfaces.

For the high depth resolution needed, a frequently used technique consists of monitoring surface compositions by Auger as the sample is sputtered away with argon ions.<sup>13</sup> However, several groups have reported conflicting results for Si(LVV) spectra from CVD- $\text{Si}_3\text{N}_4$ . For now, we will restrict the discussion to the two major peaks; detailed spectra will be given in Chapter V. We should also note that Auger peak shapes and locations depend somewhat on the type of spectrometer and on the operating voltages

used<sup>15</sup>; at best, Auger peak positions are good to  $\sim \pm 1$  eV. Instrumentational effects alone, however, cannot account for the range of data presented. Auger spectra from CVD-Si<sub>3</sub>N<sub>4</sub> were first reported by Maguire and Augustus<sup>16</sup> in 1972. On the as-loaded sample, they found a main Si peak at 82 eV and a smaller peak at 65 eV (carbon and oxygen contamination were also detected). After the contaminants had been removed by argon sputtering and annealing to 1140° C for over 2 h, the Si peaks shifted to 85 and 66 eV. In 1976, Holloway<sup>17</sup> measured a fairly different spectrum for a sample cleaned by sputtering but not annealed; the major Si peak was located at 87 eV with an inflection at 82 eV. Other groups, using the same sample preparation as Holloway, have found similar lineshapes with an inflection at 82 eV; the position of the main peak,<sup>18,19</sup> however, has varied from 88 to 92 eV. Considerable controversy has centered on the issue of whether the main peak (87-92 eV) is representative of Si in a Si<sub>3</sub>N<sub>4</sub> state or indicative of excess free silicon (X-ray photoelectron spectroscopy revealed less than 5 at% free silicon).<sup>18</sup>

Recent studies, however, have now established that the variation in the spectra is due chiefly to the effects of preferential sputtering<sup>9,20,21</sup> and residual oxygen.<sup>21,22</sup> Argon bombardment sputters away nitrogen more rapidly than silicon<sup>20</sup> and, so, destroys the stoichiometry of the surface layer. The 87-92 eV peaks arise from the resulting excess free silicon, and the particular energy depends on the degree of preferential sputtering (which is a function of the ion energy)<sup>20</sup> and on the amount of oxygen contamination.<sup>21,22</sup> The spectra of Delord, *et. al.*, from directly-nitrided silicon reveal a major peak at 84 eV and a smaller peak at 73 eV. Evidently, high-temperature annealing of sputtered CVD-Si<sub>3</sub>N<sub>4</sub> films restores

the surface stoichiometry. Hezel and Lieske,<sup>21</sup> for films cleaned by argon bombardment and annealed at 1100° C for 30 min, measured spectra very similar to those of Delord, et. al. (a main peak at 83 eV and a smaller peak at 71 eV). The data of Maguire and Augustus from annealed films was probably also representative of stoichiometric  $\text{Si}_3\text{N}_4$ ; but their data was distorted by instrumental effects: they used a retarding-field analyzer and a high modulation voltage.

## II.C. Electron-Beam Induced Adsorption

The interaction of electrons with gases adsorbed on surfaces has received considerable attention. Although many effects arise from electron bombardment, most of the work has concentrated on the electron-stimulated desorption (ESD) of gases from metal surfaces.<sup>23</sup> Another important process, electron-beam induced adsorption, has generally not been emphasized in studies of metal surfaces. One notable exception, however, is the work of Polak.<sup>24</sup> He found that molecular nitrogen, weakly bound on a W(110) plane at 95° K, was dissociated by an electron beam to form localized deposits of tightly-bound atomic nitrogen, which was stable to high temperatures ( $\sim 800^\circ \text{K}$ ); the maximum coverage of atomic nitrogen so formed was  $\sim 0.6$  monolayer.

On semiconductor surfaces, ESD has also been studied<sup>25</sup>; but much more attention has been centered on electron-beam induced adsorption. Dissociation of CO on Si has been observed<sup>26-28</sup>; and electron-beam induced adsorption of oxygen has been reported on both elemental (Ge and Si)<sup>28-35</sup> and compound (GaAs and InP)<sup>36,37</sup> semiconductors. Although several groups have measured enhanced adsorption of oxygen on silicon, we shall not review their work--the behavior of oxygen on silicon, both with and without electron bombardment,

has been (and still is) very confusing; and a discussion of the controversies involved would not be appropriate here.<sup>38</sup> The recent studies by Munoz, et. al.,<sup>33-35</sup> however, need to be singled out because their results for oxygen on silicon have some bearing on our work. Using Auger, they followed the adsorption of oxygen on a clean Si(111)-(7×7) surface at room temperature; base pressure in their system was  $\sim 3 \times 10^{-10}$  Torr. If the sample was not bombarded during exposure, the gas coverage saturated at  $\sim 0.8$  monolayer of chemisorbed oxygen; there was no evidence of SiO<sub>2</sub> formation for doses up to 2 h at  $8 \times 10^{-5}$  Torr O<sub>2</sub>. When the sample was electron bombarded (3 keV beam) during exposure, the chemisorbed state saturated at the same coverage as before; additional exposure, however, led to the onset of oxidation (growth of the 76 eV SiO<sub>2</sub> Auger peak). An SiO<sub>2</sub> layer,  $\sim 16$  Å thick, was eventually formed.

## REFERENCES FOR CHAPTER II

1. J. T. Law, J. Phys. Chem. 59, 543 (1955).
2. J. T. Law and E. E. Francois, J. Phys. Chem. 60, 353 (1956).
3. A. H. Boonstra, Philips Res. Repts. Suppl. no. 3 (1968).
4. M. J. Bennett and F. C. Tompkins, Trans. Faraday Soc. 58, 816 (1962).
5. Y. Fujinaga, S. Ino, and S. Ogawa, Japan. J. Appl. Phys. 8, 815 (1969).
6. R. Heckingbottom, in The Structure and Chemistry of Solid Surfaces, edited by G. A. Somorjai (John Wiley and Sons, New York, 1969), pp. 78-1 to 78-18.
7. T. Ito, S. Hijiya, T. Nozaki, H. Arakawa, M. Shinoda, and Y. Fukukawa, J. Electrochem. Soc. 125, 448 (1978).
8. J. A. Taylor, G. M. Lancaster, A. Ignatiev, and J. W. Rabalais, J. Chem. Phys. 68, 1776 (1978).
9. J. F. Delord, A. G. Schrott, and S. C. Fain, Jr., J. Vac. Sci. Technol. 17, 517 (1980).
10. C.-E. Morosanu, Thin Solid Films 65, 171 (1980).
11. J. Gyulai, O. Meyer, J. W. Mayer, and V. Rodriguez, Appl. Phys. Lett. 16, 232 (1970).
12. J. Gyulai, O. Meyer, J. W. Mayer, and V. Rodriguez, J. Appl. Phys. 42, 451 (1971).
13. J. S. Johannessen, C. R. Helms, W. E. Spicer, and Y. Strausser, IEEE Trans. Electron Devices ED-24, 547 (1977).
14. S. I. Raider, R. Flitsch, J. A. Aboaf, and W. A. Pliskin, J. Electrochem. Soc. 123, 560 (1976).
15. C. C. Chang, Surf. Sci. 25, 53 (1971).
16. H. G. Maguire and P. D. Augustus, J. Electrochem. Soc. 119, 791 (1972).



17. P. H. Holloway, Surf. Sci. 54, 506 (1976).
18. T. N. Wittberg, J. R. Hoenigman, W. E. Moddeman, C. R. Cothorn, and M. R. Gullett, J. Vac. Sci. Technol. 15, 348 (1978).
19. Y. E. Strausser and J. S. Johannessen, in Semiconductor Measurement Technology: ARPA/NBS Workshop IV. Surface Analysis for Silicon Surfaces, edited by A. G. Lieberman (NBS Special Publication 400-23, 1976), pp. 125-138.
20. R. S. Bhattacharya and P. H. Holloway, Appl. Phys. Lett. 38, 545 (1981).
21. R. Hezel and N. Lieske, J. Appl. Phys. 51, 2566 (1980).
22. H. H. Madden and P. H. Holloway, J. Vac. Sci. Technol. 16, 618 (1979).
23. For a review, see T. E. Madey and J. T. Yates, Jr., J. Vac. Sci. Technol. 8, 525 (1971).
24. A. J. Polak, Ph.D. Thesis, University of Illinois at Urbana-Champaign (1977).
25. See, for example, M. Nishijima and T. Murotani, Surf. Sci. 32, 459 (1972).  
M. Nishijima, K. Fujiwara, and T. Murotani, Japan. J. Appl. Phys. Suppl. 2, Pt. 2, 303 (1974).  
M. Miyamura, Y. Sakisaka, M. Nishijima, and M. Onchi, Surf. Sci. 72, 243 (1978).
26. J. P. Coad, H. E. Bishop, and J. C. Riviere, Surf. Sci. 21, 253 (1970).
27. B. A. Joyce and J. H. Neave, Surf. Sci. 34, 401 (1973).
28. R. E. Kirby and J. W. Dieball, Surf. Sci. 41, 467 (1974).
29. Y. Margoninski, J. Appl. Phys. 47, 3868 (1976).
30. Y. Margoninski, D. Segal, and R. E. Kirby, Surf. Sci. 53, 488 (1975).
31. H. Ibach, K. Horn, R. Dorn, and H. Luth, Surf. Sci. 38, 433 (1973).
32. W. Reuter and K. Wittmaack, Appl. Surf. Sci. 5, 221 (1980).

33. M. C. Munoz, V. Martinez, J. A. Tagle, and J. L. Sacedon, Phys. Rev. Lett. 44, 814 (1980).
34. M. C. Munoz, V. Martinez, J. A. Tagle, and J. L. Sacedon, J. Phys. C. 13, 4247 (1980).
35. M. C. Munoz and J. L. Sacedon, J. Chem. Phys. 74, 4693 (1981).
36. W. Ranke and K. Jacobi, Surf. Sci. 47, 525 (1975).
37. J. Olivier, P. Faulconnier, and R. Poirer, J. Appl. Phys. 51, 4990 (1980).
38. For a recent summary, see C. M. Garner, I. Lindau, C. Y. Su, P. Pianetta, and W. E. Spicer, Phys. Rev. B 19, 3944 (1979).

## CHAPTER III

## EXPERIMENTAL APPARATUS

In order to study electron-induced adsorption on clean silicon surfaces, we constructed a versatile ultrahigh vacuum system. For reproducible and well-characterized results, minimization of background contamination is essential, especially since the sample is chilled to low temperatures. Therefore, special care was exercised both in materials selection and construction techniques. In addition to surface-analysis instrumentation, the vacuum system has provisions for sputtering and dosing the sample. There is also a novel sample holder necessary for our present work: it permits both high-temperature heating and cryogenic cooling of the silicon wafer.

## III.A. Vacuum System

In Fig. 3.1, we have an overview of the system, which consists chiefly of a stainless-steel chamber and an auxiliary glass (Pyrex) gas-handling unit. The main body of the chamber was rolled from 1/8 in. thick type 304 stainless plate and measures 14 in. o.d.  $\times$  12 in. high. All joints were heli-arc welded on the inside, and all interior surfaces were electropolished.

The system is evacuated by trapped mercury diffusion pumps, which are backed by rotary mechanical pumps. In order to achieve ultrahigh vacuum, backstreaming of oil from the mechanical pumps must be eliminated by additional liquid-nitrogen traps; a schematic of the vacuum plumbing is shown in Fig. 3.2. After a ten-hour bakeout, base pressure was routinely  $\sim 1 \times 10^{-10}$  Torr throughout the system.

Figure 3.1. Overview of ultrahigh vacuum system. The system consists chiefly of a stainless-steel bell jar (on the right) and a Pyrex gas handling unit (on the left).

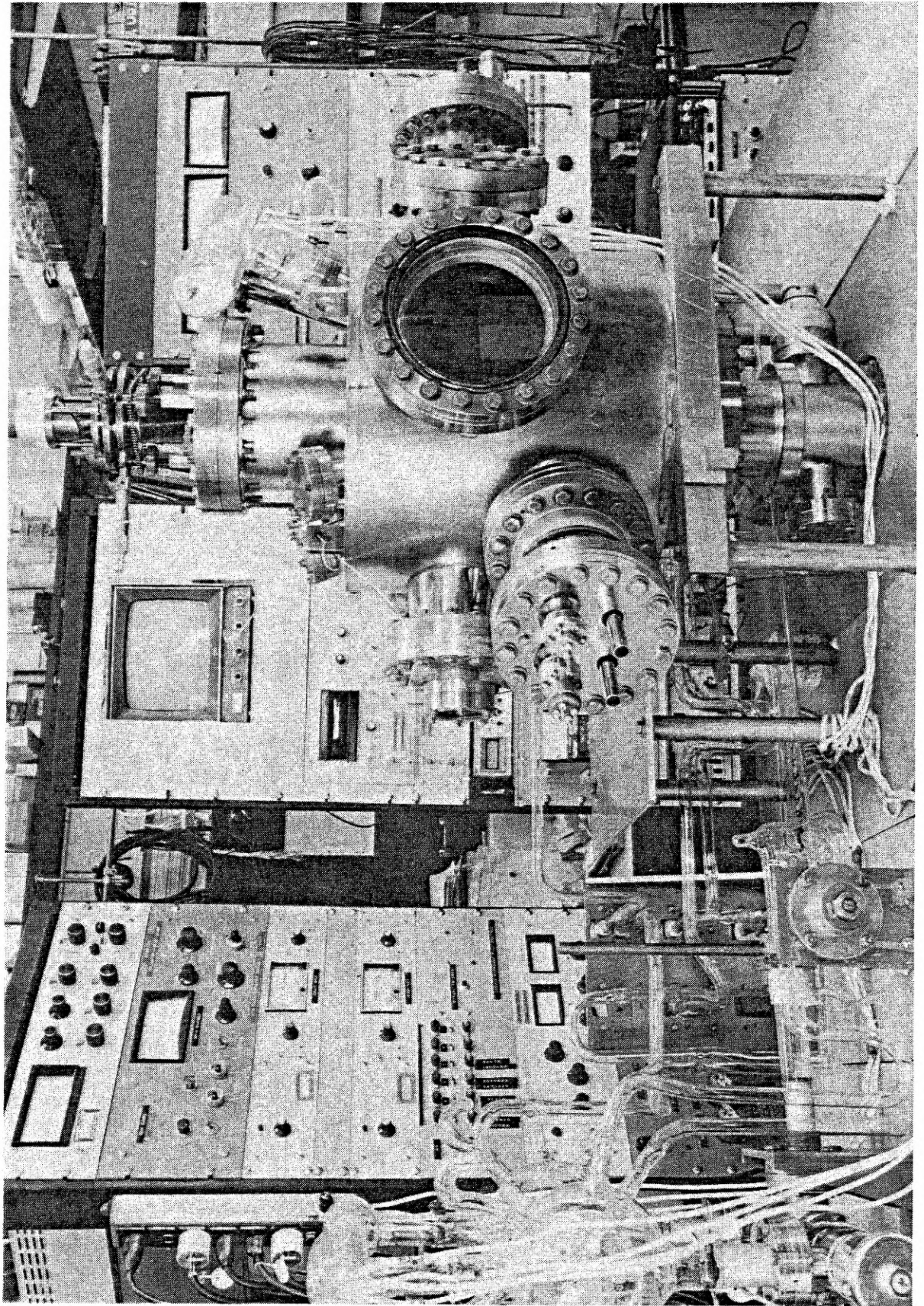
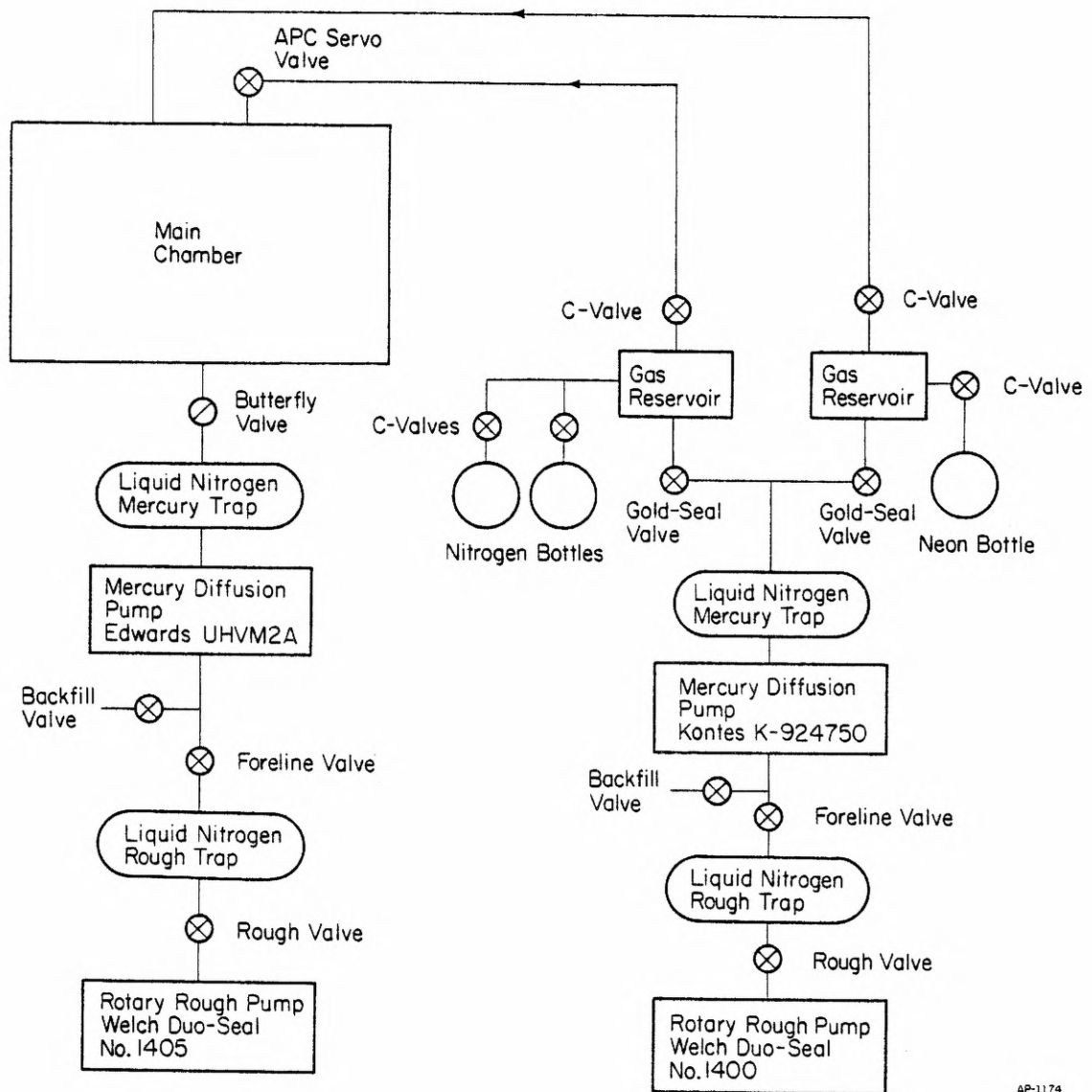


Figure 3.2. Interconnection schematic. The diagram shows the pumping and valving sequence of the vacuum system.





As shown in Figs. 3.3 and 3.4, the major instruments are arranged in a radial cluster about a central sample manipulator. Coupling between the sample and the chill feedthrough is achieved with flexible metal bellows; the sample can therefore be freely positioned in front of an Auger analyzer, auxiliary electron gun, LEED unit, or sputter ion gun. Later on, we shall describe the sample holder and chill in detail.

For reproducible gas dosing, the arrangement in Fig. 3.5 is used. If the dopant gas is not activated by hot filaments, the chamber can be maintained at a constant pressure through a closed feedback loop between the ion gauge and servo valve. If the ion gauge cannot be operated, a fixed volume of gas is first trapped between the C-valve and servo valve and then simply admitted into the main chamber.

#### III.B. Sample Holder and Chill

Construction of a proper sample holder for surface experiments is very difficult because the design requirements are so severe:

- (1) True ultrahigh vacuum design
- (2) Port-to-port swing
- (3) Precision alignment
- (4) Compact head
- (5) Electrical isolation
- (6) High-temperature heating
- (7) Cryogenic cooling.

First of all, for minimum background contamination, the sample holder should be a true ultrahigh vacuum design: fully bakeable to 250° C and incorporating only low vapor pressure materials. Secondly, in addition to permitting



Figure 3.3. Photograph of main-chamber layout.

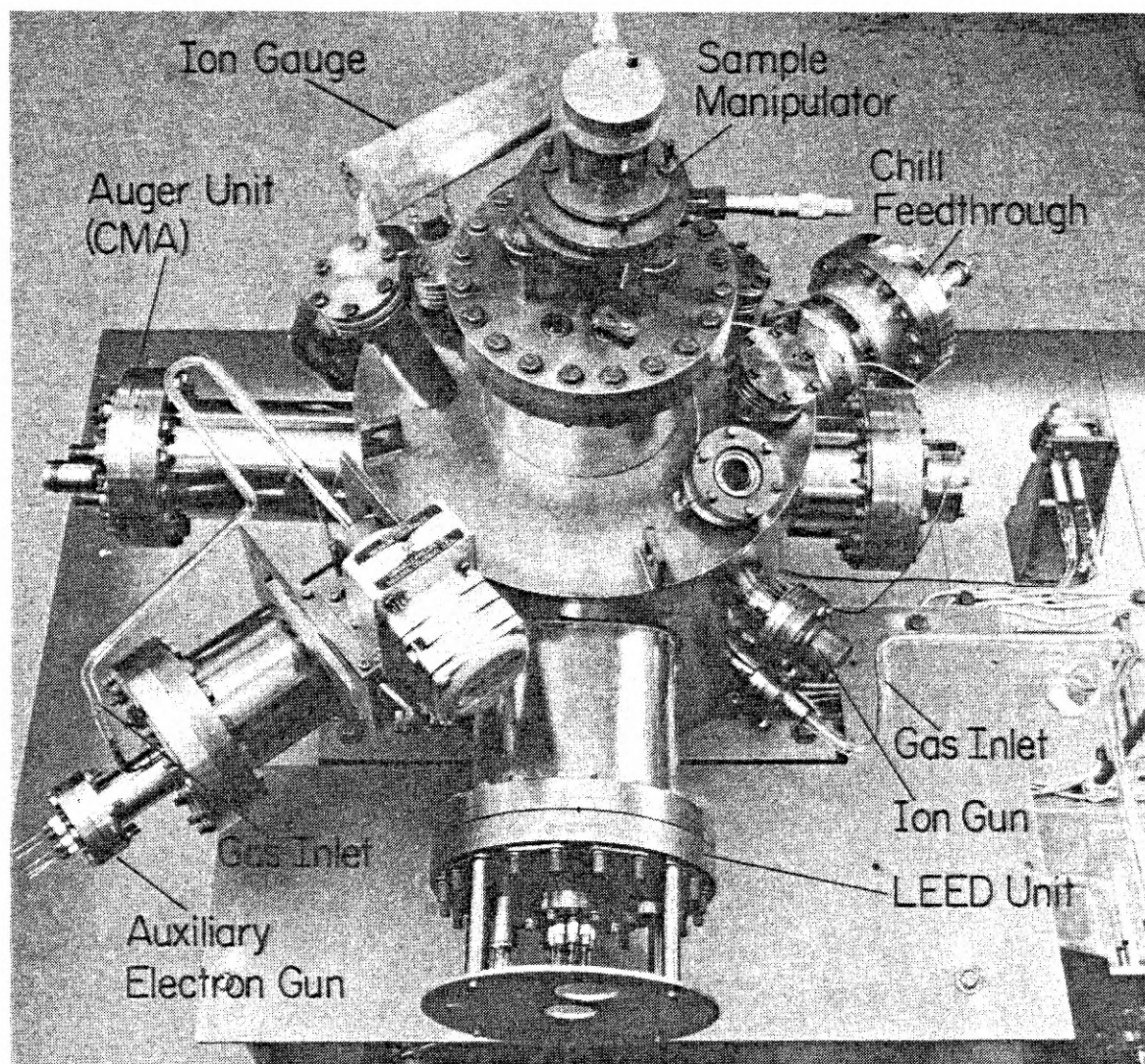


Figure 3.4. Schematic of ultrahigh vacuum system. Sample is swung from port to port by the manipulator in the center. The chill feedthrough electrically isolates the sample from the chamber. The titanium sublimator shown here was used in preliminary runs but was later removed.

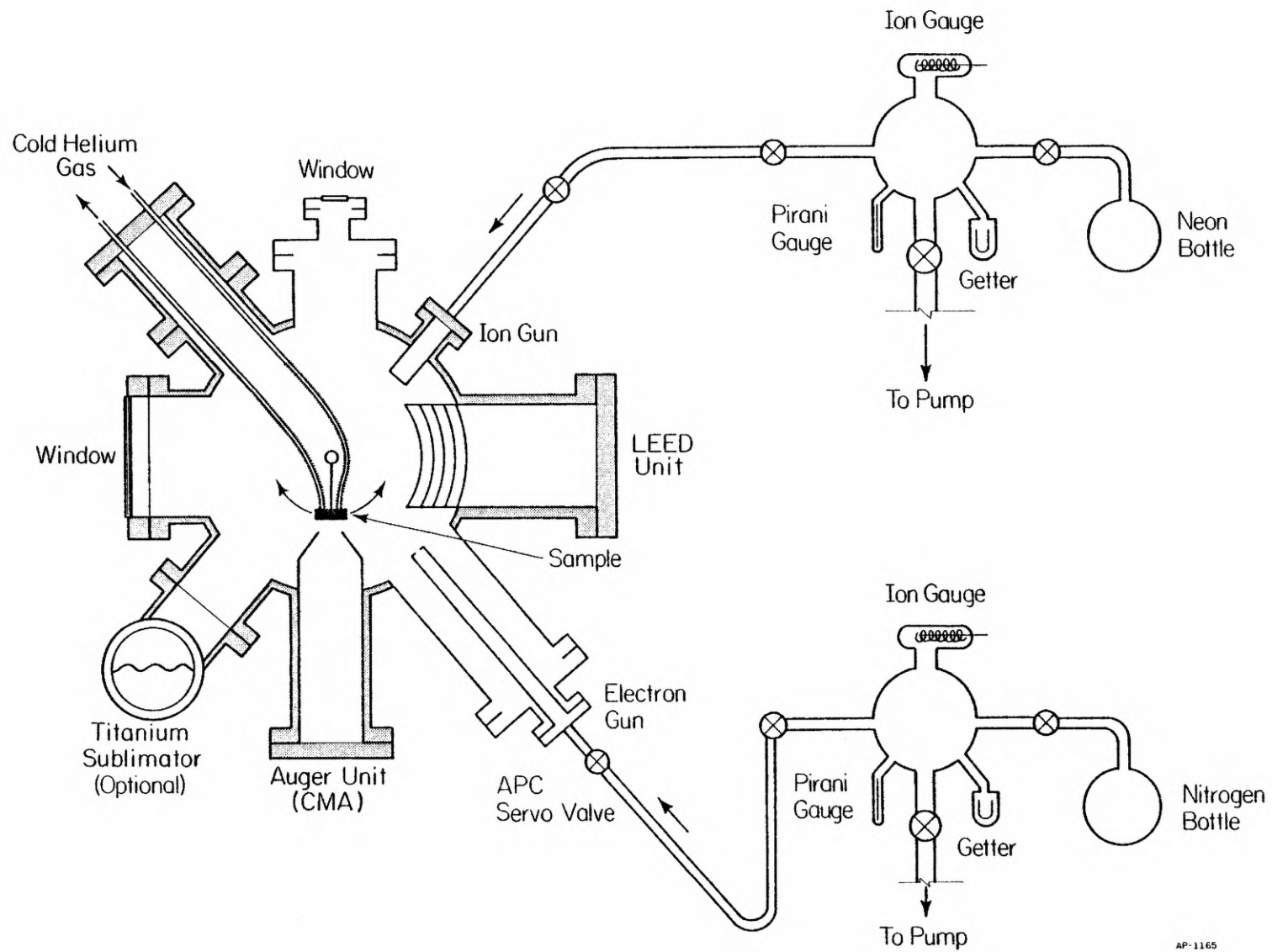
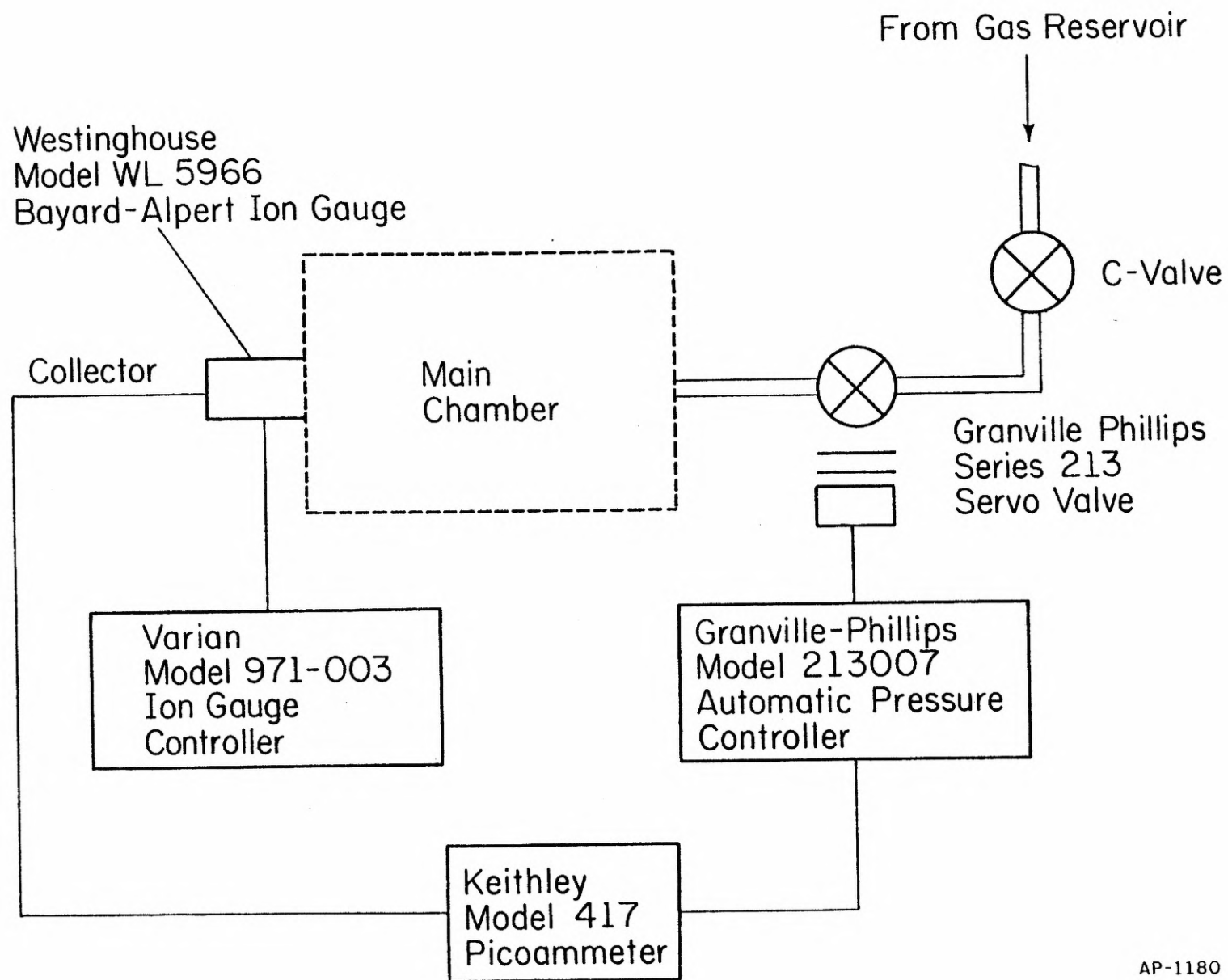


Figure 3.5. Arrangement for reproducible gas dosing. The chamber can be maintained at constant pressure by a closed feedback servo loop. If the ion gauge cannot be operated, a fixed volume of gas is trapped between the two valves and admitted into the chamber.

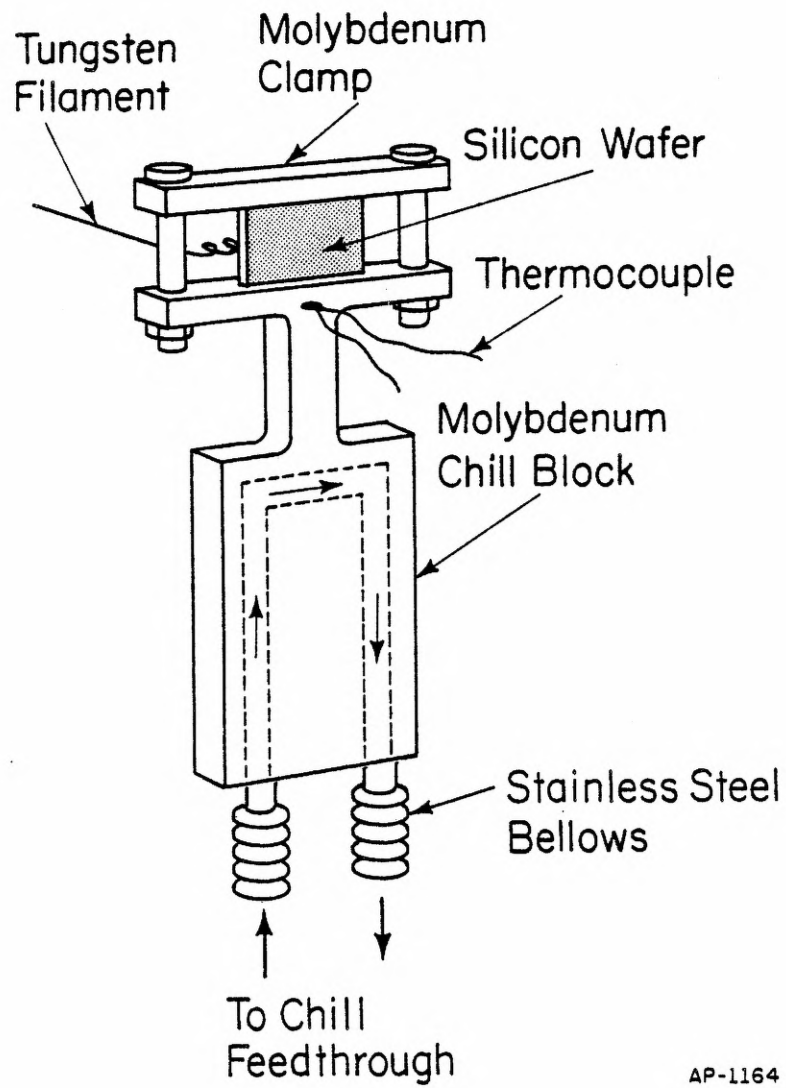


large scale movement of the sample from one instrument port to another, it must also be capable of precision alignment. For LEED work, the wafer must be held in a head which is as compact as possible. Furthermore, in many instances, the sample needs to be electrically isolated from ground (chamber walls). Lastly, for comprehensive experiments, both high-temperature heating (melting point of silicon  $\sim 1410^{\circ}\text{C}$ ) and cryogenic cooling ( $30^{\circ}\text{K}$  or better) must be accommodated. Note that the last two requirements are essentially incompatible: for high-temperature heating, the sample should be as thermally isolated from its environment as possible, whereas, cryogenic cooling requires the sample to be firmly anchored to a chill. Hence, clever design is necessary to achieve a delicate compromise.

In addition to the principal design requirements listed above, two other engineering features are stressed in our sample holder: (1) high reliability, which is essential in ultrahigh vacuum work, and (2) a high degree of modularity, which facilitates modification and repair access if needed. The key elements of our design are shown in Fig. 3.6. The silicon wafer ( $\sim 1\text{ cm square} \times 2\text{ mm thick}$ ) is tightly clamped onto a monobloc molybdenum holder, which can be chilled by flowing cold helium gas through an internal U-tube. With this arrangement, the sample can be cooled to  $\sim 30^{\circ}\text{K}$  without liquid-nitrogen shields; temperatures are monitored by a thermocouple spot-welded near the edge of the wafer. For high-temperature heating, the wafer is bombarded from the back with electrons emitted from a tungsten filament. The narrow bridge between the wafer and chill block provides a measure of thermal isolation during high-temperature heating at the expense of cooling power. Since the clamp, screws, and nuts are also made of molybdenum, the unit can be cycled up to the melting point of silicon. Fig. 3.7 is a photograph of the actual sample-holder head assembly.

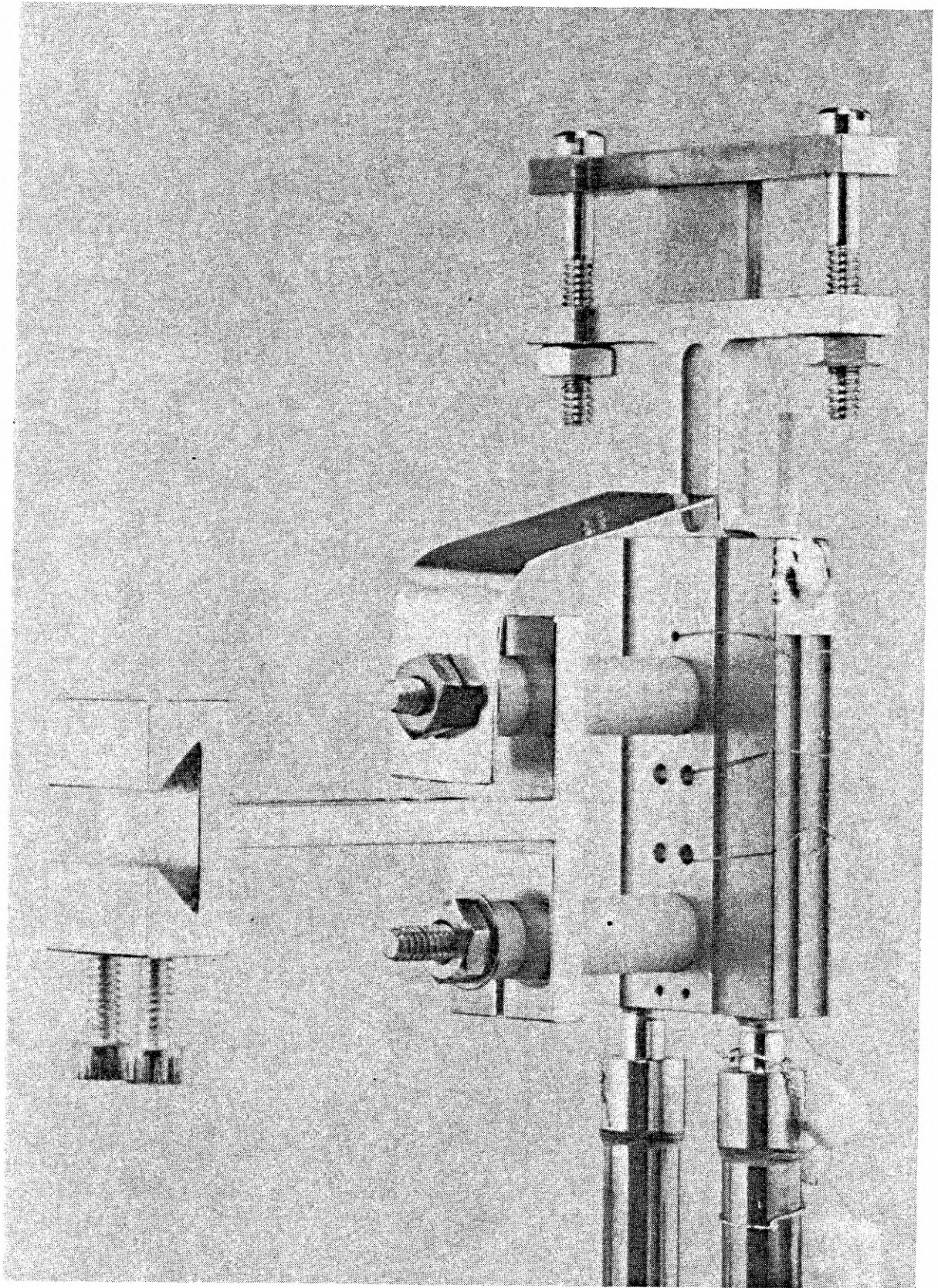
Figure 3.6. Key elements of sample holder. The silicon wafer may be heated by electron bombardment from the tungsten filament or cooled by passing cold helium gas through the bellows. The monobloc molybdenum chill can be cycled to high as well as low temperatures.





AP-1164

Figure 3.7. Photograph of sample-holder head assembly. Alumina insulators isolate the molybdenum chill block from the stainless-steel dovetail.



The complete sample holder comprises two major sections, a manipulator module and a chill module, which are coupled together inside the main chamber by a special dovetail lock; see Fig. 3.8. The manipulator module, Fig. 3.9, is attached to a commercial unit, PHI Model 10-501, providing X-Y-Z, rotation, and tilt capability. In addition to the mechanical adjustments, the manipulator module also contains the electron-bombardment assembly; flexible electrical connections are achieved through OFHC copper straps would in fishing-reel style about Pyrex insulators.

The chill module consists of three sub-assemblies which are bolted together: chill block, feedthrough flange, and isolation spool. From Fig. 3.10, we see that the chill block is coupled to the feedthrough flange via two stainless-steel flexible bellows (Cajon 321-4-X-12). Electrical isolation between the feedthrough flange and vacuum chamber is maintained by a glass spool, as shown in Fig. 3.11. In practice (refer to the functional schematic, Fig. 3.12), a liquid-helium transfer tube is inserted into the inlet of one bellows and circulates cold helium gas through the chill block (Fig. 3.6); the helium is exhausted through the other bellows. Stainless standoffs provide long thermal paths between the bellows and feedthrough flange.

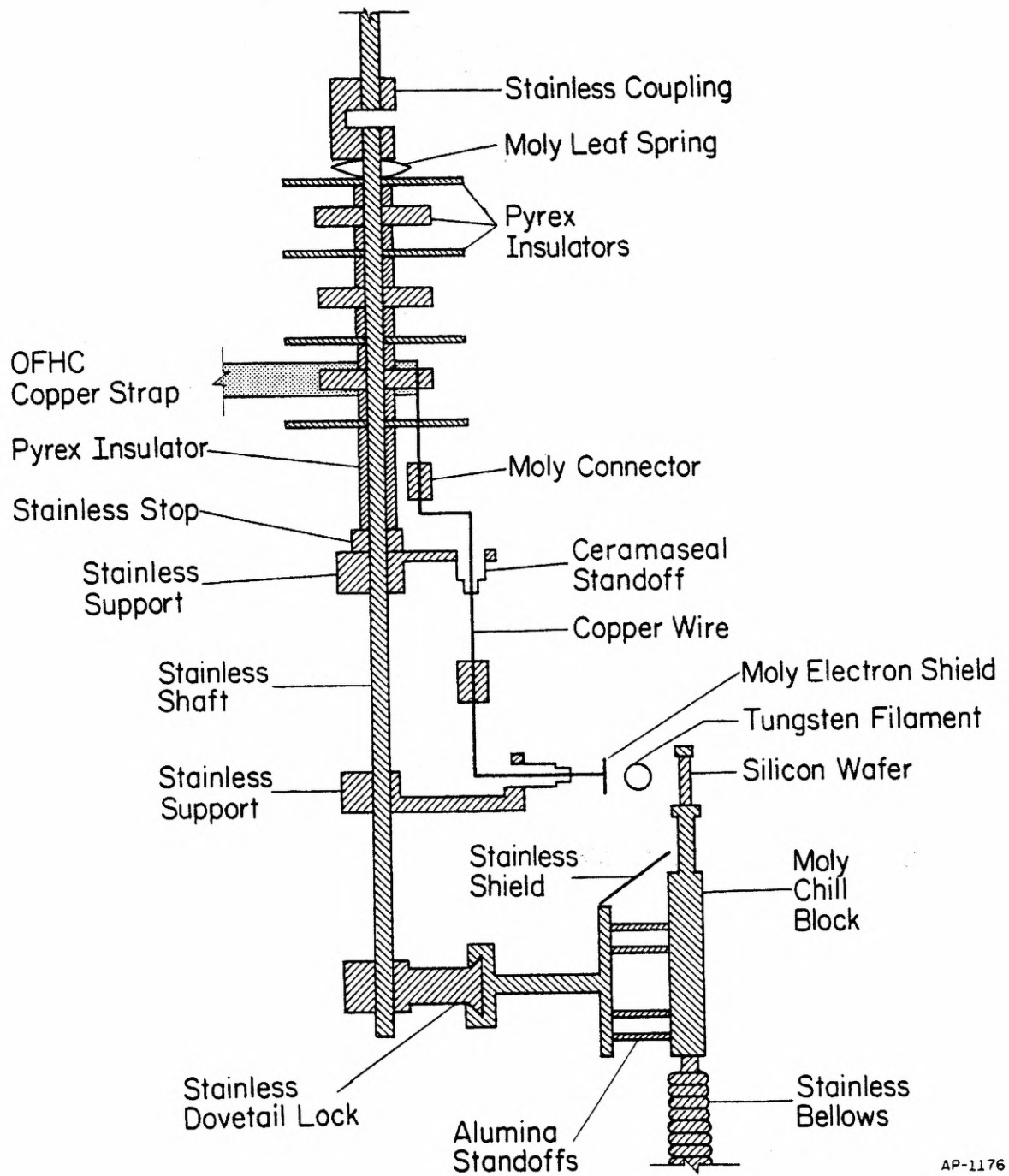
### III.C. Temperature Control

#### III.C.1. High Temperatures

As mentioned above, the sample is heated by electron bombardment from a tungsten filament. Close temperature control to  $\pm 0.3^\circ \text{C}$  is achieved by the arrangement shown in Fig. 3.13. The filament is operated near ground potential, while the sample is floated to positive high voltage. A closed

Figure 3.8. Schematic of sample holder. A special dovetail lock couples the manipulator module to the chill module. In addition to the mechanical adjustments, the manipulator module also contains the electron-bombardment assembly.

# PHI Sample Manipulator Shaft






Figure 3.9. Photograph of manipulator module. Flexible electrical connections to the electron-bombardment assembly are provided by OFHC copper straps wound about Pyrex reels.



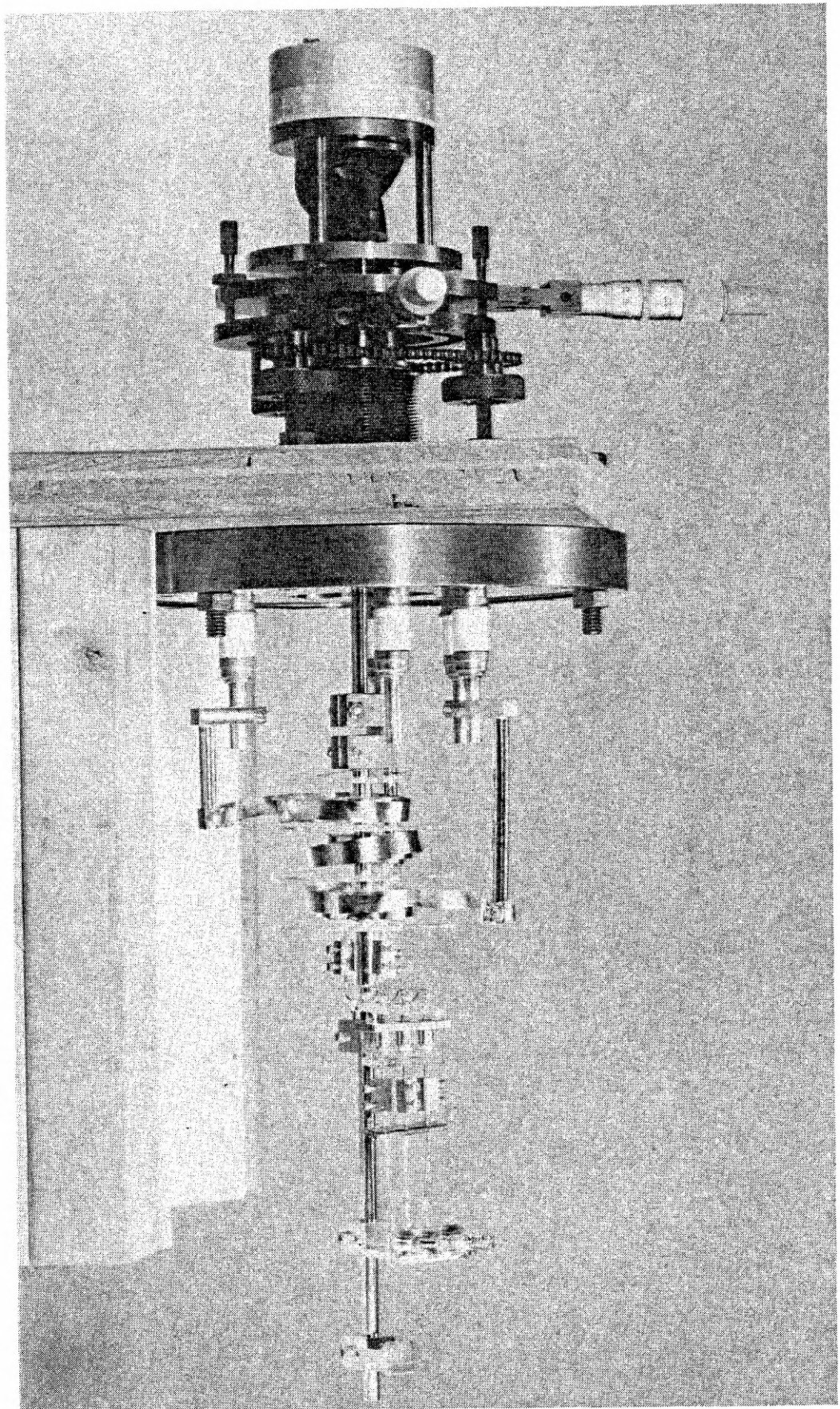




Figure 3.10. Overview of chill module. Chill block (on the right) is coupled to feedthrough flange (on the left) via flexible bellows. The isolation spool has been removed here for clarity.

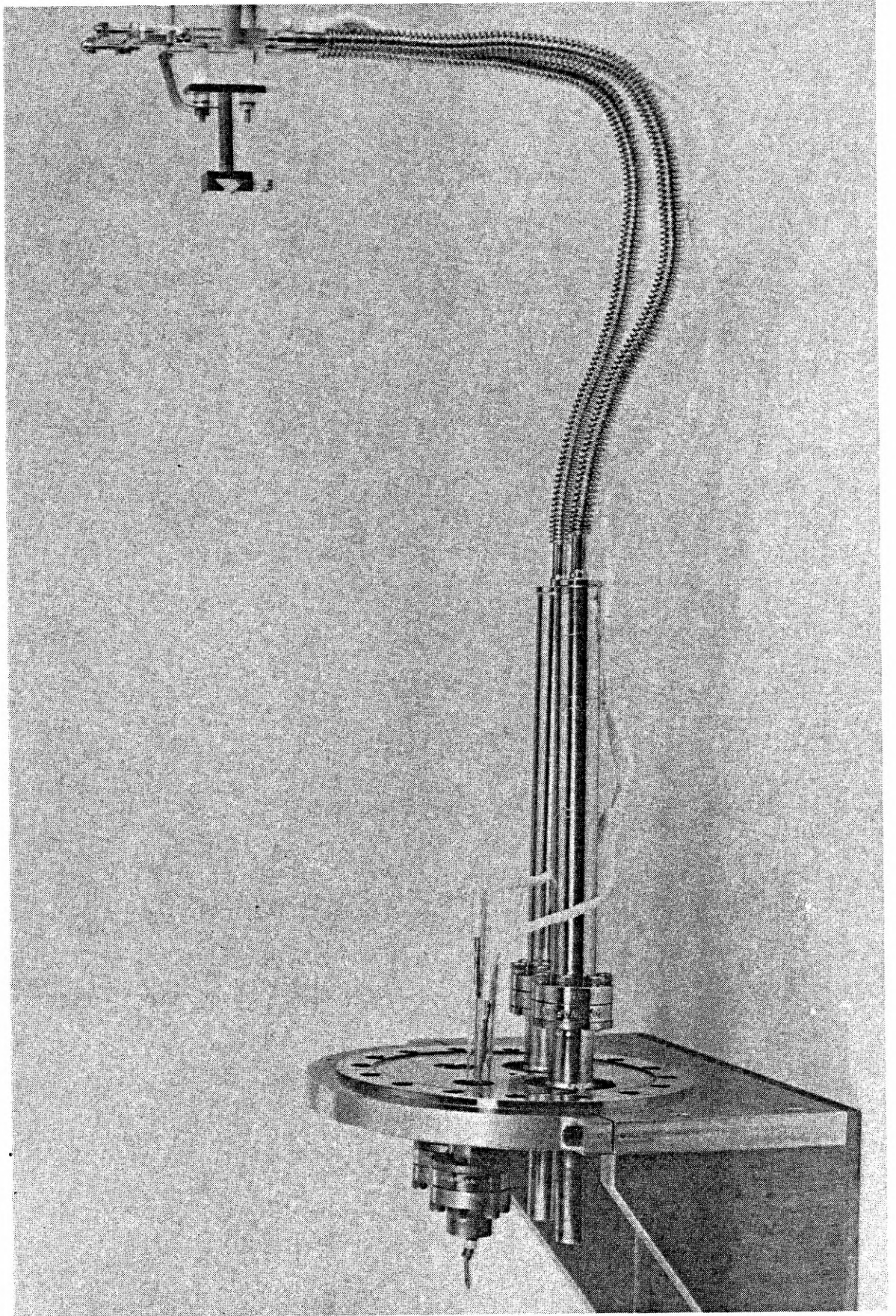


Figure 3.11. Close-up of feedthrough flange. The isolation  
spool is shown in the rear.



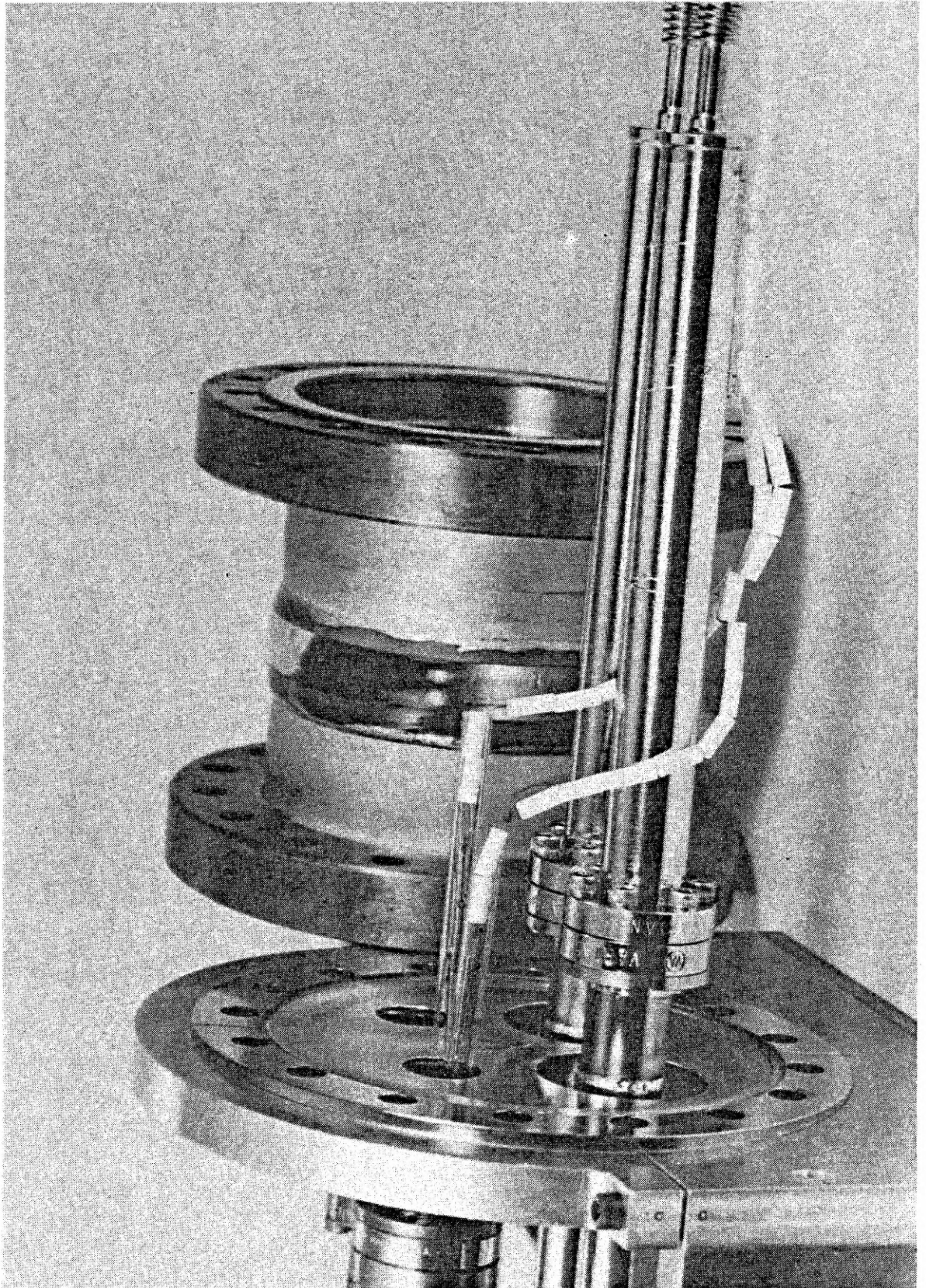


Figure 3.12. Schematic of chill feedthrough. A helium transfer tube is inserted along the guide tube to the inlet of the bellows. The standoff minimizes thermal exchange between the bellows and the flanges.

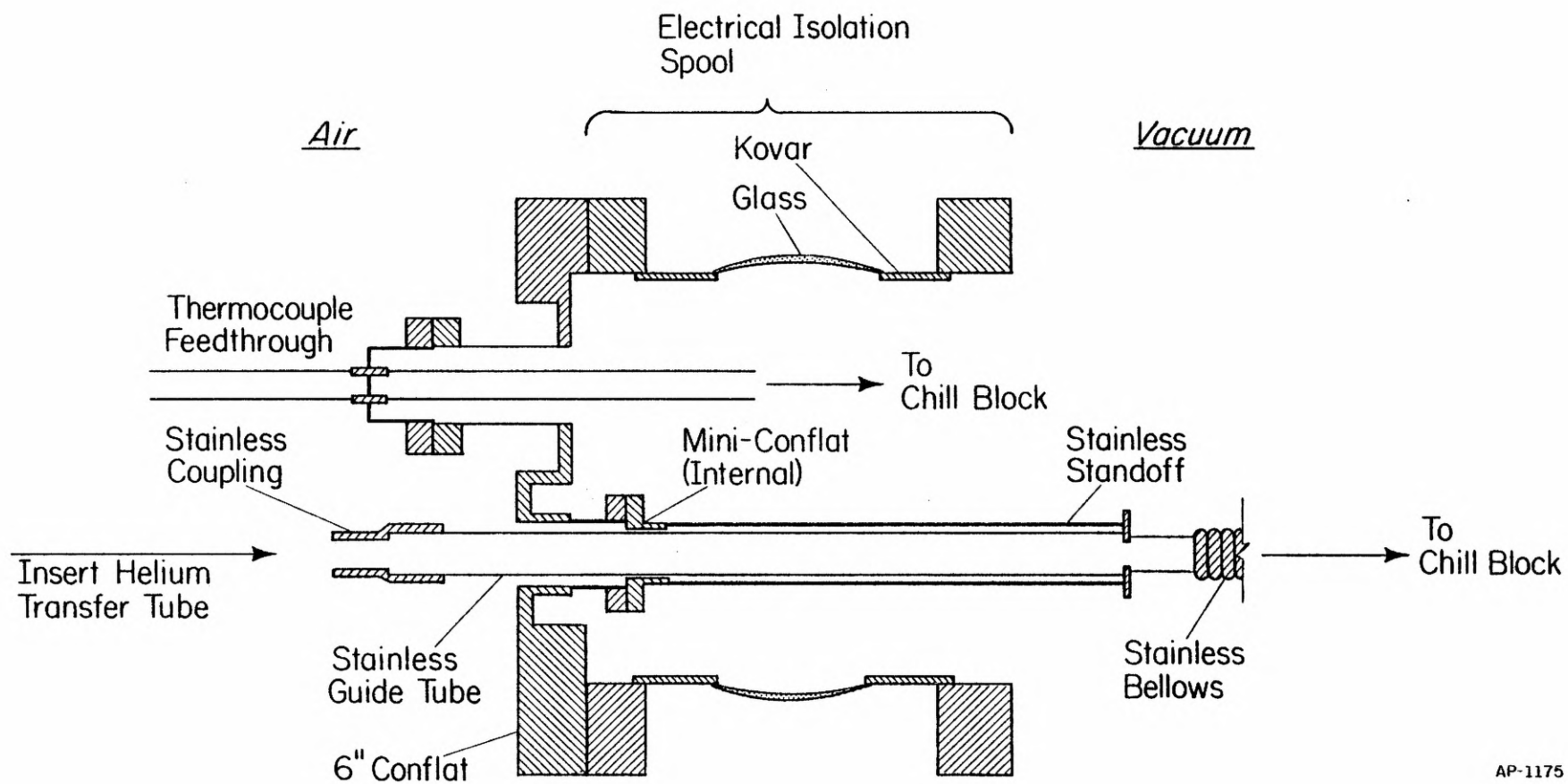
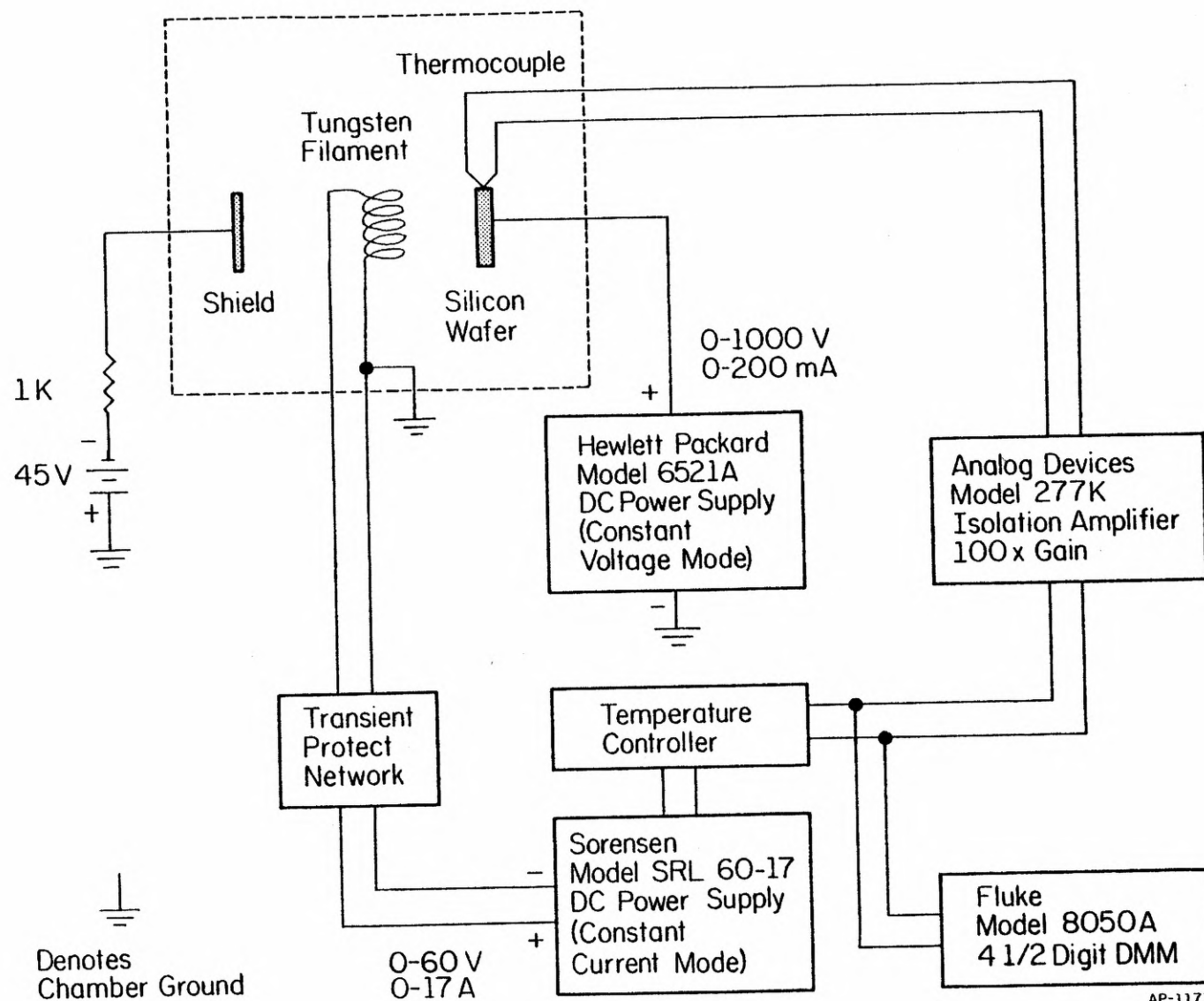


Figure 3.13. Block diagram of high-temperature control arrangement.





feedback loop between the thermocouple and the programmable current supply provides the precision temperature control. For minimum outgassing at high temperatures, a tungsten-5% rhenium/tungsten-26% rhenium thermocouple (.005 in. diameter wire) is used.

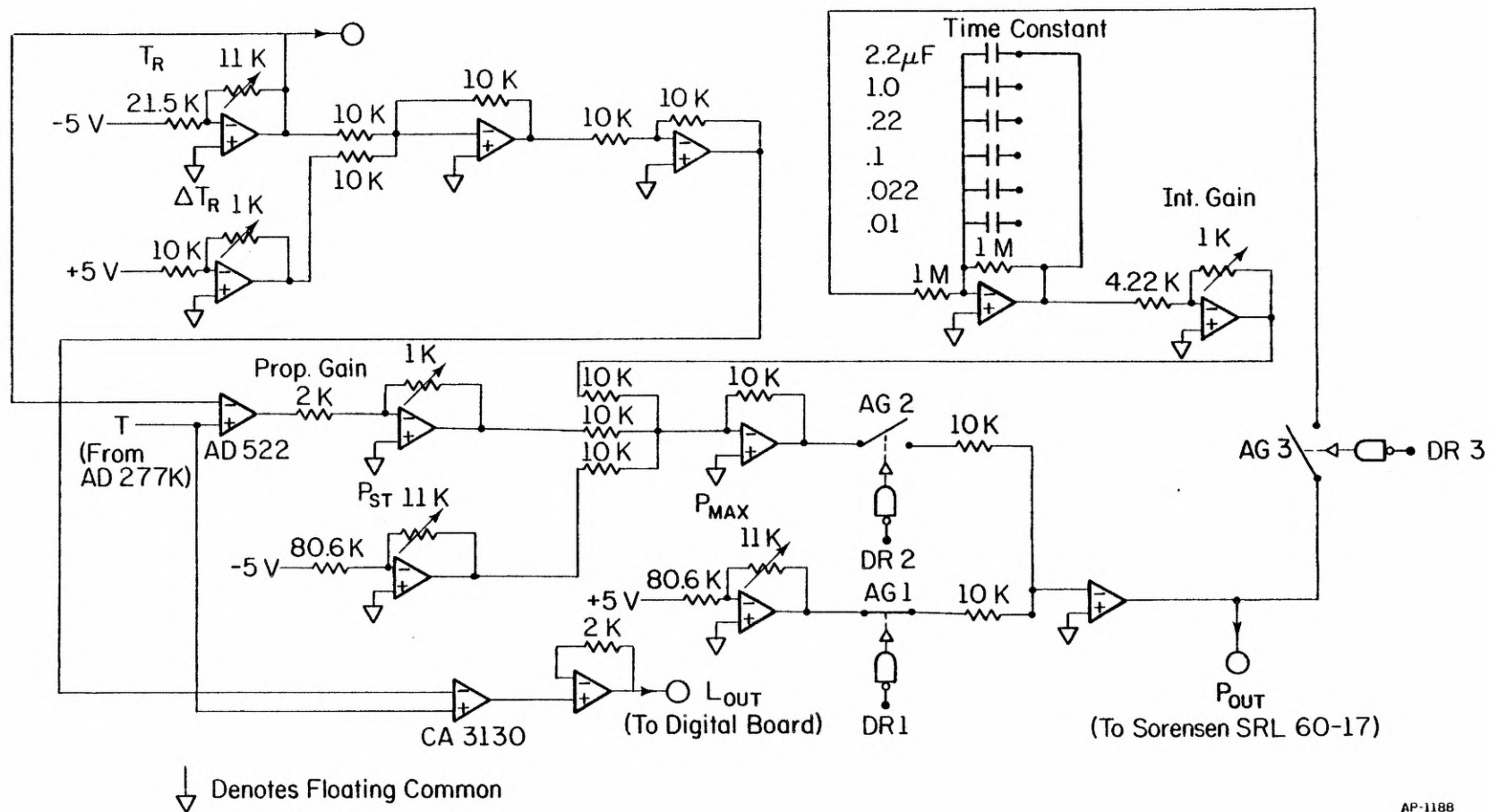
The controller circuit, shown in Figs. 3.14 and 3.15, is designed for both fast response and high stability. Here, the signal voltage  $T$  is the thermocouple voltage buffered and amplified by 100 X gain;  $T_R$  is the reference voltage corresponding to the desired control temperature. At the start of the heating, the controller maintains a constant maximum current through the filament until  $T$  exceeds the switching threshold ( $T_R - \Delta T_R$ ). By means of a quad analog gate, the controller is then digitally switched and latched into a tight proportional-integral mode. The output drive signal  $P_{OUT}$  is proportional to the error signal ( $T - T_R$ ), and damping is provided by the time-integral of the output drive signal.

### III.C.2. Low Temperatures

During cryogenic cooling, the temperature is regulated simply by varying the helium gas inlet flow (via a needle valve) to the liquid-helium supply dewar. After an  $\sim 1$  h chilldown, the temperature stabilizes to  $\pm 0.5^\circ$  K. Since the tungsten-rhenium thermocouple has not been calibrated below  $77^\circ$  K, temperatures in the range  $\sim 30^\circ$ - $60^\circ$  K were determined (after all experiments had been completed) by spot-welding a chromel/alumel thermocouple next to the tungsten-rhenium one. The resulting calibration curve is shown in Fig. 3.16.

Figure 3.14. Schematic of temperature controller circuit. Analog board.

Unless otherwise noted, all operational amplifiers are 741's.



AP-1188

Figure 3.15. Schematic of temperature controller  
Digital board.

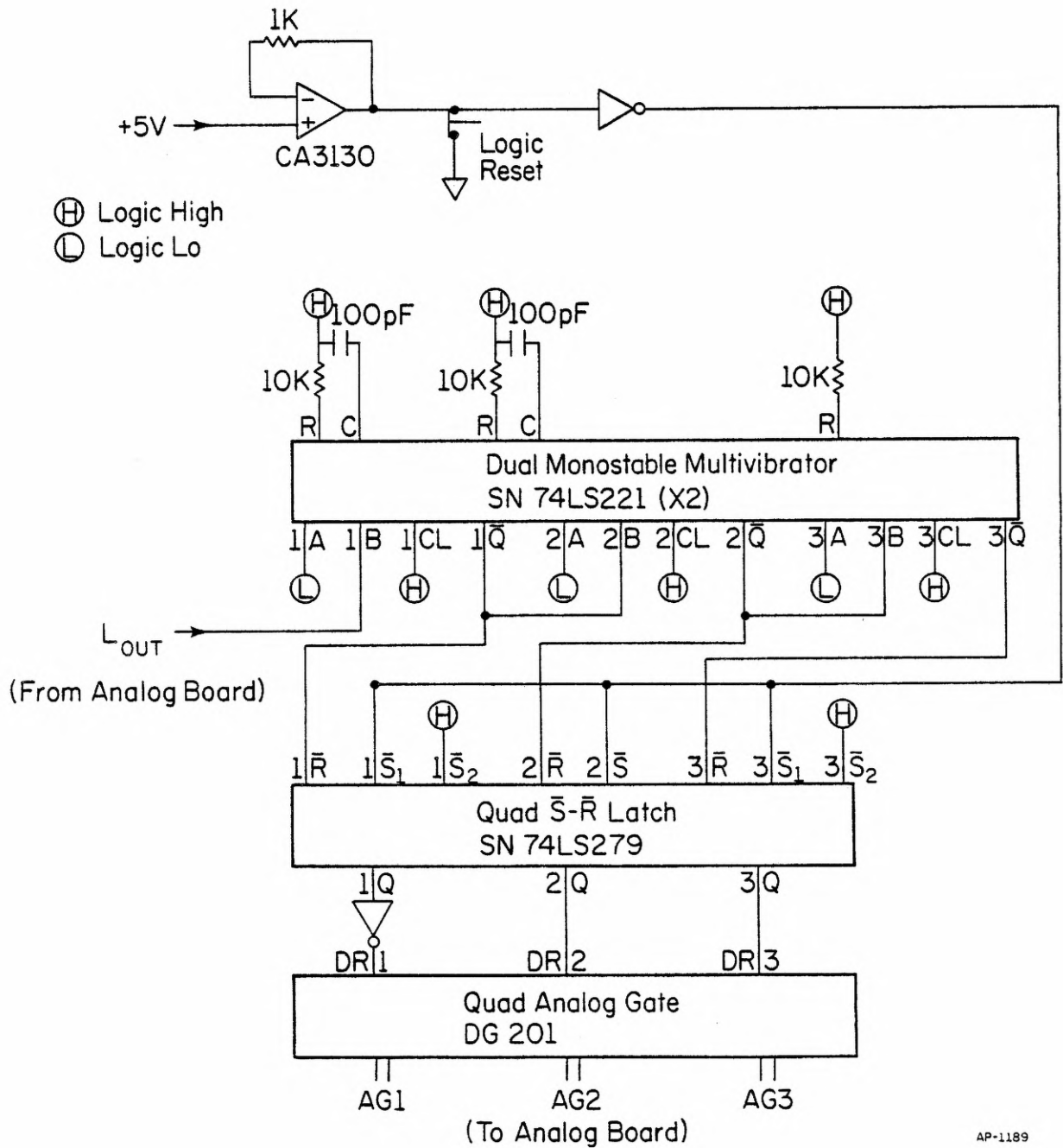
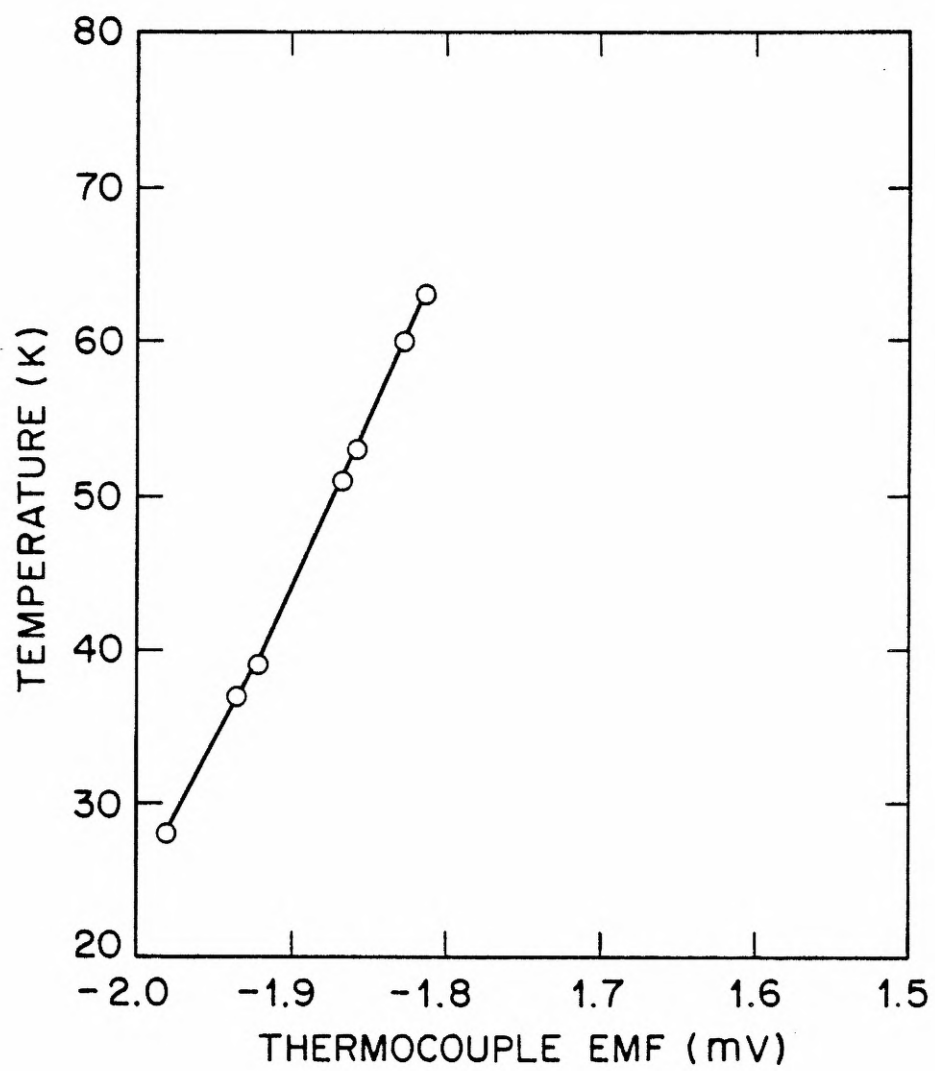


Figure 3.16. Low-temperature calibration for tungsten-5%  
rhenium/tungsten-26% rhenium thermocouple.  
Reference junction at 0° C.



### III.D. Limitations of the Present Designs

Although the apparatus described above works very well, it would be useful for us to point out some limitations and to suggest some improvements--particularly since, in some instances, the components and designs were chosen, not on the basis of best performance, but on the basis of cost constraint.

In our present set-up, the most serious limitation is the inability to swing the sample from port to port while the sample is cryogenically chilled. At low temperatures, sample movement is restricted to small distances ( $\sim 1$  cm) in order to avoid failure of the bellows. The Cajon 321-4-X-12 bellows was chosen because it is inexpensive ( $\sim \$25$  each) and readily available from stock; however, it is formed from type 321 stainless steel,<sup>1</sup> which is not rated for low-temperature use. A much superior, and considerably more expensive ( $\sim \$1,000$  each), selection would be welded bellows custom fabricated from type 304 LN stainless steel,<sup>1</sup> which is fully rated for cryogenic service. On the subject of service life, we should also mention that, although the bellows did not fail when operated under the above restriction, the braze joints between the bellows and the moly chill block (see Fig. 3.6) did spring a leak after a year of operation. (During this time, the sample had been cycled down to  $\sim 30^\circ$  K for over fifty times and up to  $\sim 600^\circ$  C for over a hundred times.) The modular design of the sample holder, however, made repair fairly easy.

Another difficulty with the sample holder is the inconvenient manner in which the wafer is changed. Initially, the moly clamp (see Fig. 3.6) was spring-loaded to facilitate changing samples; however, we found that the springs did not exert enough pressure to maintain good thermal contact



between the wafer and the chill block. In our present arrangement, the clamp is firmly bolted, and the nuts are locked in place to avoid loosening during thermal cycling. Hence, to change a wafer, we must saw apart the bolts with a jeweler's saw. However, since the sample is changed very infrequently, this inconvenience is not too serious.

Lastly, the method of gas dosing could be improved. Presently, we merely close the butterfly valve (see Fig. 3.2) and backfill the entire chamber; under this procedure, considerable gas is cryopumped onto the chill. More efficient dosing could be achieved with a molecular beam source,<sup>2</sup> which would, however necessitate an additional pumping station. Also, a quadrupole mass spectrometer<sup>3</sup> would be highly desirable for direct monitoring of impurities in the dopant gas.

### III.E. Surface-Analysis Instrumentation

#### III.E.1. LEED

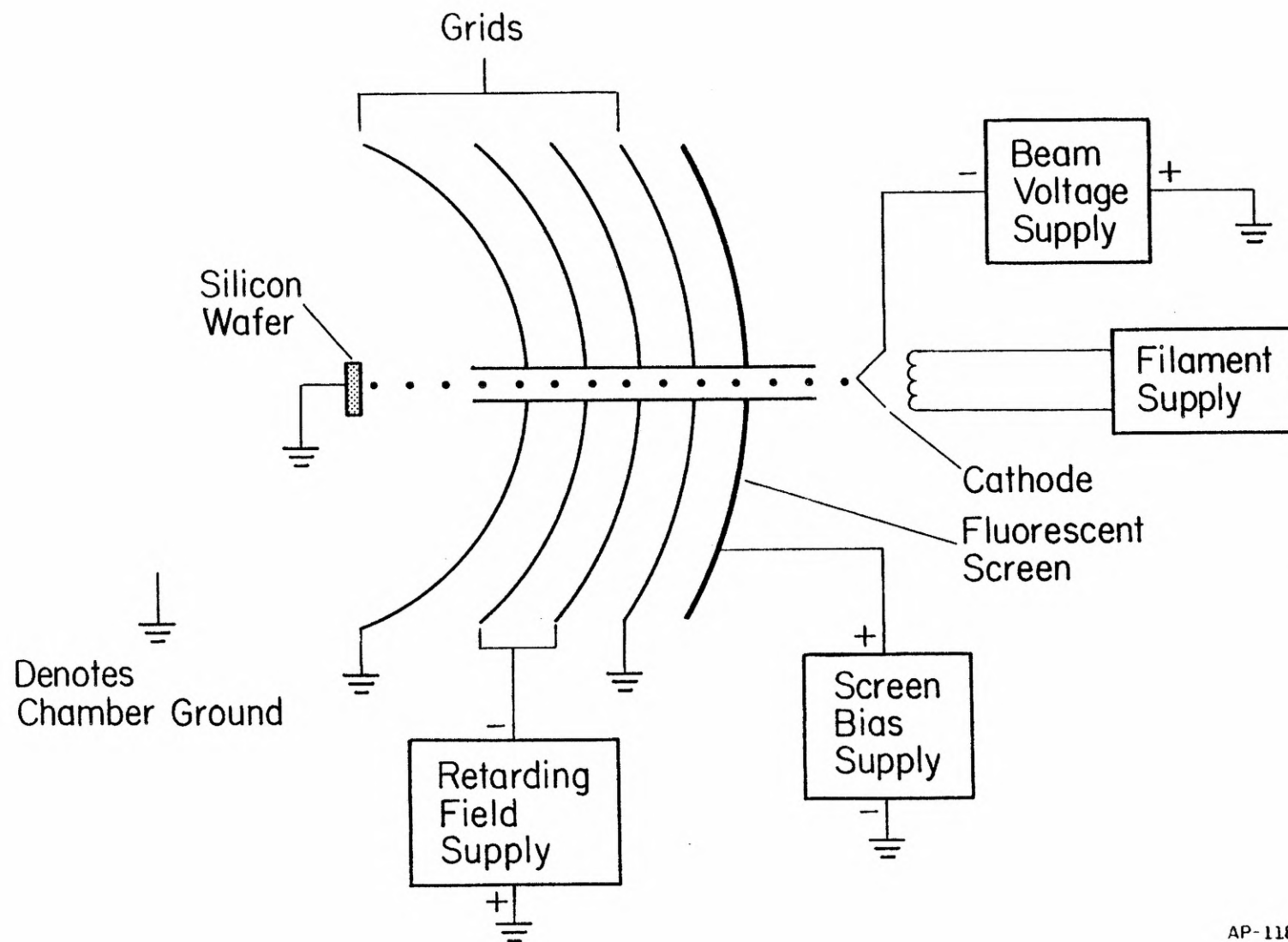
For LEED work, a conventional four-grid display unit<sup>4</sup> is used (Fig. 3.17); the LEED optics is a Varian Model 981-0024, and a Varian Model 981-0005 Control Unit supplies the operating voltages for the electron gun and screen. In order to minimize sample heating, the gun utilizes a bariated-nickel cathode indirectly heated by a tungsten filament. Typical operating parameters for the primary beam are

beam voltage: -20 to -100 V

current: 0.25-1  $\mu$ A

spot size: 0.5-1 mm.

Figure 3.17. LEED instrumentation.



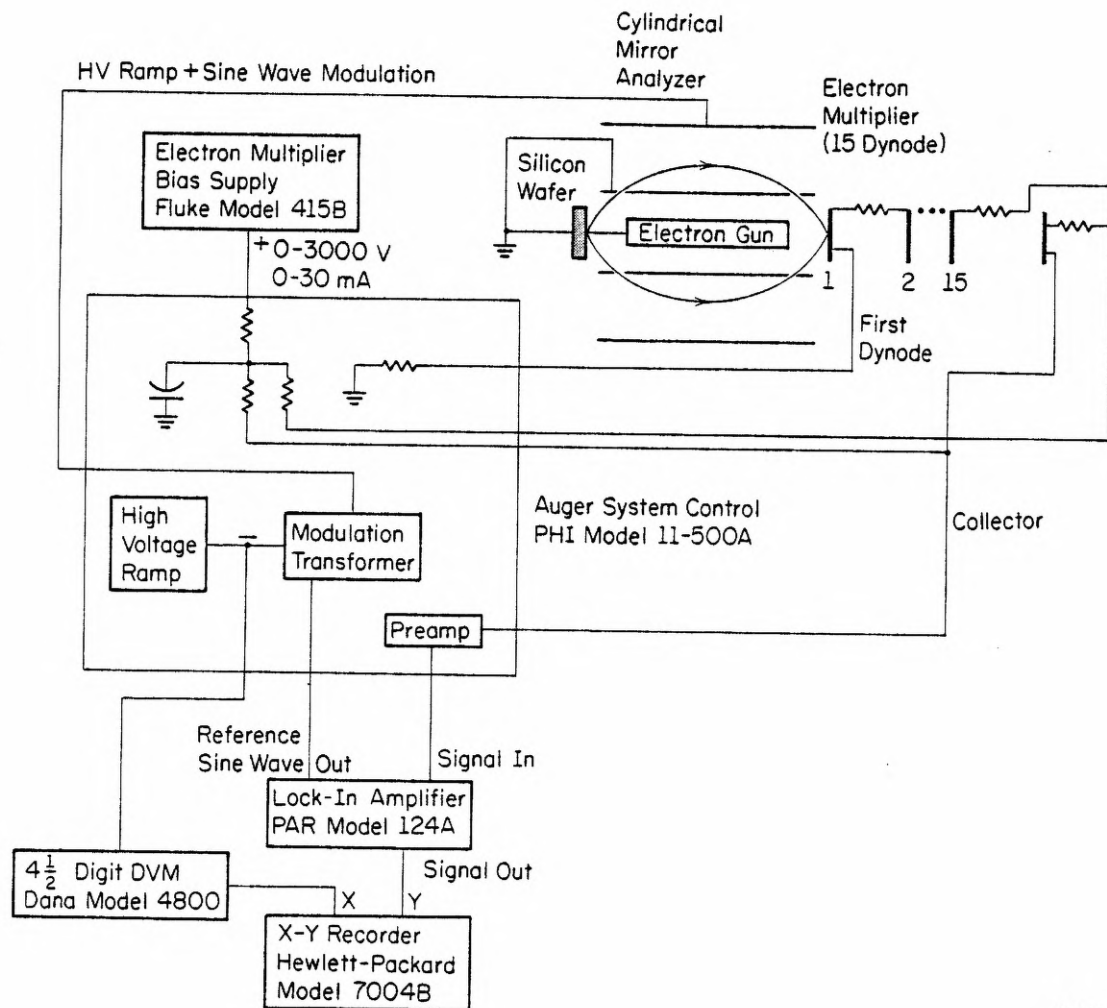
AP-1181

To repel most of the inelastic background, the retarding-field supply (Fluke Model 415B) is set at a value of (beam voltage + 5 volts). The Bragg-reflected electrons pass through the retarding grids and are accelerated by a high-voltage bias (5-6 kV) onto the fluorescent phosphor screen, which is photographed on Polaroid Type 57 High Speed Film. Typical exposure is 90 s at f/4.7.

### III.E.2. Auger

The instrumentation for Auger electron spectroscopy is shown schematically in Fig. 3.18. Since this arrangement is now fairly routine and has been discussed in detail elsewhere,<sup>5</sup> we will limit our discussion to a few particulars. The energy spectrometer is a Varian Model 981-2607 cylindrical mirror analyzer (CMA) fitted with an integral electron gun (Varian Model 981-2611); operating voltages for the gun are furnished by a Varian Model 981-2145 Electron Gun Power Module, Model 981-2147 Auger Gun Control Module, and Model 981-2157 Scanning Sample Positioner. Although the manufacturer rates the gun for 3 kV isolation, at this voltage, we found current leakage from the gun to ground (due to poor design of the mounting socket); consequently, for the most stable operation, the gun was derated to 2 kV. This particular gun, however, does have one very handy feature: the beam can be positioned by X-Y deflection plates. Additionally, the deflection plates permit a visual display of the target surface through a process usually referred to as 'absorbed current' imaging.<sup>6</sup> This process is very similar to scanning electron microscopy (SEM): as the primary beam is rapidly scanned across the surface, the electron current sunk through the sample (instead of the back-reflected secondary electron current used in SEM) is used for the Z-axis modulation of a cathode ray tube display. Resolution here is limited by the spot size of the beam ( $\sim 0.1$  mm).

Figure 3.18. Auger instrumentation.

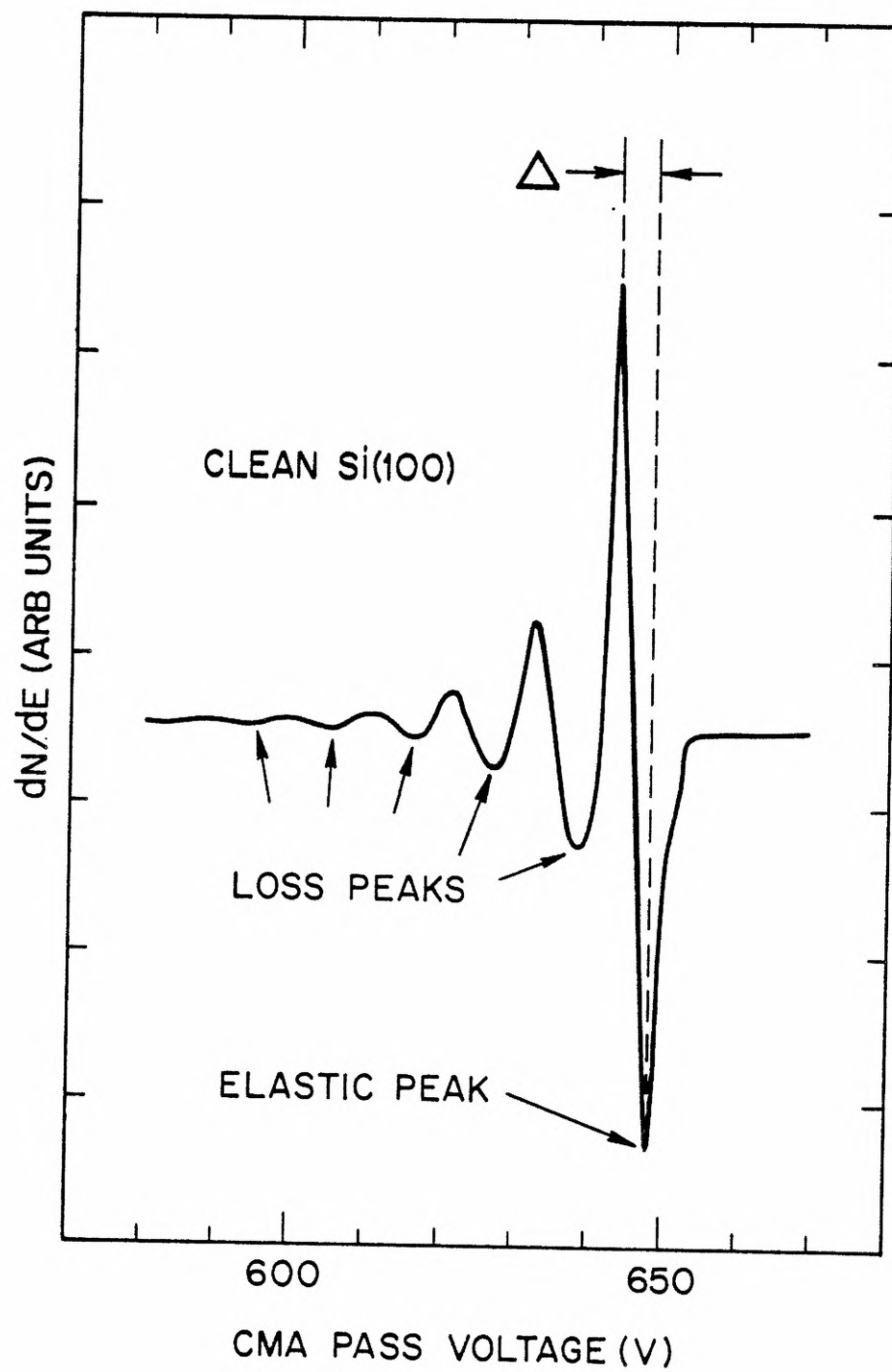


Auger spectra are taken in the conventional first-derivative mode using sine-wave modulation and lock-in detection. The standard Auger plot shows  $dN/dE$  vs.  $E$ , where  $E$  is the electron energy and  $dN(E)$  is the number of electrons in the energy window  $E, E + dE$ . In practice, the quantity measured is  $dN/dV_{CMA}$ , where  $V_{CMA}$  is the CMA pass voltage. The ratio  $(eV_{CMA}/E)$  is a constant set by the geometry of the CMA and by the alignment of the primary beam and sample with respect to the 'true' focal position of the CMA. This constant was determined by measuring the elastically reflected peak for a primary energy of  $E_p = 1000$  eV (Fig. 3.19). For this particular CMA, under conditions of highest resolution, the calibration constant is  $(eV_{CMA,p}/E_p) = 648/1000 = .648$ . Note that the electron beam and sample positions were first adjusted to give best resolution (minimum line width); from Fig. 3.19, we have

$$\text{resolution} = (\Delta/V_{CMA,p}) = 0.8\% .$$

Figure 3.19. Elastic peak from clean Si(100) surface used for calibration of CMA. Primary energy = 1000 eV.  
Modulation =  $0.5 V_{p-p}$ , 23.5 kHz.





## REFERENCES FOR CHAPTER III

1. C. Geyari, Vacuum 26, 287 (1976).
2. For a definitive treatise on molecular beams, see N. F. Ramsey, Molecular Beams (Oxford, Clarendon Press, 1956).
3. For a comprehensive treatment of quadrupole mass spectrometry, see Quadrupole Mass Spectrometry and Its Applications, edited by P. H. Dawson (Elsevier Scientific Publishing Co., Amsterdam, 1976).
4. See, for example, D. Haneman, in Surface Physics of Phosphors and Semiconductors, edited by C. G. Scott and C. E. Reed (Academic Press, London, 1975), Chap. 1, pp. 1-94.
5. See, for example, C. C. Chang, Surf. Sci. 25, 53 (1971).
6. J. M. Morabito, in Semiconductor Measurement Technology: ARPA/NBS Workshop IV. Surface Analysis for Silicon Surfaces, edited by A. G. Lieberman (NBS Special Publication 400-23, 1976), pp. 105-118.

## CHAPTER IV

## SAMPLE PREPARATION

Previous studies have shown that the adsorption of gases on silicon surfaces is strongly affected by residual surface carbon<sup>1-3</sup> and by structural defects such as atomic steps<sup>3-5</sup> and microscopic pits.<sup>6,7</sup> We have therefore taken great pains to produce homogeneous, atomically clean and ordered silicon surfaces. Production of high-grade surfaces requires stringent quality control from the initial wafering to the final vacuum processing; consequently, specialized equipment for in-house wafering was designed and constructed. In Part A, we present the procedures for producing low-damage wafers and minimizing gross contamination. Part B reviews the various in-vacuo preparation techniques and describes, in particular, the method of ion bombardment and annealing.

## IV.A. Wafer Preparation

## IV.A.1. Cutting and Grinding

Wafers were cut from a commercial (Monsanto Co.) 2 in. diameter single-crystal boule, which was grown along the [100] axis by the Czochralski method and doped with boron to a resistivity of 12-15  $\Omega$  cm. The choice of material is not critical and was mainly dictated by availability. To minimize sample charging<sup>8</sup> under electron bombardment, the resistivity should be as low as possible. The dopant level, however, should not be so high as to yield detectable concentrations of surface impurity. In Auger measurements, Thomas and Morabito<sup>9</sup> have determined that boron and phosphorus impurities in silicon are detectable for bulk resistivities  $< \sim .01 \Omega$  cm, which correspond to bulk concentrations  $> \sim 1 \times 10^{19}$  atoms/cm<sup>3</sup>.

In Fig. 4.1, we outline the wafering procedure. A square bar,  $12 \times 12 \times 50$  mm, was first cut from the boule with a high-speed diamond saw; optical orientation was used to roughly align the major axis along the [100] direction and the other faces along 110 directions. After the bar had been mounted on a special Bond holder<sup>10</sup> (Fig. 4.2), the {110} faces were precision ground to  $\pm \frac{1}{2}^\circ$  (as determined by Laue back reflection) with 400-grit silicon carbide and finished with 600-grit silicon carbide. All grinding was done with a water base and a plate-glass lap. In order to minimize subsurface damage, we built a precision abrasive-slurry saw<sup>11</sup> (Fig. 4.3) to slice the bar into wafers, 2 mm thick, which were subsequently ground to  $\pm \frac{1}{2}^\circ$  with 600-grit silicon carbide and finished with 9.5 and 3.0  $\mu\text{m}$  alumina. Final dimensions of each wafer were  $11.1 \times 11.1 \times 1.8$  mm.

#### IV.A.2. Polishing

One face of each wafer was polished with Syton (Monsanto Co.), a colloidal silica formula. Although Syton has been an industry standard for about the past decade, successful results depend upon a number of parameters which vary with the specific polishing equipment used.<sup>12,13</sup> Commercial procedures, in particular, sacrifice some surface quality for high throughput; for our work, however, we have varied the polishing parameters to yield the best surface finish without regard to processing time.

For automatic polishing, a standard metallurgical unit (Buehler Ecomet III) was fitted with the rig shown in Fig. 4.4. The wafers were mounted with thermoplastic resin (Crystalbond 509, Aremco Products, Inc.) onto a jig (Fig. 4.5), which was driven by the polishing wheel against an idler guide assembly (Fig. 4.6). Polishing solution was slowly dripped onto the pad (Politex Supreme, Geos, Inc.) from a 1-liter separatory funnel.

Figure 4.1. Procedure for preparing silicon wafers. A high-speed diamond saw is used for cuts (a)-(c). The square bar (d) is first precision ground and then sliced into wafers with an abrasive-slurry saw.

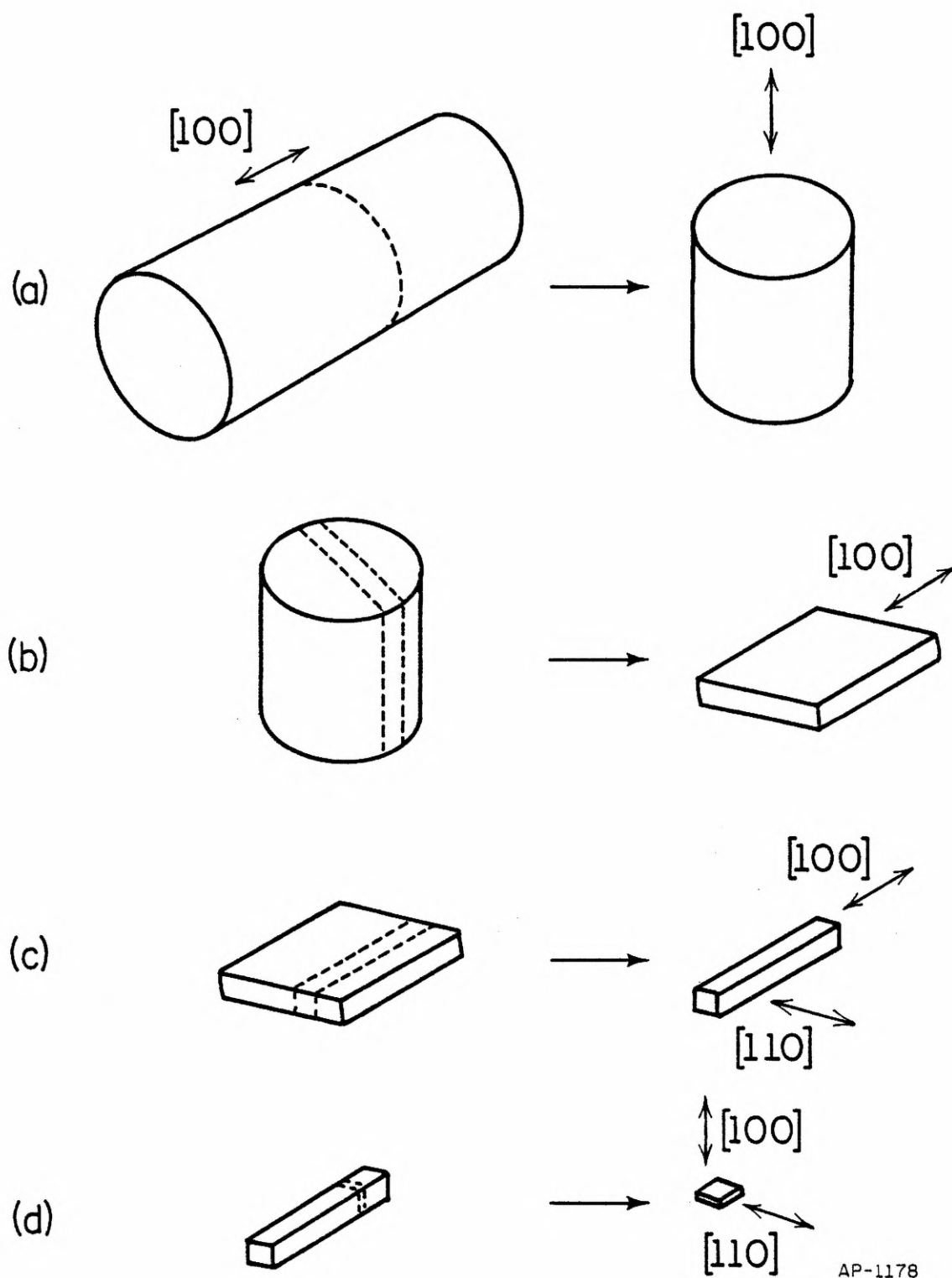


Figure 4.2. Special bond holder. The wafer is affixed to the mounting plate, which bolts onto the swivel head. The ball-and-socket joint can be rigidly locked by a clamping device not shown in the figure. The entire piston assembly is mounted on an X-ray track for Laue orientation and is inserted into the barrel for precision grinding.



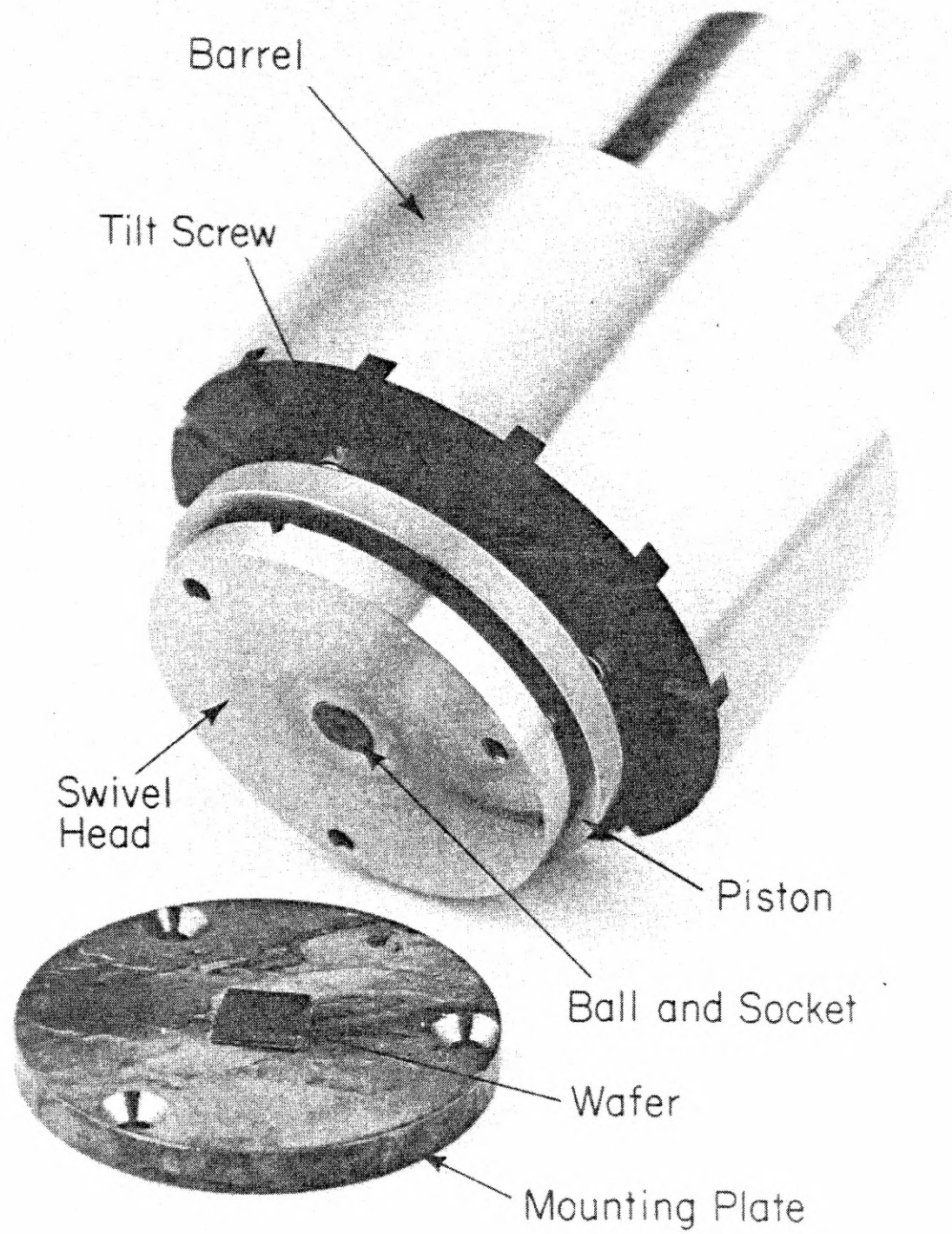


Figure 4.3. Abrasive-slurry saw. TA-tension adjust. MC-manual crank.  
IW-idler wheel. DW-drive wheel. SFC-slurry feed can.  
MS-magnetic stirrer. GW-guide wheel. DGM-depth gauge mount.  
ST-slurry trough. C-crystal. G-goniometer. MIH-micrometer  
index head. The goniometer may be directly transferred from  
an X-ray track to the saw. The abrasive-slurry, a mixture  
of 600-grit silicon carbide powder and mineral oil, is  
agitated by the magnetic stirrer and slowly dripped onto the  
cut.

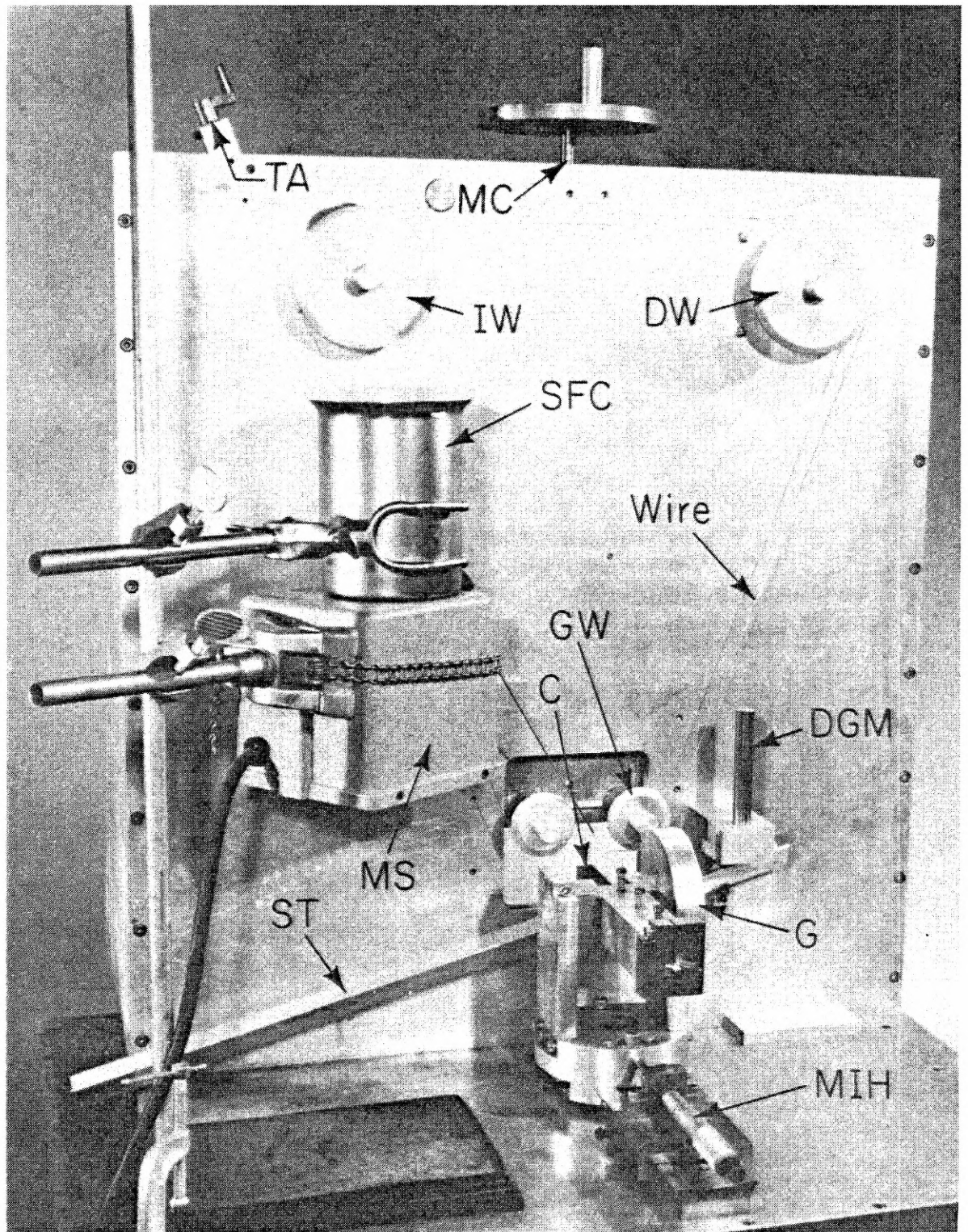


Figure 4.4. Assembly for Syton polishing. Main unit is Buehler Ecomet III metallurgical polisher. The wheel is enclosed by a Plexiglas dust cover not shown in the photograph.

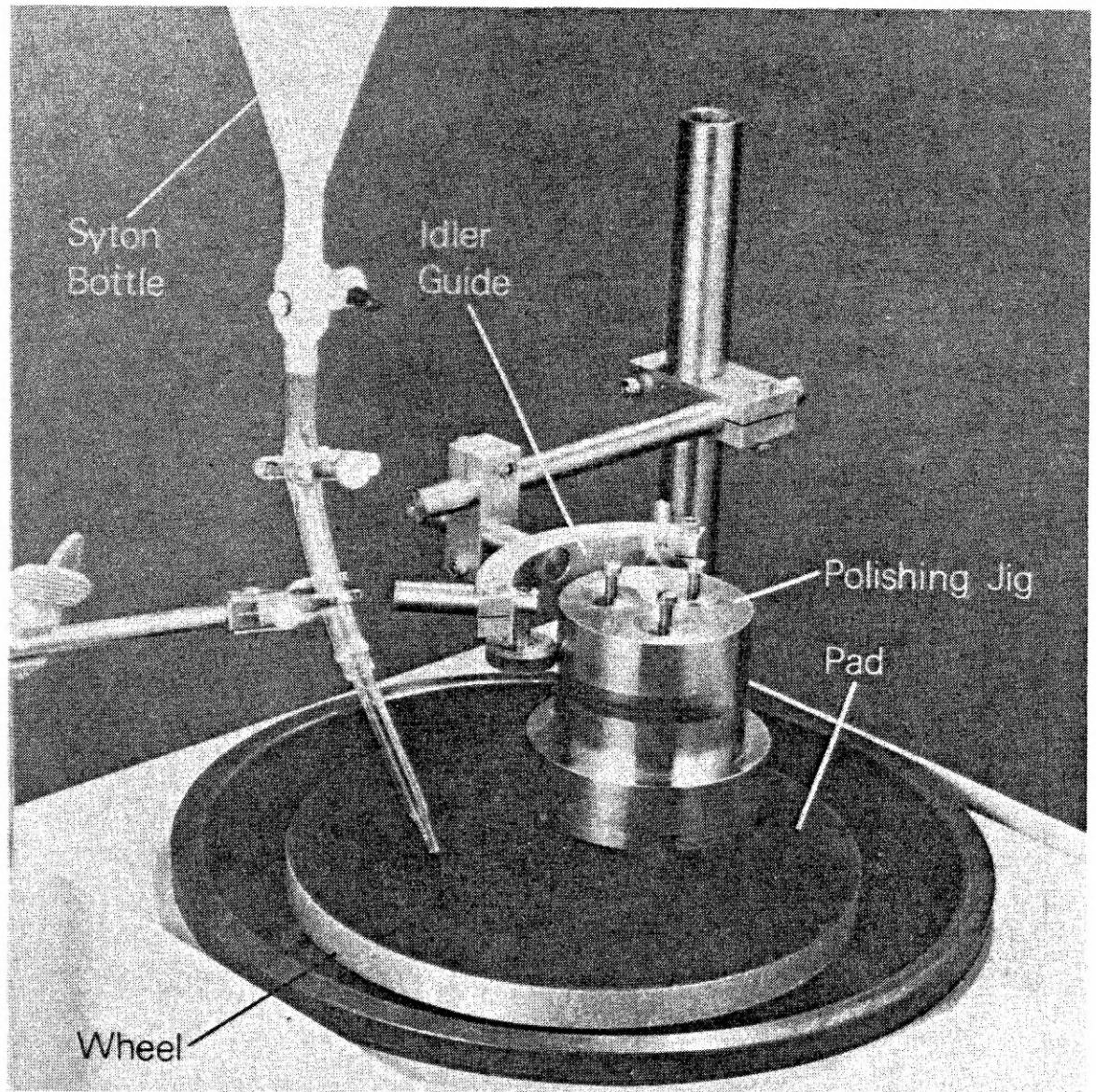




Figure 4.5. Close-up of mounting jig. The wafer is affixed to a piston, which is inserted into the barrel. Up to three wafers can be accommodated.

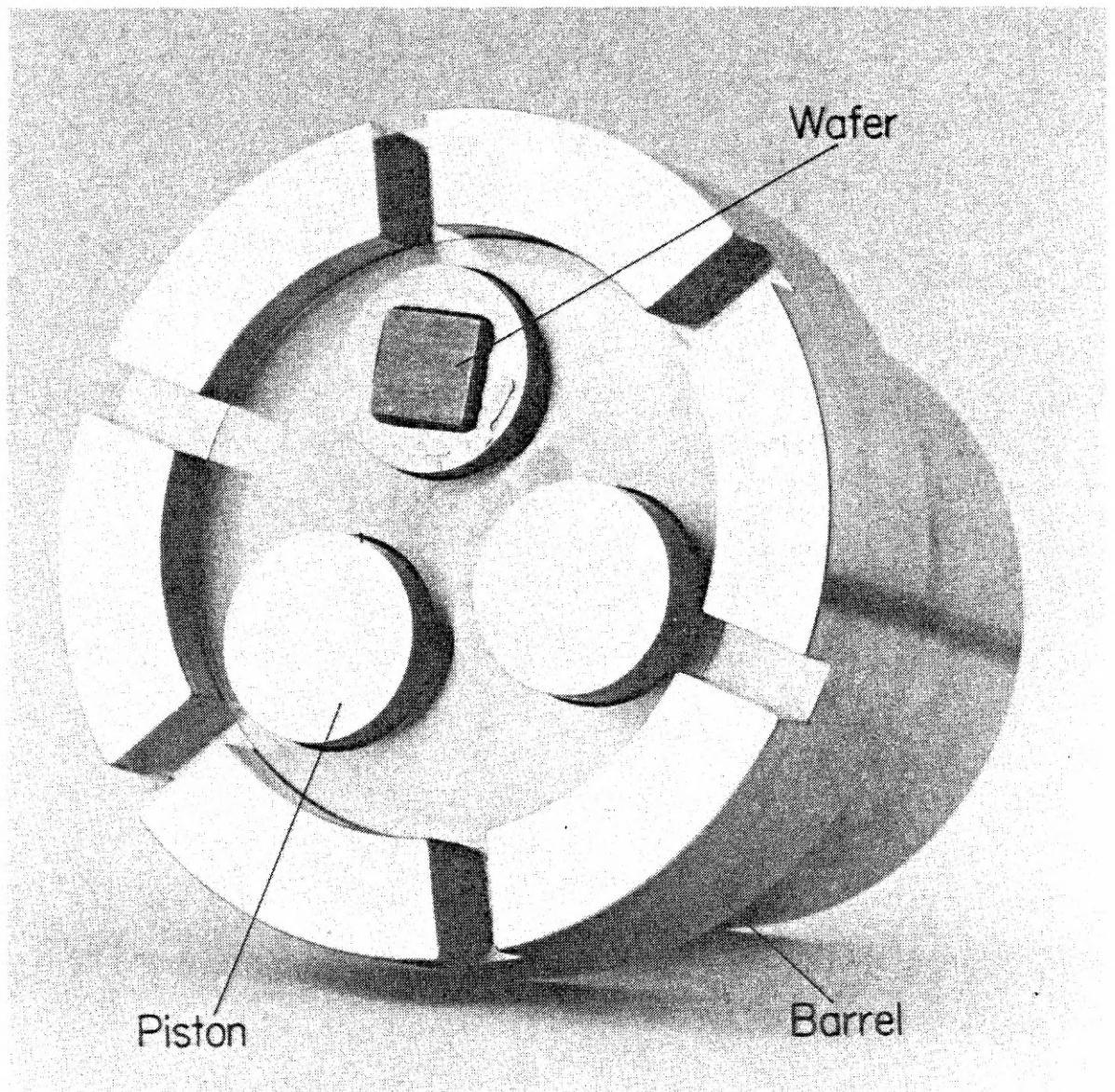
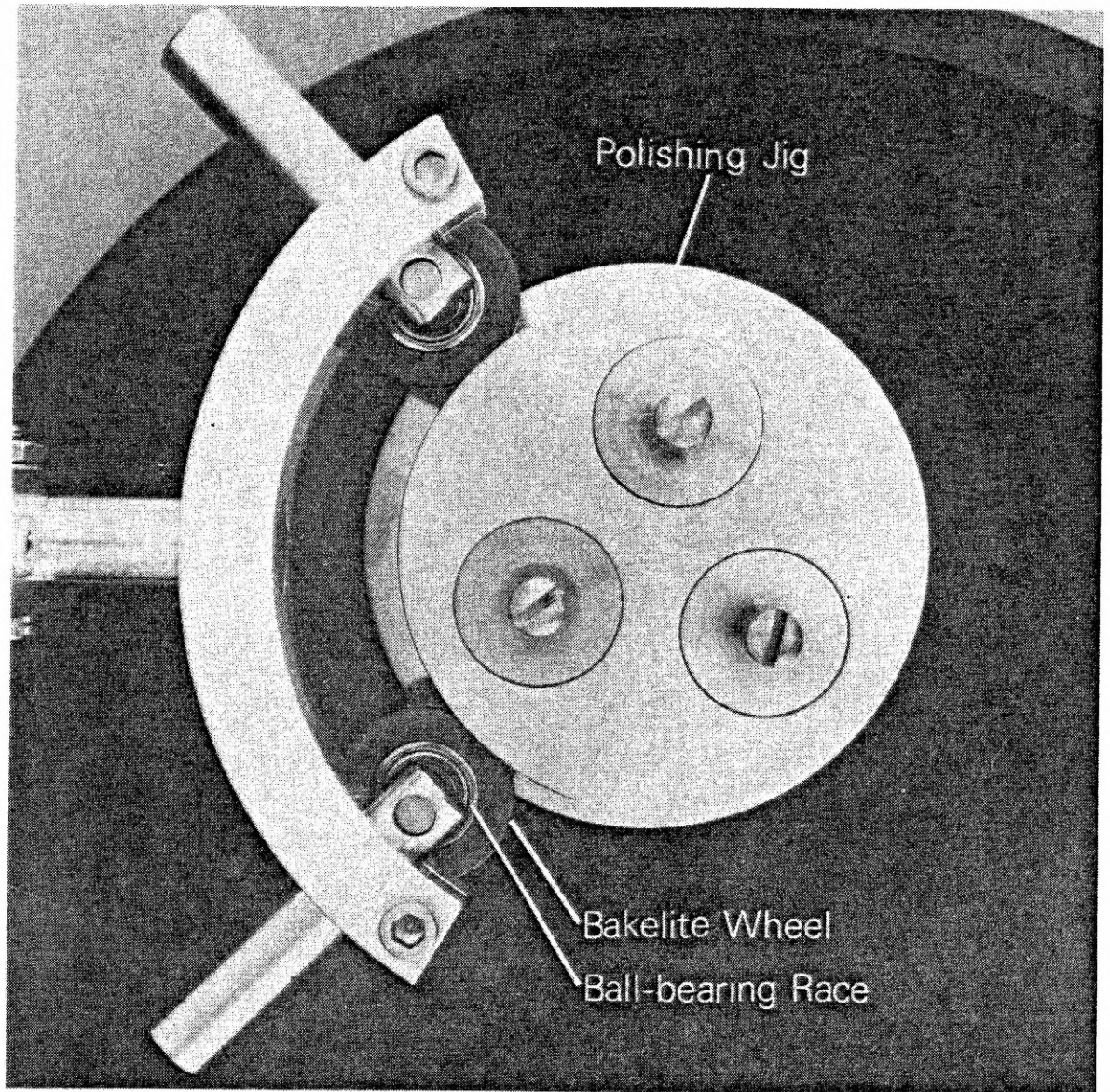


Figure 4.6. Close-up of idler assembly. The polishing jig is frictionally driven against two bakelite wheels mounted onto ball-bearing races.





The following parameters yielded surfaces free of pits and haze in  
~ 6 h polishing time:

Temperature: room

Wheel speed: 100 rpm

Solution drip rate: 1 drop/s

Solution formula:

By volume, add 1 part 10 wt% NaOH solution to 100 parts  
distilled water. Stir thoroughly, then add 50 parts  
Monsanto Syton HT-50 colloidal silica and stir thoroughly  
again. Final pH is 10-10.5.

#### IV.A.3. Chemical Cleaning

In order to minimize gross contamination, the wafers must be properly cleaned. If proper procedures are followed, we have found that the esoteric etches<sup>14,15</sup> recommended by other workers are not needed. The main source of difficulty arises from the fact that, when colloidal silica dries, it irreversibly precipitates into a hard, sticky residue.<sup>16</sup> Therefore, immediately upon completion of polishing, the wafers, still mounted on the pistons (Fig. 4.5), must be rapidly transferred to a holding tank of distilled water. In initial trials, we found that ultrasonic cleaning in either a plain distilled water or a distilled water and detergent bath was not sufficient to remove all silica particles. However, if the wafers were ultrasonically agitated in a distilled water bath and simultaneously swabbed with surgical cotton, no silica remained. After the wafers had been rinsed in distilled water and dried with nitrogen gas, they were demounted and ultrasonically cleaned in the following solvents (all reagent grade):

acetone (to remove Crystalbond residue)

trichloroethylene

acetone

ethyl alcohol.

Finally, to minimize hydrocarbon contamination, they were rinsed in a running stream of distilled water and blown dry with a blast of nitrogen gas.

#### IV.A.4. Characterization

The wafers were inspected both optically by Nomarski interference-contrast microscopy,<sup>17</sup> up to 300 x, and by scanning electron microscopy (SEM),<sup>18</sup> up to 20,000 x. Except for pits at the very edges, no defects down to 0.1  $\mu\text{m}$  were detected. Figure 4.7 shows a typical SEM photo.

#### IV.B. Vacuum Processing

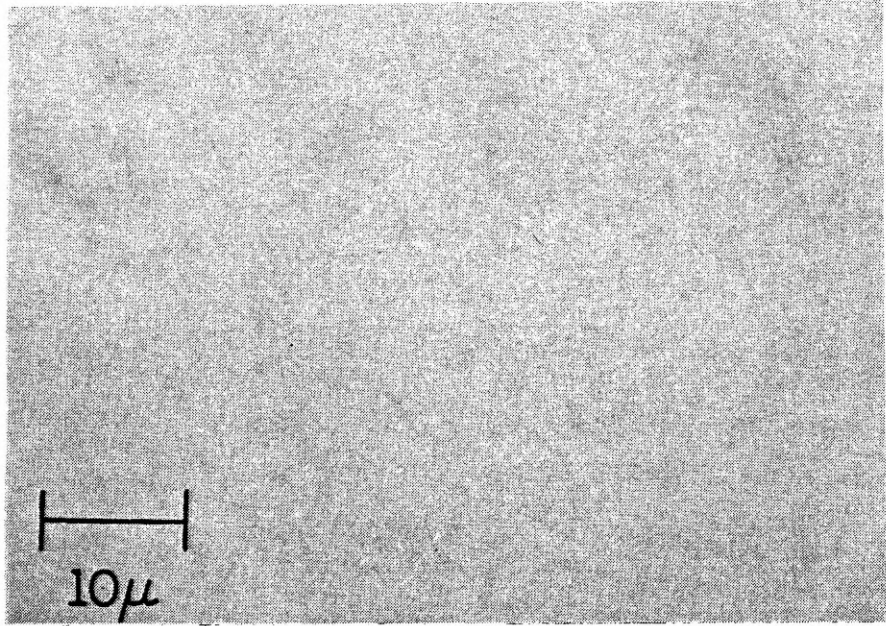
For reproducible adsorbate/surface experiments, we must start out with a homogeneous atomically clean and ordered surface. In this section, we will first review the various in-vacuo techniques for preparing silicon surfaces and then give the experimental details for one particular method (ion bombardment and annealing).

##### IV.B.1. Review of Techniques

Atomically clean and ordered surfaces have been successfully produced by four techniques

- (1) Pulsed laser annealing<sup>19,20</sup>
- (2) Cleavage<sup>21,22</sup>
- (3) Heat treatment<sup>23,24</sup>
- (4) Ion bombardment and annealing.<sup>15,24,25</sup>

Figure 4.7. Scanning electron micrograph of Syton-polishing wafer. Except for pits at the very edges of the wafer (upper portion of photograph), no defects were found. The original shown here was at 2,000 x, but scans up to 20,000 x were taken.



Pulsed laser annealing is a very recent technique developed after our work was well under way. In the future, it will probably become the standard procedure since clean and ordered surfaces can be produced in less than one second. The only disadvantage appears to be the high cost of a suitable laser ( $\sim$  \$30,000 at current prices). For details, the reader is referred to the pioneering papers by Zehner, White, and Ownby.<sup>19,20</sup>

In the past, many workers have prepared silicon surfaces by in-vacuo cleavage since it is very fast and produces surfaces with a minimum of contamination.<sup>26</sup> Cleavage, however, is a very limited technique. First of all, silicon cleaves only along the (111) plane.<sup>27</sup> Additionally, although cleaved surfaces are ordered on the local atomic level (as determined by LEED), they are not homogeneous. Optical and electron microscopy reveal nonreproducible arrays of tear marks and steps<sup>21,22</sup> which strongly affect some surface properties.<sup>28</sup> Lastly, as a practical matter, a sample large enough for multiple cleavages must be used since pumpdown and bakeout of the vacuum chamber is very time consuming. Heating and cooling (called for in many experiments) of such a large block then becomes difficult.

High-temperature heating has been frequently used as a general technique because it is fairly fast and simple. Thermal cleaning of silicon, however, requires temperatures in excess of 1200° C.<sup>23,24</sup> Since silicon melts at 1410° C and has relatively poor thermal conductivity, local or total melting of the sample is a major problem.<sup>15</sup> Also, heat-treated surfaces are often not homogeneous--thermal etching produces extensive pitting.<sup>15,29</sup> For a first-hand account of the miseries of thermal cleaning, the reader should consult the work by White.<sup>15</sup>



The most viable technique, with the exception of the aforementioned new laser process, is ion bombardment and annealing (IBA), which can yield reproducible, homogeneous, atomically clean and ordered surfaces. It would be the principal method for preparing silicon if it were not so time consuming.

#### IV.B.2. Ion Bombardment and Annealing

In this procedure, the contamination layers are first sputtered away by low-energy (typically 1000 eV or less) noble gas ions. During bombardment, however, ions are also implanted into the target surface, which is left disordered.<sup>26,30</sup> The sample then must be heated to some high temperature to drive out the embedded ions and to anneal out the damage. Although ion bombardment and annealing has been used since the early work of Farnsworth,<sup>30</sup> some of the parameters which affect the final surface quality have been determined only recently. The main factors involved are

- (1) type of ion
- (2) bombardment energy
- (3) substrate temperature during sputtering
- (4) annealing temperature
- (5) background contamination.

By far the most popular sputtering gas is argon.<sup>26</sup> Sakurai and Hagstrum, however, have shown that neon is a better choice<sup>31-33</sup>: neon bombardment produces less surface damage, which can be annealed out at a lower temperature. For silicon, neon-bombarded surfaces can be annealed at 600° C, whereas argon-bombarded surfaces<sup>15,24,34</sup> require 800°-900° C. As we shall see later, 800°-900° C is a particularly nasty temperature regime.

For a given ion energy, the degree of surface damage is largely a matter of ion size.<sup>35</sup> We would then expect helium to be the best choice; the sputter yield for helium ions is very low, however, while the yield for neon is about the same as for argon.<sup>33,36</sup> (Additionally, helium cannot be detected by Auger.)

Surface damage also decreases with lower ion energy.<sup>35,37</sup> Unfortunately, since the sputter yield, too, decreases with lower ion energy,<sup>36</sup> a compromise must be effected. Some studies have shown that surface damage may be limited to the outermost layer if the ion energy is less than 200 eV.<sup>34,35</sup> At such low energies, however, the sputter yield is so small that the high current density of a plasma discharge ( $10^{-2}$  Torr or higher) must be used to attain significant sputter rates.<sup>33,36</sup> Plasma discharges are not readily compatible with most ultrahigh vacuum systems. With commercial ion guns, reasonable sputter rates and acceptable surface damage can be achieved with 500-1000 eV ions.<sup>34</sup>

Recently, Bean et. al.<sup>34</sup> have discovered that residual damage and contamination is strongly influenced by the substrate temperature during sputtering. They prepared a series of silicon surfaces by sputtering with 1000 eV argon ions and annealing at 800° C for 10 min; substrate temperatures during sputtering were varied from 25°-800° C. In all instances, Auger revealed no residual argon in the immediate (top 5-10 Å) surface region; and reflection high energy electron diffraction (RHEED) showed well-ordered surfaces. Subsequent analysis by Rutherford backscattering, however, detected residual argon below the surface in those substrates which had been sputtered above 25° C. Additionally, analysis by transmission electron microscopy (TEM)



revealed an increase of defects with substrate temperature. Thus, for minimum subsurface (deeper than 5-10 Å) contamination and damage, the substrate must be sputtered at room temperature or below. The condition of the subsurface region needs to be considered because it affects such processes as diffusion of adsorbates into the bulk.

In cleaning silicon, the major difficulty is the elimination of residual carbon.<sup>15,38</sup> Auger studies of as-loaded wafers indicate that the major contaminants are carbon, oxygen, and (occasionally) sulfur.<sup>15,25,38</sup> Although sputtering readily removes the oxygen and sulfur, residual carbon persists in many instances. In the past, there has been much speculation concerning the origins of the carbon contamination, but a number of detailed studies have now pinpointed two major sources: (1) formation of silicon carbide precipitates before sputtering and (2) background contamination during sputtering.

Using RHEED measurements, Henderson et. al.<sup>39,40</sup> determined that, if as-loaded wafers were heated to 800°-1050° C, carbonaceous adsorbates would decompose to form silicon carbide precipitates. The degree of carbon contamination varied with the chemical pretreatment; in particular, etching in HF produced very high carbon levels.<sup>14</sup> Silicon carbide particles thus formed are very resistant to sputtering<sup>15</sup> and may be removed only by high-temperature heating (~ 1200° C).<sup>39,40</sup> As we have mentioned above, however, such heat treatment is undesirable. Thus, all adsorbates should be sputtered away before the substrate is heated near 800° C.

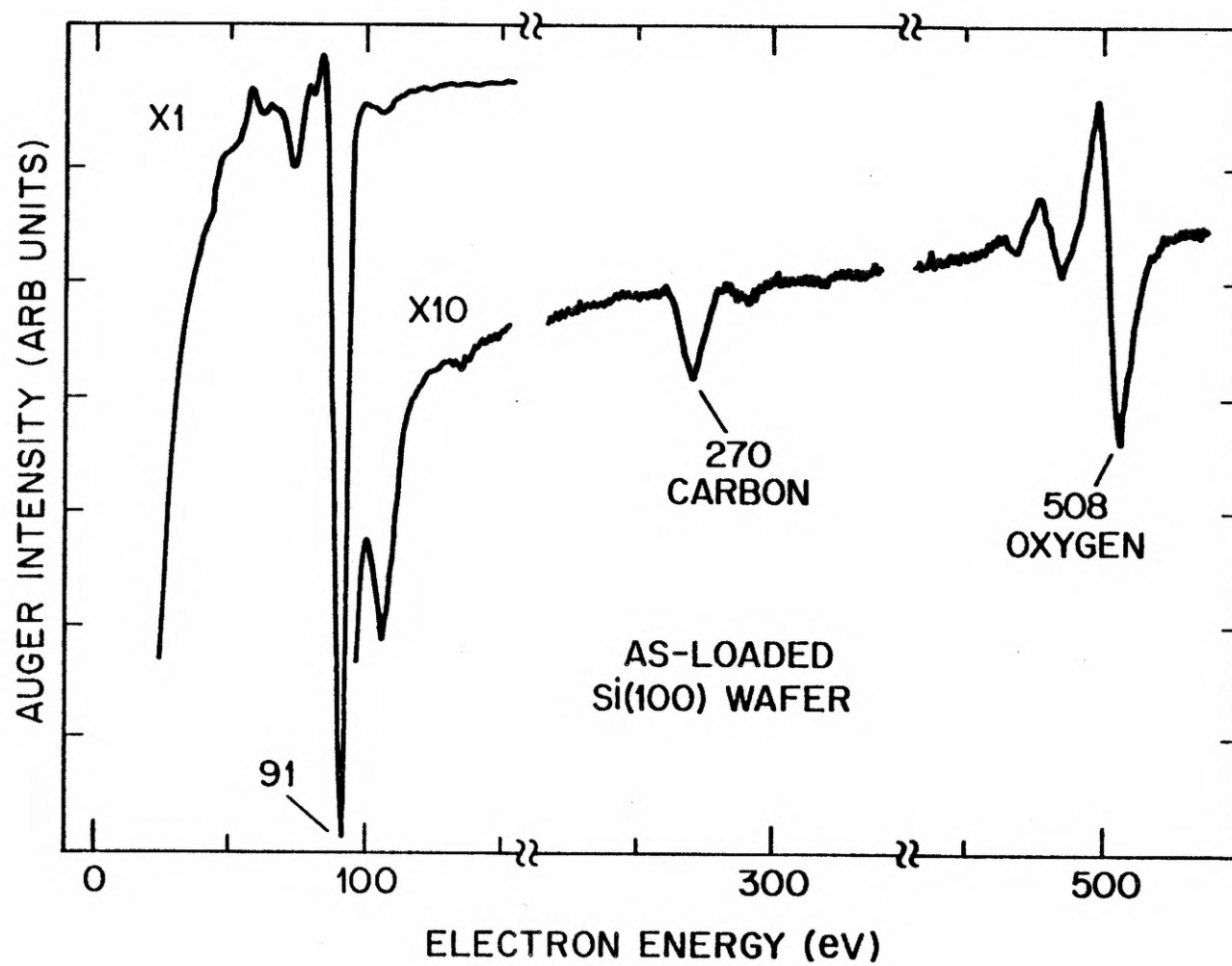
Carbon contamination can also arise from background gases during sputtering. CO and CO<sub>2</sub> are common residual gases in most ultrahigh vacuum systems.<sup>26</sup> Additionally, in ion-pumped chambers, CH<sub>4</sub> and other light hydrocarbons are evolved when the pumps are shut off for sputtering

(the usual practice).<sup>41</sup> If the background is sufficiently high, a significant amount of carbon is implanted into the silicon during ion bombardment, and silicon carbide particles may be formed.<sup>42</sup> In order to minimize contamination, the chamber and all filaments must be extensively outgassed, and very pure sputtering gas must be used.<sup>41</sup> Also, the use of mercury diffusion pumps instead of ion pumps appears to be advantageous.<sup>31-33</sup>

With the above discussions in mind, we can now proceed to the details of our in-vacuo cleaning technique.

Following Sakurai and Hagstrum, we chose neon for the sputtering gas. In addition to producing less damage, neon has two further advantages over argon. First of all, in diffusion-pumped systems, neon does not condense in liquid-nitrogen traps and, thus, pumps out faster.<sup>33</sup> Secondly, in Auger analysis, the argon lines ( $\sim 180$ - $220$  eV) overlap the lines from common impurities such as boron and molybdenum, while the neon lines are well removed ( $\sim 760$ - $810$  eV). To minimize contamination, the neon gas, supplied in reagent bottles by Airco or Linde, was further purified by molybdenum getters<sup>43</sup> before being admitted into the main chamber (see Fig. 3.4). Special passivation of the silicon wafers was not necessary since excessively high carbon levels were not found. Figure 4.8 is a typical Auger scan of a wafer after bakeout. Only small amounts of carbon and oxygen were detected; on occasion, if the analyzed region contained a dust particle (readily visible on absorbed-current images), sulfur (150 eV) was also present.

Figure 4.8. High-sensitivity Auger scan of Si(100) wafer after bakeout. Only contaminants are small amounts of carbon and oxygen. Primary energy = 2000 eV. Modulation = 4 V<sub>p-p</sub>, 23.5 kHz.



For sputtering, a commercial sputter ion gun (PHI Model 04-161) and control unit (PHI Model 20-005) were used. One major problem which we encountered with this set-up was the proper focussing of the gun. If the ion beam strikes any part of the sample holder, material (molybdenum, in our case) will be sputtered onto the silicon wafer.<sup>37,44</sup> The usual focussing procedure, as prescribed by the manufacturer, involves replacing the wafer with a specially oxidized tantalum foil test target. If the oxide is sputtered through, the focal spot can be monitored visually and adjusted accordingly. Such a procedure is, of course, tedious so we developed a simplified, in-situ method. To a first approximation, the ion current to the sample is determined by the intersection of the ion beam with the sample-- that is, a defocussed beam has a spot size larger than the wafer ( $\sim 1$  cm). Therefore, the beam can be focussed merely by maximizing the ion current to the sample. Since the beam current meter on the control unit was not sensitive enough, a Keithley Model 417 picoammeter was used to monitor the ion current.

In a typical sputtering run, the butterfly valve between the main chamber and diffusion pump was first closed (see Fig. 3.2); and the chamber was then backfilled to  $1 \times 10^{-4}$  Torr neon. In order to minimize heating from the ion gun filament, the wafer was cooled with (room-temperature) nitrogen gas flowing through the chill (see Fig. 3.6). The surface was positioned normal to the ion beam, which was operated at an energy of 800 eV. At a gun-to-wafer distance of  $\sim 2.5$  cm, a focussing voltage of  $\sim 735$  V produced a beam current of  $\sim 35\mu\text{A}$  into a spot diameter of  $\sim 8$  mm. To reduce cratering, the sample was translated across the beam;  $\sim 50$  min bombardment was needed to sputter clean a  $\sim 8 \times 11$  mm region.

After the chamber had been pumped out, the sample was annealed at 650° C for 15 min. At this stage, Auger scans revealed recontamination by carbon and oxygen (presumably from outgassing of the sample assembly and chamber walls); during the annealing period, the chamber pressure rose typically to  $1 \times 10^{-8}$  Torr. A freshly loaded wafer required approximately ten cycles of ion bombardment and annealing before no impurities could be detected. For subsequent cleaning, a single cycle was sufficient if the chamber had not been exposed to atmosphere.

The final surfaces, as characterized by Auger, LEED, and SEM, were excellent. High-sensitivity Auger scans (Fig. 4.9) revealed no impurities, including carbon, above the noise level. Typical peak-to-peak noise was  $\sim 1/2000$  times the main silicon 91 eV peak; this signal-to-noise level is representative of the cleanest surfaces produced<sup>31,32</sup> and corresponds to an impurity level<sup>9</sup> of  $\sim 0.1$  at%. LEED (Fig. 4.10) showed a very sharp ( $2 \times 1$ ) pattern indicative of a well-ordered surface. And subsequent analysis by SEM revealed no defects down to 0.1  $\mu\text{m}$  (Fig. 4.11).

Figure 4.9. High-sensitivity Auger scan of a Si(100) surface cleaned by neon bombardment and annealing. No impurities are apparent above the noise level; note the total absence of carbon at 270 eV and oxygen at 508 eV. Primary energy = 2000 eV. Modulation = 4 V<sub>p-p</sub>, 23.5 kHz.

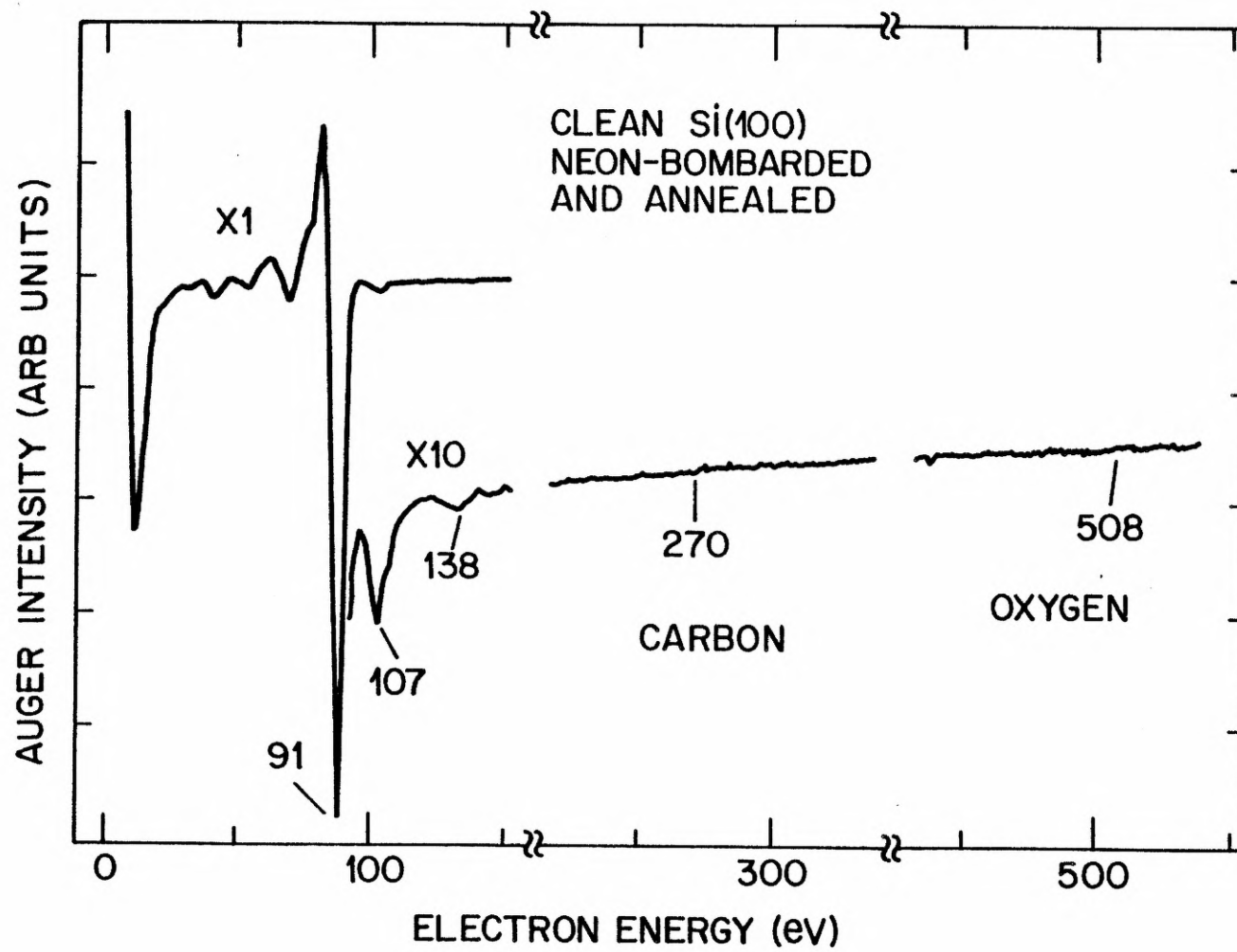




Figure 4.10. LEED picture of Si(100)-(2×1) surface produced by neon bombardment and annealing. Primary beam energy = 48 eV.

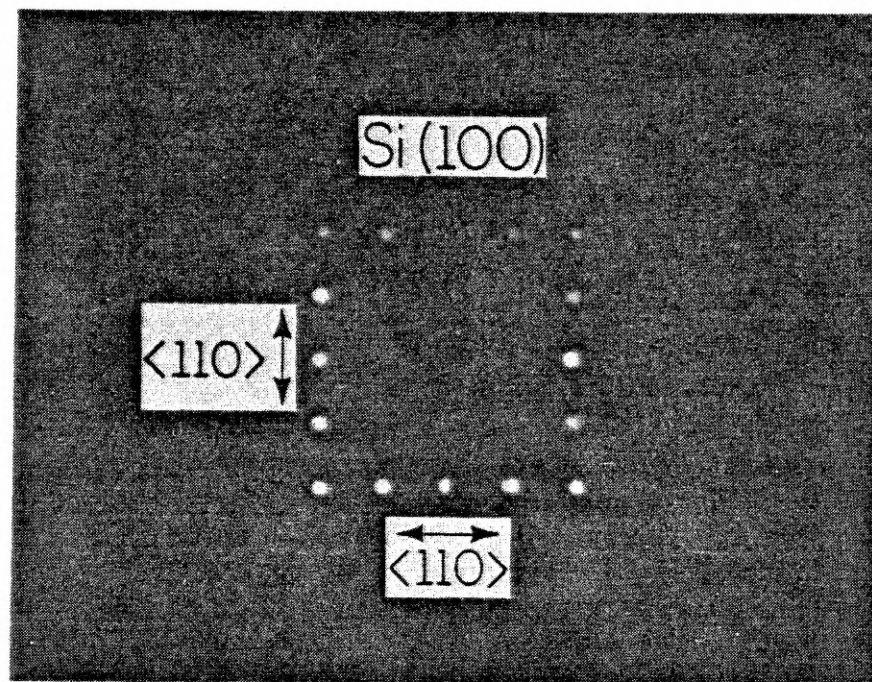
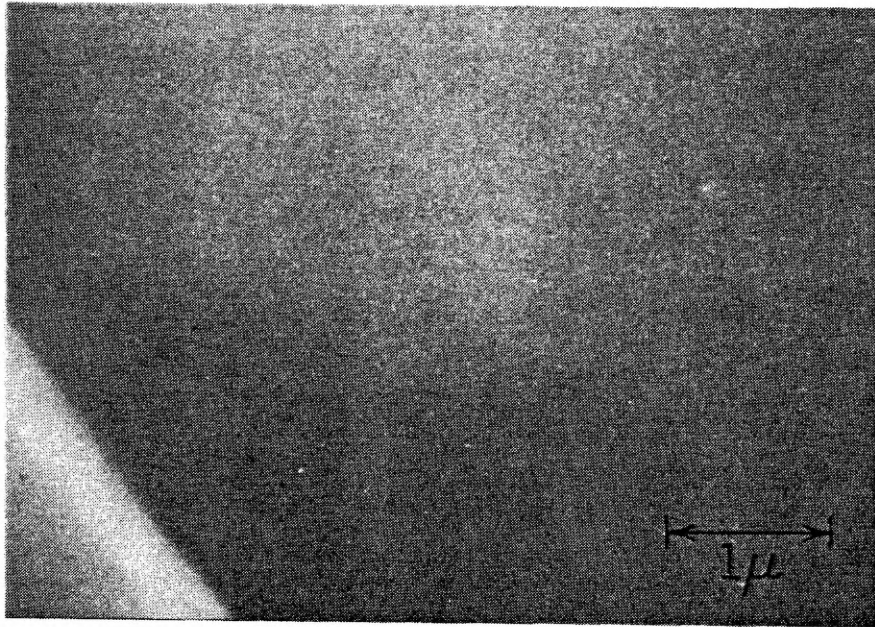


Figure 4.11. Scanning electron micrograph of neon-bombarded and annealed wafer. Original magnification = 20,000 x. No defects were found (Feature in lower left hand corner is a dust particle used for focussing.)



## REFERENCES FOR CHAPTER IV

1. J. P. Coad, H. E. Bishop, and J. C. Riviere, *Surf. Sci.* 21, 253 (1970).
2. B. Carriere and J. P. Deville, *Surf. Sci.* 80, 278 (1979).
3. N. Kasupke and M. Henzler, *Surf. Sci.* 92, 407 (1980).
4. H. Ibach, K. Horn, R. Dorn, and H. Luth, *Surf. Sci.* 38, 433 (1973).
5. G. M. Guichar, C. A. Sebenne, G. A. Garry, and M. Balkanski, *Surf. Sci.* 58, 374 (1976).
6. R. E. Kirby and J. W. Dieball, *Surf. Sci.* 41, 467 (1974).
7. H. F. Dylla, J. G. King, and M. J. Cardillo, *Surf. Sci.* 74, 141 (1978).
8. D. C. Northrop, in The Use of the Scanning Electron Microscope, edited by J. W. S. Hearle, J. T. Sparrow, and P. M. Cross (Pergamon Press, Oxford, 1972), pp. 34-37.
9. J. H. Thomas III and J. M. Morabito, *Surf. Sci.* 41, 629 (1974).
10. See, for example, E. A. Wood, Crystal Orientation Manual (Columbia University Press, New York, 1963), p. 22.
11. See, for example, W. L. Bond, Crystal Technology (John Wiley & Sons, New York, 1976), p. 188.
12. E. Mendel, *SCP and Sol. State Tech.* 10 (8), 27 (August, 1967).
13. Ludox Colloidal Silica for Use in Polishing Silicon Semiconductor Wafers, data sheet (E. I. du Pont de Nemours & Co., Wilmington, Delaware).
14. R. C. Henderson, *J. Electrochem. Soc.* 119, 772 (1972).
15. S. J. White, Ph.D. Thesis, University of Warwick (England), 1977.
16. Properties, Uses, Storage and Handling: Ludox Colloidal Silica, data sheet (E. I. du Pont de Nemours & Co., Wilmington, Delaware).
17. See, for example, J. H. Richardson, Optical Microscopy for the Materials Sciences (Marcel Dekker, New York, 1971), p. 135.

18. See, for example, O. Johari and A. V. Samudra, in Characterization of Solid Surfaces, edited by P. F. Kane and G. B. Larrabee (Plenum Press, New York, 1974), Chap. 5, pp. 107-131.
19. D. M. Zehner, C. W. White, and G. W. Ownby, Appl. Phys. Lett. 36, 56 (1980).
20. D. M. Zehner, C. W. White, and G. W. Ownby, Surf. Sci. 92, L67 (1980).
21. G. W. Gobeli and F. G. Allen, J. Phys. Chem. Solids 14, 23 (1960).
22. M. Henzler, Surf. Sci. 19, 159 (1970).
23. T. D. Poppendieck, T. C. Ngoc, and M. B. Webb, Surf. Sci. 75, 287 (1978).
24. M. J. Cardillo and G. E. Becker, Phys. Rev. B 21, 1497 (1980).
25. T. Smith, Surf. Sci. 27, 45 (1971).
26. D. Haneman, in Surface Physics of Phosphors and Semiconductors, edited by C. G. Scott and C. E. Reed (Academic Press, London, 1975), Chap. 1, pp. 1-94.
27. J. J. Gilman, in Fracture, edited by B. L. Averbach, D. K. Felbeck, G. T. Hahn, and D. A. Thomas (John Wiley & Sons, New York, 1959), Chap. II, p. 205.
28. M. Henzler, Appl. Phys. 9, 11 (1976).
29. G. J. Russell and D. Haneman, J. Electrochem. Soc. 114, 398 (1967).
30. R. E. Schlier and H. E. Farnsworth, in Semiconductor Surface Physics, edited by R. H. Kingston (University of Pennsylvania Press, Philadelphia, 1957), Chap. I, pp. 3-22.
31. T. Sakurai and H. D. Hagstrum, Phys. Rev. B 12, 5349 (1975).
32. T. Sakurai and H. D. Hagstrum, Phys. Rev. B 14, 1593 (1976).
33. T. Sakurai and H. D. Hagstrum, Phys. Rev. B 20, 2423 (1979).
34. J. G. Bean, G. E. Becker, P. M. Petroff, and T. E. Seidel, J. Appl. Phys. 48, 907 (1977).

35. G. S. Anderson and G. K. Wehner, *Surf. Sci.* 2, 367 (1964).
36. G. Carter and J. S. Colligon, *Ion Bombardment of Solids* (American Elsevier Publishing Co., New York, 1968), Chap. 7, pp. 310-353.
37. G. W. Sachse, W. E. Miller, and C. Gross, *Solid-State Electron.* 18, 431 (1975).
38. C. C. Chang, *Surf. Sci.* 23, 283 (1970).
39. R. C. Henderson, W. J. Polito, and J. Simpson, *Appl. Phys. Lett.* 16, 15 (1970).
40. R. C. Henderson, R. B. Marcus, and W. J. Polito, *J. Appl. Phys.* 42, 1208 (1971).
41. H. J. Mathieu and D. Landolt, *J. Microsc. Spectrosc. Electron.* 3, 113 (1978).
42. E. Kny, *J. Vac. Sci. Technol.* 17, 658 (1980).
43. S. Dushman, *Scientific Foundations of Vacuum Technique*, second edition (John Wiley & Sons, New York, 1962), Chap. 9, pp. 622-690.
44. P. L. Hemment, *Vacuum* 29, 439 (1979).

## CHAPTER V

## RESULTS

## V.A. Auger Spectrum of Clean Si

A high-resolution spectrum from a clean Si(100)-(2 × 1) surface is shown in Fig. 5.1. The peak shapes and energies are in good agreement with published results.<sup>1,2</sup>

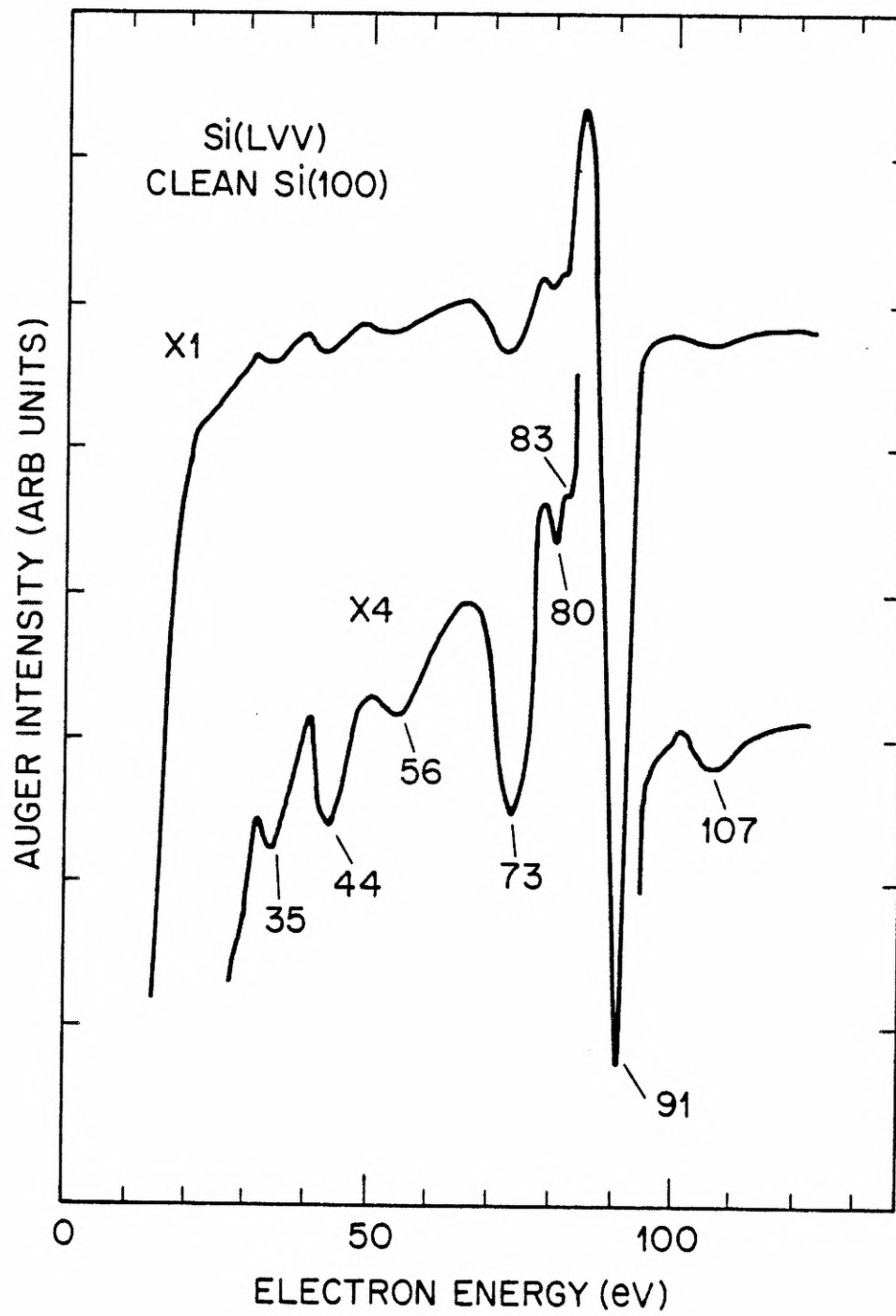
In order to obtain spectra truly representative of clean surfaces, the Auger electron gun and spectrometer must be thoroughly outgassed; at base pressures, the electron gun is the primary source of carbon and oxygen contamination. Although the requisite period of outgassing obviously depends on the initial cleanliness of the Auger unit, most workers<sup>3,4</sup> consider several days to be sufficient. For minimal carbon and oxygen contamination, we have found, however, that a new unit, carefully cleaned before installation, requires several months of outgassing. During outgassing, all normal operating potentials should be applied since contaminants on the electrodes and grids are desorbed by electron impact. In our system, at a base pressure of  $\sim 1 \times 10^{-10}$  Torr, a clean silicon surface may be continuously exposed to the electron beam (primary energy = 2000 eV, beam current =  $\sim 5$   $\mu$ A into a 0.1 mm diameter spot) for approximately four hours before accumulating detectable amounts of carbon and oxygen.

## V.B. Adsorption of Nitrogen at Room Temperature

Consistent with previous work, we found no adsorption of nitrogen on silicon at room temperature. With only the ion gauge on, the sample was exposed up to  $5 \times 10^{-5}$  Torr N<sub>2</sub> for 15 min; in our experiments, reagent-grade gas (supplied by Airco or Linde), further purified with nickel getters,<sup>5</sup>



Figure 5.1. High-resolution Si(LVV) Auger scan from a clean (100)-(2 × 1) surface produced by neon bombardment and annealing. Primary energy = 2000 eV. Modulation = 0.5 V<sub>p-p</sub>, 23.5 kHz. At higher modulation (4 V<sub>p-p</sub>), a small peak at 138 eV is also detected.



was used. After the chamber had been pumped out to  $< 3 \times 10^{-10}$  Torr, high-sensitivity Auger scans (primary energy = 2000 eV, beam current = 5-6  $\mu$ A into a 0.1 mm diameter spot, modulation = 4 V<sub>p-p</sub>) revealed no nitrogen or other impurities above the noise level.

Additionally, adsorption due to thermal<sup>6</sup> or electron-impact<sup>7</sup> activation of nitrogen in the gas phase was negligible. The sample again was exposed up to  $5 \times 10^{-5}$  Torr N<sub>2</sub> for 15 min. During exposure, every filament in the chamber was turned on, and the sample was continuously bombarded by electrons from the Auger gun (primary energy = 1000-2000 eV, beam current = 5-6  $\mu$ A into a 0.1 mm diameter spot). As before, no nitrogen or other impurities were detected by high-sensitivity Auger scans.

#### V.C. Adsorption of Nitrogen at Low Temperatures

In the next series of runs, the silicon wafer was chilled to determine the conditions under which nitrogen could be adsorbed. Before we present these results, however, we first need to clarify several key procedures.

##### V.C.1. Experimental Procedures

The first concerns the measurement of the substrate temperature. Although the sample temperature could be precisely controlled (see Sect. III.C.2.), the absolute 'surface temperature' could not be readily determined. In the following sections, temperatures ( $T_B$ ) will be stated as referenced to the thermocouple spot-welded near the bottom edge of the wafer (see Fig. 3.6). As an indication of the temperature accuracy, the temperature ( $T_T$ ) near the top edge of the wafer was checked by a chromel/alumel thermocouple (after all adsorption measurements had been completed). In the primary range of interest,  $T_B = 30^\circ - 40^\circ$  K,  $T_T$  was typically  $15^\circ$  higher than  $T_B$ . From the sample-holder geometry (Fig. 3.6), however, we would

expect most of the temperature drop to occur across the two silicon/molybdenum interfaces. The actual temperature gradient across the wafer would then be much smaller. In fact, as we shall show below, the temperature on the wafer was fairly uniform. The relation of  $T_B$  to the 'true surface temperature' should be viewed very cautiously, however, since, in our experiments, the wafer was positioned in front of a hot filament (in the Auger or LEED gun). Although the thermocouples were insensitive to thermal irradiation (they read the same whether the filament was on or off), we found that nitrogen coverages for fixed values of  $T_B$  and exposure did vary with the filament temperature. However, if the filament current and sample-to-filament geometry were kept constant, coverages were very reproducible. Unless otherwise stated, all measurements were taken with a current of 2.85 A through the filament of the Auger gun.

For reproducible gas dosing, the closed feedback loop between the ion gauge and servo valve (see Fig. 3.5) was used since the ion gauge was shown to have no effect on the adsorption process. However, if the servo valve was initially tightly closed and the controller was set for high stability ( $\sim 2\%$ ), an excessively long time (several minutes) was needed for the controller to reach the set point; the long rise time would then constitute an appreciable error to the exposure times (also several minutes). This error was eliminated by using the manual toggle switch on the controller to rapidly open the valve with a negligible rise time ( $\sim 10$  s). As the set point was approached, the controller could be switched over into automatic without any pressure overshoot. Similarly, the valve was manually closed at the end of the exposure. Thus, with a suitable combination of manual and automatic control, fast response and high stability could both be achieved.

The last procedural matter concerns gas condensation. When the sample was cooled and exposed to nitrogen, a considerable amount of gas condensed out on the transfer lines and chill block (see Fig. 3.10); at high enough exposures ( $\sim 1 \times 10^{-5}$  Torr  $N_2$  for several minutes), a visibly thick, opalescent film would form. If the sample-holder assembly was subsequently warmed up, the evaporating nitrogen would create a large pressure burst. In order to avoid contaminating the sample with CO (presumably knocked off the chamber walls and trap), all filaments had to be shut off before the sample was warmed.<sup>6</sup> In addition, the butterfly valve (see Fig. 3.2) was kept closed to avoid flooding the pump. The valve was fully opened and the filaments were turned on only after the chamber pressure had dropped to less than  $1 \times 10^{-9}$  Torr; the time necessary for pump-down was estimated from previous runs with the gauge turned on at various intervals. In the results below, unless otherwise stated, the data is representative of samples free from CO contamination.

#### V.C.2. Uniformity and Stability of Molecular Nitrogen Layers

Now that we have dispensed with the preliminaries, we can turn to a discussion of low-temperature adsorption. In a series of runs, the wafer, positioned in front of the CMA, was chilled to various temperatures  $T_B < 90^\circ \text{ K}$  and exposed to  $1 \times 10^{-5}$  Torr  $N_2$  for 5 min. During exposure, the ion gauge and Auger gun filaments were on, but the wafer was not electron bombarded. After the chamber had been pumped out to  $< 3 \times 10^{-10}$  Torr, an Auger scan was taken to detect the presence of nitrogen (the main nitrogen Auger peak occurs at 380 eV). No nitrogen was detected until the sample was chilled to

$T_B \sim 40^\circ \text{ K}$ . At this temperature, however, the adsorbed layer was not stable. After the first Auger measurement, the sample was translated slightly (the reason for this step will be explained shortly); a second Auger scan then indicated a decreased coverage. At  $T_B = 32^\circ \text{ K}$ , the adsorbed layer was sufficiently stable for reproducible results, and a more careful characterization was performed. First, the spatial uniformity of coverage was checked by translating the wafer across the CMA. The nitrogen Auger peak-to-peak height was constant (variation less than 1%) over at least the central  $5 \times 5 \text{ mm}$  region of the wafer. Next, the long-term stability was monitored. As we shall show later, the electron bombardment during an Auger measurement is sufficient to greatly change the binding state of the adsorbed nitrogen. Therefore, in order to check the stability of the initial molecular layer, an Auger scan was first taken at a time  $t_1$ ; then, at time  $t_2$ , the wafer was moved to a spot which had not been previously bombarded, and a second Auger scan was taken. Similar measurements were recorded at times  $t_3, t_4, \dots$ ; and the molecular film, at  $T_B = 32^\circ \text{ K}$ , was found to be stable (variation of nitrogen Auger peak-to-peak heights less than 1%) for up to 3 h.

#### V.D. Electron-Beam Induced Nitridation

After the samples described above had been warmed up to room temperature, adsorbed-current images revealed the presence of localized deposits ('spots') where the sample had been electron bombarded. Auger scans of the spots indicated the presence of nitrogen; no nitrogen was detected on portions of the wafer outside of the spots. Additionally, the Si(LVV) spectrum in the spots differed considerably from that of clean Si. The 91-eV clean Si peak



diminished; and a strong peak at 83 eV, characteristic of silicon nitride, was present. We concluded that electron bombardment had caused dissociation of nitrogen molecules and the growth of a partial silicon nitride layer, which was stable at room temperature.

In the next series of experiments, the Auger spectrum was carefully measured as a function of increasing nitridation. The sample was once again positioned in front of the CMA and chilled to  $T_B = 32^\circ \text{ K}$ . During exposure to nitrogen at a fixed pressure, the wafer was continuously bombarded with electrons (primary energy = 2000 eV, beam current = 5-6  $\mu\text{A}$  into a 0.2 mm diameter spot); note that the spot size was deliberately made larger than the beam diameter used for Auger measurements (0.1 mm) in order to ensure a uniform region for analysis. At five minute intervals, the exposure and electron bombardment were stopped. After the pressure had dropped to  $< 3 \times 10^{-10}$  Torr, an Auger scan was taken; the substrate was maintained at  $T_B = 32^\circ \text{ K}$  throughout the run. In Table 1, we have listed the operating parameters used in the Auger measurements. The lock-in time constant ( $\tau$ ) and preamplifier full-scale sensitivity (FS) will be listed with the individual spectra.

Three separate runs were made. In Run 1 (Figs. 5.2 and 5.3) and Run 2 (Figs. 5.4 and 5.5), the sample was dosed at  $1 \times 10^{-7}$  and  $1 \times 10^{-6}$  Torr  $\text{N}_2$ , respectively, for 0-30 min. In Run 3 (Figs. 5.6-5.8), the sample was first dosed at  $1 \times 10^{-5}$  Torr  $\text{N}_2$  for 0-30 min and then at  $1 \times 10^{-4}$  Torr  $\text{N}_2$  for 0-15 min. At the end of each run, the sample was translated to a region which had not been electron bombarded during exposure. After a preliminary electron bombardment of several minutes to stabilize surface conditions (see below), an Auger scan was taken of this region. Comparisons of the scans in the regions (a) not bombarded and (b) continuously bombarded during exposure are shown in Figs. 5.9-5.11.

Table 1.

## Operating Parameters for Auger Measurements

## A. Primary Beam

Energy = 2000 eV

Beam Current = 5-6  $\mu\text{A}$  into a 0.1 mm spot (For a given run,  
the current was stable to  $\pm 0.1 \mu\text{A}$ .)

## B. Modulation Voltage

Frequency = 23.5 kHz

Amplitude = 0.5 V<sub>p-p</sub> for Si(LVV), 4 V<sub>p-p</sub> for N(KLL)

## C. Multiplier Bias Voltage = 2100 V

## D. Lock-in

Time Constant ( $\tau$ ): varies with scan

Preamplifier Full-Scale Sensitivity (FS): varies with scan

Band-Pass Filter: Q = 20

Final Low-Pass Filter: roll-off = 12 dB/octave

E. CMA Pass Voltage: ramp rate =  $1\text{V}/(6\tau)$



Figure 5.2. Auger scans. Adsorption of nitrogen on a Si(100)-(2 × 1) surface at  $T_B = 32^\circ$  K continuously bombarded by 2000-eV electrons. Exposure times at  $1 \times 10^{-7}$  Torr  $N_2$ : (a) 5 min, (b) 10 min, (c) 15 min. Lock-in settings: (X1)  $\tau = 300$  ms, FS = 500  $\mu$ V; (X2.5)  $\tau = 300$  ms, FS = 200  $\mu$ V; (X25)  $\tau = 1$  s, FS = 20  $\mu$ V.

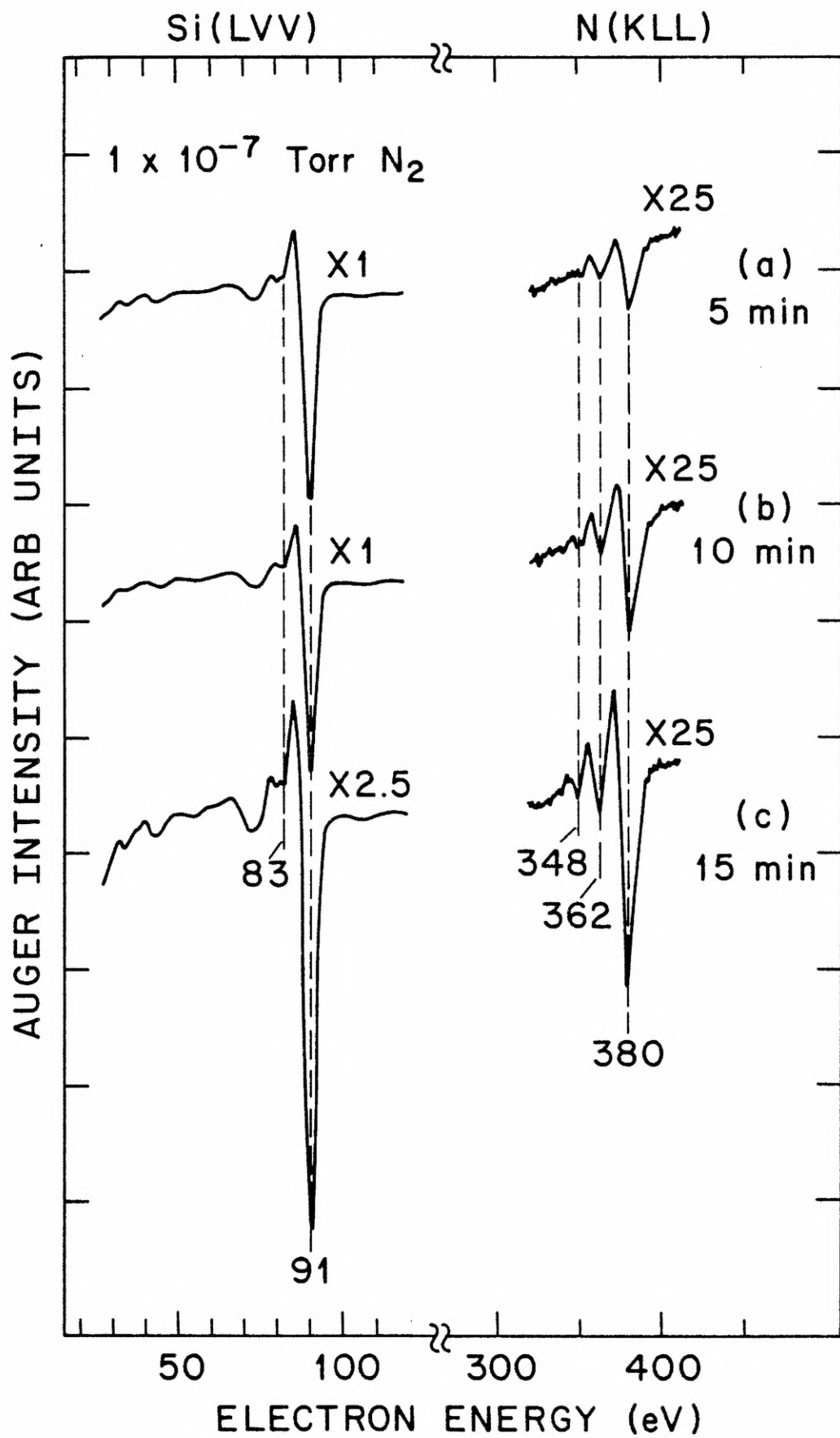


Figure 5.3. Auger scans. Adsorption of nitrogen on a Si(100)-(2 × 1) surface at  $T_B = 32^\circ$  K continuously bombarded by 2000-eV electrons. Exposure times at  $1 \times 10^{-7}$  Torr  $N_2$ : (d) 20 min, (e) 25 min, (f) 30 min. Lock-in settings: (X2.5)  $\tau = 300$  ms, FS = 200  $\mu$ V; (X10)  $\tau = 1$  s, FS = 50  $\mu$ V; (X25)  $\tau = 1$  s; FS = 20  $\mu$ V.

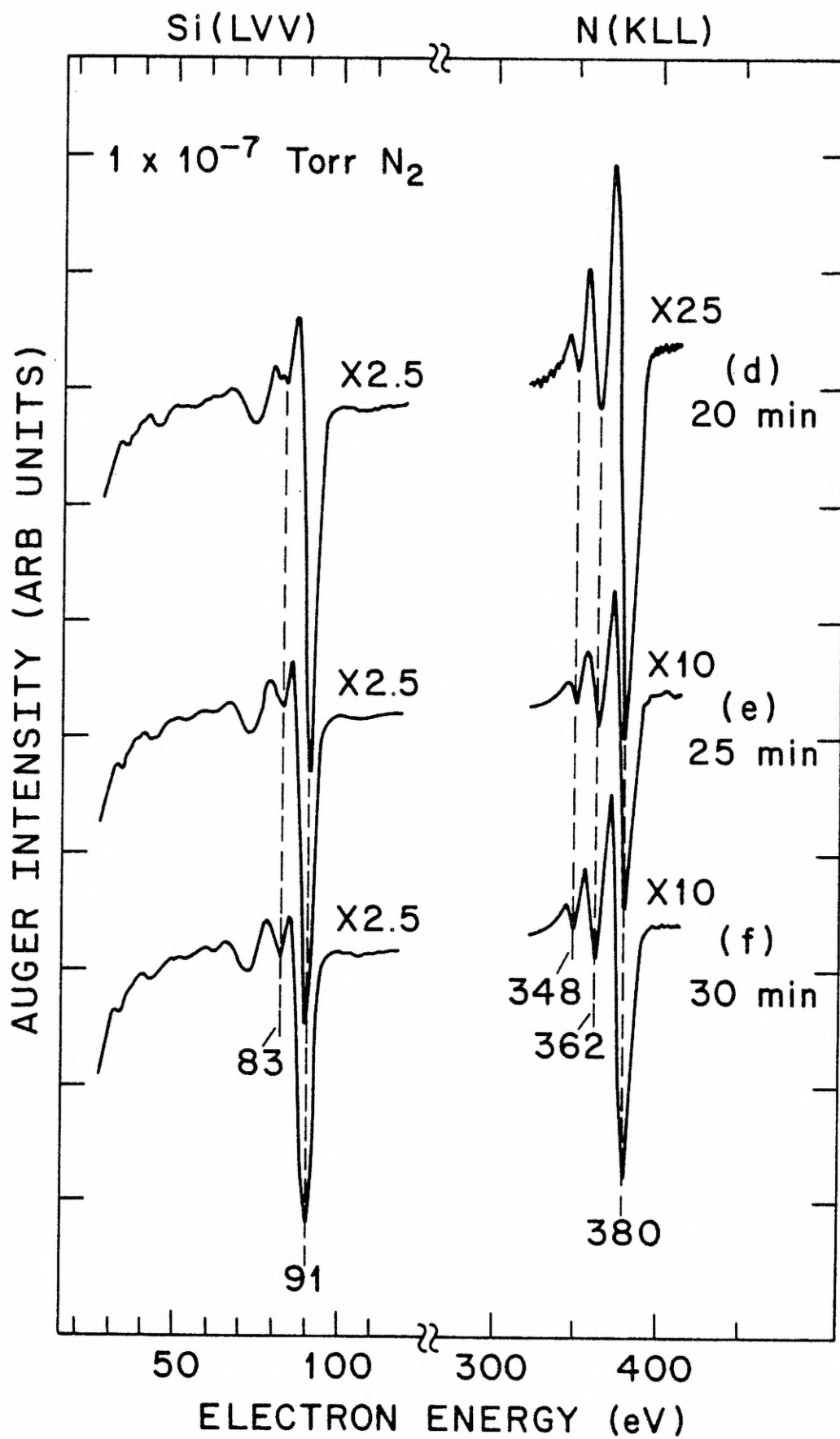


Figure 5.4. Auger scans. Adsorption of nitrogen on a Si(100)-(2 × 1) surface at  $T_B = 32^\circ \text{ K}$  continuously bombarded by 2000-eV electrons. Exposure times at  $1 \times 10^{-6} \text{ Torr N}_2$ : (a) 5 min, (b) 10 min, (c) 15 min. Lock-in settings: (X1)  $\tau = 300 \text{ ms}$ , FS = 200  $\mu\text{V}$ ; (X2)  $\tau = 300 \text{ ms}$ , FS = 100  $\mu\text{V}$ ; (X4)  $\tau = 1 \text{ s}$ , FS = 50  $\mu\text{V}$ ; (X10)  $\tau = 1 \text{ s}$ , FS = 20  $\mu\text{V}$ .

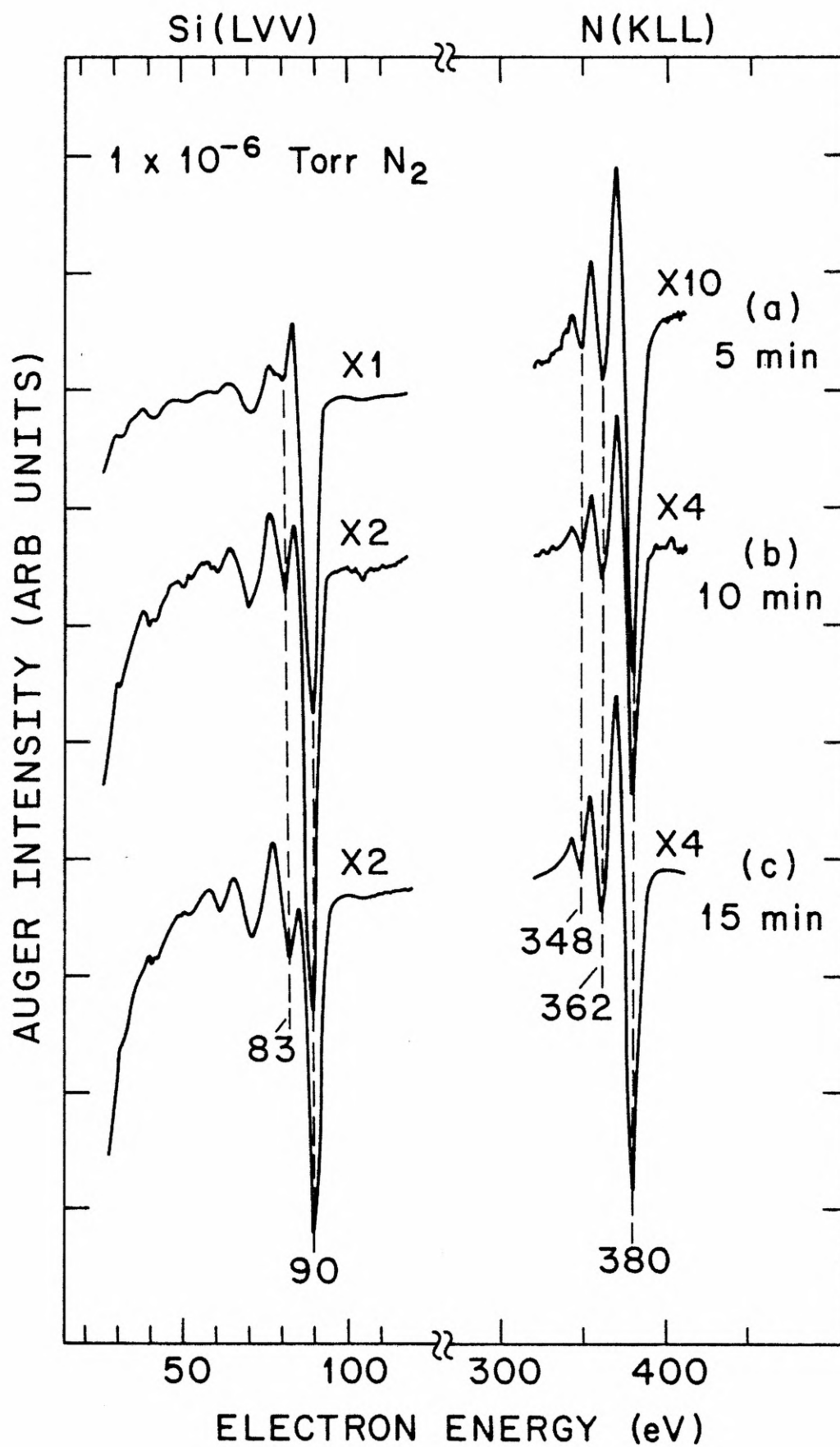


Figure 5.5. Auger scans. Adsorption of nitrogen on a Si(100)-(2 × 1) surface at  $T_B = 32^\circ$  K continuously bombarded by 2000-eV electrons. Exposure times at  $1 \times 10^{-6}$  Torr  $N_2$ : (d) 20 min, (e) 25 min, (f) 30 min. Lock-in settings: (X2)  $\tau = 300$  ms, FS = 100  $\mu$ V; (X4)  $\tau = 1$  s, FS = 50  $\mu$ V.

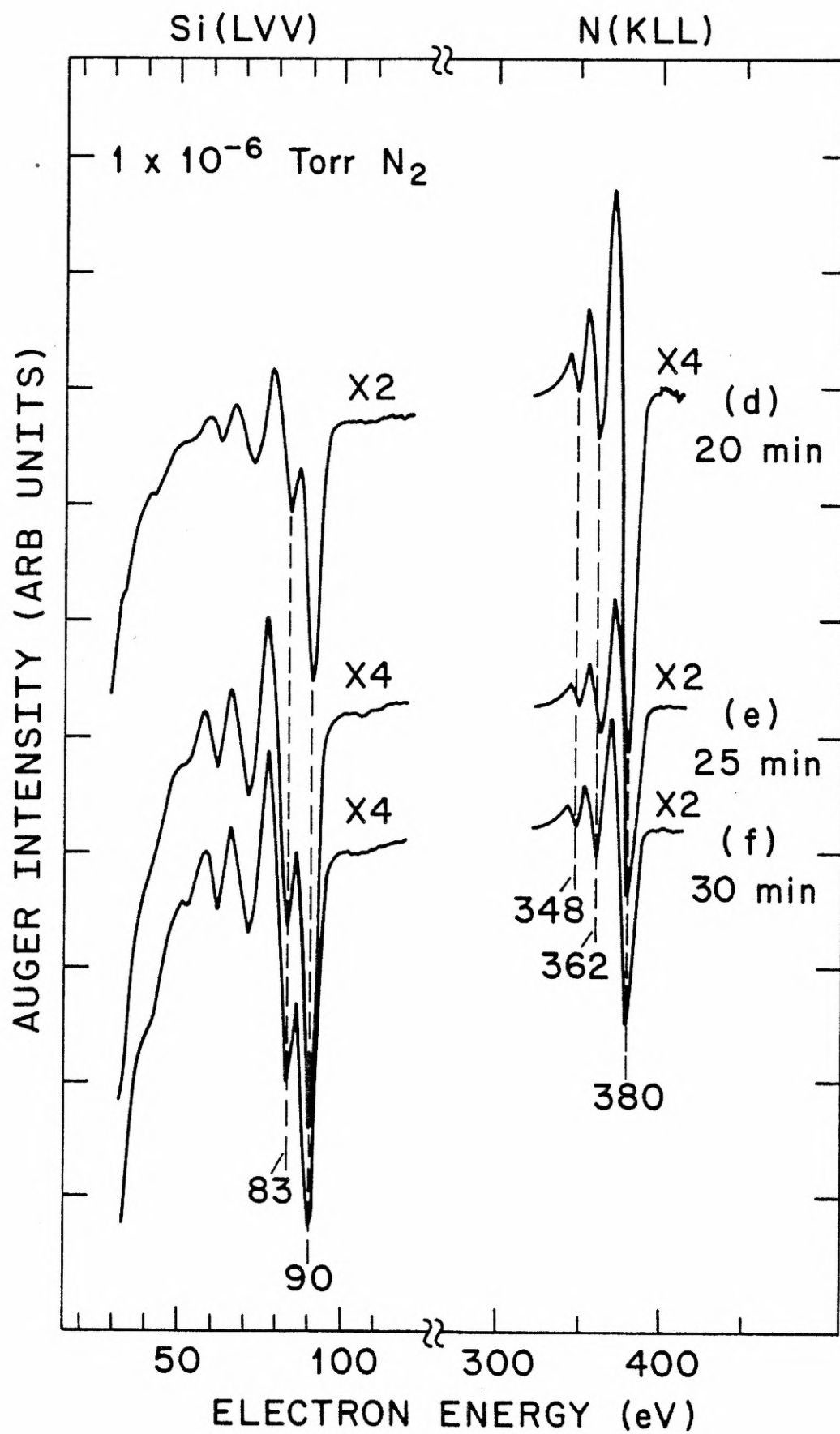




Figure 5.6. Auger scans. Adsorption of nitrogen on a Si(100)-(2 × 1) surface at  $T_B = 32^\circ \text{ K}$  continuously bombarded by 200-eV electrons. Exposure time at  $1 \times 10^{-5}$  Torr  $\text{N}_2$ : (a) 5 min, (b) 10 min, (c) 15 min. Lock-in settings: (X1)  $\tau = 300 \text{ ms}$ ,  $\text{FS} = 100 \text{ } \mu\text{V}$ ; (X2)  $\tau = 1 \text{ s}$ ,  $\text{FS} = 50 \text{ } \mu\text{V}$ .

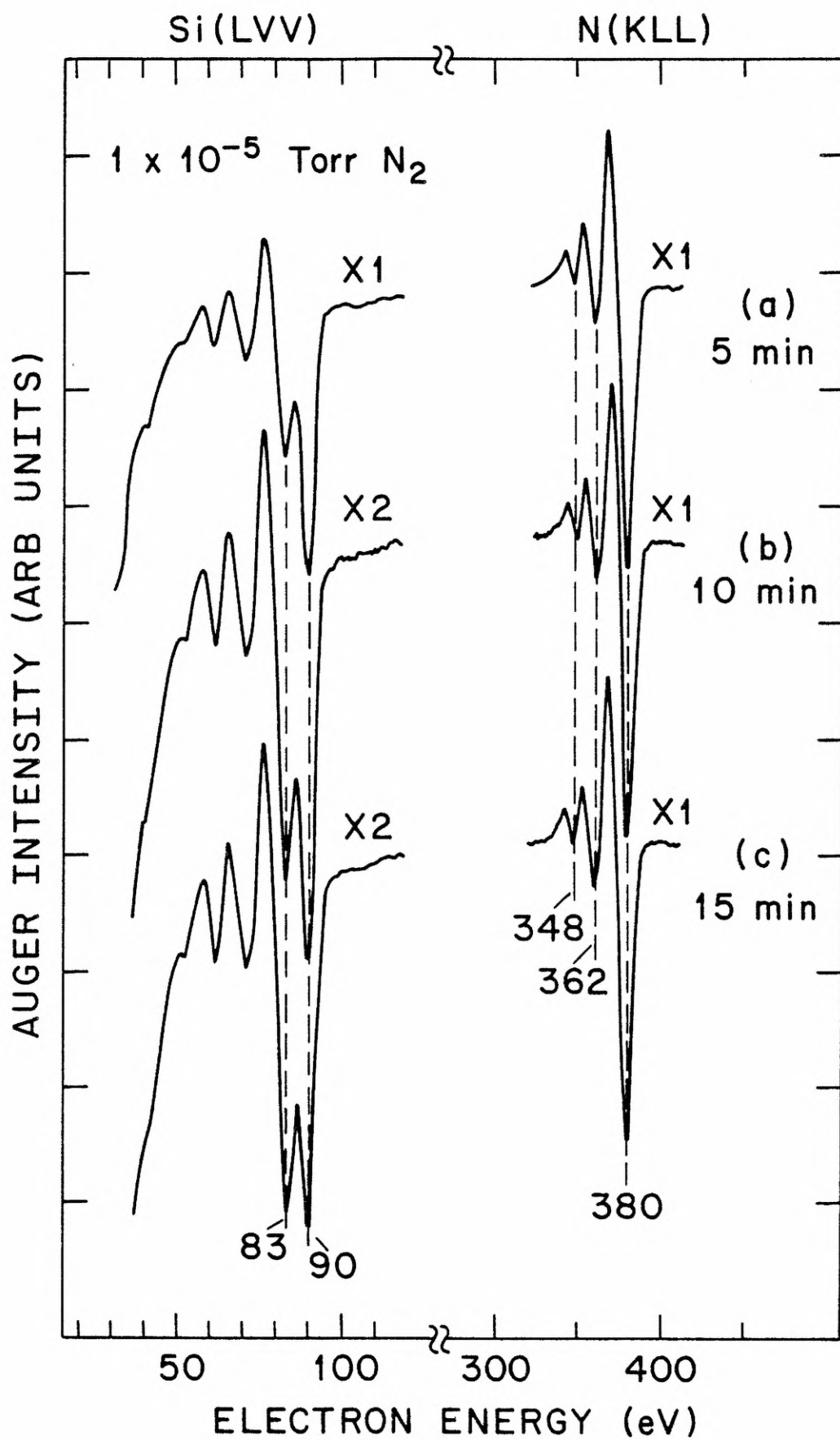


Figure 5.7. Auger scans. Adsorption of nitrogen on a Si(100)-(2 × 1) surface at  $T_B = 32^\circ$  K continuously bombarded by 2000-eV electrons. Exposure times at  $1 \times 10^{-5}$  Torr  $N_2$ : (d) 20 min, (e) 25 min, (f) 30 min. Lock-in settings: (X1)  $\tau = 300$  ms, FS = 100  $\mu$ V; (X2)  $\tau = 1$  s, FS = 50  $\mu$ V.

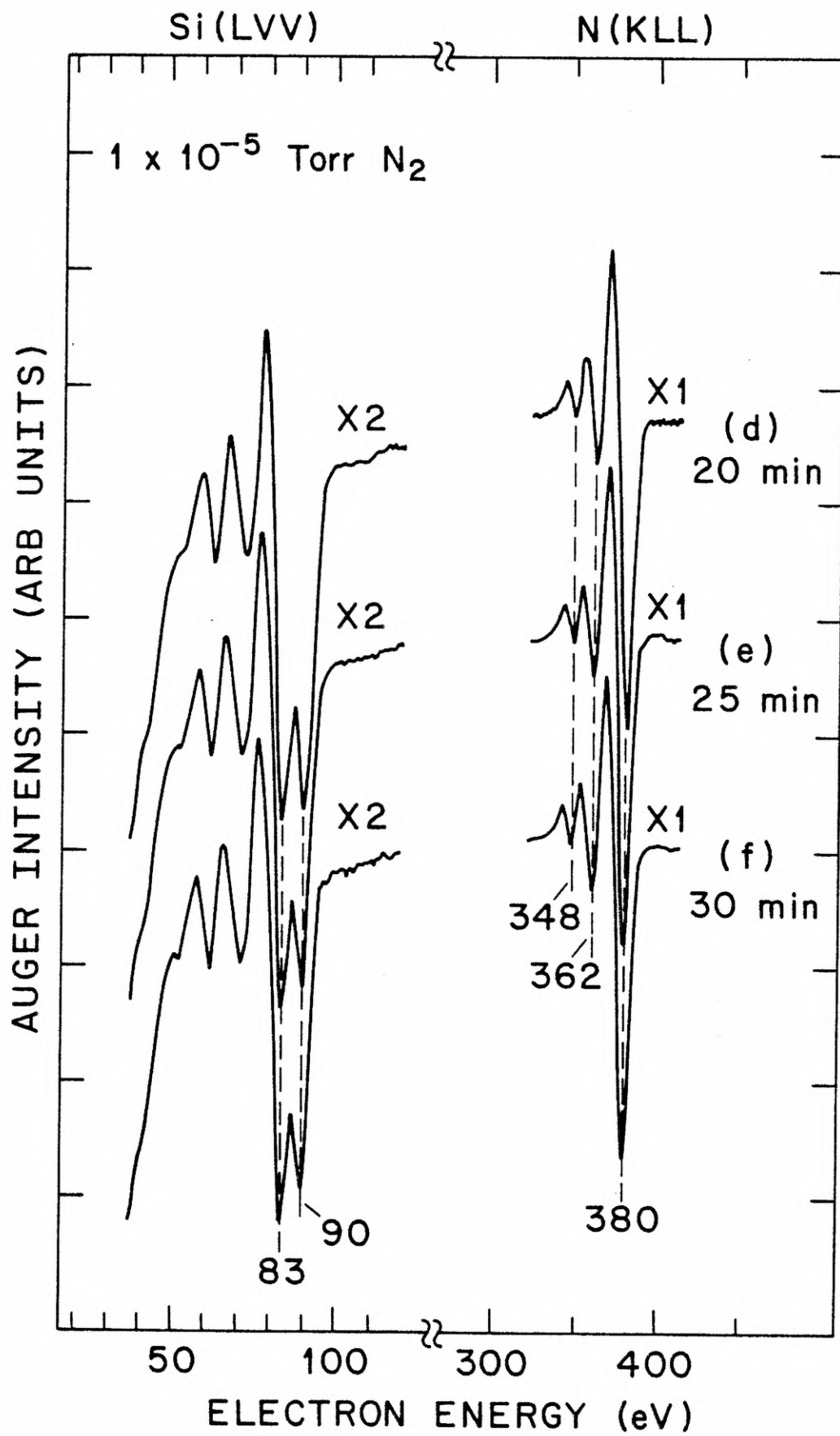


Figure 5.8. Auger scans. Adsorption of nitrogen on a Si(100)-(2 × 1) surface at  $T_B = 32^\circ$  K continuously bombarded by 2000-eV electrons. Exposure times at  $1 \times 10^{-4}$  Torr  $N_2$  after an initial exposure at  $1 \times 10^{-5}$  Torr  $N_2$  for 30 min: (g) 5 min, (h) 10 min, (i) 15 min. Lock-in settings: (X1)  $\tau = 300$  ms, FS = 100  $\mu$ V; (X2)  $\tau = 1$  s, FS = 50  $\mu$ V.

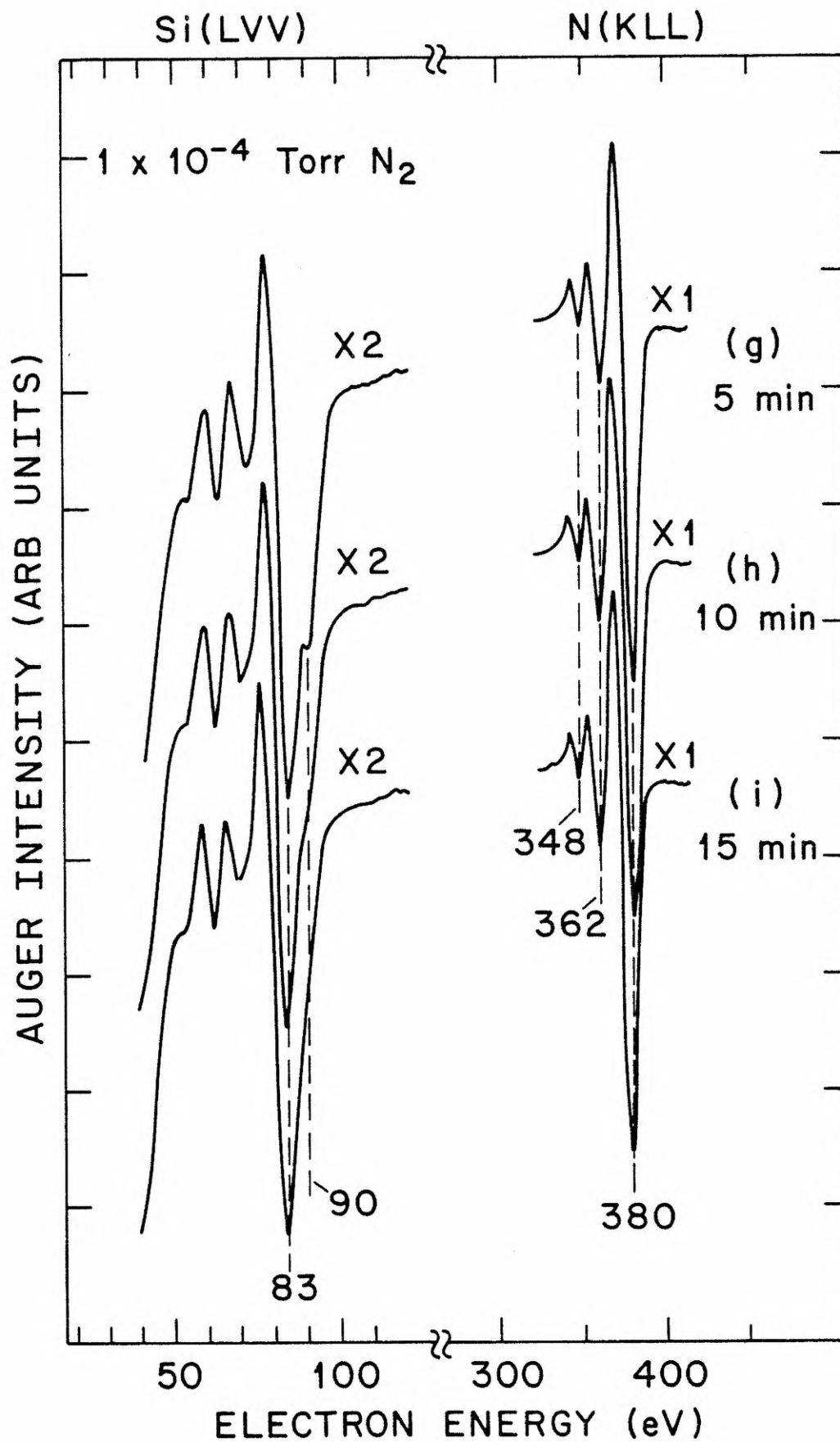


Figure 5.9. Auger scans. Si(100)-(2 × 1) surface at  $T_B = 32^\circ \text{ K}$  exposed to  $1 \times 10^{-7}$  Torr  $\text{N}_2$  for 30 min. (a) No electron bombardment during exposure. (b) Continuous electron bombardment (primary energy = 2000 eV) during exposure. Lock-in settings: (X1)  $\tau = 300 \text{ ms}$ , FS = 200  $\mu\text{V}$ ; (X4)  $\tau = 1 \text{ s}$ , FS = 50  $\mu\text{V}$ .

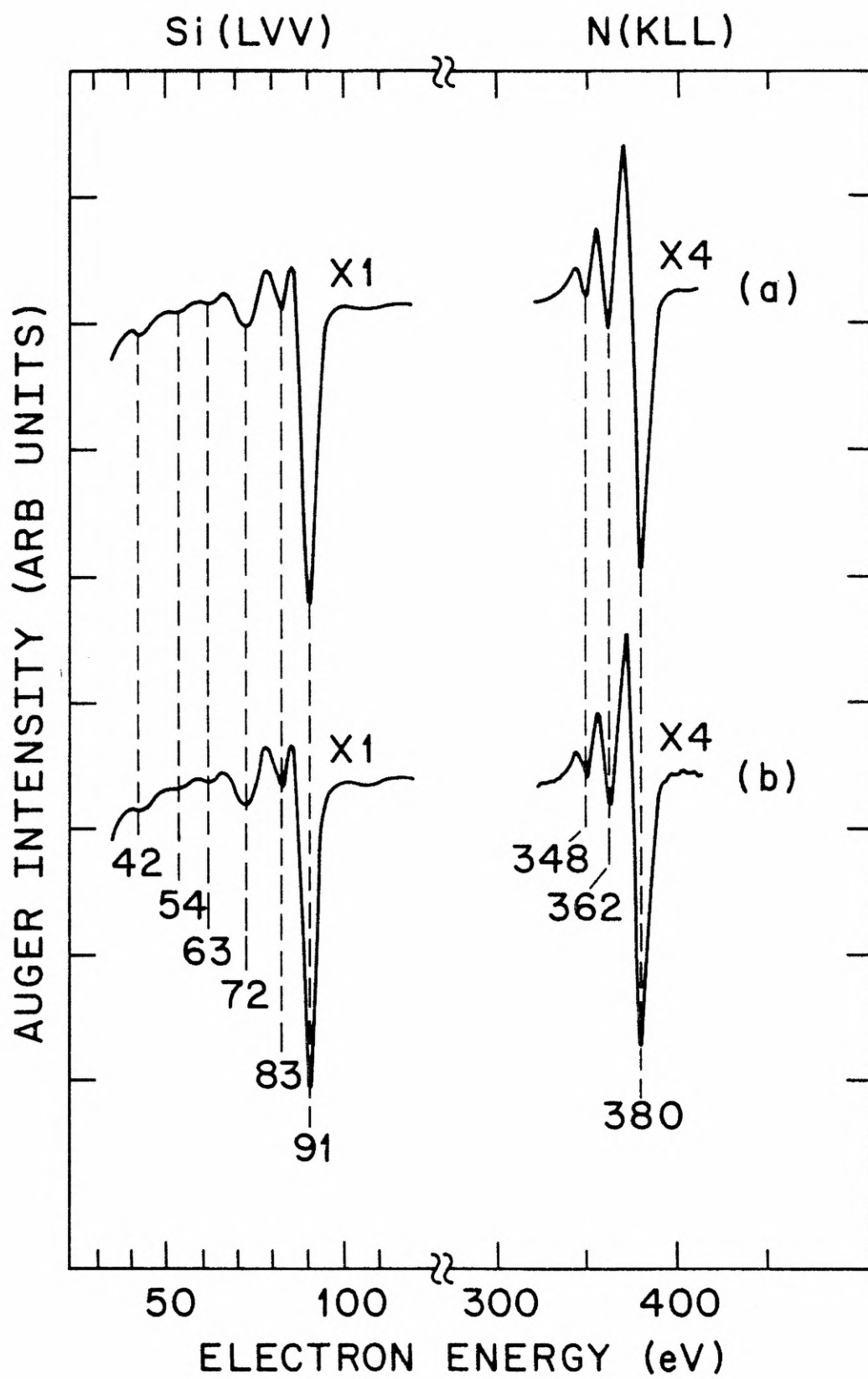




Figure 5.10. Auger scans. Si(100)-(2 × 1) surface at  $T_B = 32^\circ \text{ K}$  exposed to  $1 \times 10^{-6}$  Torr  $\text{N}_2$  for 30 min. (a) No electron bombardment during exposure. (b) Continuous electron bombardment (primary energy = 2000 eV) during exposure. Lock-in settings: (X1)  $\tau = 300 \text{ ms}$ ,  $\text{FS} = 100 \text{ } \mu\text{V}$ ; (X2)  $\tau = 1 \text{ s}$ ,  $\text{FS} = 50 \text{ } \mu\text{V}$ .

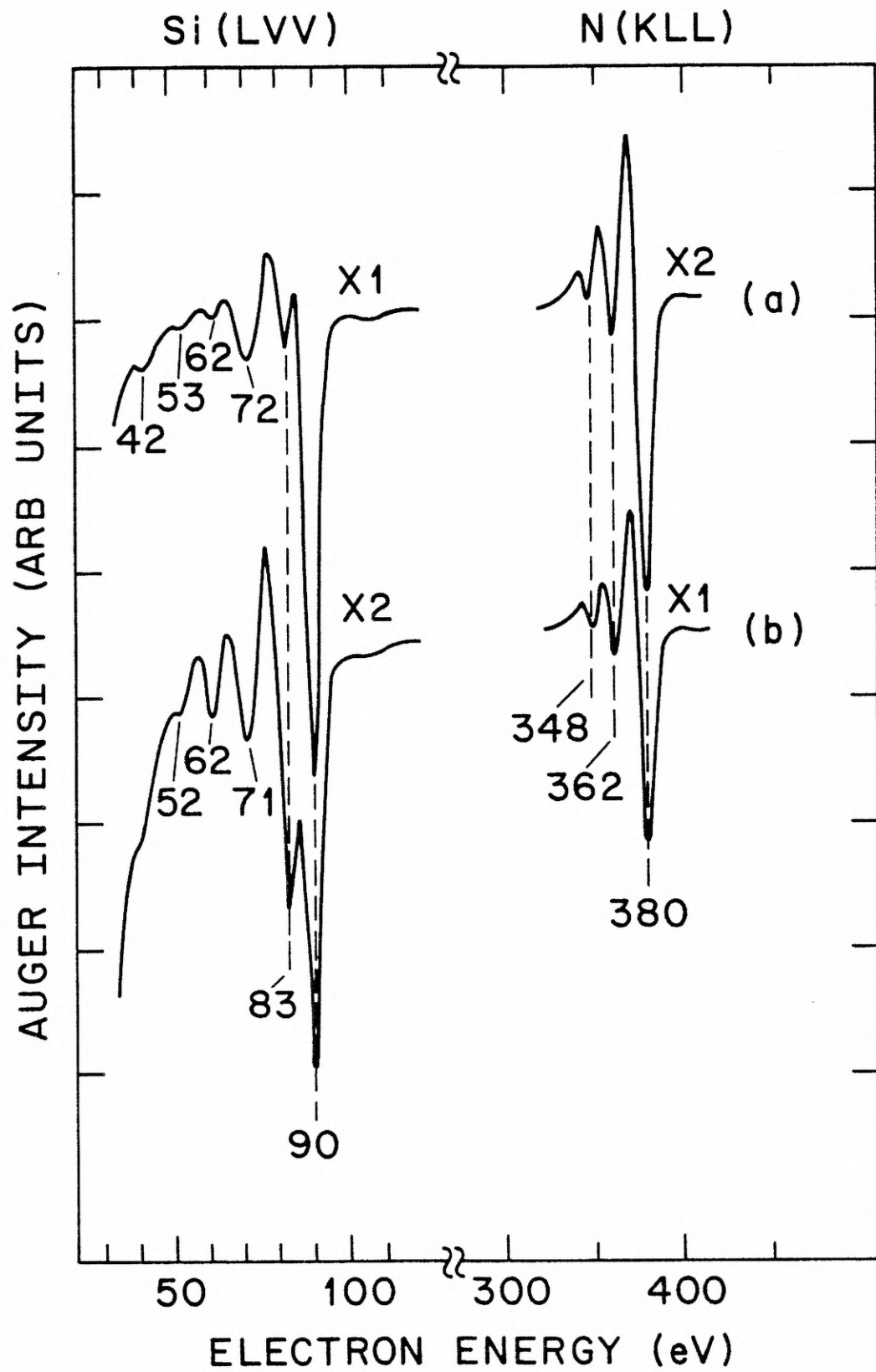
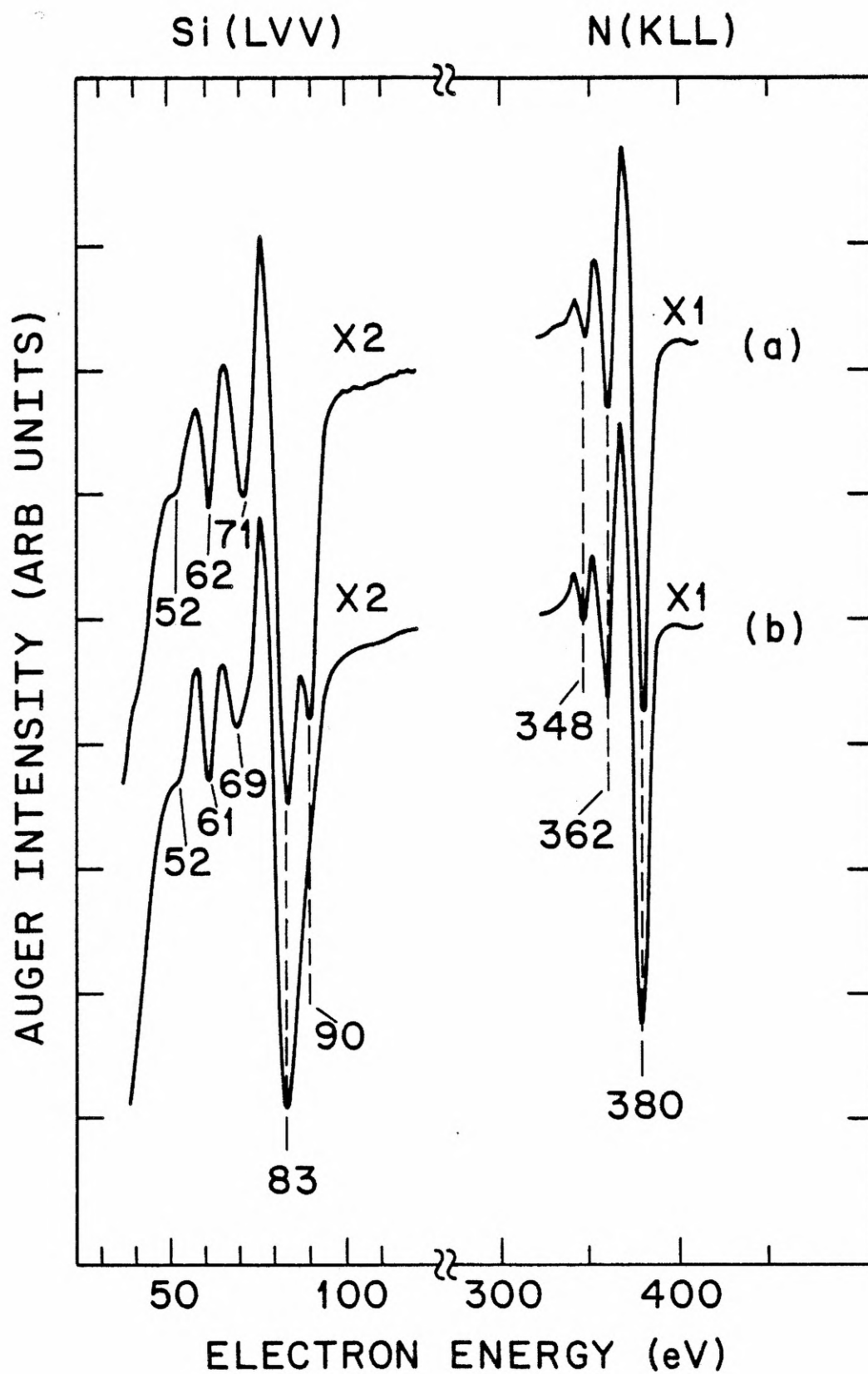


Figure 5.11. Auger scans. Si(100)-(2 × 1) surface at  $T_B = 32^\circ \text{ K}$  exposed to  $1 \times 10^{-5}$  Torr  $\text{N}_2$  for 30 min plus  $1 \times 10^{-4}$  Torr  $\text{N}_2$  for 15 min. (a) No electron bombardment during exposure. (b) Continuous electron bombardment (primary energy = 2000 eV) during exposure. Lock-in settings: (X1)  $\tau = 300 \text{ ms}$ , FS = 100  $\mu\text{V}$ ; (X2)  $\tau = 1 \text{ s}$ , FS = 50  $\mu\text{V}$ .



Before we discuss the details of these results, we should first clarify two general points concerning the low-temperature spectra. First of all, in several runs, we established that there were no significant differences between spectra taken with the substrate chilled and with the substrate at room temperature (this was true for surfaces at various stages of nitridation as well as for the clean surface). Secondly, since the substrate was at  $T_B = 32^\circ \text{ K}$ , the possibility exists that some undissociated molecular nitrogen was present. This possibility was eliminated as follows. The Auger measurement for the highest coverage at the end of each run was immediately repeated; no differences from the previous measurement were noted (in both region (a) and region (b)). If undissociated nitrogen had been present, the second Auger measurement should have shown an increase in the 83-eV nitride peak and a decrease in the 91-eV clean silicon peak, due to the additional dissociation caused by the electron bombardment during the first measurement. Thus, the spectra reported here are representative of nitrogen in a fully dissociated state. In a later section, we will discuss the minimum electron dose needed for dissociation.

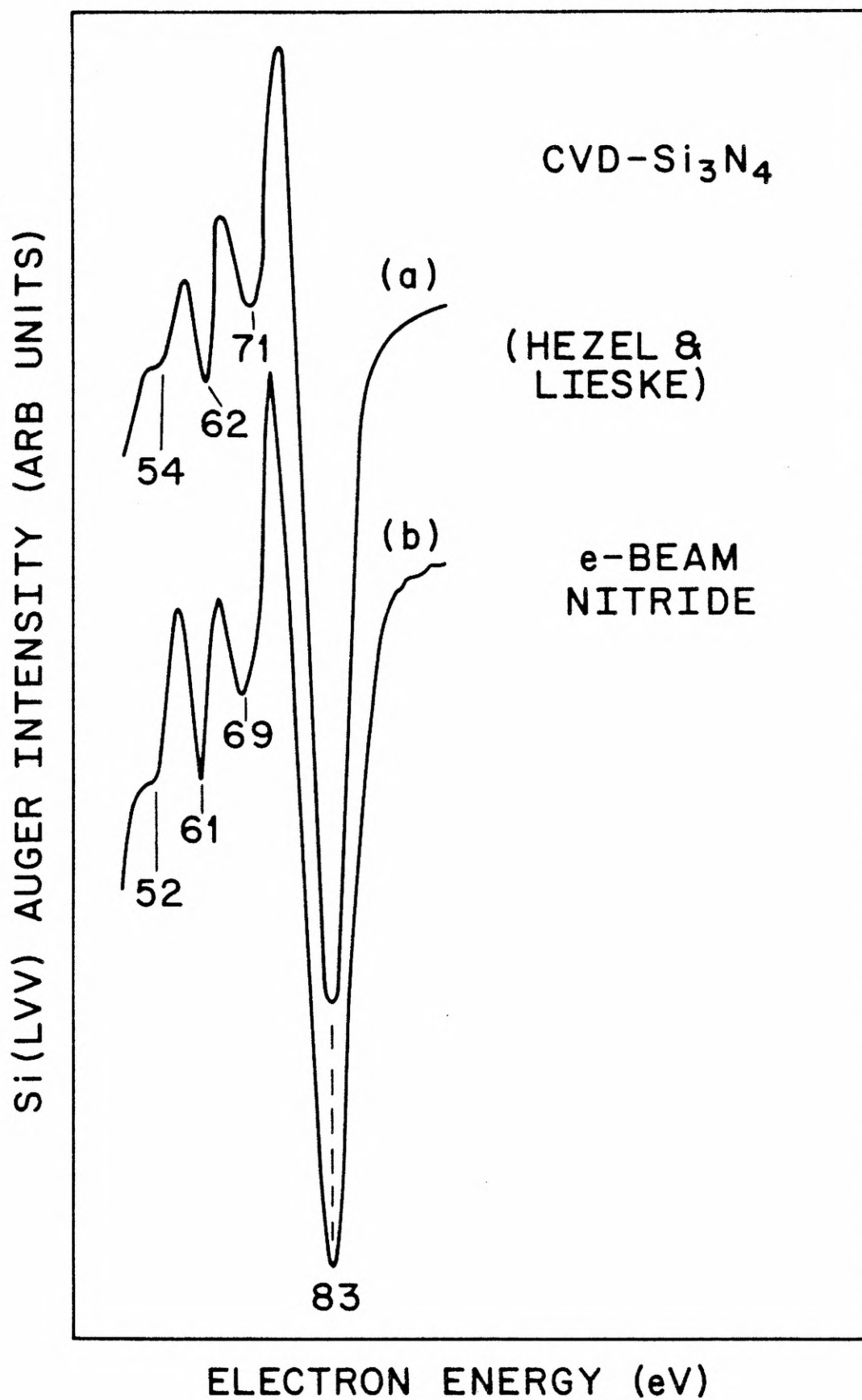
#### V.E. Key Features of the Auger Spectra

A cursory inspection of the Auger spectra reveals two general features: the N(KLL) spectra are fairly simple, whereas, the Si(LVV) spectra are very complicated. Throughout the entire range of coverages, the N(KLL) spectra consist of a well-defined triplet with constant line profiles and constant energies; the peak energies are 348, 362, and 380 eV. In accordance with standard convention,<sup>8</sup> we assign the energies of the Auger peaks to the high-energy minima in the first-derivative spectra. The accuracy with which energies can be assigned is  $\pm 0.5$  eV for sharp peaks and  $\pm 1$  eV for broad

peaks. In contrast to the N(KLL) spectra, the Si(LVV) spectra exhibit a very rich fine structure. In principle, the valence band energy levels and density of states can be extracted from this fine structure.<sup>9</sup> Indeed, much progress in developing deconvolution techniques for analyzing valence band spectra has recently been achieved<sup>10</sup>; however, these techniques are very complicated and require additional information on background corrections and energy losses.<sup>9-11</sup> Here, our goal is not an ambitious attempt to understand the detailed electronic structure but, rather, an empirical characterization of the nitridation process through quantities directly obtainable from the measured spectra.

A better appreciation of the Si(LVV) spectra may be gained by focussing our attention on the spectrum for the highest coverage (Fig. 5.8(i)), which is less cluttered than the spectra at intermediate coverages. This spectrum is shown in greater detail in Fig. 5.12, where it is also compared with Hezel and Lieske's<sup>12</sup> results for CVD-Si<sub>3</sub>N<sub>4</sub>. Considering the differences in the sample-preparation techniques and in the operating parameters used for the Auger measurements, the two spectra agree very well. On this basis, we can reasonably conclude that our final product is a stoichiometric (Si<sub>3</sub>N<sub>4</sub>) silicon nitride film on a clean silicon substrate. In the nitride spectrum, the strong 91-eV peak characteristic of clean Si has vanished and the principal peak is now at 83 eV. The more complicated spectra at intermediate coverages can be viewed principally as a convolution of a spectrum from a clean Si substrate and a spectrum from a Si<sub>3</sub>N<sub>4</sub> overlayer. The possible presence of sub-stoichiometric<sup>13,14</sup> silicon nitride, however, cannot be entirely eliminated.

Figure 5.12. Comparison of Si(LVV) Auger spectra. (a) CVD-Si<sub>3</sub>N<sub>4</sub> (from Ref. 11). (b) Final stage of electron-induced nitridation.





## V.F. Auger Intensities as a Function of Nitridation

Insight into the growth kinetics of the silicon nitride film may be gained from considering the variations of the Auger intensities as a function of nitridation. In the following discussions, we shall single out the three most representative peaks: the 91-eV silicon substrate peak, the 83-eV nitride peak, and the 380-eV nitrogen peak. Before we go on, however, we first need to clarify our procedures for determining Auger intensities.

### V.F.1. Convention for Auger Intensities

For quantitative analysis, we desire features in the Auger spectra which are directly proportional to the concentrations of elements on the surface. If  $\mathcal{N}(E)$  is the number of electrons emitted in the energy window  $E$ ,  $E + dE$ , then the area  $\int \mathcal{N}(E) dE$  under an Auger peak is the most reliable measure of surface concentration.<sup>15,16</sup> For increased sensitivity and background suppression, however, most Auger spectra are taken in the first-derivative mode,  $d\mathcal{N}(E)/dE$ .<sup>17</sup> In an early paper, Weber and Johnson<sup>18</sup> pointed out that the readily measured peak-to-peak height in the first-derivative spectrum is directly proportional to surface concentration, provided that the lineshape remains constant with concentration. Even if the lineshape does change, Auger experimentalists commonly use the peak-to-peak height anyway.<sup>19</sup> From a theoretical standpoint, this procedure, of course, cannot be rigorously defended; in practice, however, the area  $\int \mathcal{N}(E) dE$  often is no more accurate than the peak-to-peak height, for the following reasons:

(1) The area  $\int \mathcal{N}(E) dE$  is related to the surface concentration in a simple linear fashion only for sub-monolayer coverages. For multilayers, corrections for attenuation effects must be made, and these corrections are often not known to any great accuracy.<sup>15,20-22</sup> This restriction is true also for the peak-to-peak height under conditions of constant lineshape.<sup>18</sup>

(2) The use of the area  $\int \eta(E) dE$  as an accurate measure of surface concentration requires that the Auger peak in the  $\eta(E)$  spectrum be sufficiently defined for proper delimitation of the integral. In practice, errors in correcting for the background lead to uncertainties in the integration limits; overall accuracy<sup>23</sup> is reduced to only  $\sim \pm 20\%$ .

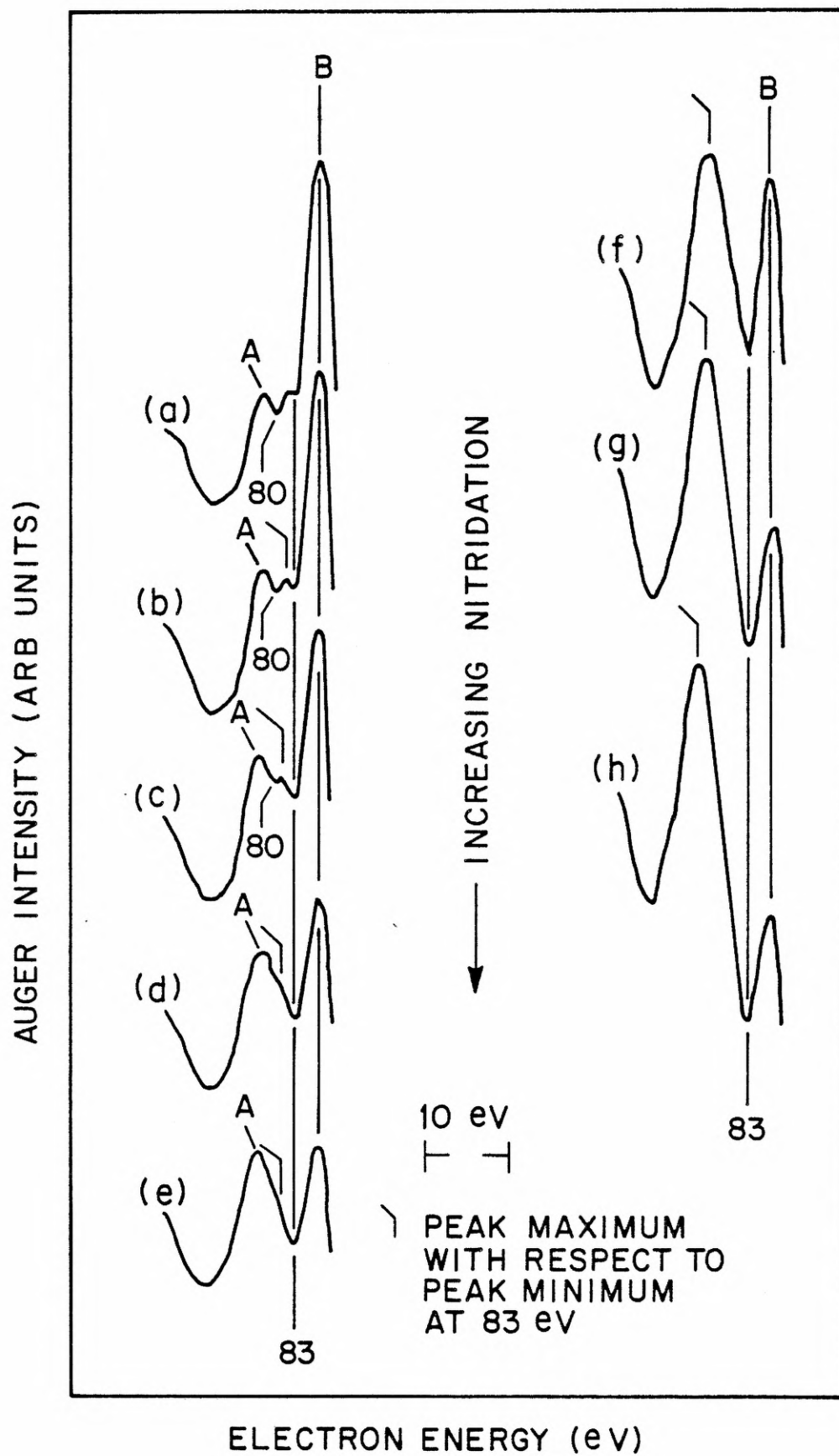
(3) One of the original motivations for using the first-derivative spectrum was the increased detectability of fine structure.<sup>17</sup> In the  $\eta(E)$  spectrum, the fine structure is washed out,<sup>24</sup> and the area under small peaks cannot be readily determined.

In summary, then, when we refer to the Auger intensity of a particular peak, we shall mean, in all instances, the peak-to-peak height in the first-derivative spectrum. With this convention, we shall be able to derive useful empirical relations involving the Auger intensities as a function of nitridation. Great caution should be exercised, however, in comparing our experimental values with accurate theoretical predictions. (At present, this is a moot point: accurate calculations do not exist.<sup>23</sup>)

#### V.F.2. Specific Features of the Auger Spectra

We are now in a position to discuss specific features of our Auger spectra. As we have already noted above, the N(KLL) peaks maintain constant energies and lineshapes as a function of coverage; hence, they require no further comment. The Si(LVV) peaks, however, need to be examined more closely. In the early stages of nitridation, the 83-eV nitride peak undergoes considerable changes in lineshape (see Fig. 5.13). The peak minimum stays constant at 83 eV, but the position of the peak maximum changes. Initially, in the clean Si spectrum (Fig. 5.13(a)), there are a small peak at 80 eV and a flat shoulder at 83 eV. At the onslaught of nitridation, the peaks at 80 eV and 83 eV are distinct (Fig. 5.13 (b),(c)). As nitridation

Figure 5.13. Evolution of the 83-eV nitride Auger peak with increasing nitridation. Point 'A' is the peak maximum with respect to the peak minimum at 80 eV. Point 'B' is the peak maximum with respect to the peak minimum at 91 eV.



progresses, the two peaks merge, but a vestigial inflection remains (Fig. 5.13 (d),(e)). At an even later stage, the inflection disappears (Fig. 5.13 (f)-(h)). Although we recognize that there is no entirely satisfactory manner of dealing with such closely convoluted peaks, much empirical information can be gleaned if we adopt a consistent convention for demarcating the peak maximum with respect to the peak minimum at 83 eV. The convention which we have adopted is shown in Fig. 5.13; the peak maximums are marked with a flag (  $\backslash$  ). In (b) and (c), there is a distinct peak maximum at the flag position, and no ambiguity arises. In (d) and (e), the flag is located at the inflection point halfway between the peak maximum at 'A' and the peak minimum at 83 eV. Deciding when the inflection disappears is, of course, problematical. A simple and reproducible, albeit arbitrary, criterion, however, can be established. When the peak maximum at 'A' is level with the peak maximum at 'B', we can consider the two peaks originally at 80 and 83 eV to have essentially melded into one. Thus, at higher stages of nitridation ((f)-(h)), the flag positions coincide with the peak maximum at 'A'; from the stage shown in (f) to the final stage of nitridation (Fig. 5.12 (b)), the peak maximum is located at 78 eV. With respect to the 91-eV Si substrate peak, there are two subtle changes to note. First of all, the position of the high-energy minimum apparently shifts from 91 eV at low coverages (Figs. 5.2 and 5.3) to 90 eV at higher coverages (Figs. 5.4-5.8); this 1 eV shift is just within our error ( $\pm 1$  eV). Additionally, the position of the low-energy peak maximum (marked 'B' in Fig. 5.13) shifts from 85 eV in clean Si to 87 eV just before the peak disappears (Fig. 5.8 (g)). These slight changes in the main Si substrate peak are probably not indicative of chemical changes but are

probably due to changes in background as the strong 83-eV nitride peak develops and to inelastic scattering of the substrate Auger electrons as they pass through the nitride overlayer.<sup>11</sup> In the following discussions, we will always refer to the main substrate peak as the clean Si 91-eV peak.

#### V.F.3. Normalization of Auger Intensities

In order to maximize the resolution of the Si(LVV) fine structure, the smallest modulation voltage ( $0.5 V_{p-p}$ ) consistent with high signal-to-noise and with reasonable scan rates was used. The weaker N(KLL) peaks, however, required a much higher modulation voltage ( $4 V_{p-p}$ ) for sufficient sensitivity. Calibration runs, with scan rates much slower than those utilized in actual experiments, verified that the N(KLL) peak-to-peak heights were accurately linear with modulation amplitude over the range  $0.5-4 V_{p-p}$ . Thus, in the following plots, the measured N(380 eV) Auger intensities have been divided by 8 to provide proper scaling with respect to the Si(91 eV) and nitride (83 eV) Auger intensities. Additionally, to compensate for variations in overall signal gain from one run to another, the intensities have been normalized as follows<sup>25,26</sup>: for each run, the measured intensities have been divided by the intensity of the 91-eV peak from the initial clean Si surface; this initial intensity has been assigned a value of 1000 arbitrary units. We have found that this normalization is good to  $\sim \pm 5\%$  if the initial surface is truly clean and if all operational parameters (such as focal position and lock-in phase) are carefully set.

#### V.F.4. Plots of Auger Intensities

To investigate the growth kinetics of the silicon nitride film, we plot the main substrate and adsorbate Auger intensities as a function of exposure time<sup>26</sup> at a fixed pressure of nitrogen (Figs. 5.14-5.17); some of the

Figure 5.14. Plot of normalized Auger peak-to-peak heights as a function of exposure time at  $1 \times 10^{-7}$  Torr  $N_2$ . Si(100)-(2  $\times$  1) surface at  $T_B = 32^\circ$  K continuously bombarded by 2000-eV electrons.

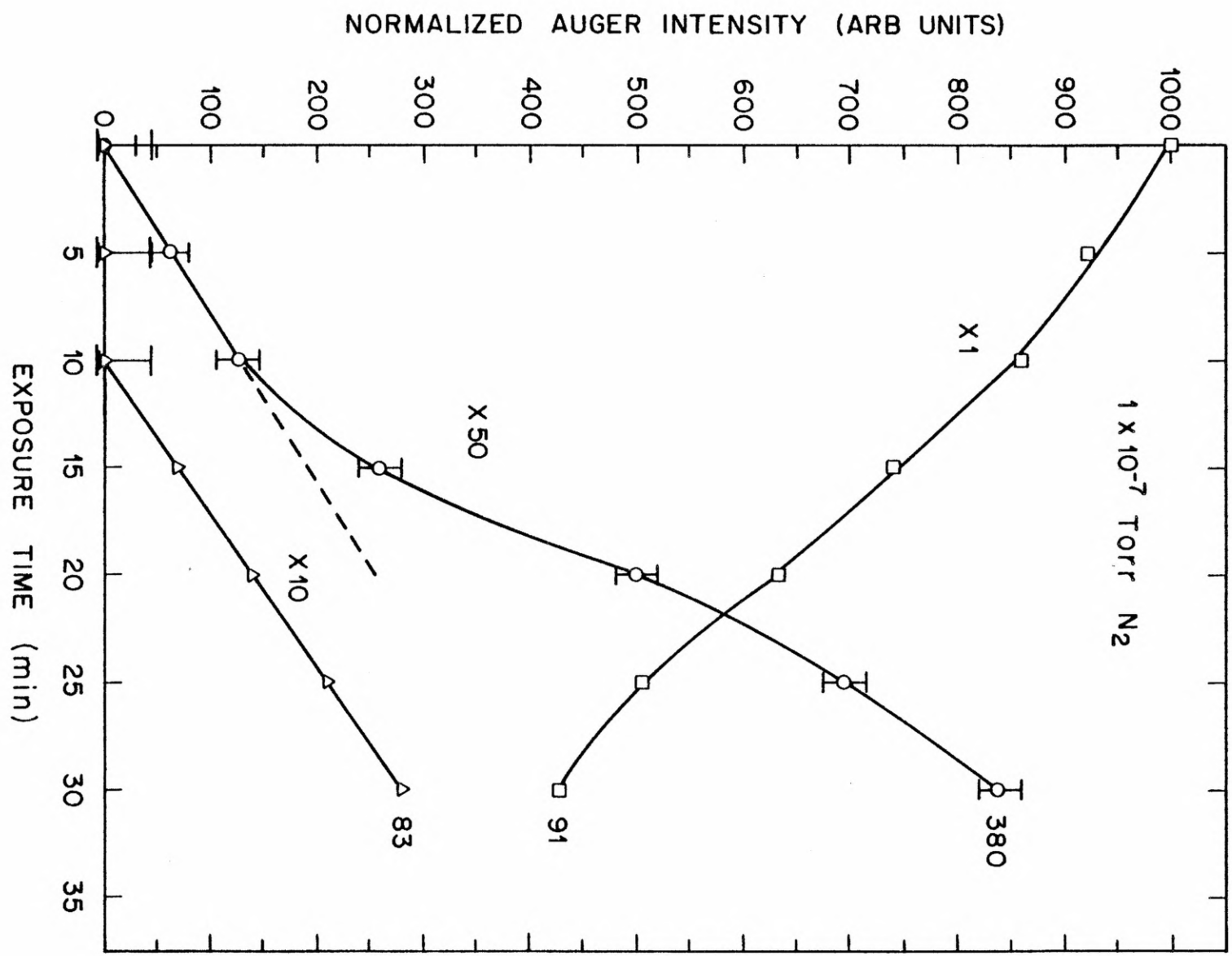




Figure 5.15. Plot of normalized Auger peak-to-peak heights as a function of exposure time at  $1 \times 10^{-6}$  Torr  $N_2$ . Si(100)-(2  $\times$  1) surface at  $T_B = 32^\circ$  K continuously bombarded by 2000-eV electrons. The initial portion of the 83-eV curve is broken because a different convention is used for measuring the Auger intensity at low coverages (see Sect. V.F.2.).

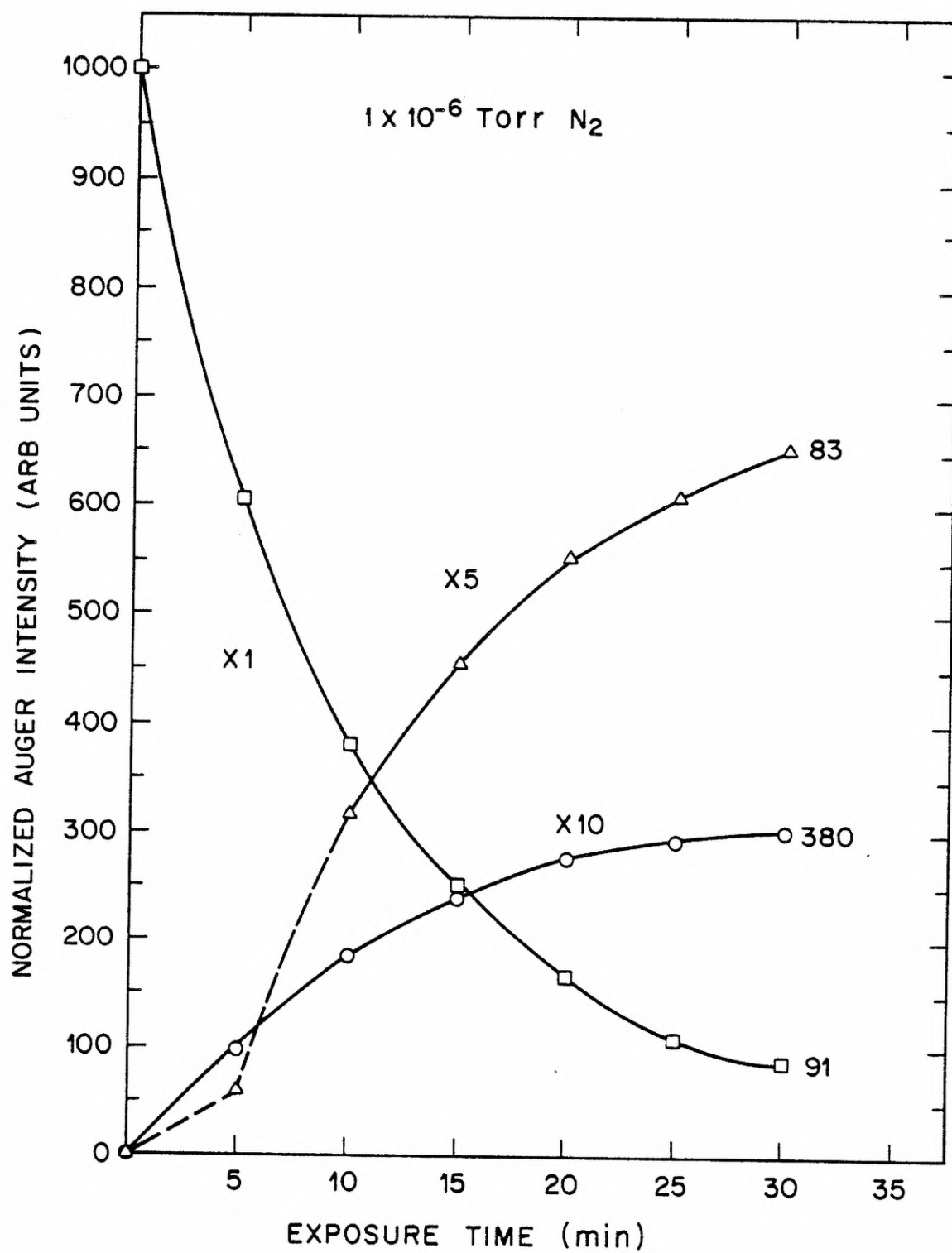


Figure 5.16. Plot of normalized Auger peak-to-peak heights as a function of exposure time at  $1 \times 10^{-5}$  Torr  $N_2$ .  
Si(100)-(2  $\times$  1) surface at  $T_B = 32^\circ$  K  
continuously bombarded by 2000-eV electrons.

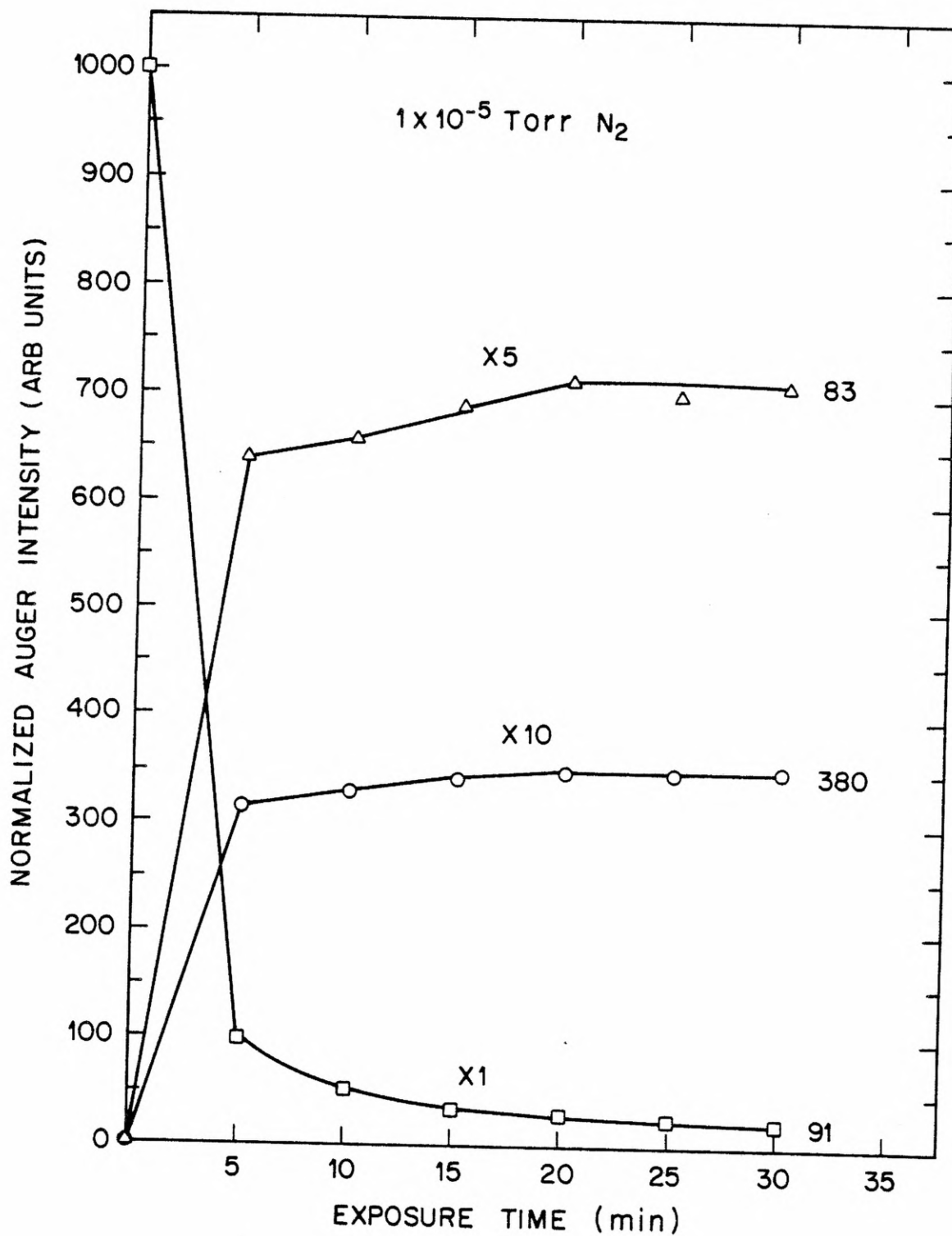
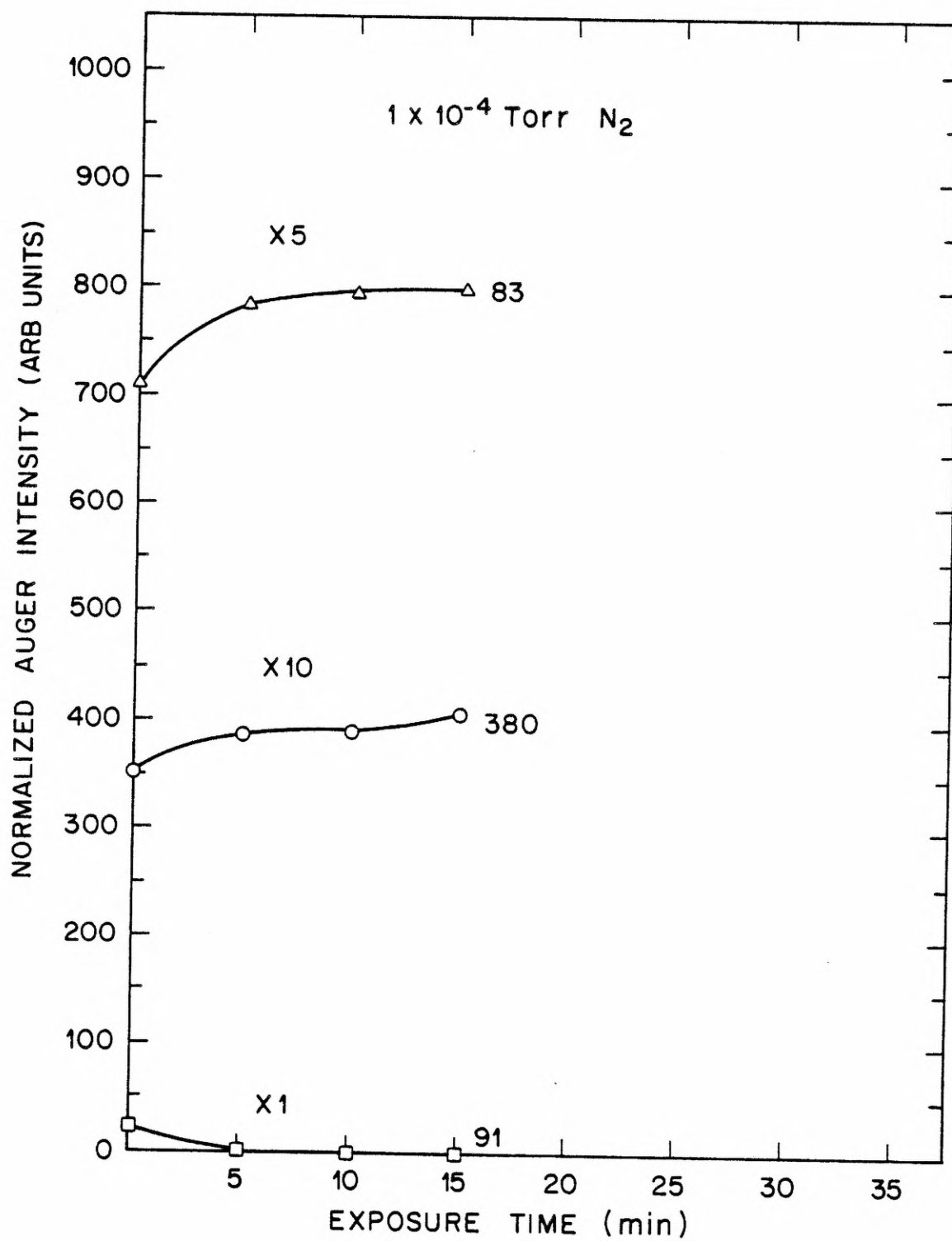


Figure 5.17. Plot of normalized Auger peak-to-peak heights as a function of exposure time at  $1 \times 10^{-4}$  Torr  $N_2$  after an initial exposure at  $1 \times 10^{-5}$  Torr  $N_2$  for 30 min. Si(100)-(2 x 1) surface at  $T_B = 32^\circ$  K continuously bombarded by 2000-eV electrons.



functional relationships are more apparent with the data in semi-logarithmic form (Figs. 5.18-5.21). Since the exposure time is linearly proportional to film thickness only for a constant growth rate, and since we cannot a priori assume a constant growth rate, we eliminate the exposure time<sup>27</sup> as a parameter by plotting the nitride(83 eV) and nitrogen(380 eV) adsorbate intensities as a function of the Si(91 eV) substrate intensity (Figs. 5.22, 5.23). From these two plots, we would surmise a simple functional relationship between the nitride(83 eV) and nitrogen(380 eV) intensities; Fig. 5.24 confirms our conjecture. The three plots of one Auger intensity vs. another are accurately piecewise linear (but note that the discontinuities in the nitride(83 eV) curves are artifacts from our procedure for measuring peak-to-peak heights). In Table 2, we have listed the best (least-mean-squares fit) linear relationships between the Auger intensities, denoted by

$I_{\text{energy of Auger peak}}$

#### V.G. Speculations on Growth Mechanisms

A perfunctory glance at electron-beam induced nitridation yields a simple picture: nitrogen molecules, adsorbed on a cold silicon surface, dissociate under electron impact and react with substrate atoms to form silicon nitride. Closer scrutiny, however, reveals a number of mechanisms for further consideration--possibilities include<sup>28,29</sup> (a) nucleation, (b) surface diffusion, (c) bulk diffusion, and (d) space-charge effects. Obviously, then, we could not expect any single analytical technique to completely characterize such a complicated system. Although the basic growth kinetics can, in principle, be extracted from the Auger data,<sup>26</sup> we must proceed with extreme caution since quantitative Auger analysis, particularly with respect to thin-film growth, is still rather rudimentary and needs considerable refinement.

Figure 5.18. Same as Fig. 5.14, except semi-logarithmic plot.



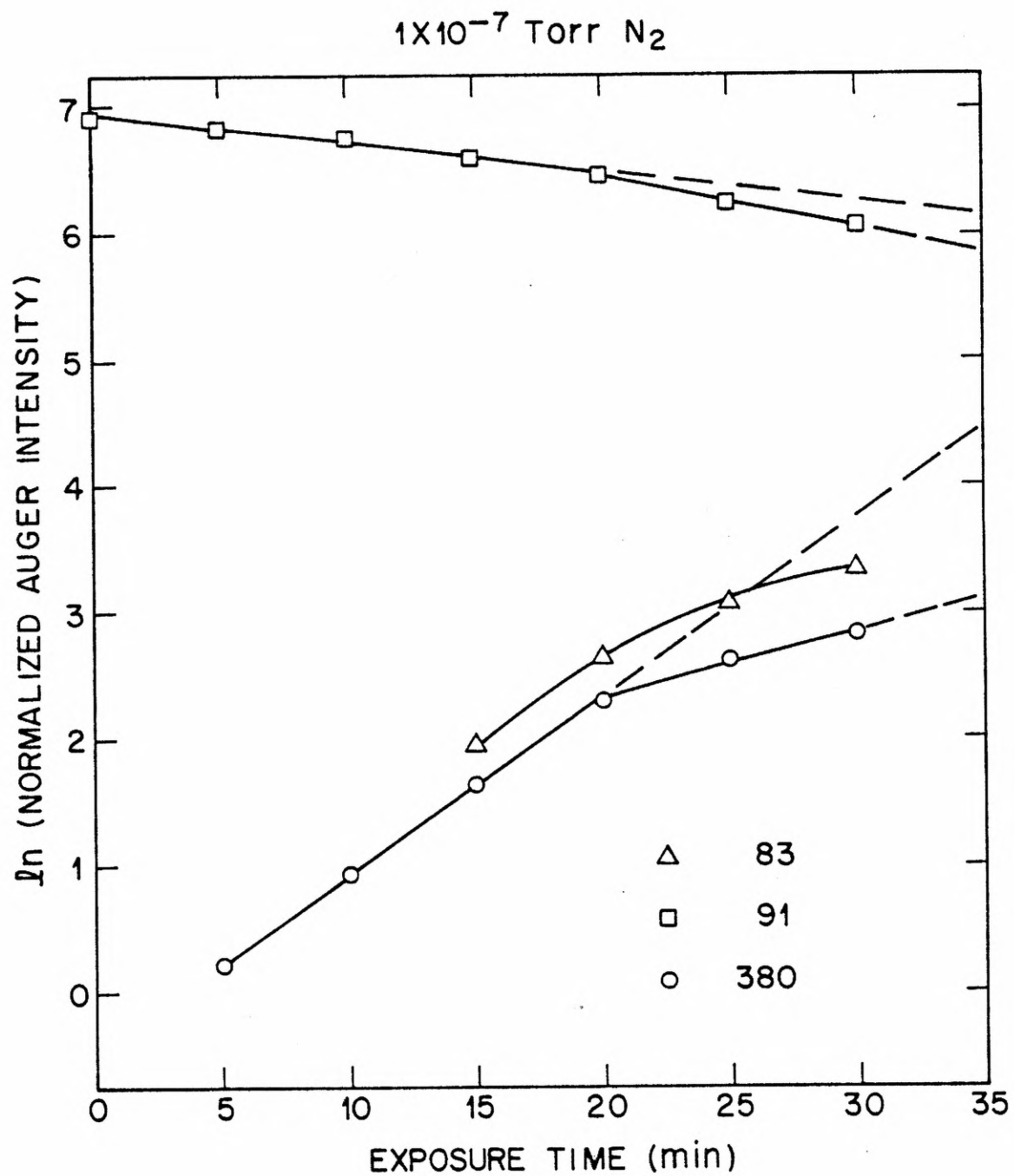


Figure 5.19. Same as Fig. 5.15, except semi-logarithmic plot.

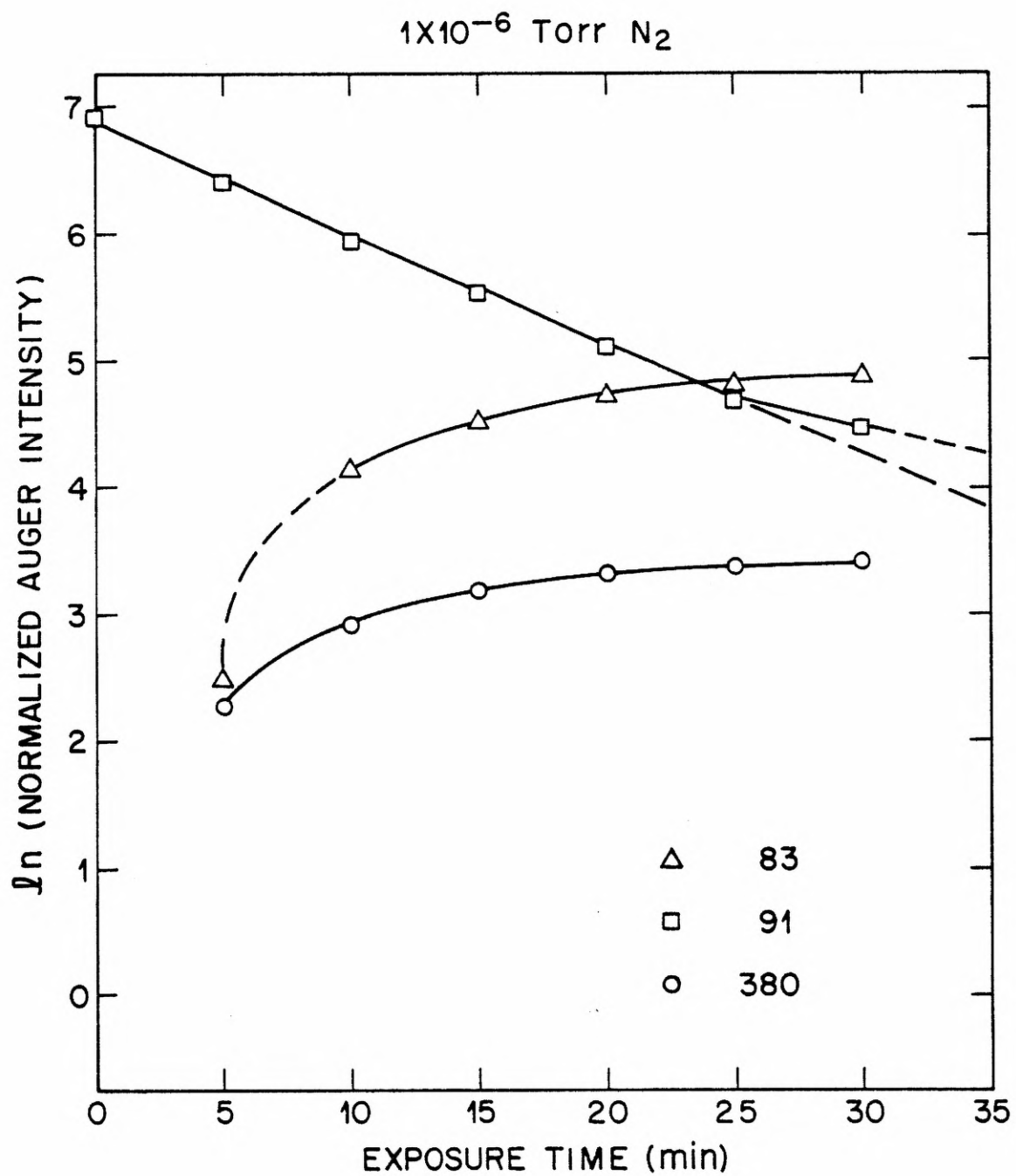


Figure 5.20. Same as Fig. 5.16, except semi-logarithmic plot.

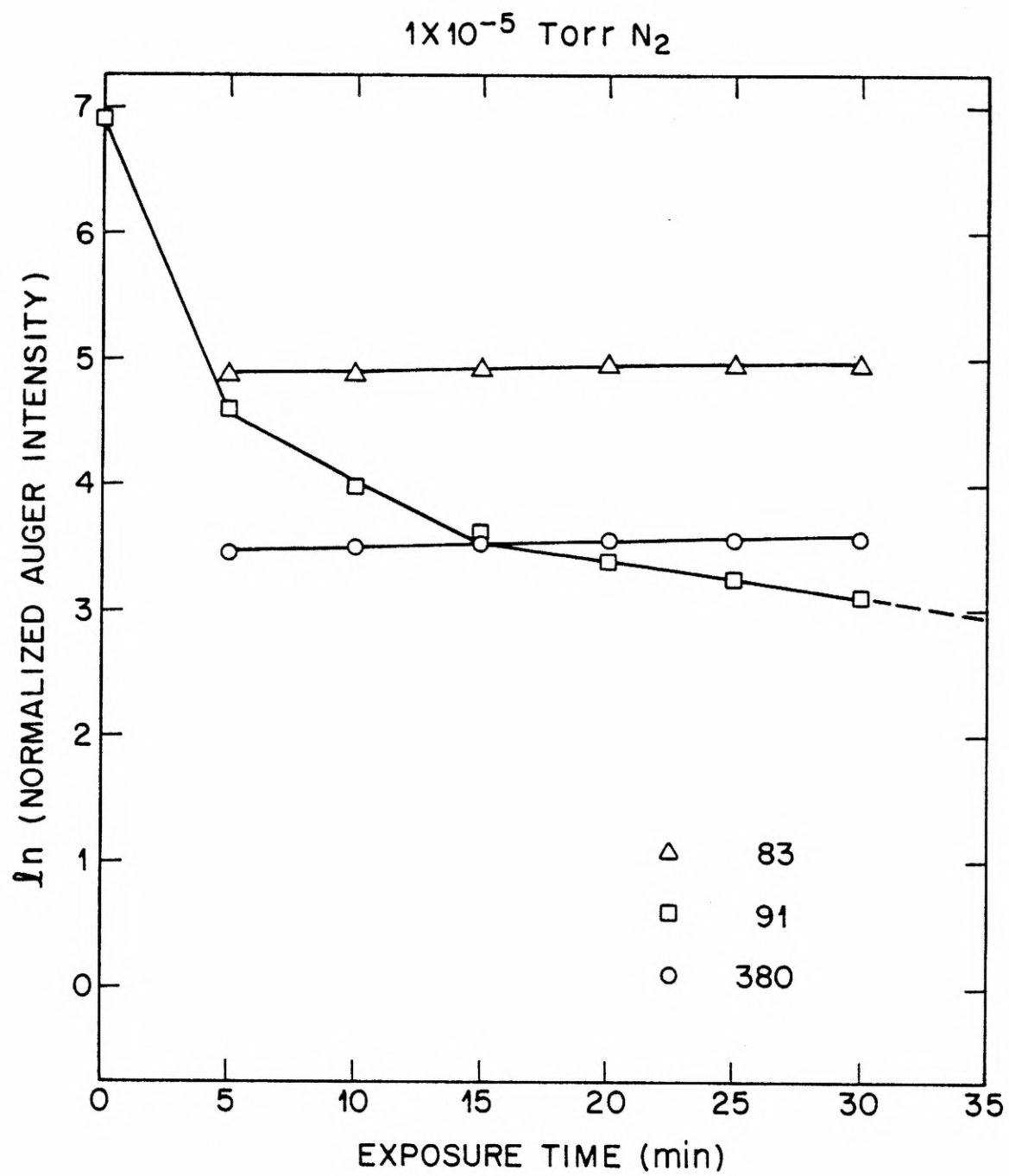


Figure 5.21. Same as Fig. 5.17, except semi-logarithmic plot.

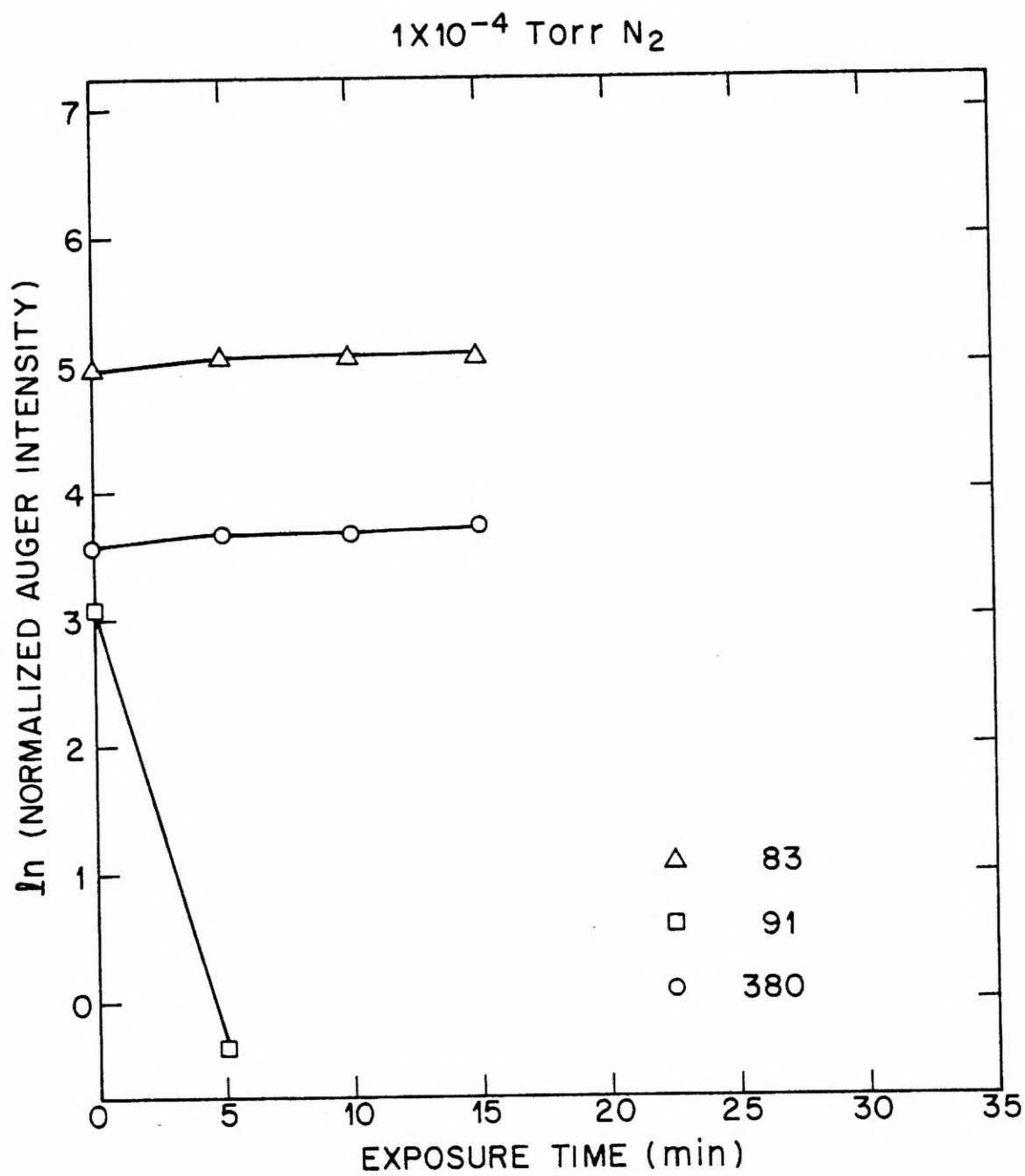


Figure 5.22. Plot of normalized nitride(83 eV) adsorbate intensity vs. Si(91 eV) substrate intensity. Discontinuity is artifact due to procedure for measuring nitride(83 eV) peak-to-peak heights.



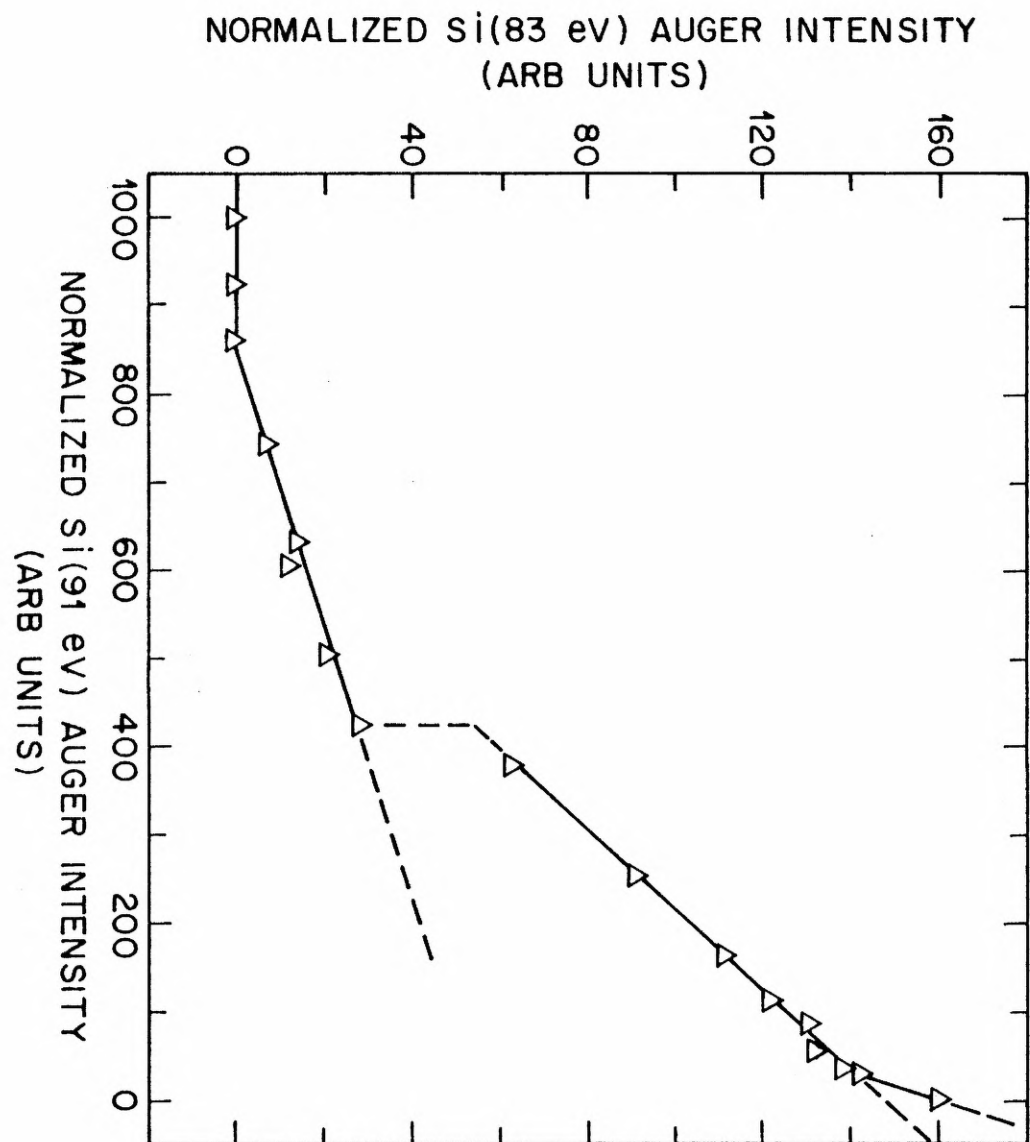


Figure 5.23. Plot of normalized nitrogen(380 eV) adsorbate intensity vs. Si(91 eV) substrate intensity. Closed circles ( $\bullet$ )--Run 1. Circles with vertical bar ( $\phi$ )--Run 2. Open circles ( $\circ$ )--Run 3. First data point ( $I_{91} = 1000$ ,  $I_{380} = 0$ ) common to all three runs.

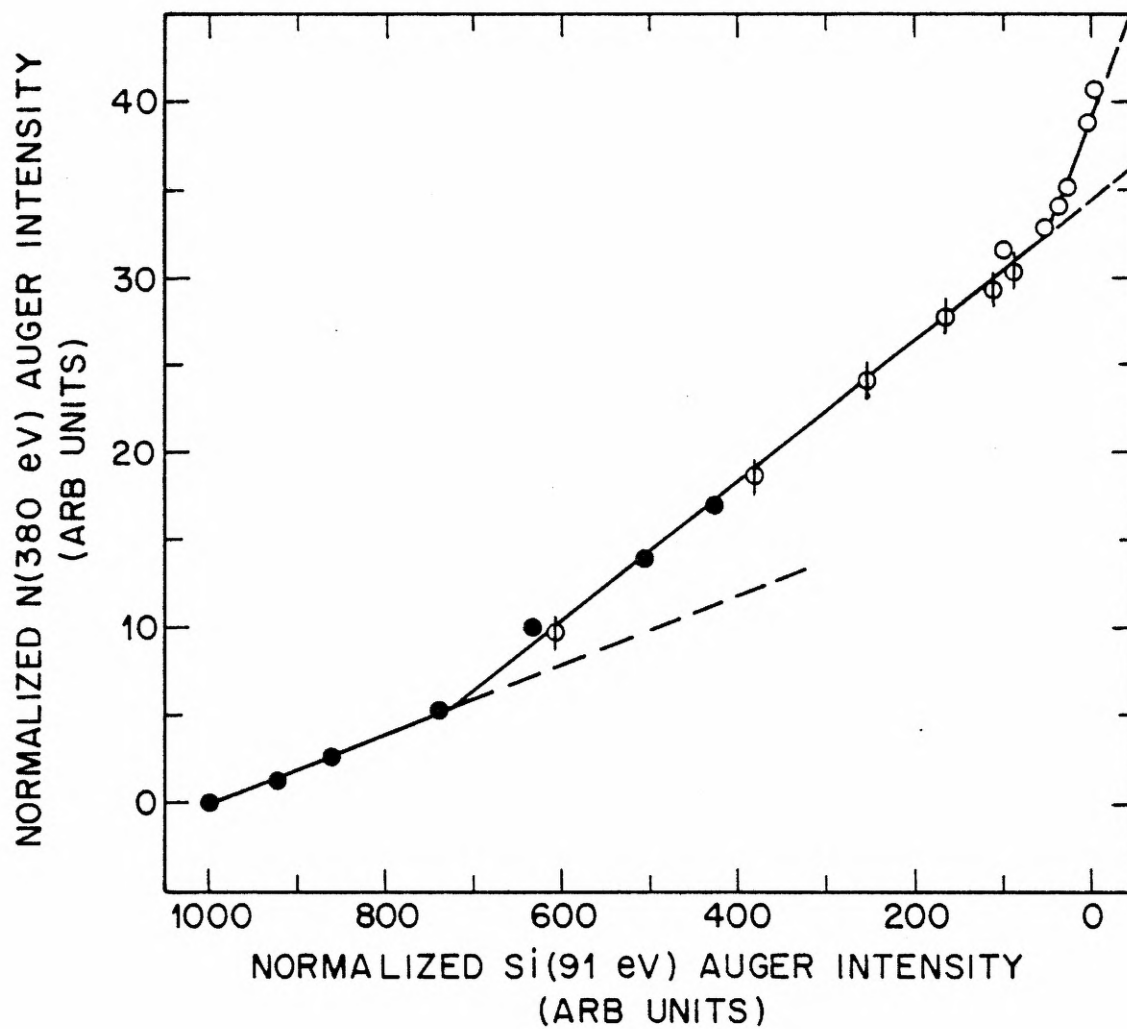


Figure 5.24. Plot of normalized nitride(83 eV) adsorbate intensity vs. nitrogen(380 eV) adsorbate intensity. Discontinuity is artifact due to procedure for measuring nitride(83 eV) peak-to-peak heights.

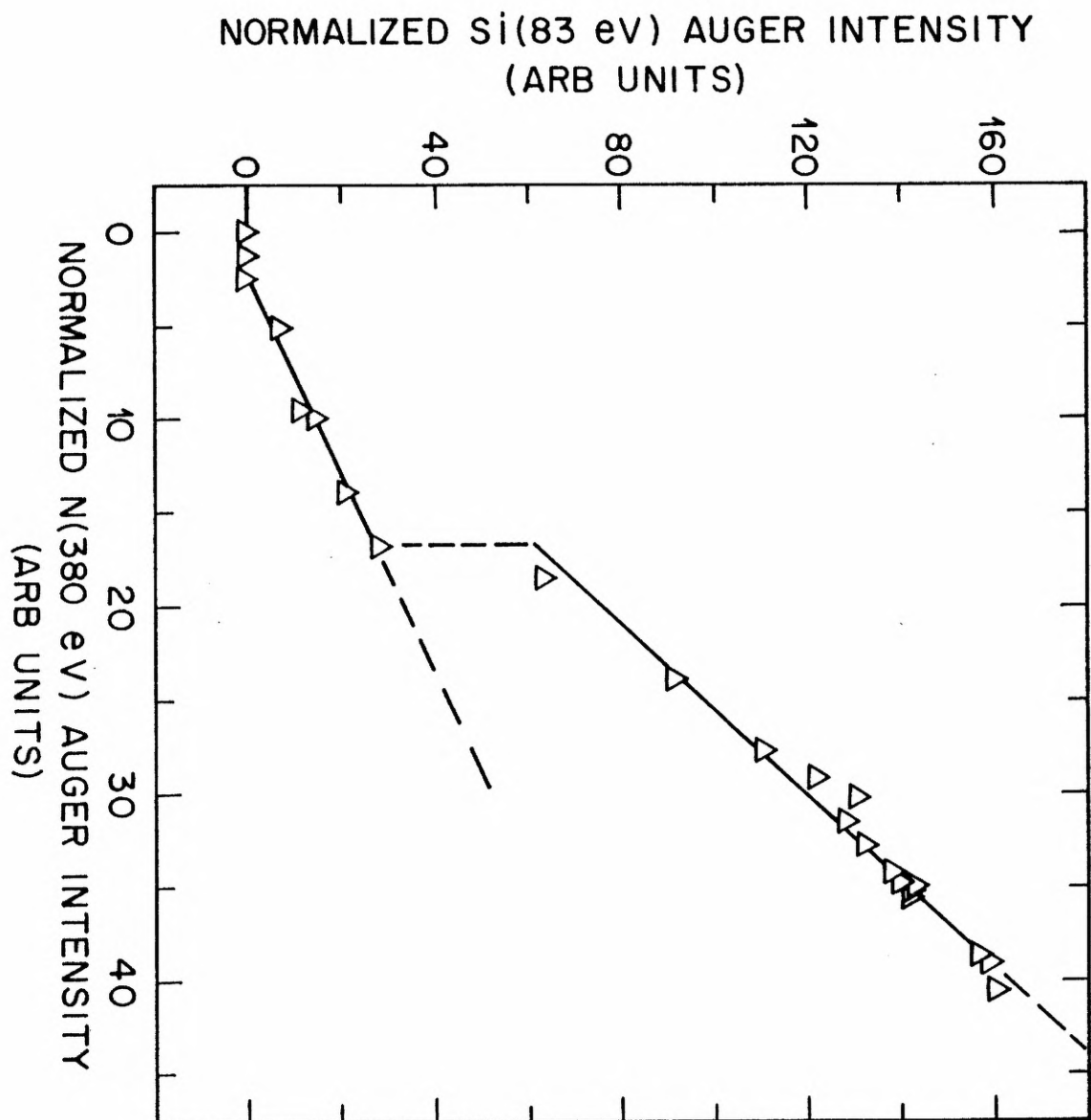


Table 2

## Linear Relationships between Auger Intensities

## A. Nitride(83 eV) vs. Si(91 eV)

- (a)  $846 \leq I_{91} \leq 1000$ ,  $I_{83} = 0$
- (b)  $428 \leq I_{91} \leq 846$ ,  $I_{83} = -0.0629 (\pm 0.0049) I_{91} + 53.2 (\pm 3.2)$
- (c)  $28.6 \leq I_{91} \leq 428$ ,  $I_{83} = -0.219 (\pm 0.006) I_{91} + 147 (\pm 1)$
- (d)  $0 \leq I_{91} < 28.6$ ,  $I_{83} = -0.610 (\pm 0.058) I_{91} + 158 (\pm 1)$

## B. Nitrogen(380 eV) vs. Si(91 eV)

- (a)  $727 \leq I_{91} \leq 1000$ ,  $I_{380} = -0.202 (\pm 0.001) I_{91} + 20.0 (\pm 0.8)$
- (b)  $49.0 \leq I_{91} \leq 727$ ,  $I_{380} = -0.400 (\pm 0.001) I_{91} + 34.4 (\pm 0.3)$
- (c)  $0 \leq I_{91} \leq 49.0$ ,  $I_{380} = -0.138 (\pm 0.017) I_{91} + 39.2 (\pm 0.5)$

## C. Nitride(83 eV) vs. Nitrogen(380 eV)

- (a)  $0 \leq I_{380} \leq 2.40$ ,  $I_{83} = 0$
- (b)  $2.40 \leq I_{380} \leq 16.8$ ,  $I_{83} = 1.87 (\pm 0.11) I_{380} - 4.47 (\pm 1.21)$
- (c)  $16.8 < I_{380} \leq 40.8$ ,  $I_{83} = 4.36 (\pm 0.19) I_{380} - 11.3 (\pm 6.3)$

Indeed, some recent experimental results indicate that the basic theoretical framework should be thoroughly re-examined.<sup>21,26</sup> To revamp quantitative Auger analysis is well beyond the scope of this work; thus, we will stick to currently accepted formalisms (but appropriate criticisms will be rendered along the way). In this section, after an estimate of the maximum film thickness (V.G.1), we will consider the three stages of nitridation corresponding to our three low-temperature runs (see Sec. V.D): (V.G.2) initial stage [Run 1, exposures at  $1 \times 10^{-7}$  Torr  $N_2$ ]; (V.G.3) intermediate stage [Run 2, exposures at  $1 \times 10^{-6}$  Torr  $N_2$ ]; and (V.G.4) final stage [Run 3, exposures at  $1 \times 10^{-5}$  and  $1 \times 10^{-4}$  Torr  $N_2$ ].

#### V.G.1. Maximum Thickness

One crucial quantity is the maximum film thickness under consideration; we can estimate this value from the decay of the Si(91 eV) substrate intensity and the standard exponential relation<sup>20</sup> (its validity will be discussed below)

$$I_{91}^d = I_{91}^o \exp[-d/(\lambda_{91} \cos \chi)] , \quad (5.1)$$

where  $I_{91}^o$  is the Auger intensity from the initial clean surface,  $I_{91}^d$  is the Auger intensity transmitted through a silicon nitride film of thickness  $d$ , and  $\lambda_{91}$  is the mean escape depth of 91-eV electrons in silicon nitride. The  $\cos \chi$  term is a geometrical correction term for the CMA<sup>20</sup>; this type of detector collects only electrons emitted into a conical shell at an angle  $\chi \sim 42^\circ$  from the surface normal (see Fig. 3.18). From Fig. 5.8, the minimum detectable Auger intensity is  $I_{91}^d/I_{91}^o \sim 10^{-3}$ . Inserting the numerical values into Eq. (5.1), we find  $d \sim 5\lambda_{91}$ . Although the mean escape depth in silicon nitride has not been measured, to first order, the mean escape depth at

91 eV is not strongly dependent on material,<sup>30</sup> so we can use the value of  $\lambda_{91} \sim 5 - 6 \text{ \AA}$  found<sup>31</sup> for  $\text{SiO}_2$ . With this value of  $\lambda_{91}$ , the final film thickness is  $d \sim 25 - 30 \text{ \AA}$ .

There are three major assumptions<sup>20</sup> implicit in Eq. (3.1):

(1) the film is uniform and homogeneous, (2) the electrons travel in a straight line through the film, and (3) the generation rate of the substrate Auger electrons remains constant with film thickness. None of these assumptions is strictly true; furthermore, the errors are difficult even to estimate.

First, let's consider the film structure. In the next section, we shall present some evidence for nucleation and growth during the early stages of nitridation---this, of course, is of no significance as long as the final film is uniform and continuous. Although adsorbed-current images of fully nitrided films did indicate some graininess, the resolution was too poor for any definite conclusions. A subsequent attempt to analyze films in a scanning electron microscope proved futile: apparently, air oxidation of the wafer had washed out all contrast between the nitride spots and the substrate. For studies of structural morphology, then, films must be grown in-situ in an ultrahigh vacuum electron microscope.<sup>32,33</sup>

The second assumption appears to have been accepted by most workers without question; however, from LEED results, we should expect multiple scattering<sup>34</sup> of 91-eV electrons to be significant, and, also, some anomalous Auger measurements<sup>21,35</sup> indicate that diffraction of Auger electrons may occur. One other important factor, the angular distribution of the Auger electrons, appears to have been largely neglected in quantitative analysis.<sup>36</sup> Since



recent studies have shown that the angular distribution is anisotropic and changes with adsorbate coverage,<sup>37</sup> there may be anomalous variations in Auger intensities as a function of coverage--measurements by a CMA, with its peculiar collection geometry,<sup>38</sup> would be particularly susceptible to angular perturbations.

The effect of the film on the generation rate of the substrate Auger electrons is also difficult to assess. Some writers<sup>22</sup> multiply the right hand side of Eq. (5.1) by a correction factor  $\exp(-d/\lambda_p)$ , where  $\lambda_p$  is the inelastic mean free path for an electron with primary energy  $E_p$ ; however, such an approach is naive in the extreme: since the critical ionization potential<sup>15</sup> for the 91-eV Auger transition is  $\sim 100$  V, we must consider the distribution of all electrons (primary, secondary, backscattered) in the energy range 100 - 2000 eV. This distribution is exceedingly difficult to determine both experimentally and theoretically<sup>39</sup>; at present, the most promising approach appears to be Monte-Carlo simulation.<sup>40</sup> Pending a considerably more thorough analysis, then, Eq. (5.1) should be viewed as the best available estimate.

#### V.G.2. Initial Stage of Nitridation

Turning from one extreme to the other, we will now consider the very curious initial stage of nitridation (Run 1, exposures at  $1 \times 10^{-7}$  Torr  $N_2$ ). From Fig. 5.14, the nitrogen(380 eV) Auger intensity grows linearly for the first  $\sim 10$  min and then increases more rapidly; similarly, the nitride(83 eV) Auger intensity either stays zero or increases very slowly for the first  $\sim 10$  min and then grows linearly. An increase in the rate of adsorption with increasing coverage is rather rare; when it is observed, it is generally attributed to a nucleation and growth mode<sup>41-43</sup> (most instances involve oxidation of metals).<sup>42</sup> Although the detailed kinetics in a

particular system depends on a number of factors (such as, density of nuclei and rate of surface diffusion), the essential behavior results from adsorption at preferential sites.<sup>42</sup> Consider one simple case: after islands have been nucleated at special surface sites (steps, for example), further adsorption takes place only at the edges of the islands. Then the rate of adsorption is proportional to the available perimeter,  $d\theta/dt \propto \sqrt{\theta}$ , where  $\theta$  is the fractional coverage and  $t$  is the exposure time. In our instance, the behavior of the Auger intensities could be due to other factors as well: for example, variations in angular distributions of Auger electrons (see discussion above). With the data available, we cannot pursue these other possibilities; but we shall show that the data at least is consistent with island growth.

The key to the analysis is the piecewise linear plot of  $I_{380}$  vs.  $I_{91}$  (Fig. 5.23); the 83-eV nitride peak is not well behaved during the early stages of nitridation, so it will not be considered here. Before proceeding, we should emphasize that Fig. 5.23 is a compilation of data points from all three runs. Since the mode of film growth may vary with the exposure conditions, our arguments here must rely only on the data for Run 1; however, no problem arises because these data points by themselves are piecewise linear. As Barthes and Rhead<sup>21</sup> and Biberian and Somorjai<sup>27</sup> have pointed out, this piecewise linear plot indicates the lateral growth of a layer at constant thickness followed by the growth of a second layer upon the completion of the first. In the following discussion, we will first assume the validity of their analysis and then offer criticisms afterwards.

Consider islands with constant height  $d_1$  growing laterally until completion of the first layer. Then, the Auger intensities at a fractional coverage  $\theta_1$  are

$$I_{91}^{\theta_1} = (1 - \theta_1) I_{91}^0 + \theta_1 \alpha I_{91}^0 \quad (5.2)$$

$$I_{380}^{\theta_1} = \theta_1 I_{380}^1, \quad (5.3)$$

where  $I_{91}^0$  is the silicon Auger intensity from the initial clean surface,  $I_{380}^1$  is the nitrogen Auger intensity from the complete first layer, and  $\alpha$  is the attenuation coefficient for 91-eV electrons passing through a layer of thickness  $d_1$ . These relationships follow simply from considering the signals emitted by exposed  $(1 - \theta_1)$  and covered  $(\theta_1)$  portions of the surface. By eliminating  $\theta_1$  between Eqns. (5.2) and (5.3), we obtain the first desired linear relation

$$I_{380}^{\theta_1} = A_1 - B_1 I_{91}^{\theta_1}, \quad 0 \leq \theta_1 \leq 1, \quad (5.4)$$

where

$$A_1 \equiv I_{380}^1 / (1 - \alpha) \quad (5.5)$$

and

$$B_1 \equiv I_{380}^1 / [(1 - \alpha) I_{91}^0] \quad (5.6)$$

After completion of the first layer, similar relations hold for the Auger intensities at fractional coverage  $\theta_2$  of the second layer (thickness  $d_2$ ):

$$I_{91}^{\theta_2} = (1 - \theta_2) \alpha I_{91}^0 + \theta_2 \beta I_{91}^0 \quad (5.7)$$

$$I_{380}^{\theta_2} = (1 - \theta_2) I_{380}^1 + \theta_2 I_{380}^2 \quad (5.8)$$

$$I_{380}^{\theta_2} = A_2 - B_2 I_{91}^{\theta_2}, \quad \theta_1 = 1, \quad 0 \leq \theta_2 \leq 1 \quad (5.9)$$

$$A_2 \equiv (\alpha I_{380}^2 - \beta I_{380}^1)/(\alpha - \beta) \quad (5.10)$$

$$B_2 \equiv (I_{380}^2 - I_{380}^1)/[(\alpha - \beta)I_{91}^0] \quad (5.11)$$

Here,  $\beta$  is the attenuation coefficient of 91-eV electrons passing through the combined first and second layers, and  $I_{380}^2$  is the nitrogen Auger intensity at the completion of the second layer. Equations (5.4) and (5.9) comprise the requisite piecewise linear relationship. In addition to the piecewise linear relation between  $I_{380}$  and  $I_{91}$ , there is another key condition that must be fulfilled for lateral island growth. From Eqns. (5.2) and (5.3) and Eqns. (5.7) and (5.8), we find

$$dI_{380}^{\theta n}/dt = -K_n dI_{91}^{\theta n}/dt, \quad n = 1, 2, \quad (5.12)$$

where  $K_n$  is a proportionality constant. In our instance, Figs. 5.14 and 5.18 verify that this condition is indeed satisfied: the 91-eV Auger intensity first decreases linearly (for approximately 5-10 min) and then decays in piecewise exponential fashion; simultaneously, the 380-eV Auger intensity first increases linearly and then grows in piecewise exponential fashion. As we have already mentioned, the precise kinetics will depend on a number of surface processes. For illustrative purposes only, however, we can cook up a simple (and purely ad-hoc!) model to account for an exponential growth. Consider the following assumptions: (1) after the initial nucleation period, the number of islands is constant, (2) nitrogen first adsorbs preferentially on top of an island, and (3) the adsorbed nitrogen rapidly diffuses to the perimeter, where it is trapped. Then, we have islands of constant height growing laterally according to  $d\theta/dt \propto \theta$ , so  $\theta \propto \exp(t)$ .

Although we do not have enough information to determine the thickness  $d_2$  of the second layer, we can calculate the thickness  $d_1$  of the first layer in the following manner. From Eqn. (5.1),

$$d_1 = -\lambda_{91} \cos \chi \ln(I_{91}^{d_1}/I_{91}^0) \quad , \quad (5.13)$$

while Eqn. (5.2) and Fig. 5.23 yield

$$I_{91}^{d_1}/I_{91}^0 = (I_{91}^{\theta_1})_{\theta_1=1}/I_{91}^0 = \alpha = 0.727 \quad . \quad (5.14)$$

So,  $d_1 \sim .24 \lambda_{91}$ . If we again assume  $\lambda_{91} \sim 5 - 6 \text{ \AA}$ , we find  $d_1 \sim 1.2 - 1.4 \text{ \AA}$ , which would suggest a monolayer of chemisorbed nitrogen. For comparison, the average Si-N bond length<sup>44</sup> in crystalline  $\text{Si}_3\text{N}_4$  is  $\sim 1.7 \text{ \AA}$ . Although the use of  $\lambda_{91} \sim 5 - 6 \text{ \AA}$  for a monolayer of gas may not, at first, appear to be justified, Auger measurements of chemisorbed oxygen<sup>45,46</sup> on silicon, which is known to saturate at  $\sim 1$  monolayer, yield a correct layer thickness of  $\sim 1.2 \text{ \AA}$  if Eqn. (5.1) is used with  $\lambda_{91} \sim 5 - 6 \text{ \AA}$  (the average Si-O bond length<sup>47</sup> in bulk oxides is  $\sim 1.5 \text{ \AA}$ ).

If we assume that our identification of the first layer as a monolayer of chemisorbed nitrogen is correct, then several other results follow. From Figs. 5.14 and 5.23, we see that the monolayer is completed a little after 15 min of exposure and that  $\sim 0.5$  monolayer is adsorbed after 10 min. Therefore, the rapid increase in adsorption rate sets in at  $\sim 0.5$  monolayer; furthermore, since the 83-eV Auger peak is present in spectra from a monolayer coverage and less of chemisorbed nitrogen, the emergence of the 83-eV peak does not coincide with the onset of  $\text{Si}_3\text{N}_4$  bonding. Lastly, from Fig. 5.14, we can estimate the initial sticking coefficient. The initial sticking coefficient is defined by the relation<sup>48</sup>

$$S^0 = \frac{N_0}{v_{PT}} \left. \frac{d\theta_1}{dt} \right|_{t=0} \quad (5.15)$$

where  $v_{PT}$  is the flux of nitrogen molecules at a pressure  $P$  and a temperature  $T$ , and  $N_0$  is the number of nitrogen molecules  $\text{cm}^{-2}$  needed for a monolayer coverage. From Fig. 5.14, we have  $\left. \frac{d\theta_1}{dt} \right|_{t=0} \sim 0.5 \text{ monolayer/600 s}$ , and  $v_{PT}$  is readily determined from kinetic<sup>49</sup> theory to be  $3.8 \times 10^{13} \text{ molecules cm}^{-2} \text{ s}^{-1}$  ( $P = 1 \times 10^{-7} \text{ Torr N}_2$ ,  $T = 300^\circ \text{ K}$ ). However, the configuration of nitrogen chemisorbed on a  $\text{Si}(100)-(2 \times 1)$  surface is not known; for an estimate, we shall simply assume that a monolayer coverage consists of one nitrogen atom for each silicon atom on an ideal (100) surface. For an ideal  $\text{Si}(100)$  surface, there are  $6.8 \times 10^{14} \text{ atoms cm}^{-2}$ ; then,  $N_0$  is one-half of this value,  $3.4 \times 10^{14} \text{ molecules cm}^{-2}$ . Inserting all the numerical values into Eqn. (5.15), we find  $S^0 \sim 7 \times 10^{-3}$ . Strictly,  $S^0$  here should be considered an 'effective' sticking coefficient because the surface was electron bombarded during exposure. From Fig. 5.9, however, we see that the total coverage at the end of Run 1 did not depend on electron bombardment during exposure. If we assume that the coverage at any intermediate stage was also independent of electron bombardment, then the 'effective' sticking coefficient is equal to the true sticking coefficient.

Now that we have completed our analysis of the early stage of nitridation, we would like to take a closer look at the fundamental equations, Eqns. (5.2) and (5.3). In the absence of any anomalous effects due to variations in the angular distribution or generation rate of the Auger electrons, these equations appear quite intuitive--as we have already mentioned, they follow simply from considering the signals emitted by the exposed and covered portions of the wafer. Although Eqn. (5.3) is correct as it stands, Eqn. (5.2) is not quite



correct because it holds only for electrons emitted along the surface normal. Realistically, however, Auger electrons are emitted over a wide angular distribution<sup>37</sup>; only those emitted at  $\chi \sim 42^\circ$  are collected by the CMA. We should, therefore, expect shadow effects as the substrate Auger electrons pass through the overlayer; the extent of shadowing will depend in a complicated manner both on the angular distribution of the Auger electrons and on the number, size, shape, and distribution of the islands. Since Eqns. (5.2) and (5.3) have been verified in a number of cases (particularly at submonolayer coverages),<sup>26,27</sup> fortuitous cancellation of shadow effects may occur; however, in any particular instance, we should be aware that shadow effects may be significant.

#### V.G.3. Intermediate Stage of Nitridation

For exposures at  $1 \times 10^{-6}$  Torr  $N_2$  (Run 2), we see that the six data points in the  $I_{380}$  vs.  $I_{91}$  plot (Fig. 5.23) corresponding to  $t \geq 5$  min in Fig. 5.15 fall on the same line as the data points from the second layer of Run 1. At first glance, this linear behavior would seem to indicate island growth at constant height; however, inspection of Figs. 5.15 and 5.19 shows that Eqn. (5.12), the relation between the decay rate of  $I_{91}$  and the growth rate of  $I_{380}$ , is not fulfilled.

An alternative mode is suggested by Fig. 5.19. Over most of the range,  $I_{91}$  decays at a constant exponential rate

$$I_{91}(t) = I_{91}^0 \exp(-t/\tau_{91}) . \quad (5.16)$$

A best straight line fit of the six data points with  $0 \leq t \leq 25$  min yields  $\tau_{91} = 11.5$  min. If we assume a uniform layer whose thickness  $d$  is increasing at a constant rate  $r$ , so that

$$d = rt \quad ; \quad (5.17)$$

then, we have a continuous layer growth<sup>20</sup> described by Eqn. (5.1)

$$I_{91}^d = I_{91}^o \exp[-d/(\lambda_{91} \cos \chi)]$$

and

$$I_{380}^d = I_{380}^\infty \{1 - \exp[-d/(\lambda_{380} \cos \chi)]\} , \quad (5.18)$$

where  $\lambda_{380}$  is the escape depth at 380 eV, and  $I_{380}^\infty$  is the asymptotic value of the nitrogen Auger intensity for thick films. Depending on the specific values of the parameters, a plot of  $I_{380}$  vs.  $I_{91}$  for continuous layer growth may yield a quasi-linear curve, so this model can be consistent with the experimental results. To confirm this model, we need to verify Eqn. (5.18); rearranging terms in this equation, we find

$$\ln[1 - I_{380}(t)/I_{380}^\infty] = -t/\tau_{380} , \quad (5.19)$$

where  $\tau_{380} = (\lambda_{380} \cos \chi)/r$  and  $I_{380}^\infty = 41$  (at the final coverage of Run 3). From Fig. 5.25, we see that this relation is well satisfied for  $0 \leq t \leq 25$  min; a best straight line fit of these six data points yields  $\tau_{380} = 19.2$  min. In Fig. 5.26, the experimental points are compared to the theoretical curve of  $I_{380}$  vs.  $I_{91}$  calculated from the parametric equations

$$I_{91}(t) = 1000 \exp(-t/11.5) \quad (5.20)$$

and

$$I_{380}(t) = 41[1 - \exp(-t/19.2)] , \quad (5.21)$$

where  $t$  is expressed in min; obviously, the fit is fairly good.



Figure 5.25. Plot of  $-\ln(1 - I_{380}/I_{380}^{\infty})$  vs. exposure time. Straight line is best fit for the six data points with  $0 \leq t \leq 25$  min.

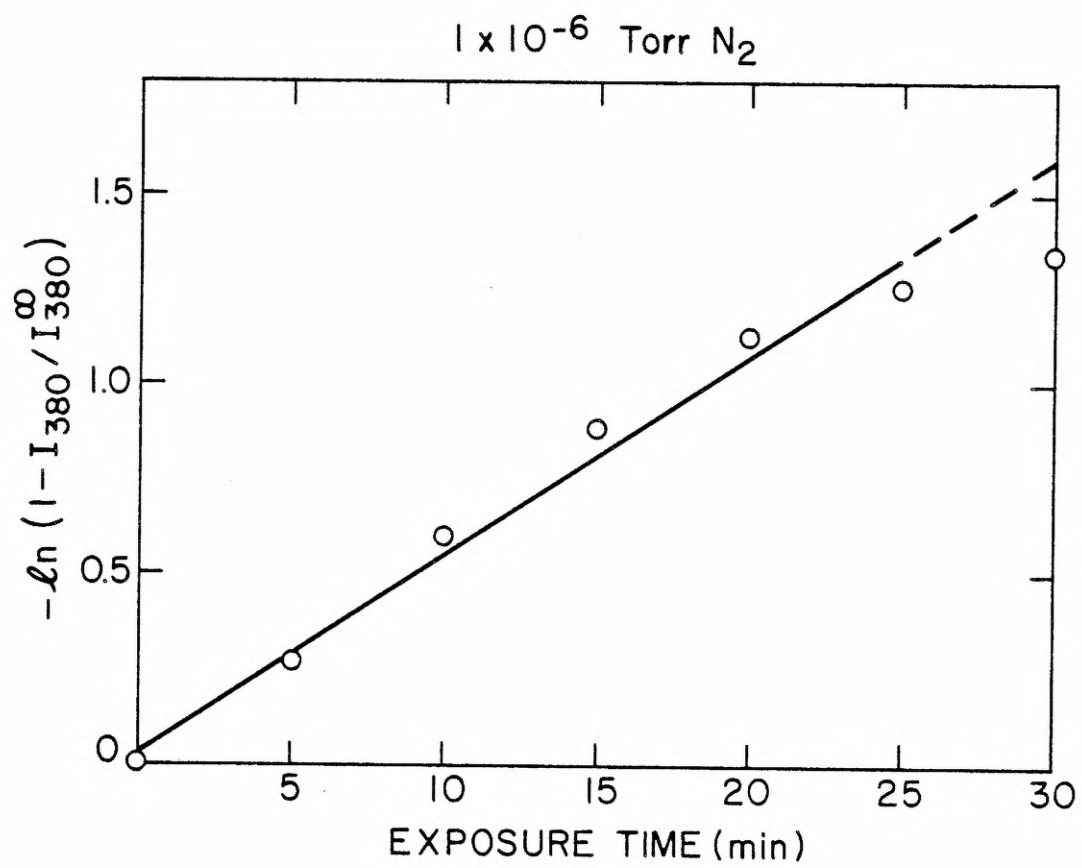
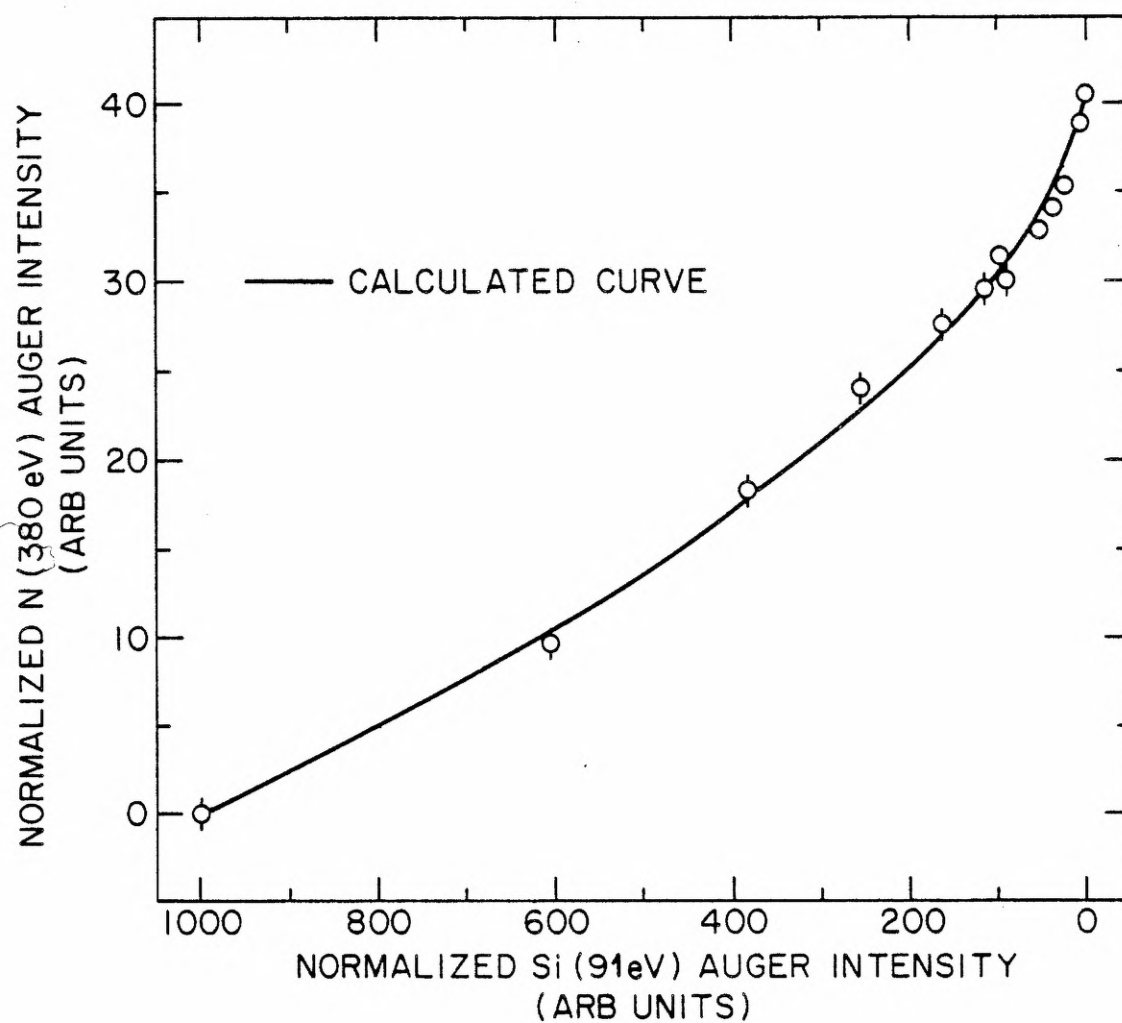


Figure 5.26. Plot of  $I_{380}$  vs.  $I_{91}$ . Comparison of theoretical curve calculated for continuous layer growth with experimental points of Run 2 ( $\phi$ ). Also shown are experimental points of Run 3 (O).



As a further check on this model, we calculate the ratio of the escape depths from the time decay constants:

$$r = (\lambda_{380} \cos \chi) / \tau_{380} = (\lambda_{91} \cos \chi) / \tau_{91} \quad , \quad (5.22)$$

so

$$\lambda_{380} / \lambda_{91} = \tau_{380} / \tau_{91} \quad . \quad (5.23)$$

With our experimentally derived values for the decay constants,  $\lambda_{380} = 1.67 \lambda_{91}$ . If we again use  $\lambda_{91} = 5 - 6 \text{ \AA}$ , then  $\lambda_{380} = 8 - 10 \text{ \AA}$ , which agrees favorably with the published values<sup>50-52</sup> of  $8 - 13 \text{ \AA}$ .

#### V.G.4. Final Stage of Nitridation

At  $1 \times 10^{-5}$  Torr  $N_2$ , there is an initial period of rapid adsorption followed by a very slow uptake (Fig. 5.16); an increase in pressure to  $1 \times 10^{-4}$  Torr  $N_2$  is necessary to grow, in a reasonable time, a film thick enough to suppress the substrate Auger emission (Fig. 5.17). From Fig. 5.26, we see that the data points of Run 3 fall on the curve calculated for continuous layer growth in Run 2; however, this agreement is fortuitous (probably due to compression in the tail of the curve) because the parametric relations, Eqns. (5.20) and (5.21), are not satisfied. Since the Si(91 eV) Auger intensity decays in roughly piecewise exponential fashion (Figs. 5.20 and 5.21), we might consider a continuous layer mode with a varying growth rate. But, if we satisfy Eqn. (5.16) for  $I_{91}(t)$  with four different values of  $\tau_{91}$  over the exposure range, we find that the predicted behavior for  $I_{380}(t)$ , Eqn. (5.19), does not agree with experiment.

Although the experimental data is consistent with lateral island growth, a purely lateral mode of growth can probably be dismissed: the island height would be an improbably large  $25-30 \text{ \AA}$ . Additionally, the slow rate of growth that predominates in Run 3 is more consistent with an increasing film thickness.

For nitridation to occur at all, either nitrogen must diffuse through the interface to the substrate or silicon must diffuse through the interface to the surface (both processes may occur, of course); therefore, as the film thickness increases, we would expect the growth rate to decrease considerably as it becomes limited by diffusion. In summary, the film growth in the final stage of nitridation cannot be described by any simple model.

#### V.H. Beam-Enhanced Adsorption

We would now like to return briefly to Figs. 5.9-5.11, which compare the coverages at the end of Runs 1-3 in the regions (a) not bombarded and (b) continuously bombarded during exposure. At the end of 30 min exposure at  $1 \times 10^{-7}$  Torr  $N_2$ , the Auger scans from the two regions are identical (Fig. 5.9). For exposures at higher pressures (Figs. 5.10 and 5.11), however, more nitrogen is adsorbed in the continuously bombarded region. Although we are not in a position to pinpoint the cause of this effect, for future work, a discussion of the two most probable mechanisms would be instructive:

(a) Variable Sticking Coefficient. With continuous electron bombardment during exposure, nitrogen molecules first impinge on a clean silicon surface; later, they impinge on either a chemisorbed nitrogen or silicon nitride layer. In the absence of electron bombardment, on the other hand, the incoming molecules land first on a clean silicon surface, as before, but, later, on a molecular nitrogen layer. The experimental results then suggest the following: at low coverages, the sticking coefficients on silicon nitride and molecular nitrogen are the same; but, at higher coverages, the sticking coefficient on silicon nitride is higher than on molecular nitrogen.

(b) Electron-Beam Induced Desorption. We have shown that adsorbed nitrogen molecules are dissociated by electron impact; however, some molecules could be desorbed as well. If we assume that a 'thin' molecular layer is sufficiently bound to the silicon substrate so that electron-induced desorption is negligible, then the coverage is independent of electron bombardment during exposure. For a 'thick' molecular layer, we further assume that the outermost molecules are more loosely bound and may be desorbed by the electron beam. If the surface is continuously bombarded during exposure, such a 'thick' molecular layer never develops since the molecules are continuously dissociated; additionally, any desorbed molecules would be replenished from the ambient. However, if a 'thick' layer is bombarded under vacuum, the desorbed molecules are lost, and, consequently, the final coverage is less.

We would like to emphasize that both mechanisms may take place and that considerably more work is necessary to determine their importance. For practical purposes, however, the basic fact to remember is this: except at very low coverages, the nitridation rate is increased by electron bombardment during exposure.

#### V.I. Further Characterization

To further characterize the nitridation process, we (1) used LEED to examine the surface structure during nitridation and (2) determined the saturation electron dose for complete dissociation of a molecular nitrogen layer.

##### V.I.1. LEED Examination

The wafer, positioned in front of the LEED unit (filament on, but electron beam off), was chilled to  $T_B = 32^\circ \text{K}$  and dosed at a pressure of  $1 \times 10^{-8}$  Torr  $\text{N}_2$  in one run and  $1 \times 10^{-7}$  Torr  $\text{N}_2$  in a second run; the sample was dosed for up to 25 min in 5 min increments. After the chamber had been

pumped out, the LEED beam (primary energy = 48 eV, beam current = 1.2  $\mu$ A into a 1 mm diameter spot) was turned on. Upon completion of one measurement, the sample was translated to a new spot for the next dose and measurement. Before proceeding, we would like to strongly emphasize one point: due to pronounced electron-beam effects, LEED examination of a molecular nitrogen layer under stable conditions was not possible; static conditions existed only for dissociated nitrogen layers. The dissociated nitrogen layers examined here were produced by the interaction of the LEED beam with initial molecular layers.

Except for the highest exposure, the LEED pattern remained ( $2 \times 1$ ), but the background increased with exposure. Immediately after the beam had been turned on, the background would start to decrease; this effect was too rapid to be photographed (noticeable changes within seconds). For exposures in the  $10^{-8}$  Torr range, the background appeared to stabilize after  $\sim 2$  min, while the exposures in the  $10^{-7}$  Torr range required  $\sim 5$  min. At the highest exposure, 25 min at  $1 \times 10^{-7}$  Torr, the LEED pattern remained entirely diffuse (no remnants of the ( $2 \times 1$ ) pattern) even after  $\sim 30$  min of observation. Once a LEED pattern had stabilized, we varied the beam voltage from 15 - 500 V to search for unusual surface structures; none were found. After the samples had been warmed up to room temperature, adsorbed-current images and Auger scans revealed deposits of nitrogen. However, we cannot conclude that the surface ordering induced by the LEED beam was due entirely to dissociation of the nitrogen molecules; the decrease in background could also have resulted partly from electron-induced desorption of some molecules. Although no pressure rise was detected by the ion gauge during electron bombardment, we would not expect the gauge to be very sensitive under the particular experimental



conditions; there was no line-of-sight from the sample to the gauge, and any desorbed molecules would probably have been strongly cryopumped by the chill assembly. To check desorption effects, a mass spectrometer with a line-of-sight to the sample surface would be needed.

From the LEED measurements, then, we can conclude the following. Chemisorbed nitrogen and silicon nitride layers on a Si(100) -  $(2 \times 1)$  surface at  $T_B = 32^\circ \text{ K}$  are disordered. The lack of any ordered structures at low coverages is consistent with the model of nucleation and growth of islands which we used to explain the Auger data (Sec. V.G.2).

#### V.I.2. Saturated Electron Dose

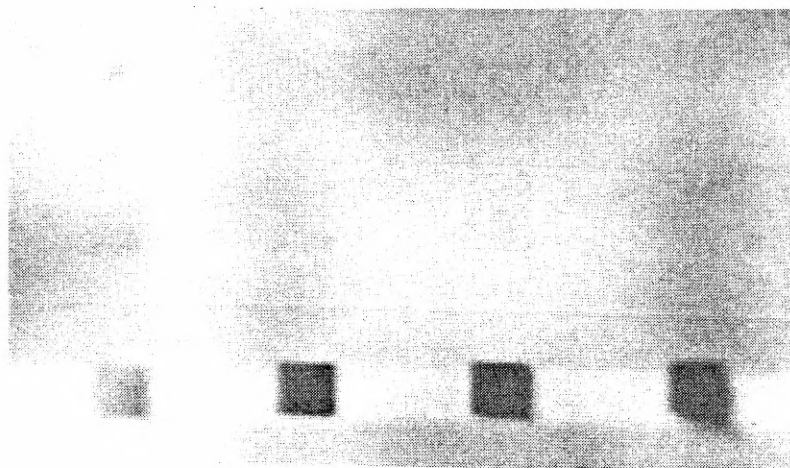
For three initial coverages of molecular nitrogen, the saturation electron dose for complete dissociation was determined in the following manner. As before, the wafer was positioned in front of the CMA (filament on, beam off), chilled to  $T_B = 32^\circ \text{ K}$ , and exposed to nitrogen at a pressure  $P$  for a time  $t$ . After the chamber had been pumped out, and an Auger scan had been taken to determine the coverage, the sample, with the beam off, was translated to a fresh spot, which received an electron dose  $D_e$ . The sample was then similarly translated to other spots and bombarded with different electron doses. In practice, the electron beam, with primary energy = 2000 eV and beam current =  $i$ , was rastered into a  $\ell \times \ell$  square for a period of  $t_{\text{bomb}}$ ; the beam was rapidly turned on and off with the extractor voltage control. The electron dose  $D_e$  is then readily determined from

$$D_e = \frac{i}{e} \frac{t_{\text{bomb}}}{\ell^2} \quad . \quad (5.24)$$

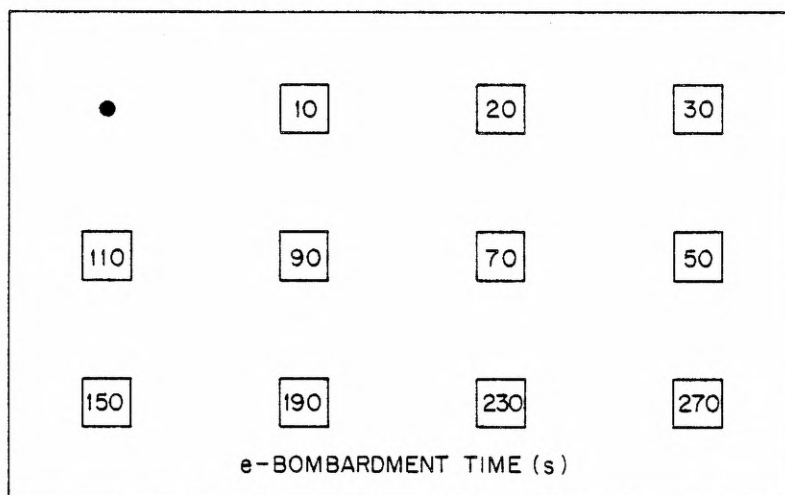
With  $i$  in amperes,  $e$  (electronic charge) in coulombs,  $t_{\text{bomb}}$  in seconds and  $\ell$  in centimeters,  $D_e$  is measured in electrons per square centimeter ( $e/\text{cm}^2$ ). After the sample had been warmed to room temperature, the patches of dissociated nitrogen were located by adsorbed-current imaging for subsequent Auger analysis; an example of a patch array is shown in Fig. 5.27.

Before presenting the results, we would like to clear up a few procedural matters. First of all, measurements were obtained for three different initial exposures:  $1 \times 10^{-7}$  Torr  $\text{N}_2$  for 5 min,  $1 \times 10^{-7}$  Torr  $\text{N}_2$  for 15 min, and  $1 \times 10^{-5}$  Torr  $\text{N}_2$  for 5 min. When the beam was rastered into squares with  $\ell \sim 0.5 - 1.0$  mm, initial runs indicated that very low beam currents, down to  $\sim 0.5$   $\mu\text{A}$ , the minimum stable current, were needed for reasonable bombardment times ( $\geq 10$  s). Since the extractor control was used to turn the beam from full on to full off, the beam current had to be reduced by turning down the filament current (to  $\sim 2.7$  A). Consequently, the effective surface temperature here was lower than in the previous Auger measurements, and the coverages were higher. Additionally, the measurements required so much time that some CO contamination was inevitable. (After the patches had been formed,  $\sim 5$  h were needed for warm-up, pump-down, and re-stabilization; several more hours were needed for all the Auger scans.) In this instance, the slight CO contamination had no serious effect; however, it prevented consistent normalization of the Auger intensities. In the data below, the Auger intensities only within a given run should be compared. We would like to emphasize that Auger scans taken at low temperatures were always free of impurities; therefore, the CO did not influence the nitridation process. And one last point. At very low coverages of dissociated nitrogen, the patches could not be observed by adsorbed-current

Figure 5.27. Array of dissociated nitrogen patches on silicon substrate used in measurement of saturation electron dose. Initial exposure = 5 min at  $1 \times 10^{-5}$  Torr  $N_2$ . Electron beam: primary energy = 2000 eV, beam current = 2.5  $\mu$ A rastered into a  $0.6 \times 0.6$  mm square. (a) Adsorbed-current image. (b) Schematic showing bombardment times. Dot in upper left hand corner is position of Auger scan at low temperature.



(a)



(b)

imaging. With our equipment, an image was just discernable for a coverage of  $\sim 0.5$  monolayer (detectable 83 eV peak). These 'invisible patches', however could be located for Auger analysis by reference to nearby 'visible patches' (see Fig. 5.27).

Now, the results. In Fig. 5.28, we have shown the Auger scans corresponding to the maximum coverages at the three exposures: (a)  $1 \times 10^{-7}$  Torr  $N_2$  for 5 min, (b)  $1 \times 10^{-7}$  Torr  $N_2$  for 15 min, and (c)  $1 \times 10^{-5}$  Torr  $N_2$  for 5 min. Under our particular beam conditions, dissociation for the two lowest exposures was too rapid to permit detailed examination of intermediate stages. For the highest exposure, however, we could follow, in detail, the gradual evolution of the Auger spectra as a function of electron dose. From Figs. 5.29-5.31, we see that the behavior is similar to our previous results for Auger spectra as a function of exposure.

The Auger intensities of the principle peaks, Si(91 eV), nitride(83 eV), and nitrogen(380eV) are plotted as a function of electron dose in Figs. 5.32-5.35. From these plots, we extract the following values of the saturation electron doses:

Initial Nitrogen Exposure ( $N_2$ molecules/cm <sup>2</sup> )	Saturation Electron Dose $D_e^0$ (e/cm <sup>2</sup> )
$1.1 \times 10^{16}$	$1.4 (\pm 0.3) \times 10^{16}$
$3.4 \times 10^{16}$	$3.7 (\pm 0.8) \times 10^{16}$
$1.1 \times 10^{18}$	$1.1 (\pm 0.2) \times 10^{18}$

The errors shown are combined (worst case) errors: they include not only the uncertainty in determining the onset of saturation in the plots but also the following experimental errors:  $\Delta t_{\text{bomb}} = \pm 1$  s,  $\Delta l = \pm 0.005$  cm, and  $\Delta i = \pm 0.1$   $\mu$ A. Within the limited accuracy, the saturation electron dose is linear with exposure over at least two orders of magnitude. This fact

Figure 5.28. Auger scans. Maximum coverages used in

measurement of saturation electron dose.

Initial exposure: (a) 5 min at  $1 \times 10^{-7}$  Torr  $N_2$ , (b) 15 min at  $1 \times 10^{-7}$  Torr  $N_2$ , (c) 5 min

at  $1 \times 10^{-5}$  Torr  $N_2$ . Lock-in settings: (a)

Si-- $\tau$  = 3 s, FS = 50  $\mu$ V; N-- $\tau$  = 3 s, FS = 20  $\mu$ V.

(b) Si-- $\tau$  = 1 s, FS = 100  $\mu$ V; N-- $\tau$  = 1 s,

FS = 50  $\mu$ V. (c) Si-- $\tau$  = 1 s, FS = 50  $\mu$ V;

N-- $\tau$  = 1 s, FS = 100  $\mu$ V.

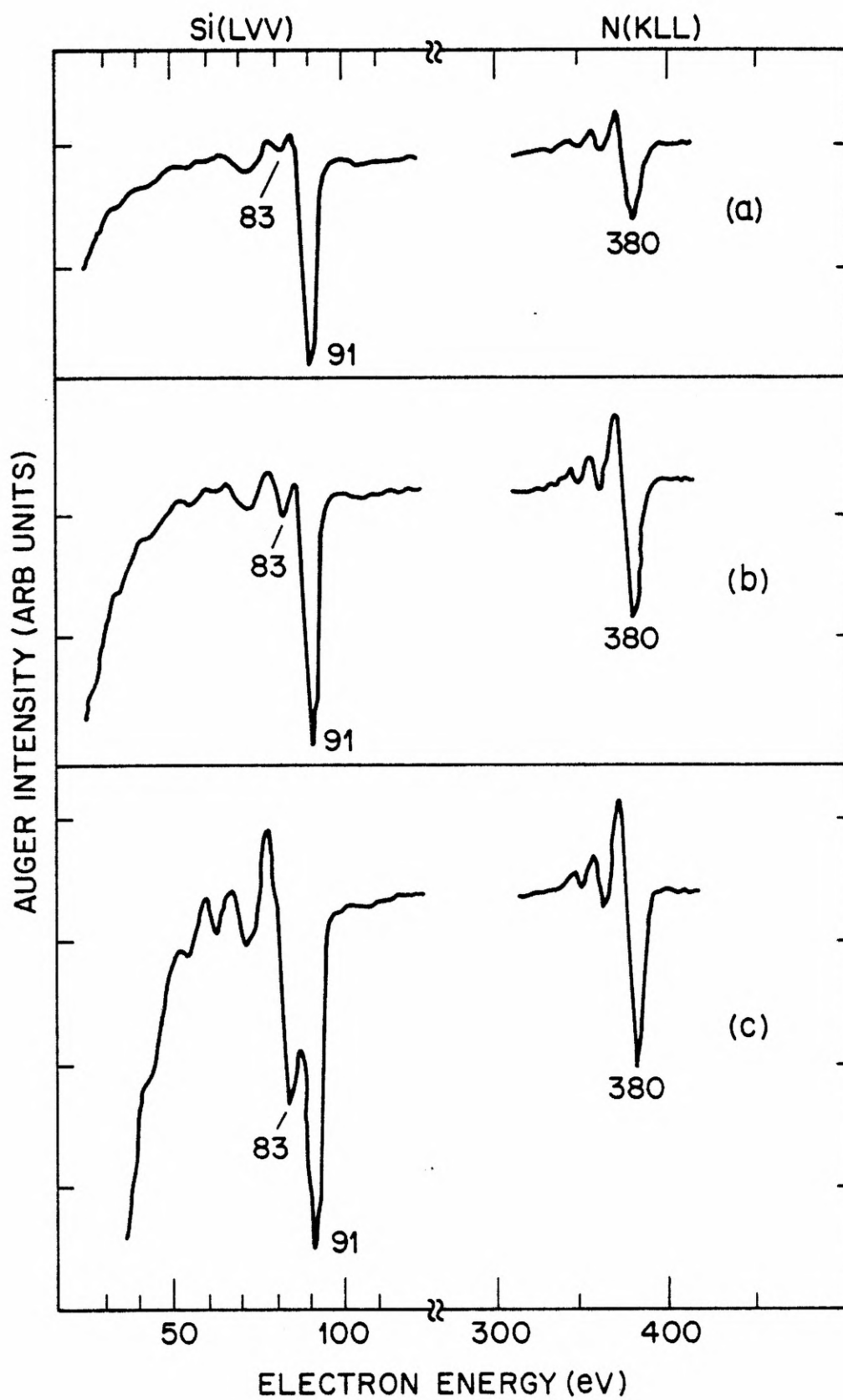


Figure 5.29. Auger scans of patches in Fig. 5.27. Bombardment times:  
(a) 30 s, (b) 50 s, (c) 70 s. Lock-in settings: (X1)  $\tau = 1$  s,  
FS = 200  $\mu$ V; (X10)  $\tau = 3$  s, FS = 20  $\mu$ V.



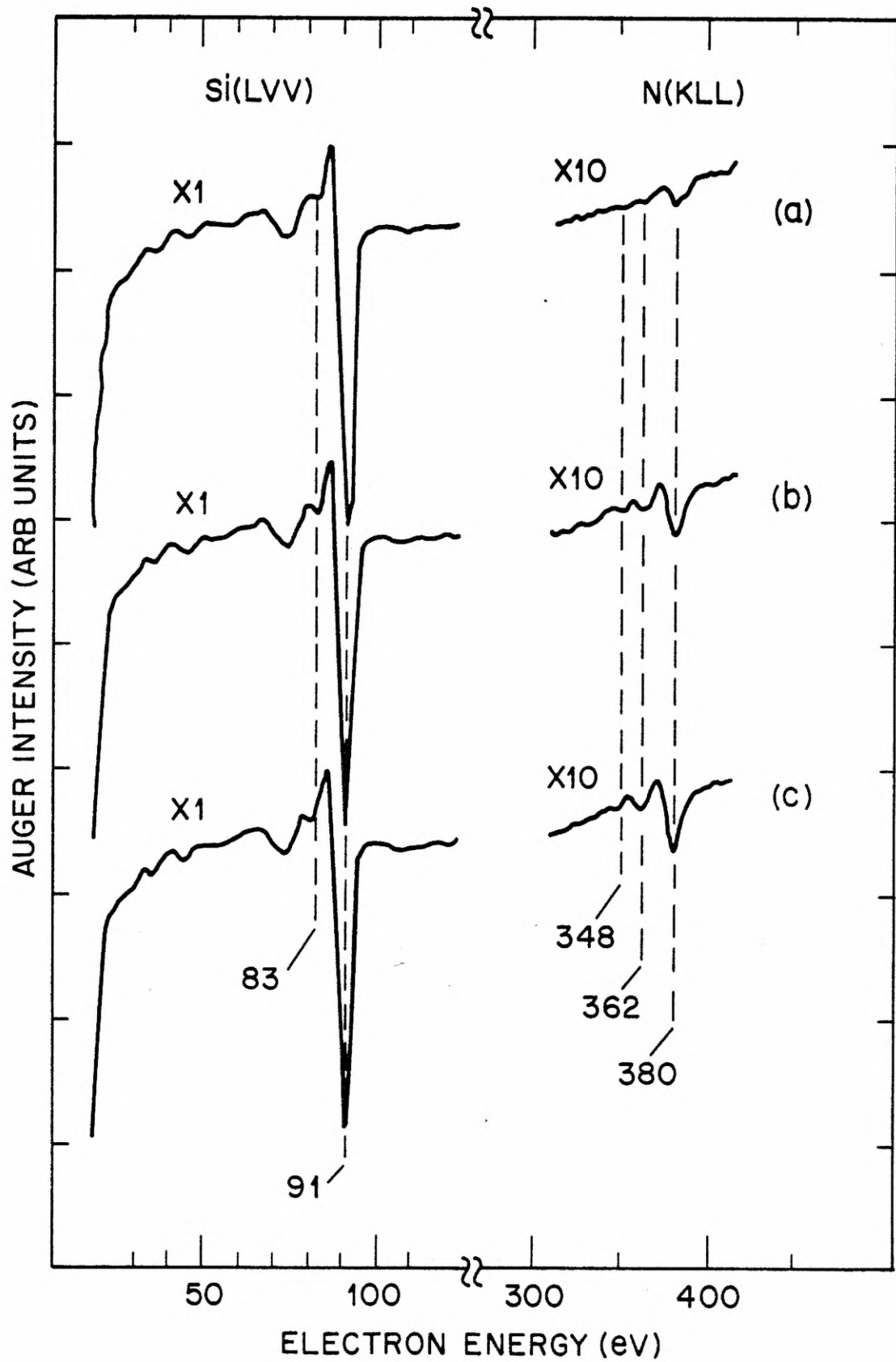


Figure 5.30. Auger scans of patches in Fig. 5.27. Bombardment times: (d) 90 s, (e) 110 s, (f) 150 s. Lock-in settings: (X1)  $\tau = 1$  s, FS = 100  $\mu$ V; (X4)  $\tau = 3$  s, FS = 50  $\mu$ V; (X10)  $\tau = 3$  s, FS = 20  $\mu$ V.

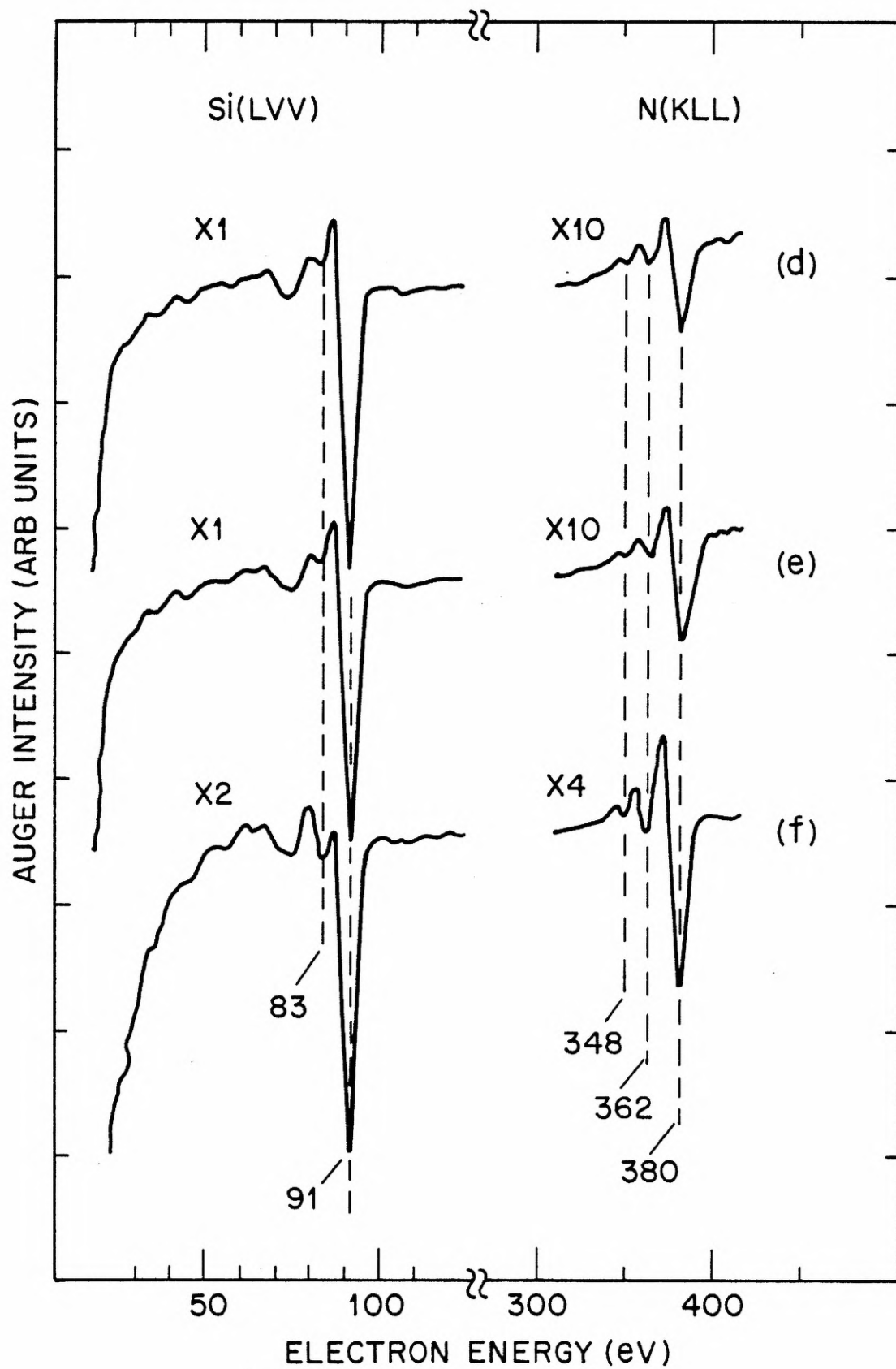


Figure 5.31. Auger scans of patches in Fig. 5.27. Bombardment times:

(g) 190 s, (h) 230 s, (i) 270 s. Lock-in settings:

(X2)  $\tau = 1$  s, FS = 100  $\mu$ V; (X4)  $\tau = 1$  s, FS = 50  $\mu$ V.

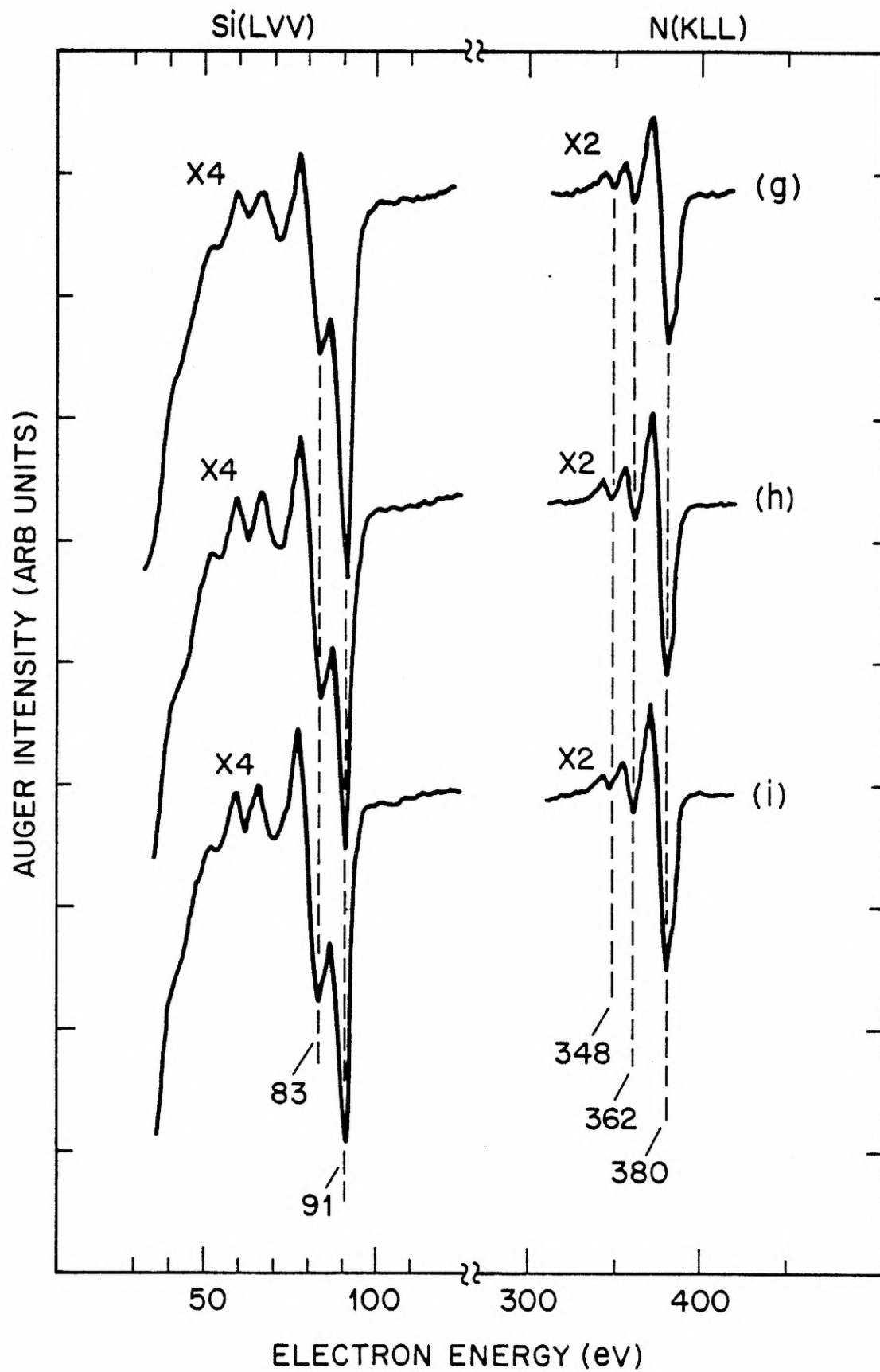


Figure 5.32. Plot of Auger intensities vs. electron dose. Initial exposure = 5 min at  $1 \times 10^{-7}$  Torr  $N_2$ . Data in saturation region extends out to  $1.1 \times 10^{17}$  e/cm<sup>2</sup>.

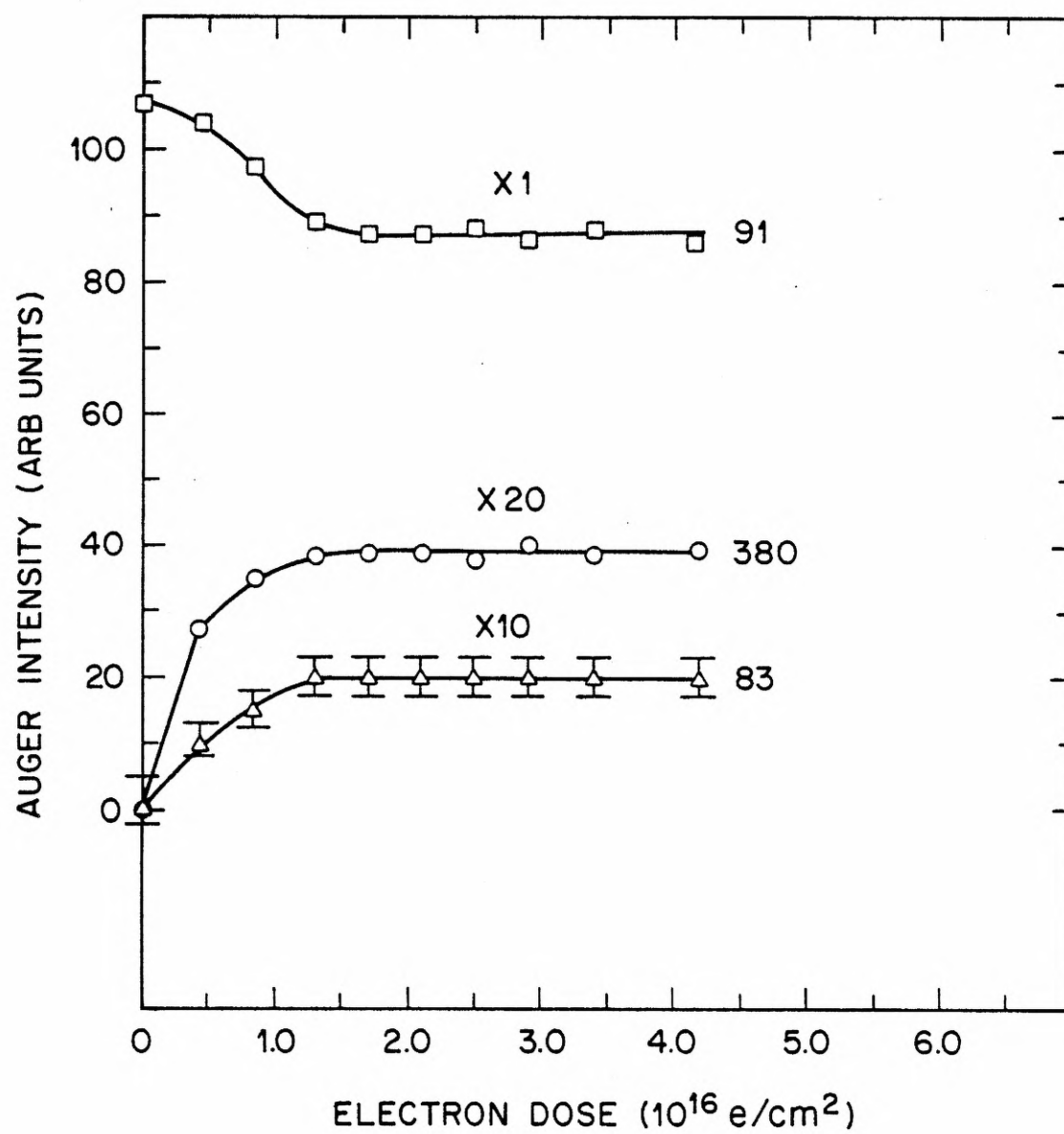


Figure 5.33. Plot of Auger intensities vs. electron dose.

Initial exposure = 15 min at  $1 \times 10^{-7}$  Torr  $N_2$ .

Data in saturation region extends out to

$9.6 \times 10^{17}$  e/cm<sup>2</sup>.



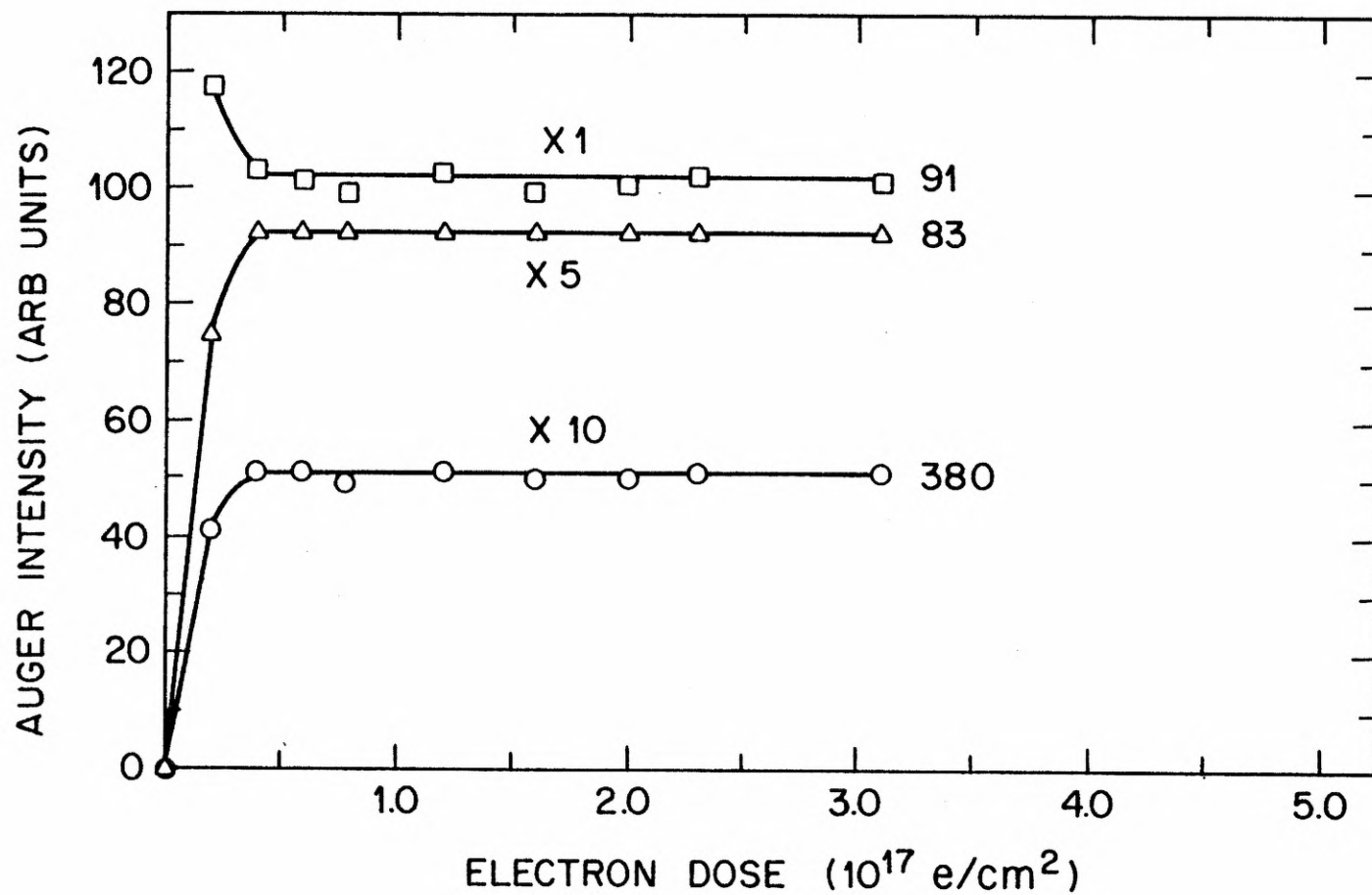


Figure 5.34. Plot of Auger intensities vs. electron dose.

Initial exposure = 5 min at  $1 \times 10^{-5}$  Torr  $N_2$ .

Data in saturation region extends out to

$1.6 \times 10^{19}$  e/cm<sup>2</sup>.

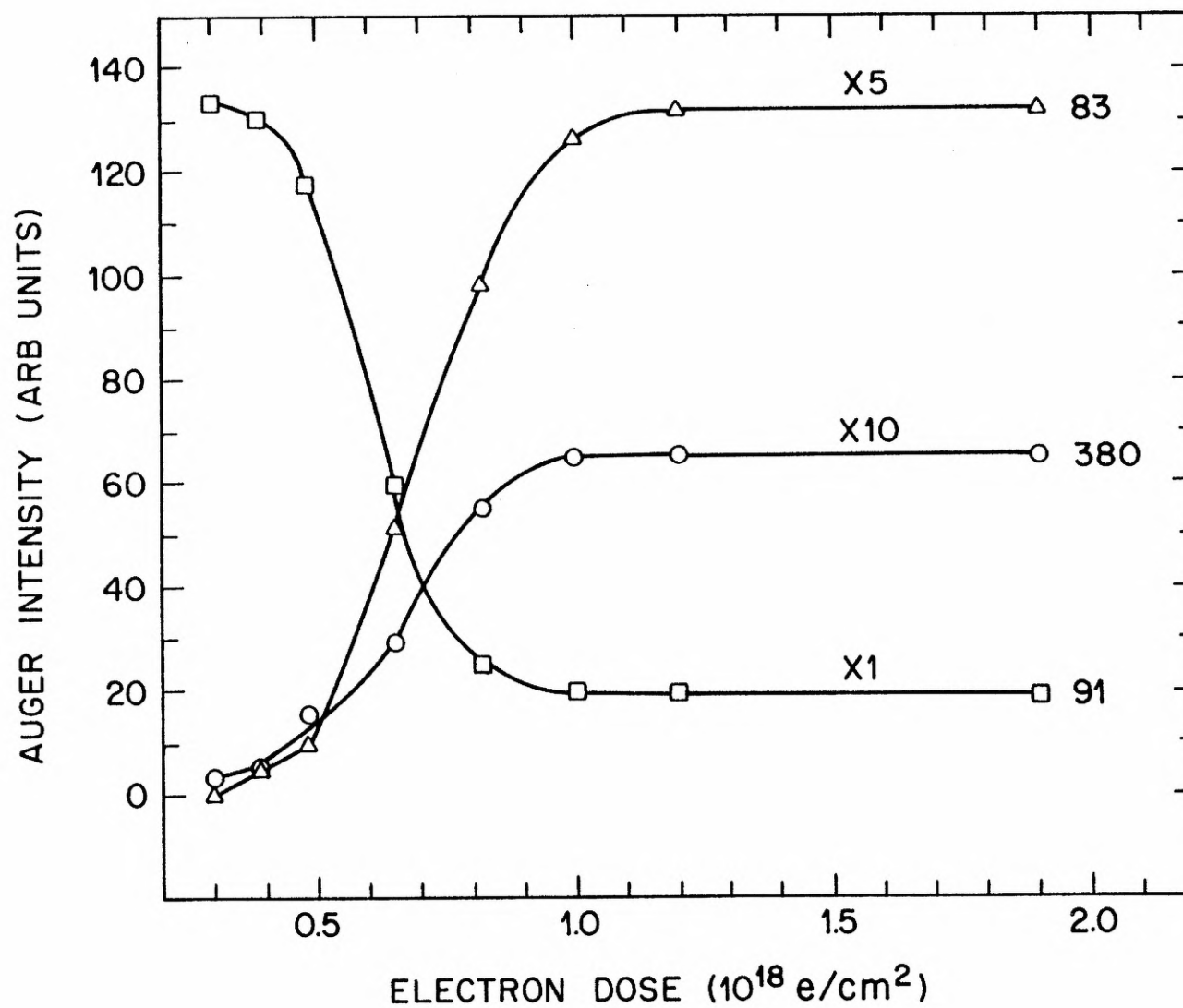
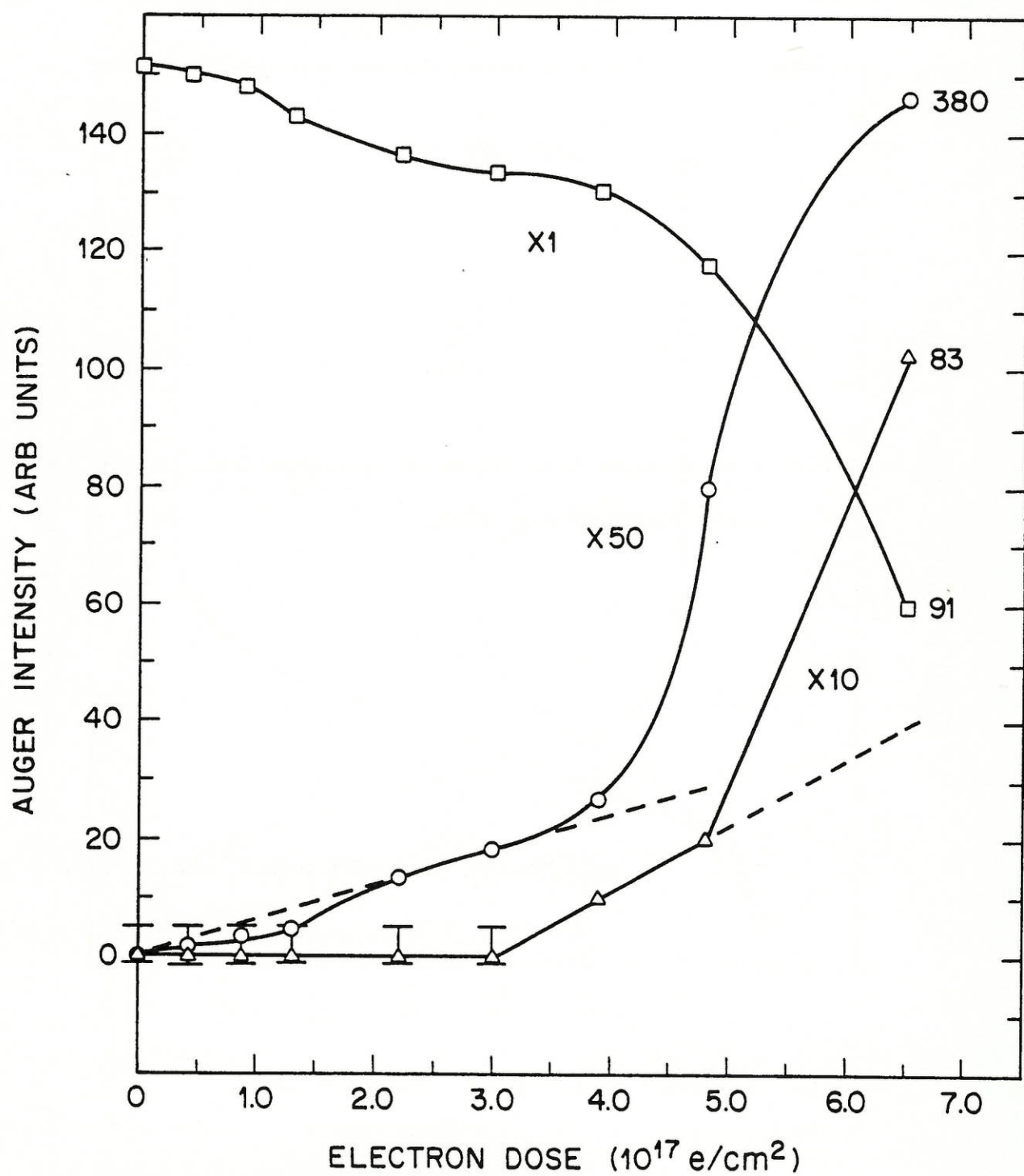


Figure 5.35. Plot of Auger intensities vs. electron dose. Detail of early stages of Fig. 5.34.



suggests the following (deceptively) simple picture for this exposure range: (1) molecular nitrogen adsorbs with a constant sticking coefficient so that the coverage is linear with exposure and (2) the effective (dissociation cross section per nitrogen molecule) per incident electron is constant. The rather awkward phrasing in (2) is necessary because we are dealing with multilayers adsorbed on a substrate; therefore, (a) backscattered and secondary electrons may dissociate nitrogen molecules and (b) an electron may multiply scatter and dissociate more than one molecule. For simplicity, we will refer to the quantity in (2) as the 'effective dissociation cross section'. Based on this model, however, a rough estimate of the coverages involved leads to an absurd result. By comparing the Auger spectra in Fig. 5.28 (a) with the spectra in Figs. 5.2 and 5.3, we find that the coverage here for an initial exposure of  $1.1 \times 10^{16}$  molecules/cm<sup>2</sup> is the equivalent of 2 - 3 monolayers of nitrogen; then the coverage for an initial exposure of  $1.2 \times 10^{18}$  molecules/cm<sup>2</sup> would be the equivalent of 200 - 300 monolayers! Thus, we are led to a more complicated scenario: (1) the sticking coefficient varies with coverage, (2) the effective dissociation cross section varies with coverage, and (3) the two variations fortuitously cancel in such a manner that  $D_e^0$  is linear with exposure.

We can get a rough estimate of the effective dissociation cross section for an initial coverage of one monolayer as follows. As we have shown above, the coverage for an initial exposure of  $1.1 \times 10^{16}$  molecules/cm<sup>2</sup> is 2 - 3 monolayers; extrapolation of our data for  $D_e^0$  to 1 monolayer yields  $D_e^0 = (3.7 - 8.5) \times 10^{15}$  e/cm<sup>2</sup>. Although the kinetics in our instance may be anomalous, for an estimate of the effective dissociation cross section, we shall assume first-order kinetics up to one monolayer<sup>54</sup>:

$$N(D_e) = N_0 \exp(-Q D_e) \quad , \quad (5.25)$$

where  $N_0$  is the initial surface concentration of nitrogen molecules,  $N(D_e)$  is the concentration of molecules after an electron dose  $D_e$ , and  $Q$  is the effective dissociation cross section. Then, the fraction of dissociated molecules is

$$f(D_e) \equiv -N(D_e)/N_0 = 1 - \exp(-Q D_e) \quad . \quad (5.26)$$

Under our experimental conditions, we have  $f(D_e^0) \sim 0.99$ , so

$$Q \sim -[\ln(0.01)]/D_e^0 \quad , \quad (5.27)$$

and, finally,  $Q = (0.54 - 1.2) \times 10^{-15} \text{ cm}^2$ . In comparison, the total ionization cross section<sup>55</sup> by electron impact of  $N_2$  molecules in the gas phase is  $< 9 \times 10^{-17} \text{ cm}^2$  for 2000 eV electrons (the total dissociative ionization cross section<sup>56</sup> is  $< 4 \times 10^{-17} \text{ cm}^2$ ). Our value is also considerably higher than Polák's<sup>57</sup> cross section,  $Q_{\text{diss}} \sim 3 \times 10^{-18} \text{ cm}^2$ , for the dissociation of a sub-monolayer coverage of  $\gamma$ -nitrogen on W(110) by 2500-eV electrons. Our results, however, are in agreement with the measurements of Holloway, et. al.,<sup>58</sup> for damage produced by 1500-eV electrons in condensed multilayers of  $H_2O$ ,  $CH_3OH$ , and  $(CH_3)_2O$ ; using an Auger analysis similar to ours, they determined an effective 'damage' cross section of  $(0.3 - 3) \times 10^{-15} \text{ cm}^2$ .

From the plots of the Auger intensities vs. electrons dose (Figs 5.32-5.35), we may glean two other points of interest. First of all, the extensive flat saturation regions verify that silicon nitride films are very resistant to electron-induced desorption.<sup>59</sup> Secondly, from Fig. 5.35, we see that the anomalous initial stage of film growth (increase in rate of adsorption with increasing coverage) persists even in the presence of a large excess of molecular nitrogen.



V.J. Silicon Nitride Structures Formed by Direct Electron-Beam Writing:  
Thermal Stability and Spatial Profile

Although our work here has principally utilized a primary beam of 2000 eV, which can be focussed into a small spot, we were able to create nitride deposits with primaries as low as 40 eV (the exact threshold was not determined); this result is really not very surprising, however, because the critical dissociative ionization potential<sup>60</sup> in gaseous  $N_2$  is 24.3 eV. Figure 5.36 is an adsorbed-current image of a broad nitride spot formed by the LEED gun with  $E_p = 400$  eV. In Fig. 5.37, we show high-sensitivity Auger scans taken at (a) the edge and (b) the center of the spot. After this particular sample had been heated to 500° C for 5 min and then cooled back to room temperature, the Auger scans were unchanged; thus, the deposit was thermally very stable.

More complicated structures could be created by rastering the electron beam from the Auger gun (Fig. 5.38). As an example of the edge sharpness attainable, the nitrogen Auger peak-to-peak heights as a function of distance across the square patch were measured by translating the wafer across the CMA (Fig. 5.39); we see that the edge profile is comparable to the beam diameter (0.1 mm).

V.K. Summary: Nitrogen on Si(100)

Here, in outline form, we shall summarize our principle results for nitrogen on Si(100):

(a) Room Temperature Adsorption. With the substrate at room temperature, no nitrogen is adsorbed for exposures up to 15 min at  $5 \times 10^{-5}$  Torr  $N_2$ . Adsorption induced by electron bombardment of the surface during exposure is also negligible.



Figure 5.36. Absorbed-current image. Localized deposit of silicon nitride formed by LEED gun ( $E_p = 400$  eV).

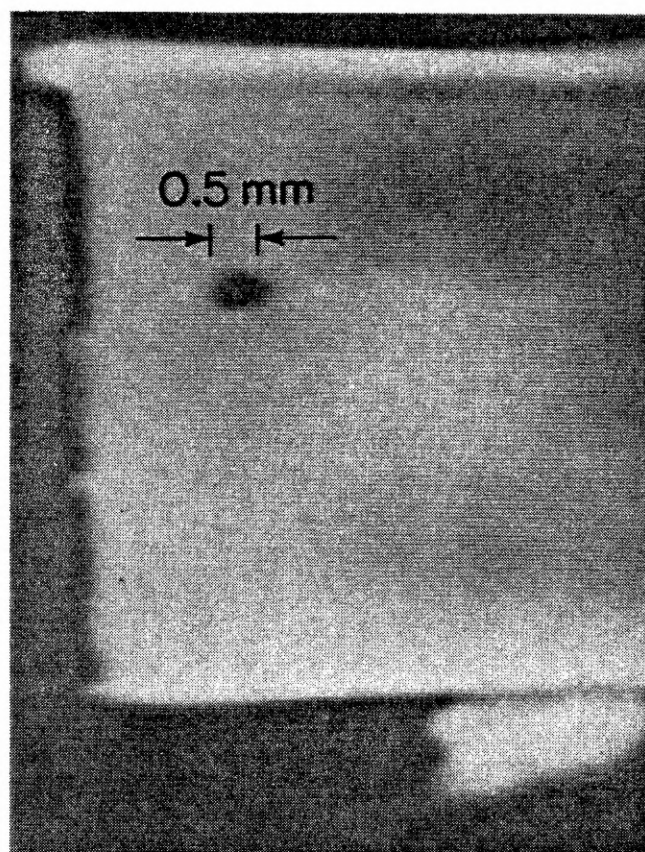


Figure 5.37. High-sensitivity Auger scans of deposit shown in Fig. 5.36.

Primary energy = 2000 eV. Modulation =  $4 V_{p-p}$ , 23.5 kHz.

(a) Edge of spot. (b) Center of spot.

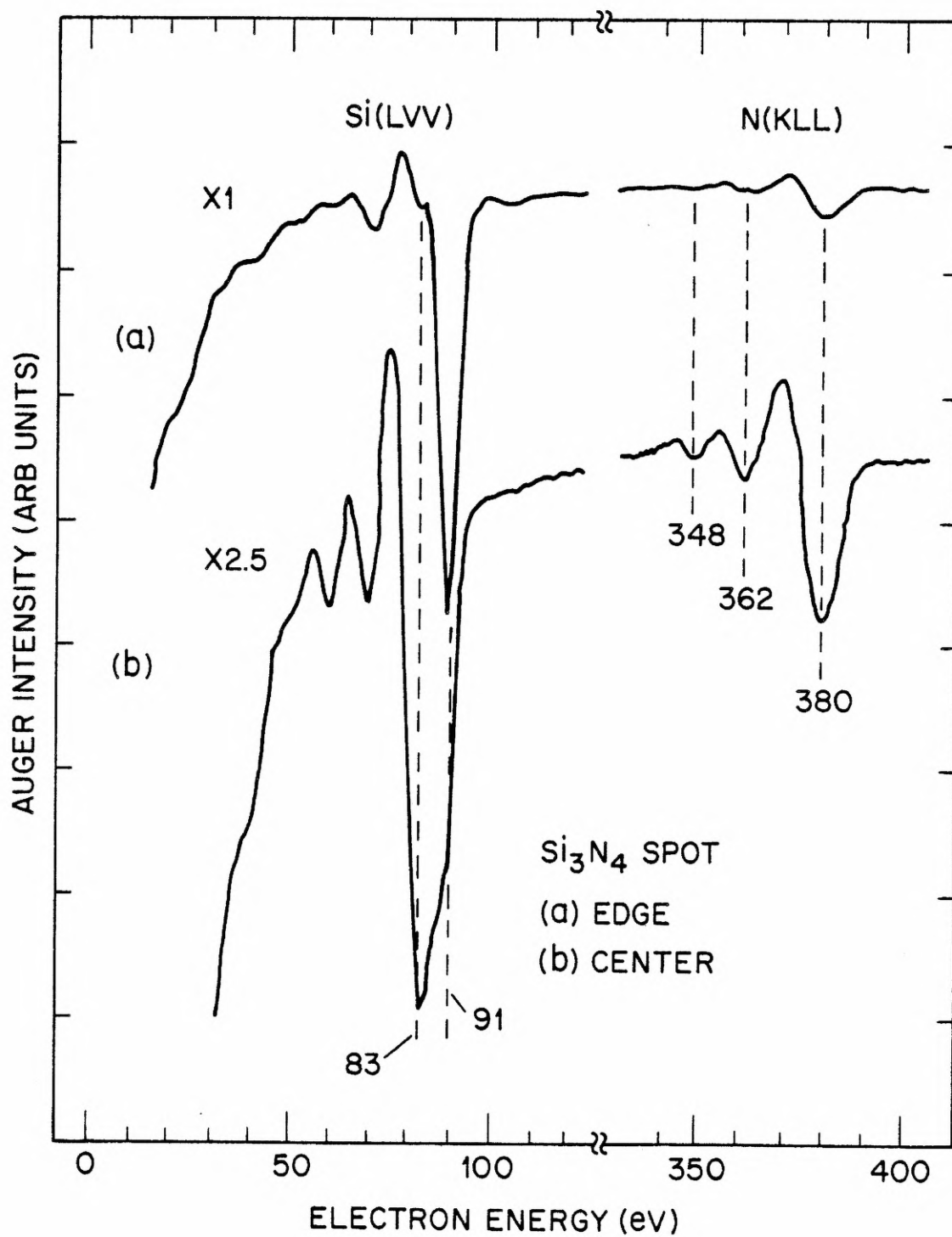


Figure 5.38. Absorbed-current images. Silicon nitride structures  
formed by scanning Auger gun.

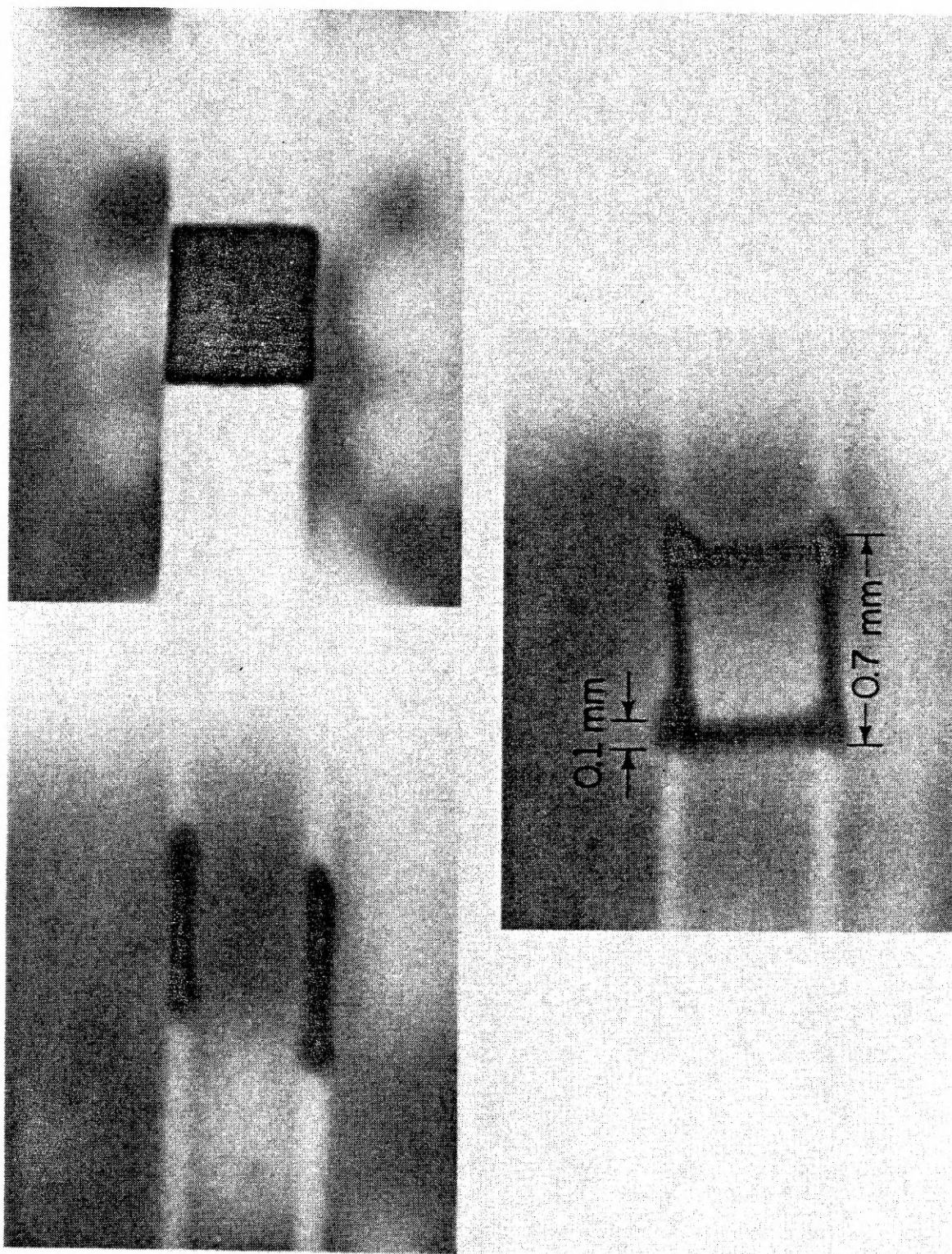
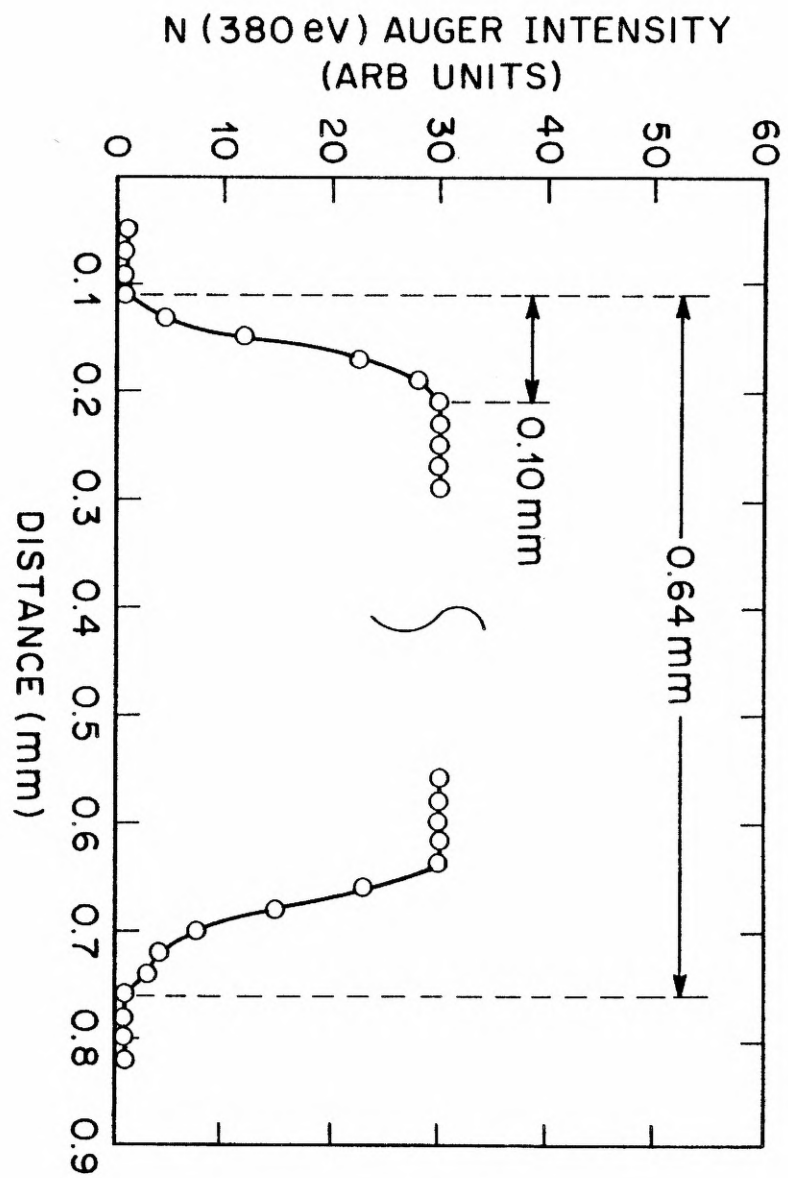


Figure 5.39. Plot of nitrogen Auger peak-to-peak heights vs. distance across square patch of silicon nitride shown in Fig. 5.38 (upper right-hand corner).





(b) Low Temperature Adsorption. At  $T_B = 32^\circ \text{ K}$ , molecular nitrogen is condensed onto the substrate for exposures as low as 5 min at  $1 \times 10^{-7}$  Torr  $\text{N}_2$ ; the initial sticking coefficient is estimated to be  $\sim 7 \times 10^{-3}$ . For exposures greater than 15 min at  $1 \times 10^{-7}$  Torr  $\text{N}_2$ , multilayers form. At  $T_B = 32^\circ \text{ K}$ , the molecular layers are stable for at least 3 h under vacuum; however, they desorb rapidly for  $T_B > 40^\circ \text{ K}$ .

(c) Electron-Induced Nitridation. Electron bombardment of a condensed molecular nitrogen layer produces localized deposits of silicon nitride, which are stable to at least  $500^\circ \text{ C}$ . For an initial coverage of one monolayer of molecular nitrogen, the effective dissociation cross section (primary electron energy = 2000 eV) is  $\sim (0.54 - 1.2) \times 10^{-15} \text{ cm}^2$ . Our Auger and LEED data indicates that the initial stage of electron-induced adsorption is the formation of a monolayer of chemisorbed nitrogen via the nucleation and lateral growth of islands. For practical film growth, the substrate should be exposed to an ambient of  $1 \times 10^{-4}$  Torr  $\text{N}_2$  and simultaneously bombarded with electrons. In our experiments, we have achieved a film thickness of  $\sim 25 - 30 \text{ \AA}$ ; however, this thickness should not necessarily be viewed as a saturation value because our method for determining film thickness (from the decay of the substrate Auger peak) is not sensitive to greater values.

(d) Auger Spectra of  $\text{Si}_3\text{N}_4$ . The Si(LVV) spectrum from a silicon nitride film rigorously free of impurities and sputtering damage is characterized by a strong peak at 83 eV; for a sufficiently thick film, the 91-eV peak characteristic of clean Si vanishes entirely.

In conclusion, we have shown that localized deposits of silicon nitride can be formed by electron bombardment of nitrogen molecules condensed on a cold silicon substrate. This process, which we have termed formation of silicon nitride structures by direct electron-beam writing, makes it possible to study,

without sputtering artifacts, silicon nitride films and silicon nitride/silicon interfaces under atomically clean conditions. This process also looks promising for VLSI applications.

#### V.L. Formation of Silicon Dioxide Structures by Direct Electron-Beam

##### Writing: Preliminary Results

Although the electron-stimulated oxidation of silicon has been studied by a number of workers,<sup>61</sup> all previous experiments have been performed on substrates at room temperature. At this temperature, electron-stimulated oxidation proceeds slowly<sup>61</sup>; furthermore, even at an ambient of  $1 \times 10^{-4}$  Torr  $O_2$ , the oxide thickness<sup>61</sup> is limited to  $\sim 16 \text{ \AA}$ . By chilling the substrate to cryogenic temperatures where multilayers of oxygen can condense onto the surface, there is the possibility of attaining faster oxidation rates and greater oxide thicknesses. Our main goal here is to explore this possibility for forming localized deposits. In addition, the electron-stimulated oxidation of Si(100) at cryogenic temperatures would provide an interesting comparison to our work on nitridation. In contrast to our anomalous results during the early stages of nitridation, the early stages of electron-stimulated oxidation at room temperature are fairly well behaved: the oxygen Auger intensity first increases linearly with exposure and then asymptotically approaches a saturation value.<sup>61</sup> It would be very interesting to see whether the oxidation kinetics at low temperatures show any anomalies.

Although our main interest here is in electron-stimulated oxidation at low temperatures, a considerable amount of background work must first be done. Due to its reactivity, oxygen presents special problems in ultrahigh vacuum work. The nature and extent of these problems varies with the

apparatus and must be determined for the vacuum system at hand. In addition, since Auger measurements of silicon dioxide films are plagued by electron-beam induced desorption,<sup>62</sup> the operational parameters for reliable measurements must be ascertained.

#### V.L.1. Chemisorption of Oxygen on Si(100) at Room Temperature

In our first runs, we wished to verify that exposure of Si(100) at room temperature to low pressures ( $< 1 \times 10^{-4}$  Torr  $O_2$ ) does not lead to oxidation provided that the surface is not electron bombarded during exposure. After the wafer, positioned in front of the CMA, had been exposed to oxygen from 5 min at  $1 \times 10^{-6}$  Torr to 30 min at  $1 \times 10^{-5}$  Torr, an Auger scan was taken when the background had dropped to  $< 1 \times 10^{-8}$  Torr. For our experiments, reagent-grade gas, supplied by Linde or Airco, was admitted into the chamber without further purification. Although hot filaments affect the rate of chemisorption,<sup>63</sup> both the ion gauge and Auger gun filaments were on during exposure since we are interested only in the final coverage. The Auger scan for the maximum exposure was the same as that for the minimum exposure; therefore, an exposure of 5 min at  $1 \times 10^{-6}$  Torr  $O_2$  was sufficient to form a saturation coverage, whose Auger spectrum is shown in Figs. 5.40 and 5.41. (Unless otherwise stated, the operating parameters for the Auger measurements here are those listed in Table 1; the C(KLL) and O(KLL) peaks are treated in the same manner as the N(KLL) peaks.) As we clearly see, the Si(LVV) spectrum is different from that of clean Si; however, there is no peak at 76 eV indicative<sup>12</sup> of  $SiO_2$ . Similar results have been observed for chemisorbed oxygen on<sup>10,61,64</sup> Si(111) and<sup>65</sup> Si(110).

Figure 5.40. Auger scan. Saturation coverage: chemisorbed  
oxygen on Si(100). Lock-in settings:  $\tau = 3\text{s}$ ,  
FS = 20  $\mu\text{V}$ .

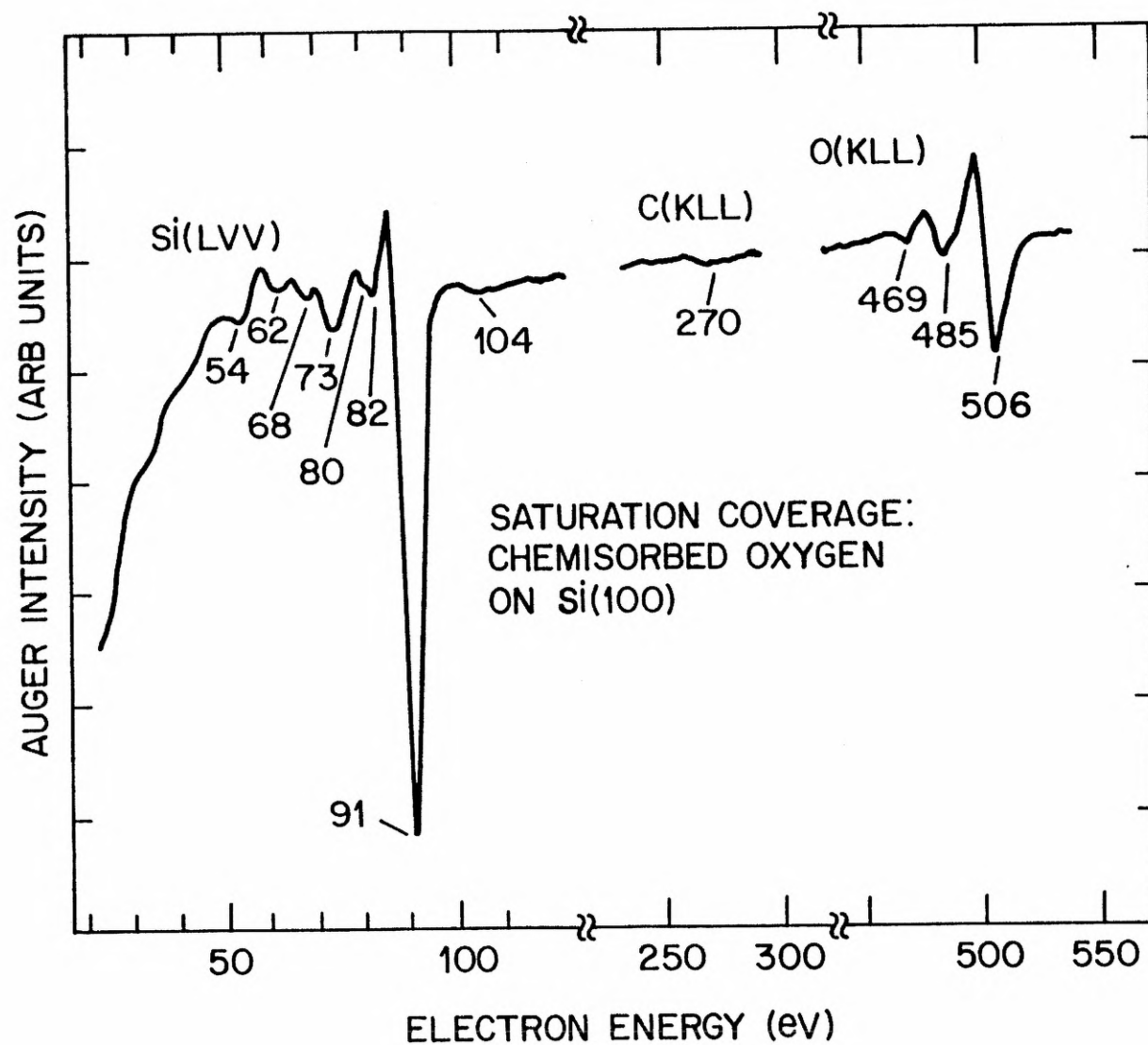
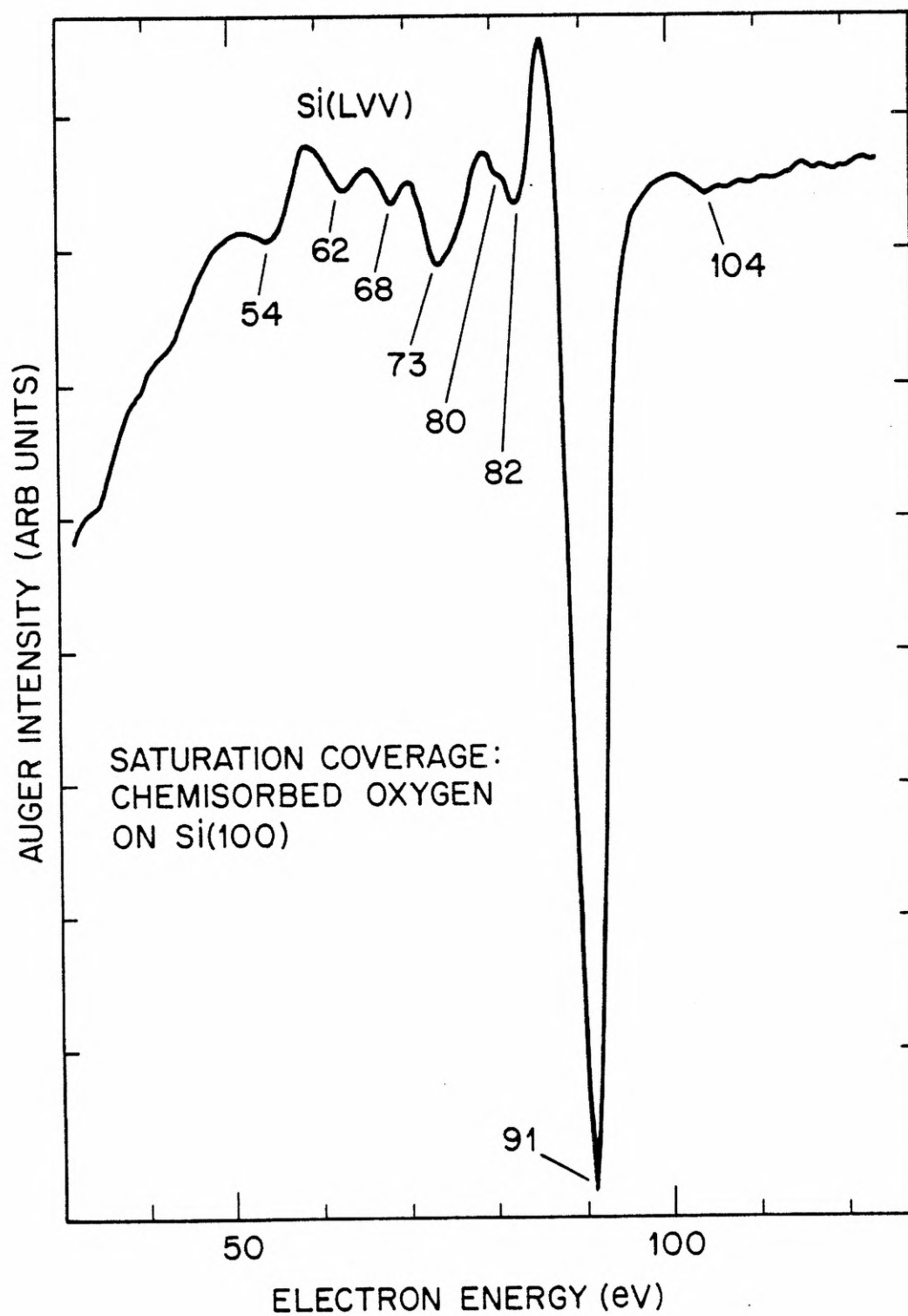


Figure 5.41. Auger scan. Saturation coverage: chemisorbed oxygen on Si(100). Close-up of Si(LVV) spectrum. Note absence of  $\text{SiO}_2$  peak at 76 eV.



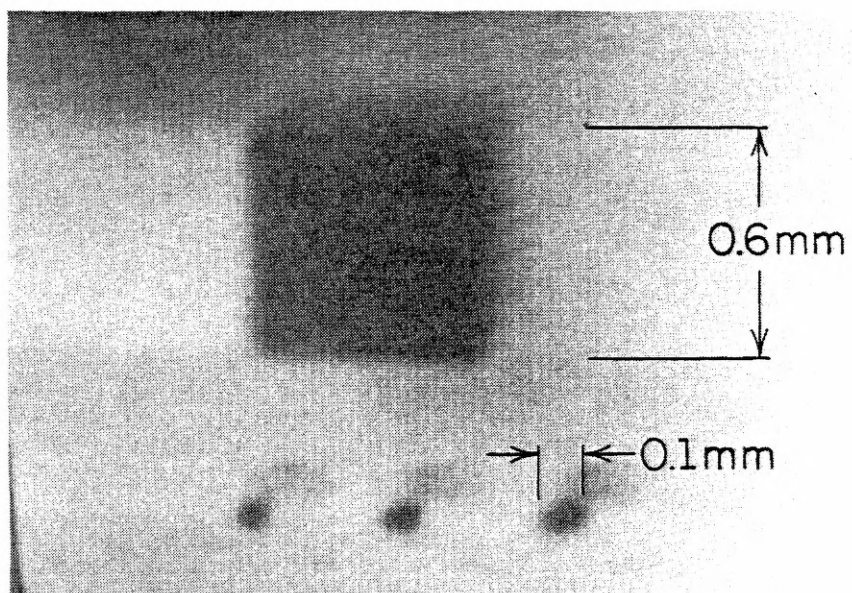
In these runs, a number of procedural problems immediately became apparent. The most serious, fortunately, was also transitory. After the first oxygen exposure, the Auger scan showed a significant carbon peak. We determined that the contamination did not arise from impurities in the dopant gas but from CO evolved by oxygen reacting with hot tungsten filaments<sup>66</sup>: after all the filaments had been aged in a  $1 \times 10^{-6}$  Torr  $O_2$  ambient for  $\sim 10$  h, subsequent runs showed very low carbon levels (Fig. 5.40 and following). Two other problems, however, were more persistent. First of all, once the chamber had been backfilled with oxygen, it pumped out very slowly. Several hours were needed to reach  $\sim 1 \times 10^{-8}$  Torr; furthermore, the base pressure,  $\sim 1 \times 10^{-10}$  Torr, could not be re-established unless the chamber walls were degassed overnight (the sample heater filament was used to 'internally bake-out' the chamber). Additionally, oxygen exposure seriously affected the emission characteristics of the Auger gun; after exposure, several hours were also needed for the beam current to stabilize. Although these problems were extremely irksome, they were sufficiently tractable. Oxygen did have one highly beneficent quality: once a silicon surface had been saturated with oxygen, it was very passive; Auger scans taken two days after the initial exposure showed no increase in carbon levels. So, sample contamination during the lengthy time needed for pump-down of the chamber and for re-equilibration of the beam current was negligible. Furthermore, Auger spectra could be measured in a background of  $\sim 1 \times 10^{-8}$  Torr without any artifacts. Ten Auger scans taken in succession from the same spot were reproducible within the noise: there were no indications either of electron-induced adsorption from the background or of electron-induced desorption.



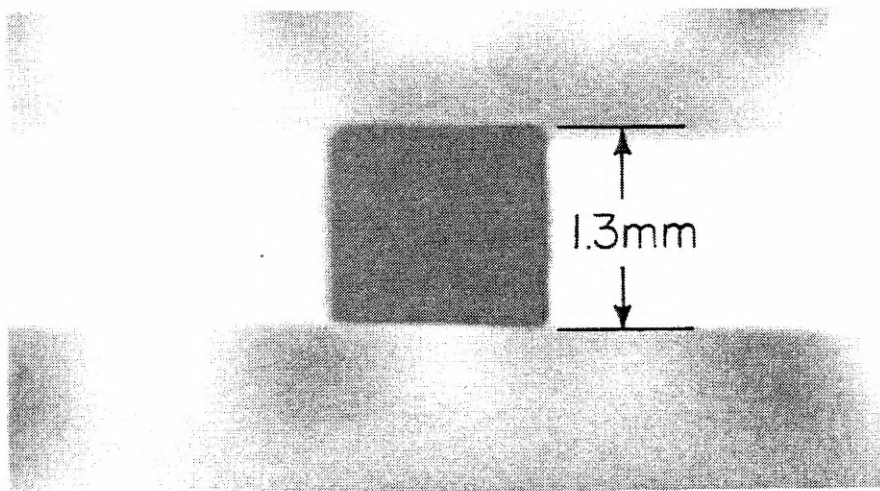
### V.L.2. Electron-Stimulated Oxidation at Room Temperature

At room temperature, localized deposits of  $\text{SiO}_2$  could be produced by electron bombardment of the wafer during exposure to oxygen (Fig. 5.42 (a)). For reliable Auger measurements, we took special precautions to avoid beam-induced desorption.<sup>62</sup> During these particular experiments, desorption effects were exacerbated by a decreased gain in the electron multiplier: to maintain high signal-to-noise in the Auger measurements, a high beam current ( $\sim 8 \mu\text{A}$ ) and a long time constant (1 - 3s) were necessary. If the beam was focussed into a 0.1 mm diameter spot, a second Auger scan taken immediately after the first indicated a pronounced desorption of oxygen. Desorption effects were minimized by rastering the beam into a  $0.6 \times 0.6$  mm square; in calibration runs, we determined that the high resolution of the CMA was maintained within this focal region. Under this procedure, Auger scans taken in succession indicated negligible desorption. To ensure a uniform region for analysis, however, an  $\text{SiO}_2$  patch  $\sim 1.3 \times 1.3$  mm square was needed. Since oxygen also decreased the electron emission from the Auger gun, beam current densities during the oxidation runs were considerably lower than those in the nitridation experiments. Consequently, even at the maximum exposure, 30 min at  $1 \times 10^{-5}$  Torr  $\text{O}_2$ , the oxide coverage was minimal; the Auger scan in Fig. 5.43 (b) shows only a small 76 eV peak. During exposure, the beam current ( $E_p = 2000$  eV) to the sample was  $\sim 3 \mu\text{A}$ ; the filament current was manually adjusted to maintain the beam current within  $\pm 0.3 \mu\text{A}$  throughout the run.

Figure 5.42. Adsorbed-current images. Silicon dioxide structures formed by direct electron-beam writing under an ambient of  $1 \times 10^{-5}$  Torr  $O_2$ . (a) Substrate at room temperature during exposure. Very light oxide layers yield poor contrast. (b) Substrate at  $T_B = 32^\circ$  K during exposure. Heavier oxide yields good contrast.

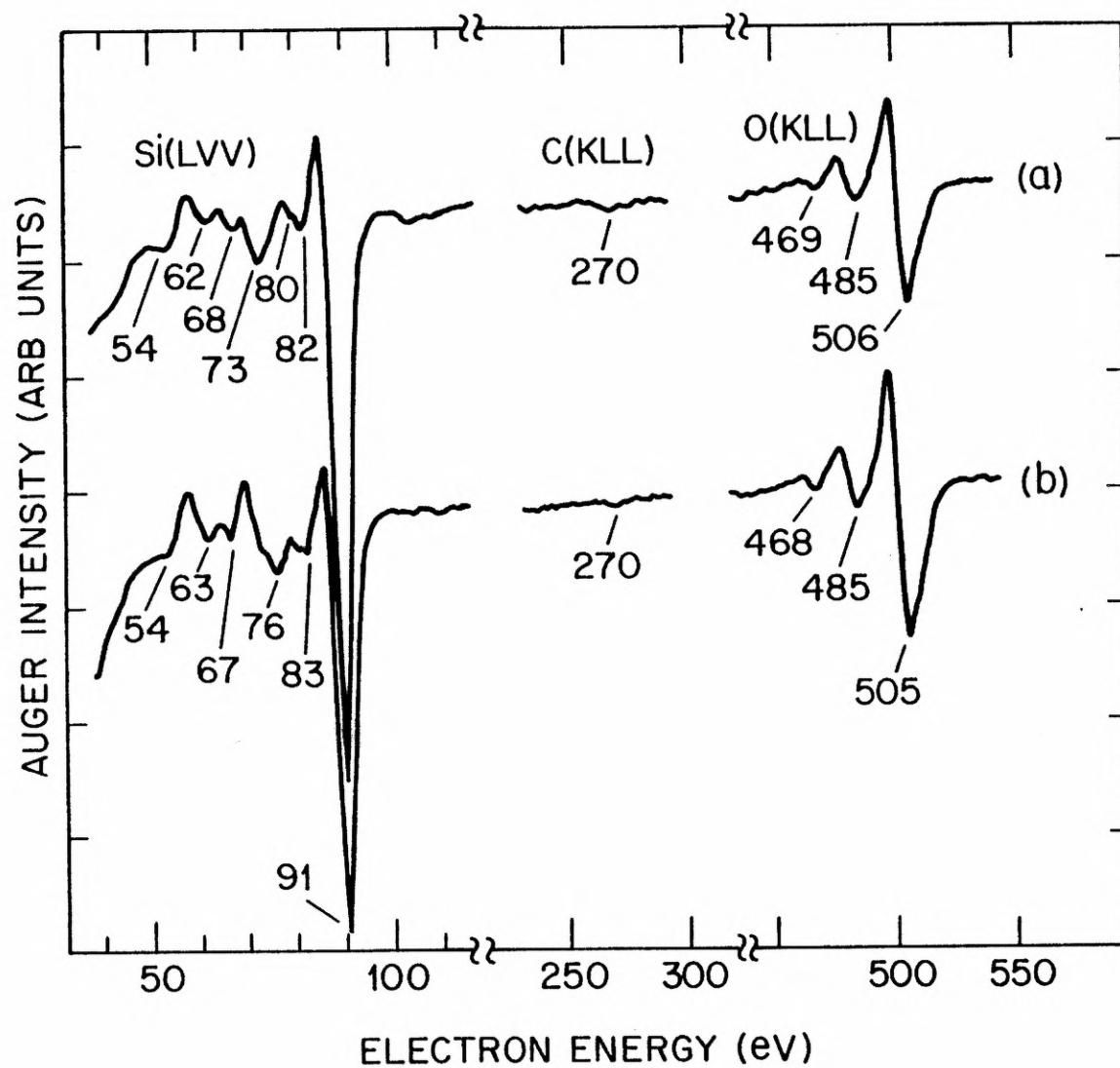


(a)



(b)

Figure 5.43. Auger scans. Si(100) wafer at room temperature exposed to  $1 \times 10^{-5}$  Torr  $O_2$  for 30 min. (a) No electron bombardment during exposure. (b) Continuous electron bombardment (primary energy = 2000 eV) during exposure. Lock-in settings:  $\tau = 3$  s, FS = 20  $\mu$ V.



### V.L.3. Electron-Stimulated Oxidation at Low Temperatures

In the first run, the sample was chilled to  $T_B = 32^\circ \text{ K}$  and subjected to the same exposure (30 min at  $1 \times 10^{-5}$  Torr  $\text{O}_2$ ) and bombardment (primary energy = 2000 eV, beam current = 3  $\mu\text{A}$  rastered into a  $1.3 \times 1.3$  mm square) as before. After the chamber had been pumped out, different regions were bombarded from 15 - 900 s (same beam conditions). At room temperature, the regions were located by adsorbed-current imaging for subsequent Auger analysis (Figs 5.42 (b) and 5.44). Comparing Figs. 5.43 (b) and 5.45 (b), we see that, for the same exposure and bombardment, considerably more oxide was formed at  $T_B = 32^\circ \text{ K}$  than at room temperature; using Eq. (5.1), we estimate the thickness of the film formed at  $T_B = 32^\circ \text{ K}$  to be  $\sim 5 \text{ \AA}$ . Note that the background scan in Fig. 5.45 (a) also contains a small 76-eV peak; however, it is not clear whether this is due to the initial low-temperature adsorption or to subsequent adsorption during the large pressure burst arising from evaporating oxygen as the sample-holder assembly was warmed. In Fig. 5.46, we compare Auger scans from patches bombarded for different times. For patches bombarded from 15 - 210 s, Auger scans showed only a marginal increase in adsorption over the background (Fig. 5.46 (a)). Bombardment times from 300 - 900 s produced a gradual increase in oxidation (Fig. 5.46 (b)-(d)); however, the coverages were considerably less than that attained by continuous bombardment during exposure (Fig. 5.46 (e)).

In a second run, we attempted to create a heavier oxide by increasing the ambient to  $1 \times 10^{-4}$  Torr  $\text{O}_2$ . At such a high pressure, the beam current dropped to only  $\sim 0.6 \mu\text{A}$ ; consequently, the resulting oxide was thinner than the one formed under  $1 \times 10^{-5}$  Torr  $\text{O}_2$  (Fig. 5.47).

Figure 5.44. Adsorbed-current image. Silicon dioxide structures formed at  $T_B = 32^\circ \text{ K}$  under various bombardment conditions. Each square measures  $1.3 \times 1.3 \text{ mm}$ .

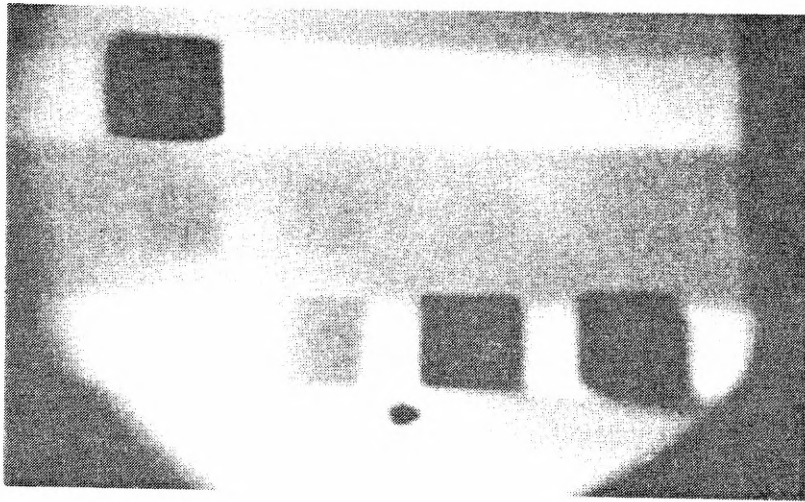




Figure 5.45. Auger scans. Si(100) wafer at  $T_B = 32^\circ \text{ K}$  exposed to  $1 \times 10^{-5}$  Torr  $\text{O}_2$  for 30 min. Auger scans taken at room temperature. (a) No electron bombardment during exposure. (b) Continuous electron bombardment (primary energy = 2000 eV) during exposure. Lock-in settings:  $\tau = 3 \text{ s}$ ,  $\text{FS} = 20 \text{ } \mu\text{V}$ .

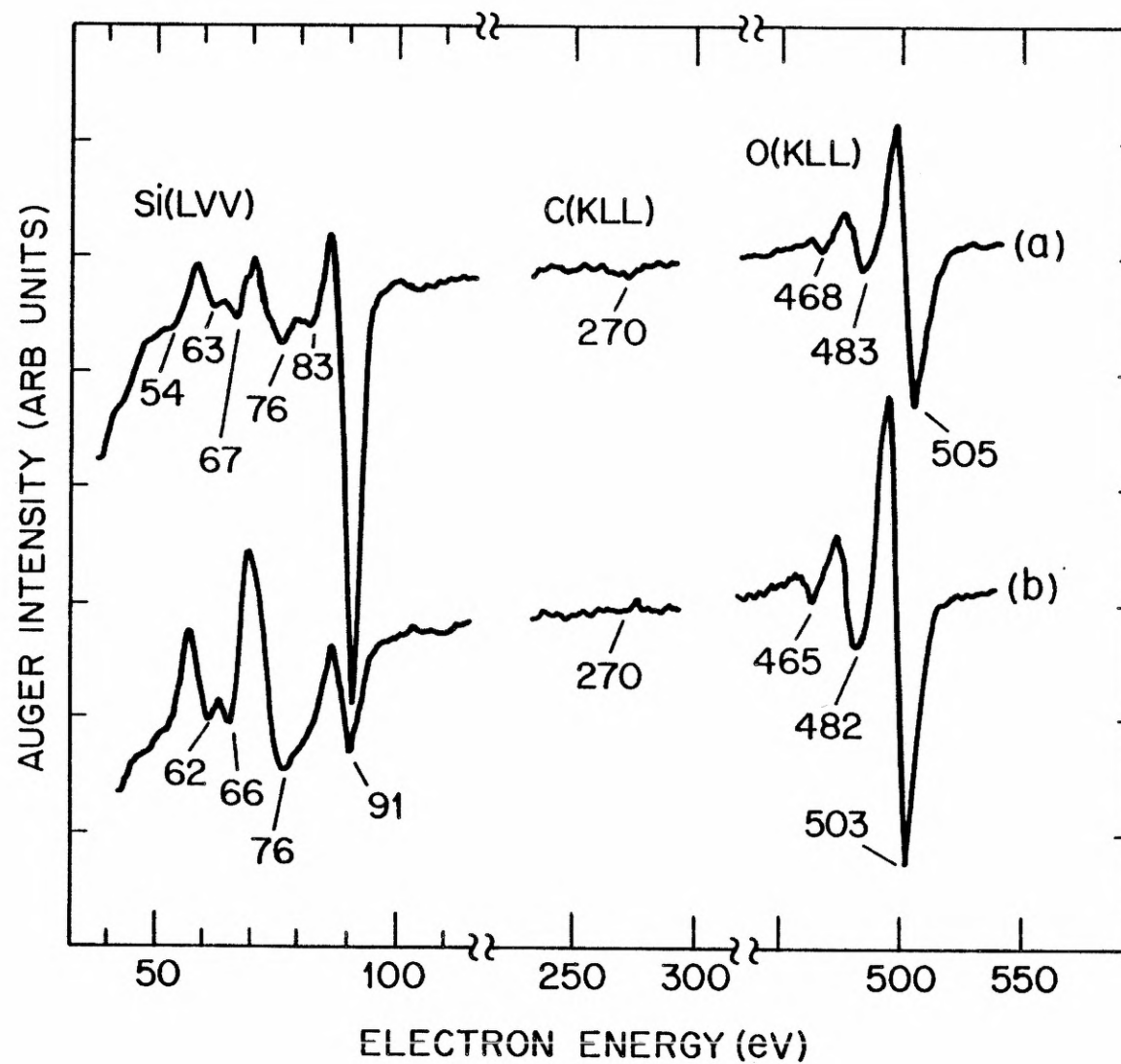


Figure 5.46. Auger scans. Si(100) wafer at  $T_B = 32^\circ \text{ K}$  exposed to  $1 \times 10^{-5}$  Torr  $\text{O}_2$  for 30 min. (a) No electron bombardment during or after exposure. (b) 300-s electron bombardment after exposure. (c) 600-s electron bombardment after exposure. (d) 900-s electron bombardment after exposure. (e) Continuous electron bombardment during exposure. Primary energy for electron bombardment = 2000 eV. Auger scans taken at room temperature. Modulation voltage =  $2 V_{\text{p-p}}$  for all scans. Lock-in settings: (X1)  $\tau = 1 \text{ s}$ , FS = 100  $\mu\text{V}$ ; (X2)  $\tau = 1 \text{ s}$ , FS = 50  $\mu\text{V}$ ; (X5)  $\tau = 3 \text{ s}$ , FS = 20  $\mu\text{V}$ .

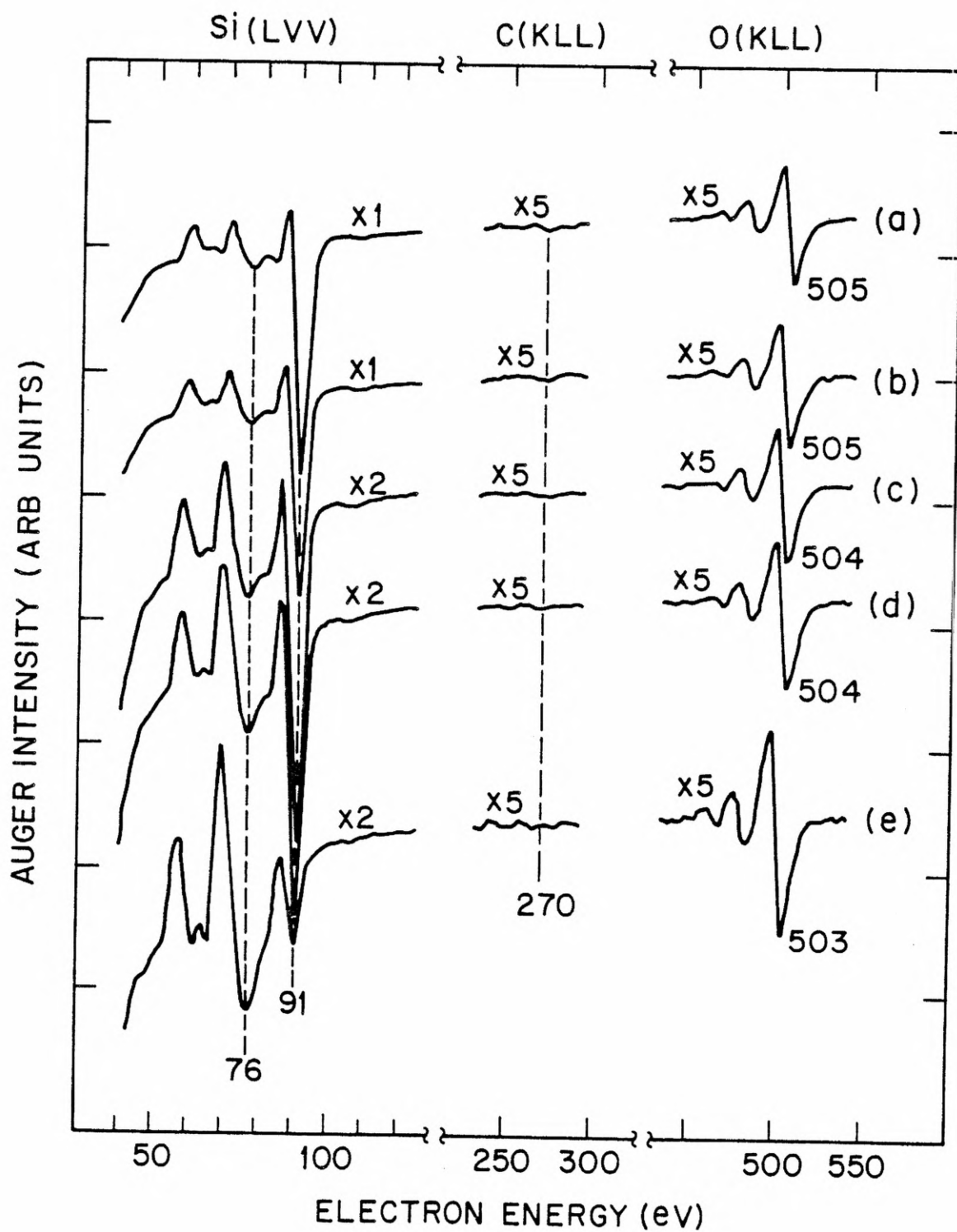
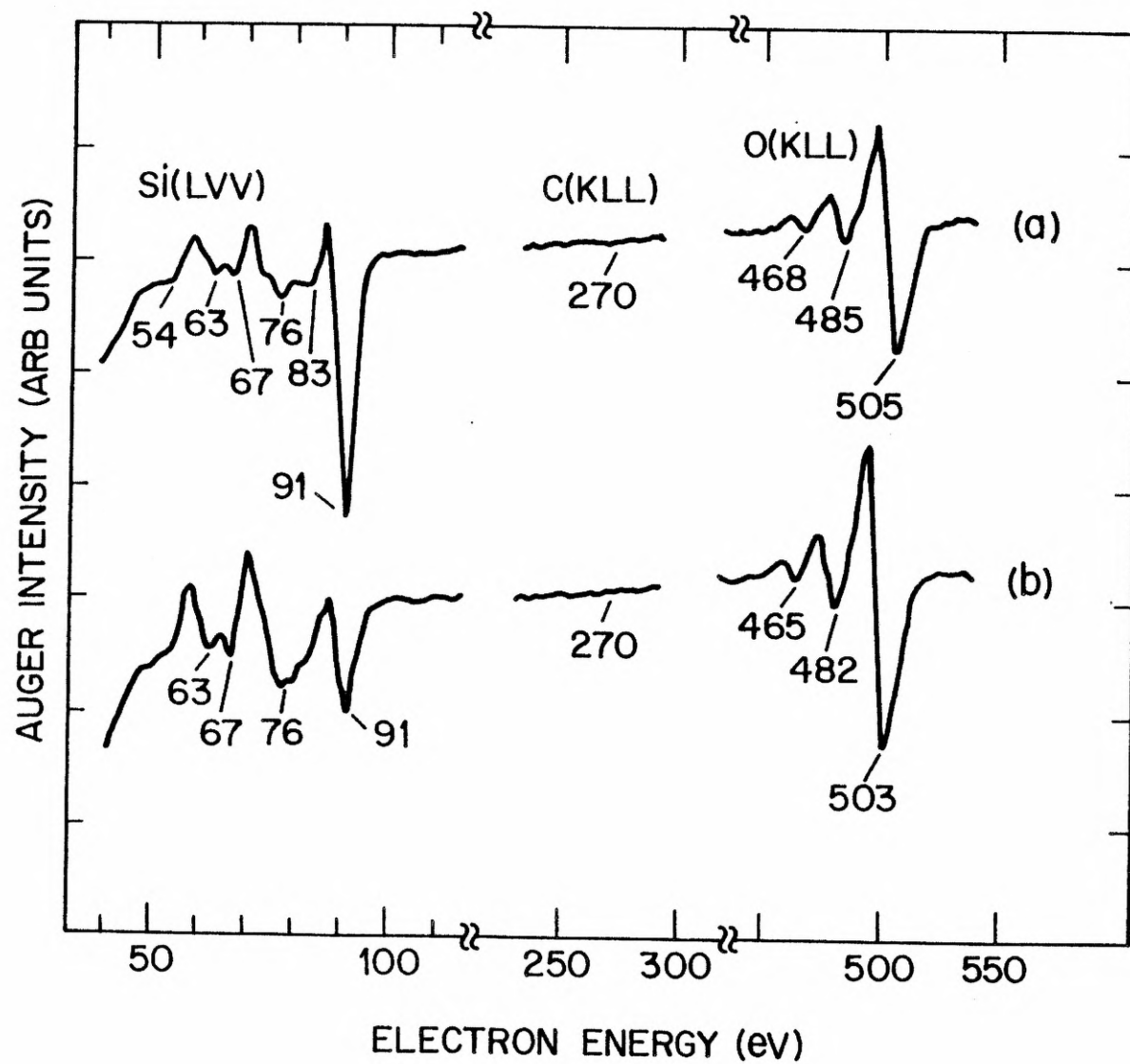


Figure 5.47. Auger scans. Si(100) wafer at  $T_B = 32^\circ \text{ K}$  exposed to  $1 \times 10^{-4}$  Torr  $\text{O}_2$  for 30 min. Auger scans taken at room temperature. (a) No electron bombardment during exposure. (b) Continuous electron bombardment (primary energy = 2000 eV) during exposure. Lock-in settings:  $\tau = 3 \text{ s}$ ,  $\text{FS} = 20 \text{ } \mu\text{V}$ .



Two final observations. First of all, the main O(KLL) peak shifts from 506 eV for the chemisorbed state (Fig. 5.40) to 503 eV for the highest oxide coverage (Fig. 5.45 (b)). This shift is not a measurement artifact: previous work has established that the O(KLL) spectrum is very sensitive to the chemical environment.<sup>67,68</sup> Secondly, in all the Auger spectra, the carbon levels are very low--within or just above the noise level. In particular, the carbon level never increased with electron bombardment during exposure (in fact, it often appeared to decrease). Our results do not support Morgen's<sup>65</sup> contention that electron-stimulated oxidation of silicon occurs via intermediate reactions between oxygen and beam-deposited surface carbon; in his experiments on Si(110), the carbon level increased as the wafer was simultaneously exposed to oxygen and bombarded with electrons. We believe that our results are indicative of more careful vacuum processing, resulting in lower background CO contamination.

#### V.L.4. Summary: Oxygen on Si(100)

At room temperature, for exposures ranging from 5 min at  $1 \times 10^{-6}$  Torr  $O_2$  to 30 min at  $1 \times 10^{-5}$  Torr  $O_2$ , a saturation layer of chemisorbed oxygen is formed if the silicon surface is not bombarded with electrons during exposure. In addition to being resistant to background contamination, this chemisorbed layer is stable with respect to electron bombardment under vacuum. Simultaneous electron bombardment during exposure results in the formation of  $SiO_2$ , as indicated by the growth of a 76-eV peak in the Si(LVV) Auger spectrum. For the same exposure and bombardment, considerably more oxide is formed with the substrate at  $T_B = 32^\circ$  K than at room temperature. As noted by others, oxygen

in the  $\text{SiO}_2$  state is readily desorbed by electron bombardment; therefore, special precautions must be observed for reliable Auger measurements. Through prolonged outgassing of all hot filaments in an oxygen ambient, we are able to reduce background CO to minimal levels; consequently, electron-stimulated oxidation proceeds without the simultaneous growth of a beam-deposited carbon layer. Our results clearly demonstrate that the formation of silicon dioxide structures by direct electron-beam writing is a viable process. For further development, a molecular beam source is essential for dosing the sample: to avoid lengthy pump-downs and to maintain stable emission from electron guns, the background pressure should be kept below  $1 \times 10^{-6}$  Torr  $\text{O}_2$  throughout the run.



## REFERENCES FOR CHAPTER V

1. M. F. Chung and L. H. Jenkins, *Surf. Sci.* 26, 649 (1971).
2. W. Monch, in Festkorperprobleme XIII, edited by H. J. Queisser (Friedr. Viewig, Braunschweig, 1973), pp. 241-274.
3. D. R. Arnott and D. Haneman, *Surf. Sci.* 45, 128 (1974).
4. N. Kasupke and M. Henzler, *Surf. Sci.* 92, 407 (1980).
5. G. Ehrlich and F. G. Hudda, *J. Chem. Phys.* 35, 1421 (1961).
6. See, for example, T. Sakurai and H. D. Hagstrum, *Phys. Rev. B* 20, 2423 (1979).
7. H. F. Winters, D. E. Horne, and E. E. Donaldson, *J. Chem. Phys.* 41, 2766 (1964).
8. H. E. Bishop and J. C. Riviere, *Surf. Sci.* 17, 462 (1969).
9. For a recent reivew, see H. H. Madden, *J. Vac. Sci. Technol.* 18, 677 (1981).
10. See, for example, M. C. Munoz, V. Martinez, J. A. Tagle, and J. L. Sacedon, *Phys. Rev. Lett.* 44, 814 (1980) and references therein.
11. W. M. Mularie and W. T. Peria, *Surf. Sci.* 26, 125 (1971).
12. R. Hezel and N. Lieske, *J. Appl. Phys.* 51, 2566 (1980).
13. J. A. Taylor, *Appl. Surf. Sci.* 7, 168 (1981).
14. J. F. Delord, A. G. Schrott, and S. C. Fain, Jr., *J. Vac. Sci. Technol.* 17, 517 (1980).
15. C. C. Chang, in Characterization of Solid Surfaces, edited by P. F. Kane and G. B. Larrabee (Plenum Press, New York, 1974), Chap. 20, pp. 509-575.
16. J. E. Houston, *Surf. Sci.* 38, 283 (1973).
17. L. A. Harris, *J. Appl. Phys.* 39, 1419 (1968).
18. R. E. Weber and A. L. Johnson, *J. Appl. Phys.* 40, 314 (1969).

19. Of the many examples available in the literature, two illustrative examples are E. Kny, J. Vac. Sci. Technol. 17, 658 (1980) and J. P. Biberian and G. A. Somorjai, Appl. Surf. Sci. 2, 352 (1979). See, also, the careful discussion by J. T. Grant, T. W. Haas, and J. E. Houston, Surf. Sci. 42, 1 (1974).
20. M. P. Seah, Surf. Sci. 32, 703 (1972).
21. M. G. Barthes and G. E. Rhead, J. Phys. D 13, 747 (1980).
22. F. Pons, J. Le Hericy, and J. P. Langeron, Surf. Sci. 69, 565 (1977).
23. C. C. Chang, J. Vac. Sci. Technol. 18, 276 (1981).
24. An excellent comparison between differentiated and undifferentiated structures is given in Ref. 9.
25. G. G. Tibbetts, J. Chem. Phys. 70, 3600 (1979).
26. G. E. Rhead, M.-G. Barthes, and C. Argile, Thin Solid Films 82, 201 (1981).
27. J. P. Biberian and G. A. Somorjai, Appl. Surf. Sci. 2, 352 (1979).
28. For a review of thin-film growth, see J. A. Venables and G.L. Price, in Epitaxial Growth, Part B, edited by J. W. Matthews (Academic Press, New York, 1975), Chap. 4, pp. 381-436.
29. The growth of metal oxides and the effects of space charge have been comprehensively treated by A. T. Fromhold, Jr., Theory of Metal Oxidation,
  - (a) Volume I-Fundamentals (North-Holland, Amsterdam, 1976)
  - (b) Volume II-Space Charge (North-Holland, Amsterdam, 1980).
30. See, for example, C. J. Powell Surf. Sci. 44, 29 (1974).
31. C. M. Garner, I. Lindau, C. Y. Su, P. Pianetta, and W. E. Spicer, Phys. Rev. B 19, 3944 (1979).
32. J. A. Venables, J. Derrien, and A. P. Janssen, Surf. Sci. 95, 411 (1980).

33. G. Honjo and K. Yagi, in Current Topics in Materials Science, V.6, edited by E. Kaldis (North-Holland, Amsterdam, 1980), Chap. 3, pp. 195-307.
34. See, for example, J. B. Pendry, Low Energy Electron Diffraction (Academic Press, London, 1974).
35. C. C. Chang, Appl. Phys. Lett. 31, 304 (1977).
36. A. Sepulveda and G. E. Rhead, Surf. Sci. 66, 436 (1977).
37. See, for example, S. J. White, D. P. Woodruff and L. McDonnell, Surf. Sci. 72, 77 (1978).
38. C. F. Eagen and E. N. Sickafus, Rev. Sci. Instrum. 48, 1269 (1977).
39. See, for example, H.-J. Fitting, H. Glaefke, W. Wild, and G. Neumann, J. Phys. D. 9, 2499 (1976).
40. S. Ichimura, M. Aratama, and R. Shimizu, J. Appl. Phys. 51, 2853 (1980).
41. J. M. Blakely, Introduction to the Properties of Crystal Surfaces (Pergamon Press, Oxford, 1973), p. 248.
42. K. R. Lawless, Rep. Prog. Phys. 37, 231 (1974).
43. D. Kashchiev, J. P. Van der Eerden, and C. Van Leeuwen, J. Crystal Growth 40, 47 (1977).
44. H. M. Jennings, J. O. Edwards, and M. H. Richman, Inorganica Chimica Acta 20, 167 (1976).
45. B. Lang, P. Scholler, and B. Carriere, Surf. Sci. 99, 103 (1980).
46. M. C. Munoz, V. Martinez, J. A. Tagle, and J. L. Sacedon, J. Phys. C 13, 4247 (1980).
47. M. Chen, I. P. Batra, and C. R. Brundle, J. Vac. Sci. Technol. 16, 1216 (1979).
48. See, for example, T. N. Rhodin and D. L. Adams, in Treatise on Solid State Chemistry, V. 6A, edited by N. B. Hannay (Plenum Press, New York, 1976), Chap. 5, pp. 343-484.

49. See, for example, S. Dushman, Scientific Foundations of Vacuum Technique, second edition (John Wiley, New York, 1962), p. 14.
50. C. J. Powell, Surf. Sci. 44, 29 (1974).
51. J. Szajman, J. G. Jenkin, J. Liesegang, and R. C. G. Leckey, J. Electron Spectrosc. Relat. Phenom. 14, 41 (1978).
52. M. Klasson, A. Berndtsson, J. Hedman, R. Nilsson, R. Nyholm, and C. Nordling, J. Electron Spectrosc. Relat. Phenom. 3, 427 (1974).
53. For reviews on gas-surface interactions, see, for example,
  - (a) W. A. Steele, The Interaction of Gases with Solid Surfaces (Pergamon Press, Oxford, 1974).
  - (b) G. M. Rosenblatt, in Treatise on Solid State Chemistry, V. 6A, edited by N. B. Hannay (Plenum Press, New York, 1976), Chap. 3, pp. 165-240.
  - (c) G. A. Somorjai, in Surface Science, V.I (International Atomic Energy Agency, Vienna, 1975), pp. 173-263.
54. T. E. Madey and J. T. Yates, Jr., J. Vac. Sci. Technol. 8, 525 (1971).
55. D. Rapp and P. Englander-Golden, J. Chem. Phys. 43, 1464 (1965).
56. D. Rapp, P. Englander-Golden, and D. D. Briglia, J. Chem. Phys. 42, 4081 (1965).
57. A. J. Polak, Ph.D. Thesis, University of Illinois at Urbana-Champaign (1977).
58. P. H. Holloway, T. E. Madey, C. T. Campbell, R. R. Rye, and J. E. Houston, Surf. Sci. 88, 121 (1979).
59. Y. E. Strausser and J. S. Johannessen, in Semiconductor Measurement Technology: ARPA/NBS Workshop IV. Surface Analysis for Silicon Surfaces, edited by A. G. Lieberman (NBS Special Publication 400-23, 1976), pp. 125-138.

60. H. S. W. Massey, E. H. S. Burhop, and H. B. Gilbody, editors,  
Electronic and Ionic Impact Phenomena, V.II. Electron Collisions with  
Molecules and Photo-Ionization (Oxford, Clarendon Press, 1969), p. 978.
61. M. C. Munoz and J. L. Sacedon, J. Chem. Phys. 74, 4693 (1981); see, also,  
references therein.
62. S. Thomas, J. Appl. Phys. 45, 161 (1974).
63. F. Meyer and M. J. Sparnaay, in Surface Physics of Phosphors and  
Semiconductors, edited by C. G. Scott and C. E. Reed (Academic Press,  
London, 1975), Chap. 6, pp. 321-410.
64. M. C. Munoz, V. Martinez, J. A. Tagle, and J. L. Sacedon, J. Phys. C.  
13, 4247 (1980).
65. P. Morgen, J. Vac. Sci. Technol 18, 908 (1981).
66. R. E. Schlier, J. Appl. Phys. 29, 1162 (1958).
67. B. Carriere and B. Lang, Surf. Sci. 64, 209 (1977).
68. P. Legare, G. Maire, B. Carriere, and J. P. Deville, Surf. Sci. 68,  
348 (1977).

## VITA

Brymer Han-Yu Chin was born in Brookline, Massachusetts, on October 5, 1952. After graduating from Boston Latin School in May, 1970, he entered the Massachusetts Institute of Technology with a National Merit Special Scholarship from the Gillette Company. At M.I.T., he majored in physics and graduated with a Bachelor of Science degree in May 1974; his bachelor's thesis, entitled On the Propagation of Heat Pulses in Germanium, was supervised by Professor M.W.P. Strandberg. In August, 1974, he then entered the Physics Department of the University of Illinois at Urbana-Champaign with a Graduate Fellowship. Since receiving his Master of Science degree in May, 1975, he has been pursuing graduate research with Professor Gert Ehrlich. They are co-authors of the publication

"Formation of Silicon Nitride Structures by Direct Electron Beam Writing," Brymer H. Chin and Gert Ehrlich, Appl. Phys. Lett. 38, 253 (1981).